APPLIED COMPUTATIONAL ELECTROMAGNETICS SOCIETY JOURNAL

August 2013
Vol. 28 No. 8
ISSN 1054-4887

The ACES Journal is abstracted in INSPEC, in Engineering Index, DTIC, Science Citation Index Expanded, the Research Alert, and to Current Contents/Engineering, Computing & Technology.

The illustrations on the front cover have been obtained from the research groups at the Department of Electrical Engineering, The University of Mississippi.

AUGUST 2013 REVIEWERS

Osama Abo-SeidaIftikhar
Mohamed Abouzahra
Abdul Ali Babar
Sami Barmada
Toni Bj
Kyle Byers
William Coburn
Satya Dubey
He Huang
Haider Khaleel
Branko Koprivica
Zamzam Kordiboroujeni
Jerome Glaser
Anan Kruesubthaworn
Chao Li
Angelo Liseno
Truong Khang Nguyen
wang song
Yasuhiro Tsunemitsu
Fan Yang
Xiaohua Yi
Qiang Yu
Amir Zaghloul
Hua Zeng
Zhi-Li Zhou

THE APPLIED COMPUTATIONAL ELECTROMAGNETICS SOCIETY

JOURNAL

Vol. 28 No. 8 August 2013

TABLE OF CONTENTS

Time Domain Analysis of Ultra-Wide Band Signals from Buried Objects Under Flat and Slightly Rough Surfaces

S. MakalYucedag and A. Kizilay

Department of Electronics and Communications Engineering
Yildiz Technical University, Istanbul, 34349, Turkey
smakal@yildiz.edu.tr and akizilay@yildiz.edu.tr

***Abstract* ─** The analysis of transient scattering for TM_z (horizontally) polarization from a cylindrical perfectly conducting (PEC) object buried in a lossy medium is considered. Flat and slightly surface cases are considered for the dielectric half-space. Our previous work using a decomposition method solution in frequency domain of TM_z polarization is utilized to solve this scattering problem. Then, an inverse Fourier transform is used to get the time domain signals. Timing analysis is done by calculating the travelling time of reflected signals in the possible paths. Then, multiple reflections are identified using these travelling times. Finally, the results from the flat and slightly rough surface profiles are used to compare the effects of multipath propagation.

Index Terms - Buried object, electromagnetic scattering, and multipath analysis.

I. INTRODUCTION

There exists much interest in ground penetrating radar (GPR). Therefore, significant attention has been directed toward the study of scattering from buried targets and several techniques have been employed to calculate the scattered fields [1-5]. Then, these results are used to obtain information for buried objects and design new GPR systems [6-13].

Recently, the applications of GPR using ultra-wideband (UWB) short-pulse radars attract more interest than the ones using narrow-band radars [14-22]. This is because the field scattered by targets illuminated by an UWB short pulse contains information such as location, strength of diffracting centers, dispersive phenomena and resonances [23]. Also, if buried targets are interrogated by an UWB short pulse, clutter and multipath interference in received signal are reduced [24]. In order to examine the scattering of UWB short-pulse radars signal from buried targets, UWB short-pulse plane-wave scattering from buried PEC object is considered in this study. Also, to understand the effect of the surface roughness on UWB scattering, flat, and slightly rough surface profiles are used.

Consider a TM_z plane wave with the incident angle ϕ_i and it is assumed to be incident on a cylindrical object of arbitrary cross-section buried in a two-dimensional infinite surface as shown in

Fig. 1. A PEC object is located h_c below the x-axis. The distance between the y-axis and the object axis is indicated by x_c, the height and width of one period of the rough surface are represented by h_p and w_p, respectively.

Previously, a decomposition solution method has been obtained for the electromagnetic field scattered by a PEC cylindrical object with an arbitrary cross-section buried in a lossy dielectric half space with flat surface in [25] and periodic surface in [26]. Using this solution method, the scattered electric field is obtained in an ultra-wide frequency band, and then the time-domain scattered fields are synthesized via inverse Fourier transform. Finally, these scattering results are used to investigate the effects of multipath.

II. MULTIPATH ANALYSIS

To analyze the multiple reflections from a PEC cylindrical object buried in a sinusoidal surface, initially the scattering from a cylinder under a flat surface is considered. Gathering the basic knowledge of the multipath phenomenon

Submitted On: June 29, 2012
Accepted On: Aug. 29, 2013

from the flat surface model, the analysis extended to a sinusoidal periodic surface case.

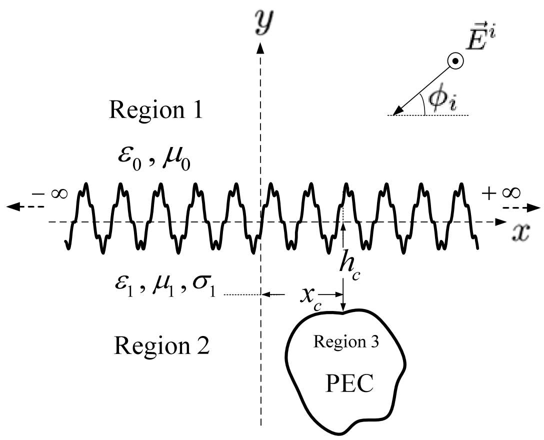

Fig. 1. Geometry of cylindrical object buried inside a lossy half-space with periodic surface.

The geometries and parameters of the buried PEC cylinder in medium with flat and sinusoidal surface indicated in Fig. 2 (a) and (b) are used for time domain results. As seen in these figures, the object is chosen to be a PEC cylinder with circular cross-section of radius r_a. The surface represents by,

$$y(x) = h_p \cos\left(2\pi x / w_p\right). \tag{1}$$

The transient signal scattered by a buried PEC cylinder's temporal characteristics can be identified easily using ray tracing. For the normal incidence ($\phi_i = 90^0$), the first two reflections from a cylinder under an infinite flat surface are shown in

Fig. 3. The first one is coming from the cylinder (L_1) and the second one is coming from the flat surface-cylinder-flat surface path (L_2). The time passing between these two reflections is calculated by

$$\Delta t_{1c} = \frac{\left(L_2 - L_1\right)\sqrt{\varepsilon_{r1}}}{c}, \tag{2}$$

where ε_{r1} is the relative permittivity of the medium and c is the speed of light in space [20]. It is expected to have more reflections because of multiple bounce of the signal between the surface and the target. Other reflection's travelling paths are going to be multiples of L_1. Therefore, the time past between two successive reflections can be calculated by a generalized form of equation (2),

$$\Delta t_c = \frac{L_1\sqrt{\varepsilon_{r1}}}{c}. \tag{3}$$

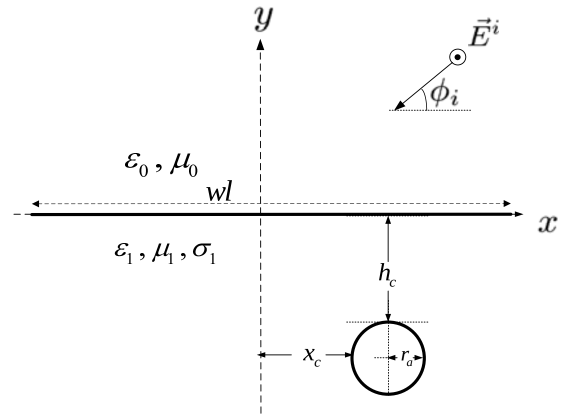

(a)

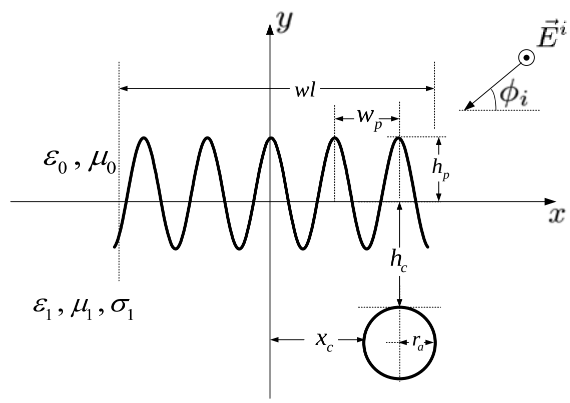

(b)

Fig. 2. The medium with (a) flat surface and (b) sinusoidal surface.

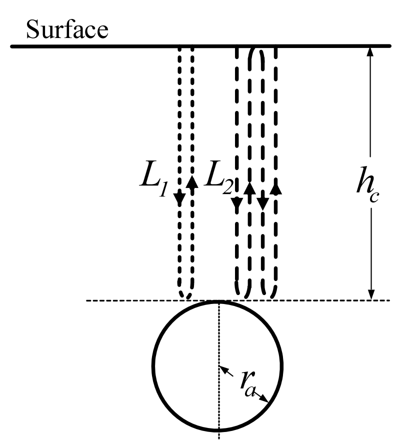

Fig. 3. Expected reflections from a buried cylindrical object.

III. TIME DOMAIN RESULTS

The incident signal is constructed from a frequency spectrum of 1-30 GHz with 726 data points. This frequency data is weighted using a double Gaussian function,

$$W_{dg}(f)=\sqrt{\frac{\pi}{\alpha_1}}a_1\exp\left(-\frac{(\pi f)^2}{\alpha_1}\right)-\sqrt{\frac{\pi}{\alpha_2}}a_2\exp\left(-\frac{(\pi f)^2}{\alpha_2}\right) \quad (4)$$

$$\alpha_1=\frac{\pi}{\tau_1^2}\ ,\ \alpha_2=\frac{\pi}{\tau_2^2}\ , \quad (5)$$

$$a_1=\frac{\sqrt{\alpha_1}}{\sqrt{\alpha_1}-\sqrt{\alpha_2}}\ ,\ a_2=\frac{\sqrt{\alpha_2}}{\sqrt{\alpha_1}-\sqrt{\alpha_2}}\ , \quad (6)$$

with the values of $\tau_1 = 0.04 \times 10^{-9}$ and $\tau_2 = 0.0625 \times 10^{-9}$ and shown in Fig. 4 (a). Then, the weighted frequency data is transformed into time domain using an inverse Fourier transform. The resulting transient incident TM_z signal is shown in Fig. 4 (b). The backscattered field from a PEC cylinder in free space is shown in both the frequency and time domains in Fig. 5. As expected the reflected field has a sign change because of a single reflection from a PEC surface seen in time domain result in Fig. 5 (b).

The backscattered field from a buried PEC cylinder is shown in time domain in Fig. 6. In Fig. 6, $L_1 = 2h_c$, $L_2 = 2L_1$, and ε_{r1} is chosen as 15. In TableI, the time past between two signals calculated by using equation (3) and the time found from the figure are indicated by Δt_c and Δt_r, respectively. In the figures, ϕ_s is the scattering angle. To investigate the effect of the burial depth of the cylinder, it is located nearer to the surface than the one in Fig. 6. Then, the backscattered field is calculated and shown in time domain in Fig. 7. It is observed that the time between the reflections decreases. There are four main reflections following the paths L_1, L_2, L_3, and L_4. Here, $L_1 = 2h_c$, $L_2 = 2L_1$, $L_3 = 3L_1$, $L_4 = 4L_1$, and TableII shows the comparison of timings.

The effect of the medium loss to the time domain signal is shown in Fig. 8. As expected, as the loss of the medium increases, the amplitude of the scattered field decreases. To investigate effect of the incidence angle on the scattered field, the incident angle is chosen as $\phi_i = 20^0$. Then, the backscattered field is calculated and shown in time domain in Fig. 9. The time between the successive reflections can be calculated by,

$$\Delta t_c' = \frac{L_1\sqrt{\varepsilon_{r1}}}{\sin(\phi_t)c} \quad (7)$$

where ϕ_t is the angle measured from normal of the surface and found as $\phi_t = 14^0$. The comparison of timings is given in

TableIII.

The backscattered field from a PEC cylinder under a slightly rough surface is shown in Fig. 10 to 13. In Fig. 10, the expected paths are L_1, L_2, L_3, L_4, L_5. For the slightly rough surface case, the roughness should be included in the timing analysis so $L_1=h_c+h_p$ and the lengths of other paths are multiples of L_1. The signals are assumed to travel the same paths as the signals in the flat surface case. The comparisons of timings for Fig. 10 are given in TableIV. The results are very close to flat surface results. To investigate the effect of the depth of the object, the object is buried deeper and the result is shown in Fig. 11. The expected paths are L_1, L_2, and L_3. The comparisons of timings for Fig. 11 are given in TableV. As it is expected the number of signals is reduced because the signals travel greater distances and as a result attenuate more. However, the results are still very close to flat surface results.

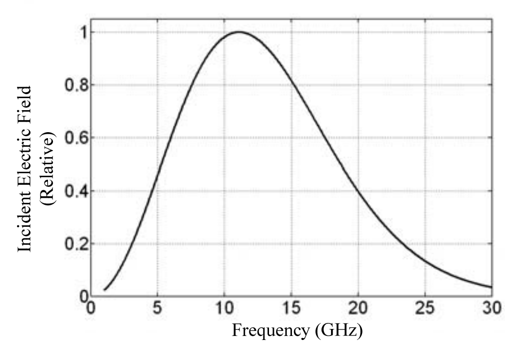

(a)

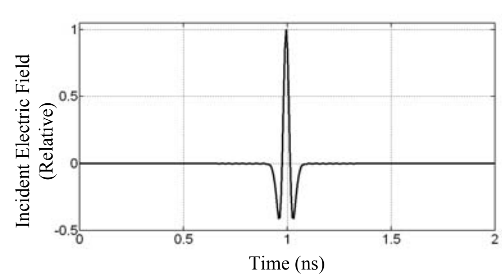

(b)

Fig. 4. The incident E-field waveform (a) in frequency and (b) time domains.

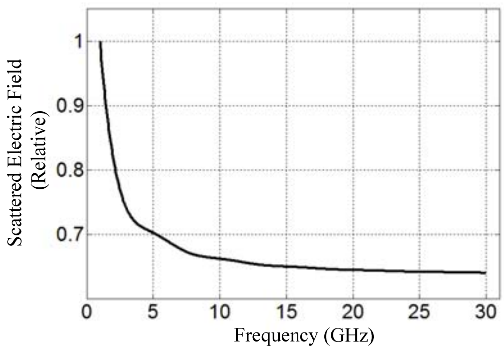

(a)

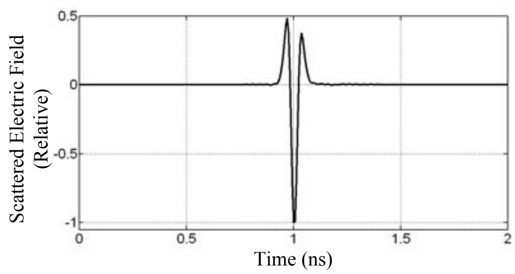

(b)

Fig. 5. TM_z backscattered field from a cylindrical PEC object with r_a = 0.01 m (a) at frequency and (b) time domains.

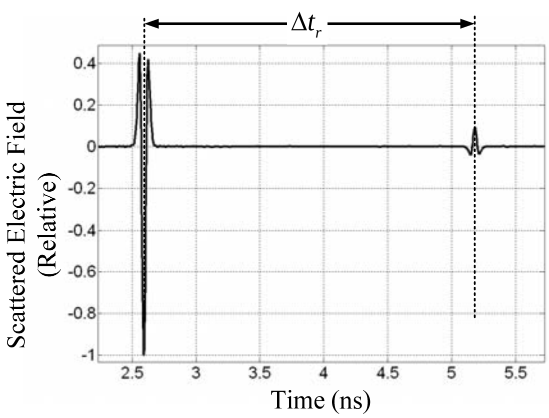

Fig. 6. TM_z backscattered field from a buried cylindrical PEC object for r_a = 0.01 m, h_c = 0.1 m, wl = 2 m, x_c / r_a = 0.0, $\varepsilon_1 = 15\ \varepsilon_0$ F/m, $\mu_1 = \mu_0$ H/m, $\phi_i = \phi_s = 90^0$, and σ_1 = 0.001 Sm^{-1}.

Table I: Comparison of timings for the case shown in Fig. 6.

Δt_c ***(ns)***	Δt_r ***(ns)***
2.582	2.594

The depth of the object is increased and results are shown in Fig. 12 and 13, for $\phi_i = \phi_s = 90^0$ and $\phi_i = \phi_s = 20^0$, respectively. But the results are very complicated compare to the flat surface results. It is observed that the surface roughness started to affect the scattered field greatly because the incident wave can find more paths to reflect from the object. The relative time Δt_r between this two groups are found from Fig. 12 and 13 as 2.6260 ns and 2.8420 ns, respectively. These time values are similar to the case of flat surface found from Fig. 6 and 9. Thus, the beginning of the first group and the last group of reflections are following the paths of L_1 and L_2, respectively. These groups of reflections contain some reflections caused by the surface roughness. However, their paths are difficult to identify.

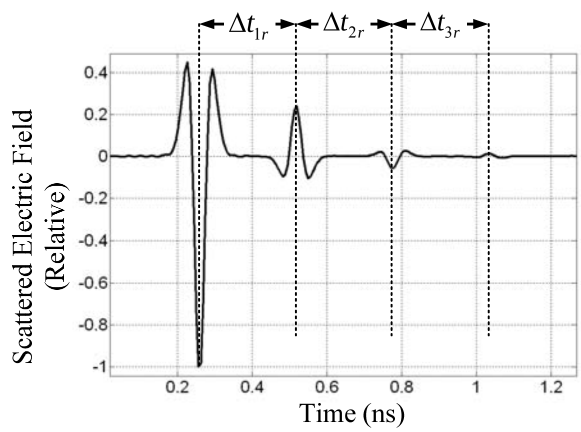

Fig. 7. TM_z back scattered field from a buried cylindrical PEC object for r_a = 0.01 m, h_c = 0.01 m, wl = 2 m, x_c / r_a = 0.0, $\varepsilon_1 = 15\ \varepsilon_0$ F/m, $\mu_1 = \mu_0$ H/m, $\phi_i = \phi_s = 90^0$, and σ_1 = 0.001 Sm^{-1}.

Table II: Comparison of timings for the case shown in Fig. 7.

n	Δt_c ***(ns)***	Δt_{nr} ***(ns)***
1	0.2582	0.2625
2	0.2582	0.2564

3	0.2582	0.2597

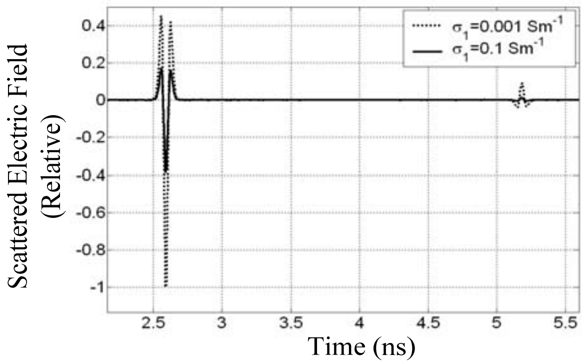

Fig. 8. TM_z back scattered field from a buried cylindrical PEC object for r_a = 0.01 m, h_c = 0.1 m, wl = 2 m, x_c / r_a = 0.0, $\varepsilon_1 = 15\ \varepsilon_0$ F/m, $\mu_1 = \mu_0$ H/m, and $\phi_i = \phi_s = 90^0$.

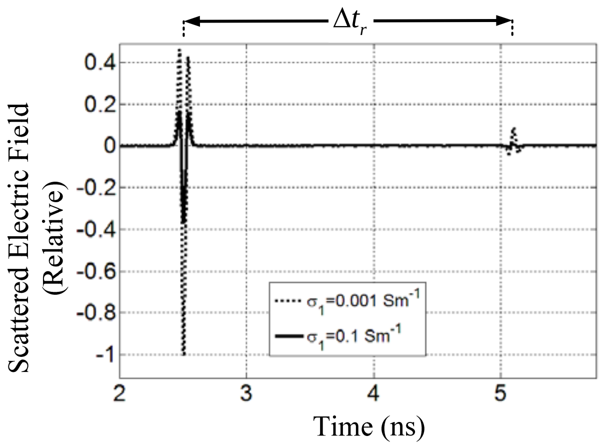

Fig. 9. TM_z back scattered field from a buried cylindrical PEC object for r_a = 0.01 m, h_c = 0.1 m, wl = 2 m, x_c / r_a = 0.0, $\varepsilon_1 = 15\ \varepsilon_0$ F/m, $\mu_1 = \mu_0$ H/m, $\phi_i = \phi_s = 20^0$, and $\sigma_1 = 0.001$ Sm^{-1}.

Table III: Comparison of the timings for the case shown in Fig. 9.

$\Delta t_c'$ ***(ns)***	Δt_r ***(ns)***
2.661	2.594

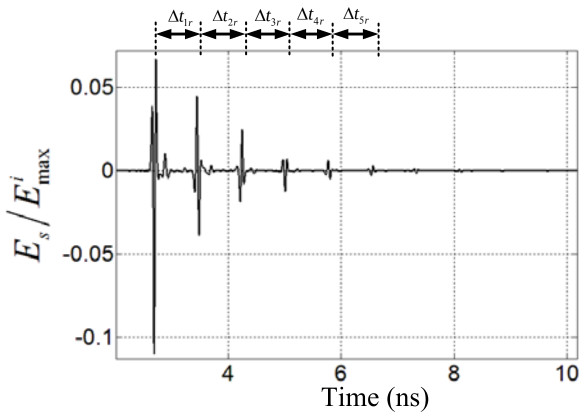

Fig. 10. TM_z back scattered field from a buried cylindrical PEC object for r_a = 0.01 m, h_c = 0.02 m, wl = 2 m, x_c / r_a = 0.0, $\varepsilon_1 = 15\ \varepsilon_0$ F/m, $\mu_1 = \mu_0$ H/m, $\phi_i = \phi_s = 90^0$, w_p = 0.1 m, h_p/w_p = 0.1, and σ_1 = 0.001 Sm^{-1}.

Table IV: Comparison of timings for the case in Fig. 10.

n	Δt_c ***(ns)***	Δt_{nr} ***(ns)***
1	0.7750	0.7520
2	0.7750	0.8
3	0.7750	0.7630
4	0.7750	0.7570
5	0.7750	0.8

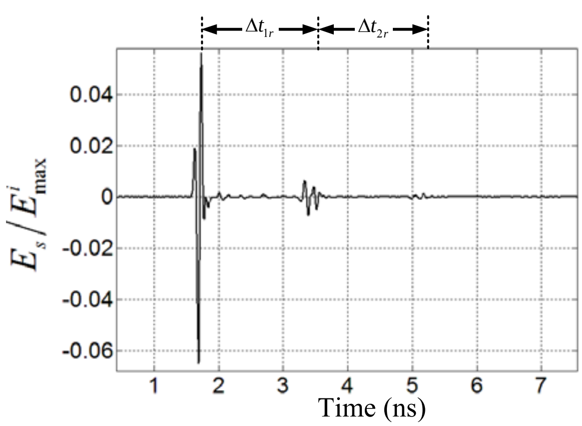

Fig. 11. TM_z back scattered field from a buried cylindrical PEC object for r_a = 0.01 m, h_c = 0.06 m, wl = 2 m, x_c / r_a = 0.0, $\varepsilon_1 = 15\ \varepsilon_0$ F/m, $\mu_1 = \mu_0$ H/m, $\phi_i = \phi_s = 90^0$, w_p = 0.1 m, h_p/w_p = 0.1, and σ_1 = 0.001 Sm^{-1}.

Table V: Comparison of timings for the case shown in Fig. 11.

n	Δt_c ***(ns)***	Δt_{nr} ***(ns)***
1	1.807	1.7030
2	1.807	1.7890

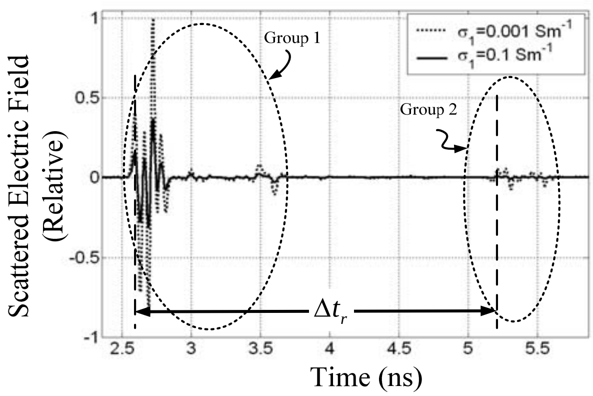

Fig. 12. TM_z back scattered field from a buried cylindrical PEC object for r_a = 0.01 m, h_c = 0.1 m, wl = 2 m, x_c / r_a = 0.0, $\varepsilon_1 = 15\ \varepsilon_0$ F/m, $\mu_1 = \mu_0$ H/m, $\phi_i = \phi_s = 90^0$, w_p = 0.1 m, and h_p/w_p = 0.1.

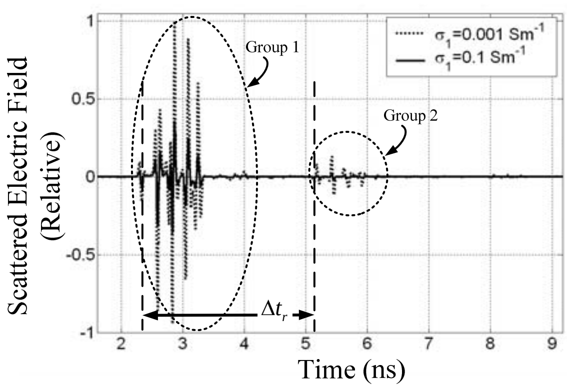

Fig. 13. TM_z back scattered field from a buried cylindrical PEC object for r_a = 0.01 m, h_c = 0.1 m, wl = 2 m, x_c / r_a = 0.0, $\varepsilon_1 = 15\ \varepsilon_0$ F/m, $\mu_1 = \mu_0$ H/m, $\phi_i = \phi_s = 20^0$, w_p = 0.1 m, and h_p/w_p = 0.1.

IV. CONCLUSION

A two-dimensional model having a PEC cylindrical object buried in a lossy medium having a flat and slightly rough surface is developed for multipath analysis. A decomposition method solution is used to solve this scattering problem in our previous works. After getting the time domain signals, the possible paths are identified by using the travelling time of reflected signals. Timing analysis shows that there are good agreements between the calculations and the relative results.

ACKNOWLEDGMENT

This research has been supported by Yildiz Technical University Scientific Research ProjectsCoordination Department. Project number: 2010-04-03-DOP01.

REFERENCES

[1] J. D. Kanellopoulos and N. E. Buris, “Scattering from conducting cylinders embedded in a lossy medium,” *International Journal of Electronics*, vol. 57, no. 3, pp. 391-401, 1984.

[2] T. J. Cui, W. C. Chew, and W. Hong, “New approximate formulations for EM scattering by dielectric objects,”*IEEE Transactions on Antennas and Propagation*, vol. 52, no. 3, pp. 684-692, 2004.

[3] D. E. Lawrence and K. Sarabandi, “Electromagnetic scattering from a dielectric cylinder buried beneath a slightly rough surface,” *IEEE Transactions on Antennas and Propagation*, vol. 50, no. 10, pp. 1368-1376, 2002.

[4] Y. Altuncu, A. Yapar, and I. Akduman, “On the scattering of electromagnetic waves by bodies buried in a half-space with locally rough interface,” *IEEE Trans. Geosci. Remote Sens.*, vol. 44, no. 6, pp. 1435-1443, 2006.

[5] Q. A. Naqvi, A. A. Rizvi, and Z. Yaqoob, “Scattering of electromagnetic waves from a deeply buried circular cylinder,” *Progress in Electromagnetics Research*, vol. 27, pp. 37-59, 2000.

[6] Y. Altuncu, I. Akduman, and A. Yapar, “Detecting and locating dielectric objects buried under a rough interface,” *IEEE Geoscience and Remote Sensing Letters*, vol. 4, no. 2, pp. 251-255, 2007.

[7] C. C. Chiu and Y. W. Kiang, “Electromagnetic inverse scattering of a conducting cylinder buried in a lossy half-space,” *IEEE Transactions on Antennas and Propagation*, vol. 40, pp. 1562-1565, 1992.

[8] T. Dogaru and L.Carin, “Time-domain sensing of targets buried under a rough air–ground interface,” *IEEE Transactions on Antennas and Propagation*, vol. 46, no. 3, pp. 360-372, 1998.

[9] C. Huang, C. Chen, C. Chiu, and C. Li, “Reconstruction of the buried homogenous dielectric cylinder by FDTD and asynchronous particle swarmoptimization,” *Applied Computational Electromagnetics Society (ACES) Journal*, vol. 25, no. 8, pp. 672-681, August 2010.

[10] F. Deek and M. El-Shenawee, "Microwave detection of cracks in buried pipes using the complex frequency technique," *Applied Computational Electromagnetics Society (ACES) Journal*, vol. 25, no. 10, pp. 894-902, Oct. 2010.
[11] K. P. Prokopidis and T. D. Tsiboukis, "Modeling of ground-penetrating radar for detecting buried objects in dispersive soils," *Applied Computational Electromagnetics Society (ACES) Journal*, vol. 22, no. 2, pp. 287-294, July 2007.
[12] C. H. Huang, C. C. Chiu, C. J. Lin, and Y. F. Chen, "Inverse scattering of inhomogeneous dielectric cylinders buried in a slab medium by TE wave illumination," *Applied Computational Electromagnetics Society (ACES) Journal*, vol. 22, no. 2, pp. 295-301, July 2007.
[13] R. Araneo and S. Barmada, "Advanced image processing techniques for the discrimination of buried objects," *Applied Computational Electromagnetics Society (ACES) Journal*, vol. 26, no. 5, pp. 437-446, May 2011.
[14] P. Falorni, L. Capineri, L. Masotti, and C. G. Windsor, "Analysis of time domain ultra-wide band radar signals reflected by buried objects," *Progress In Electromagnetics Research* (*PIERS*), vol. 3, no. 5, pp. 662-665, 2007.
[15] C. G. Windsor, L. Capineri, and P. Falorni, "The estimation of buried pipe diameters by generalized Hough transform of radar data," *Progress In Electromagnetics Research Symposium*, Hangzhou, China, pp. 345-349, August 2005.
[16] S. Vitebskiy, K. Sturgess, and L. Carin, "Short-pulse plane-wave scattering from buried perfectly conducting bodies of revolution," *IEEE Transactions on Antennas and Propagation*, vol. 44, no. 2, pp. 143-151, February 1996.
[17] S. Vitebskiy and L. Carin, "Moment-method modeling of short-pulse scattering from and the resonances of a wire buried inside a lossy, dispersive half-space," *IEEE Transactions on Antennas and Propagation*, vol. 43, no. 1, pp. 1303-1312, November 1995.
[18] J. A. Fuller and J. R. Wait, "Electromagnetic pulse transmission in homogeneous dispersive rock," *IEEE Transactions on Antennas and Propagation*, vol. 20, no. 4, pp. 530-533, July 1972.
[19] D. L. Moffai and R. J. Puskar, "A subsurface electromagnetic pulse radar," *Geophys.*, vol. 41, pp. 506-518, June 1976.
[20] L. Peters Jr. and J. D. Young, *Applications of Subsurface Transient Radars*, in Eme Domain Measurements in Electromagnetics, New York Van Nostrand Reinhold, E. K. Miller, Ed., 1986.
[21] G. S. Smith and W. R. Scotr Jr., "A scale model for studying ground penetrating radars," *IEEE Trans. Geosci. Remote Sensing*, vol. 27, no. 4, pp. 358-363, 1989.
[22] C. Liu and C. Shen, "Numerical simulation of subsurface radar for detecting buried pipes," *IEEE Trans. Geosci. Remote Sensing*, vol. 29, no. 5, pp. 795-798, Sept. 1991.
[23] M. Jaureguy and P. Borderies, "Modelling and processing of ultra wide band scattering of buried targets," *EUREL International Conference on The Detection of Abandoned Land Mines: A Humanitarian Imperative Seeking a Technical Solution*, no. 431, p.119-123, 1996.
[24] F. Sabath, *Ultra-Wideband Short-Pulse Electromagnetics 7*, Springer 2007.
[25] kal and A. Kizilay, "A decomposition method for the electromagnetic scattering from a conductive object buried in a lossy medium," *Applied Computational Electromagnetics Society (ACES) Journal*, vol. 26, no. 4, pp. 340-347, 2011.
[26] S. Makal and A. Kizilay, "Computation of the scattered fields from a dielectric object buried in a medium with a periodic surface by a decomposition method," *IET Microwaves, Antennas and Propagation*, vol. 5, no. 14, pp. 1703-1709, 2011.

Senem MakalYucedag was born in Tunceli, Turkey, in 1983. She received B.Sc., M.Sc., and Ph.D. degrees in Electronics and Communications Engineering from Yildiz Technical University in 2005, 2007, and 2012, respectively. She is a senior researcher in the Center of Research for Advanced Technologies of Informatics and Information Security (TUBITAK). Her main research interests include electromagnetic wave theory, electromagnetic scattering, artificial neural networks, and radar target identification.

Ahmet Kizilay was born in Istanbul, Turkey, in 1969. He received B.Sc. degree in Electronics and Communications Engineering from Yildiz University in 1990, M.Sc. and Ph.D. degrees in Electrical Engineering from Michigan State University in 1994 and 2000, respectively. In July 2001, he joined the Department of Electronics and Communications Engineering at Yildiz Technical University, where he is currently working as Associate Professor. His main research interests include time domain electromagnetic scattering, electromagnetic wave theory, and fiber optics.

Efficient Volume Reduction of Optimally Designed Pyramidal Log-Periodic Antennas via Meander Elements

Stamatios A. Amanatiadis, Antonios X. Lalas, Nikolaos V. Kantartzis, and Theodoros D. Tsiboukis

Department of Electrical and Computer Engineering
Aristotle University of Thessaloniki, Thessaloniki GR-54124, Greece
samanati@auth.gr, lant@faraday.ee.auth.gr, kant@auth.gr and tsibukis@auth.gr

Abstract **─** A class of volume-optimized pyramidal log-periodic antennas (PLPAs) with an adjustable ultra wideband performance is introduced in this paper. To this aim, a parametric analysis is initially conducted to decrease the total size of the prototype Euclidean-toothed PLPA. The new structures are based on the concept of meander curves, which leads to efficient substitutes of the conventional device with drastically reduced dimensions, but equivalent behavior. For the design procedure, the radiation features of all antennas are accurately evaluated via a 3-D finite-difference time-domain (FDTD) algorithm. Extensive investigation reveals that the prior volume-confinement method and the proposed radiators can provide very compact setups for a variety of modern communication systems.

Index Terms **─** FDTD methods, log-periodic antennas, pyramidal antennas, and volume optimization.

I. INTRODUCTION

Log-periodic antennas (LPAs) exhibit a notable frequency-independent behavior with a relatively sensible size, so constituting an ideal choice for broadband applications. A mainstream and easily fabricated kind is the planar LPA that combines the majority of wideband antenna benefits with the functional attributes of planar topologies [1-6]. However, since the 3-dB main lobe contour of the particular radiator is elliptical, its use as a feeder for parabolic reflectors is rather prohibitive. Fortunately, this defect can be overcome by a two-arm non-planar LPA configuration, in which the inclination angle of its two arms equals the corresponding single arm opening angle [7]. In this manner, a unidirectional beam with a circular 3-dB contour, that maximizes the directivity of the reflector, is obtained. Also, the main lobe polarization is quasi-linear, thus leading to a dual polarization property in the case of a pyramidal structure formed by two such vertically polarized antennas. Operating independently, these radiators are proven fairly profitable, since they attain a double bandwidth, when employed for the same application or, alternatively, as distinct transmission and reception [8].

Therefore, it becomes apparent that pyramidal log-periodic antennas (PLPAs) can be used in ultra wideband (UWB) systems, which is optimum for substantial directivity like space-based radars [9-13] and specialized microwave remote sensing arrangements [14-18]. These structures nonetheless should have a very limited overall size; a critical necessity that can be hardly satisfied by traditional PLPAs. Hence, it is the purpose of this paper to present a novel family of volume-controllable PLPAs with confined dimensions and advanced radiation characteristics. The design process starts with a PLPA of Euclidean elements, whose size is consistently minimized to allow cost-effective solutions in diverse realizations. In this context, a comprehensive parametric study is conducted for the optimization of the appropriate antenna traits in terms of compactness. Essentially, the key asset of the proposed PLPA class lies on the systematic incorporation of meander elements whose unique geometry achieves significant volume reductions without affecting the devices' desired performance. The radiators so developed, apart from being fabricated, are precisely analyzed via a 3-D finite-difference time-domain (FDTD) method. Results indicate the efficiency of the volume-reduction

Submitted On: Sept. 15, 2012
Accepted On: June 3, 2013

method and confirm the advantages of the proposed antennas.

II. SYSTEMATIC DESIGN OF COMPACT UWB PLPAs

A. Theory and geometric description

A practical antenna geometry, which can sufficiently support a frequency-independent behavior is specified by two or more angles, a scale factor, and two finite segments. Fulfilling these design criteria, the PLPA with Euclidean elements exhibits a broadband performance. The pattern of a single arm, as depicted in Fig. 1, is formed via similarly-shaped rectangles of thickness t_n, attached in electric contact to a central conductor ("boom") with adjacent element dimensions differing by a constant scale factor $\tau < 1$. In particular, linear segments $l_{\max}$ and $l_{\min}$ determine the minimum and maximum operating frequency of the structure, respectively. Note that two opposite elements, in the same arm, act like $\lambda/2$ dipoles; thus $l_{\max}$ should be $\lambda_{\min}/4$ long, for $\lambda_{\min}$ the wavelength corresponding to the minimum desired operating frequency. However, these valuable properties can be acquired only when more than one elements are tuned, and therefore the dimension of the largest tooth has to be increased by about 70 %. Likewise, the smallest element in the arm must be $\lambda_{\max}/4$ long, with $\lambda_{\max}$ the wavelength associated to the maximum desired frequency, while, owing to the aforementioned reason, its dimension needs to be decreased by almost 75 %.

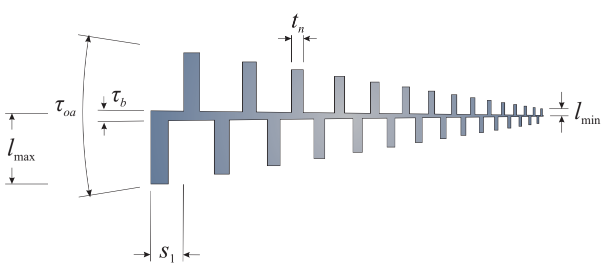

Fig. 1. Geometry of a Euclidean-toothed arm.

On the other hand, τ_{oa} and τ_b indicate the opening angles of the arm and the central boom, respectively, whereas τ_a (Fig. 2 (a)) denotes the inclination angle between two opposite arms. Based on these variables the remaining geometrical details of the single arm can be readily obtained. Specifically, the length of the antenna arm is given by,

$$L = \left(l_{\max} - l_{\min}\right)\cot\left(\tau_{oa}/2\right) \tag{1}$$

with its teeth number calculated in terms of

$$N = 1 + \frac{\log\left(l_{\min}/l_{\max}\right)}{\log\tau}, \tag{2}$$

on condition that $l_{\min} = l_{\max}\tau^{N-1}$ and N is an integer. Then, the distance s_n between two consecutive elements (designating as s_1 its largest possible value) is computed via the recursive formula of,

$$s_n = s_{n-1}\tau = s_1\tau^{n-1}, \quad \text{for } s_1 = \frac{l_{\max}\left(1-\tau^{N-1}\right)}{\tan\left(\tau_{oa}/2\right)}\frac{1-\tau}{1-\tau^N} \tag{3}$$

taking into account that

$$L = \sum_{n=1}^{N} s_1\tau^{n-1} = s_1\frac{1-\tau^N}{1-\tau}. \tag{4}$$

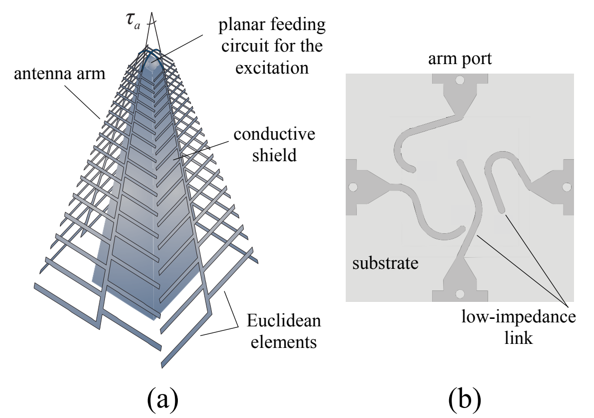

Fig. 2. The four-arm PLPA with Euclidean elements and a pyramidal grounded conductive shield for (a) perspective view and (b) planar feeding circuit.

Consistent with the previous geometric analysis, the proposed four-arm PLPA is illustrated in Fig. 2 (a). In its hollow pyramidal-shaped interior, we place a grounded highly conductive shield to create an effectively screened from internal electromagnetic fields storage space, which can conveniently accommodate the feeding electronics of the antenna close to its terminals. The typical shape of the shield is square pyramidal with an opening angle of about half the τ_a value [8]; a selection which improves the gain of the radiator and considerably maintains its frequency independence. It is stressed that τ_a should be equal to τ_{oa} in order to accomplish a circular 3-dB main lobe contour. Moreover, the entire device is fed by a properly developed planar circuit (Fig. 2 (b)), located on the narrow apex of the pyramidal shield, whose main goal is to guarantee constant low-impedance links between the arms of the PLPA and its electronics. In this way, the radiation modes of the antenna are not disrupted, while the common need for long transmission line cables (and their undesired inevitable losses) is avoided. Finally, our radiator is designed to operate in the broad range of nearly 20 GHz to 80 GHz. This indicates that the electrical lengths of its largest and smallest elements are chosen (and kept fixed throughout this paper) to be 6.35 mm and 0.41 mm, respectively. Observe that for the case of Euclidean teeth, these values are equal to $l_{\max}$ and $l_{\min}$.

B. Computational implementation aspects

The radiating characteristics of the antennas, under study, are obtained in terms of a 3-D FDTD method. Its spatial increments, which specify the appropriate cell size, are set to $\Delta x = \Delta y = 0.039$ mm and $\Delta z = 0.102$ mm, while the corresponding time-step is $\Delta t = 27.65$ fs, according to the Courant stability condition. The computational space is excited via the bandpass Gaussian pulse

$$f(t) = e^{-\left(t/t_p - 6\right)^2/2} \sin\left(2\pi f_0 t\right), \qquad (5)$$

placed at the planar feeding circuit of Fig. 2. To attain our antenna's operational range, the waveform parameters of the excitation are selected as $t_p = 5.55$ ps and $f_0 = 62.5$ GHz, thus producing an ample spectrum from 5 GHz to 120 GHz. In this way, the very satisfactory grid resolution of approximately $\lambda/55$ (λ the smallest wavelength of the simulation) is accomplished. Open boundaries are terminated by a perfectly matched layer (PML) [19-22] with an air buffer of 0.6 λ from the radiator. The PML is $\delta = 8$ layers (cells) thick, while for its attenuation parameters: (a) the loss grading σ (similarly σ^*) is set to be quadratic ($n = 2$), i.e., $\sigma(\rho) = \sigma_{\max}(\rho/\delta)^n$ ($\rho = x, y, z$) and (b) the reflection factor $R = \exp\{-2\sigma_{\max}\delta/(n+1)\varepsilon_0 c\}$ is set to $R = 10^{-6}$, with c the vacuum speed of light. In particular, (σ, σ^*) vary quadratically along the ρ direction from 0 at each vacuum-PML interface to the peak values of ($\sigma_{\max} = 1.23\times10^5$ S/m, $\sigma^*_{\max} = 1.64\times 10^{10}$ Ω/m), allowing trivial reflections only below –80 dB across the entire source spectrum. It is stressed that the above numerical setup remains the same for every example in the paper. Hence, we are able to certify the profits of our volume reduction method by modifying only the size of the lattice. Lastly, all simulations are conducted on a 3.47 GHz Intel™ Xeon dual-processor X5690 computer with 96 GB RAM for a total number of 82.678 time-steps.

C. Numerical results and measurements

Recalling the basic geometric features of the proposed antenna, our initial realization has $\tau = 0.975$, $\tau_{oa} = \tau_a = 20^{\circ}$, and $\tau_b = 0.67^{\circ}$, which create a total volume of 1.906 cm^3. For its discretization, an FDTD mesh of 407×407×359 ≈ 59.47 million cells (around 3.52 GB RAM and 11 hours of CPU time) is generated. Since the new PLPAs must exhibit a satisfactory performance for diverse arm geometries, our investigation focuses, first, on the impact of their teeth thickness t_n variation as a percentage of distance s_n. So retaining constant the rest of the design parameters. Figure 3 presents a set of directivity and half-power beamwidth angle (HPBA) comparisons. As derived, t_n variations do not considerably affect the main PLPA radiation features, especially when thicker elements are employed. This deduction is also confirmed by the radiation patterns of Fig. 4, computed for two different φ angles at the limits of the desired frequency range. Bearing in mind the prior aspects, t_n is set equal to the 20 % of s_n, for the remainder of this study, which is proven a very practical choice. Notice that HPBA is similar over the two ($\varphi = 0^{\circ}$, 90°) perpendicular planes, a fact which certifies the fulfillment of the important condition for a circular 3-dB contour. Also a closer inspection of Figs. 3 and 4 reveals that the frequency spectrum for an efficient operation of the novel PLPA extends approximately from 15 GHz to 110 GHz; an important profit, which amply meets the standards of modern UWB applications. Indeed, in this practically 100 GHz frequency range, no main lobe deviations or directivity reductions have been observed. Moreover, Fig. 5 illustrates the surface current density on one arm of the PLPA, with its maximum values detected at the larger teeth for higher frequencies.

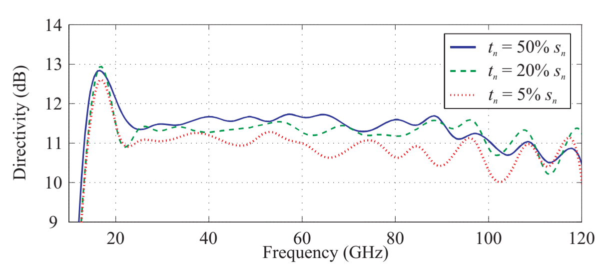

(a)

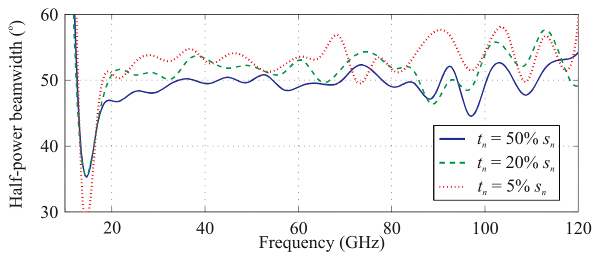

(b)

Fig. 3. Performance comparison of several PLPAs for different t_n values as a percentage of s_n; (a) directivity and (b) half-power beamwidth angle.

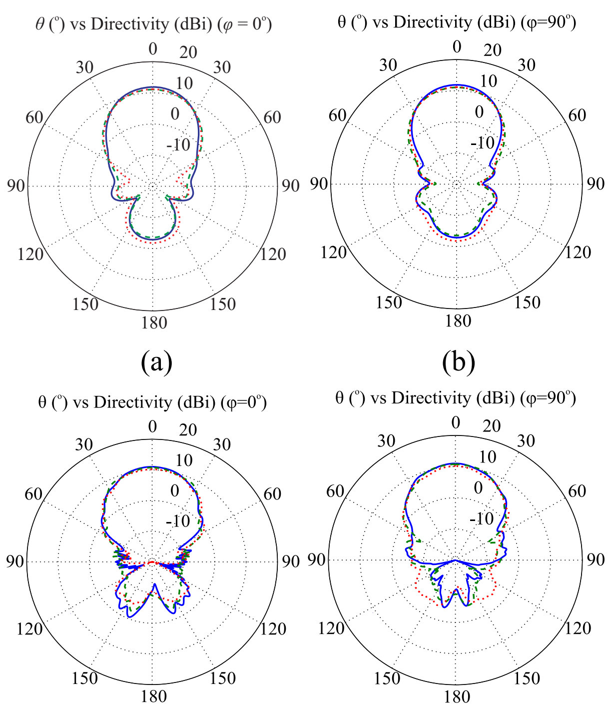

(a) (b) (c) (d)

Fig. 4. Radiation patterns of various PLPAs with $t_n = 0.5s_n$ (blue continuous line), $t_n = 0.2s_n$ (green dashed line), and $t_n = 0.05s_n$ (red dotted line) at (a), (b) $f = 20$ GHz and (c), (d) $f = 100$ GHz.

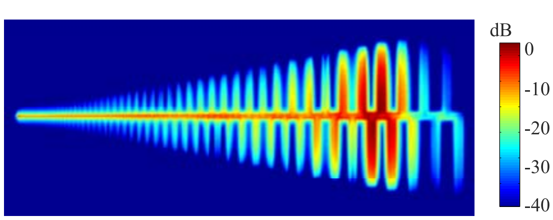

(a)

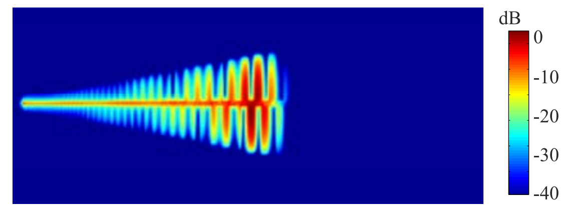

(b)

Fig. 5. Surface current density of the proposed PLPA at (a) $f = 20$ GHz and (b) $f = 40$ GHz.

Proceeding with our analysis, we now concentrate on the factors that can more prominently influence the antenna's volume, namely angles τ_{oa} and τ_a, which, as already explained, must be equal. To this objective, a parametric study pertaining to the variations of these angles is conducted, with the rest of the PLPA features set to their initial values. In this context, Fig. 6 shows the results of our simulations, compared with the performance of the already modeled initial device, i.e., $\tau_{oa} = \tau_a = 20^o$. Specifically, keeping all the FDTD implementation details of subsection II. B the same, for the case of $\tau_{oa} = \tau_a = 25^o$, we build a grid with 407 × 407 × 289 ≈ 48.87 million cells (about 2.83 GB RAM and 8.85 hours of CPU time), whereas for $\tau_{oa} = \tau_a = 30^o$ a mesh of 407 × 407 × 243 ≈ 40.25 million cells (about 2.36 GB RAM and 7.44 hours of CPU time). It occurs that as τ_a increases, the directivity is significantly reduced, while HPBA is slightly augmented. Also, the radiation patterns of Fig. 7 indicate that larger angles introduce amplified side lobes, with regard to the main one. However, the most advantageous asset of this optimization process is the notably decreased overall volume of the resulting device and the required FDTD lattice, as well. In fact, the PLPA total volume minimizes with the increment of τ_{oa}, as deduced by equation (1). Explicitly, this reduction is about 21.1 % for $\tau_{oa} = \tau_a = 25^o$ and around 35.4 % for $\tau_{oa} = \tau_a = 30^o$; a fact also deduced by the corresponding grid sizes. Consequently, it is evident that the above process can lead to very proficient and compact PLPAs for UWB designs.

In order to validate the advantages of the improved PLPAs, a set of prototypes has been carefully fabricated. In particular, two different antennas have been constructed with respect to angle τ_a i.e., a triangular-toothed PLPA with $\tau_a = 25^o$ and a Euclidean-toothed PLPA with $\tau_a = 30^o$, as indicatively illustrated in Fig. 8, along with the measurement setup. So, Fig. 9 provides the comparisons between measured data and simulated outcomes concerning the isolation of the two vertical polarizations for each one of the two fabricated PLPAs. As deduced, their agreement is very satisfactory, thus proving the significant contribution of the proposed technique in the performance of the specific radiators.

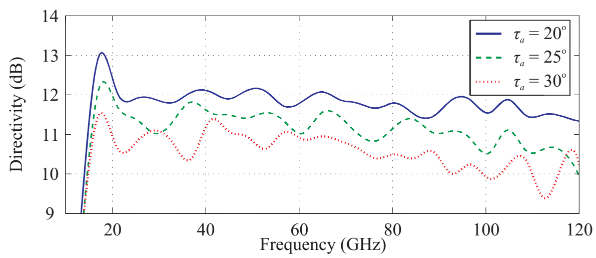

(a)

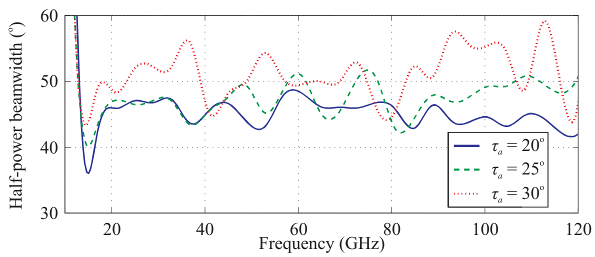

(b)

Fig. 6. Performance comparison of several PLPAs for different τ_a values, (a) directivity and (b) half-power beamwidth angle.

III. THE VOLUME-OPTIMIZED MEANDER-TOOTHED PLPA

A. Development of the design procedure

A meander line is a self-avoiding closed curve, which can intersect with a straight line at a finite number of points. The principal aim of its use at the teeth of the new PLPAs is the substantial overall size reduction it attains, as it leads to a smaller single tooth with the same electrical length. A typical 2nd-order meander curve is depicted in Fig. 10 (a) along with its basic design parameters applied to its entire length. To evaluate the desired electrical length l_{en}, the approximation of

$$l_{en} = l_n + 2c_n = 2a_n + b_n + 2c_n , \qquad (6)$$

with the restriction $b_n > 2t_n$, is deemed a viable selection to avoid overlapping. Nevertheless, when the meander elements are placed together to form the antenna arm, some additional conventions need to be determined. Firstly, the distance w_n between two consecutive same-sided elements is finite and therefore the value of c_n should have an upper limit. Exploiting the pattern of the elements, Fig. 10 (c) shows that w_n can be precisely expressed as

$$w_n = s_n + s_{n-1} = s_n\left(1+\tau^{-1}\right). \qquad (7)$$

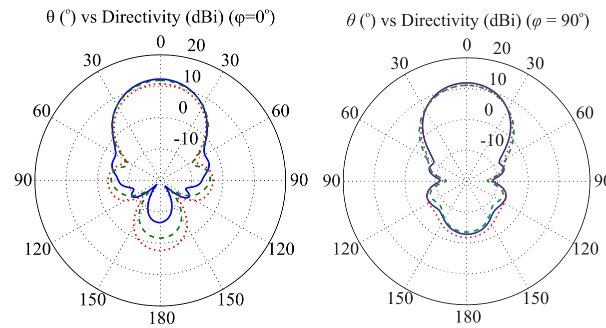

(a) (b)

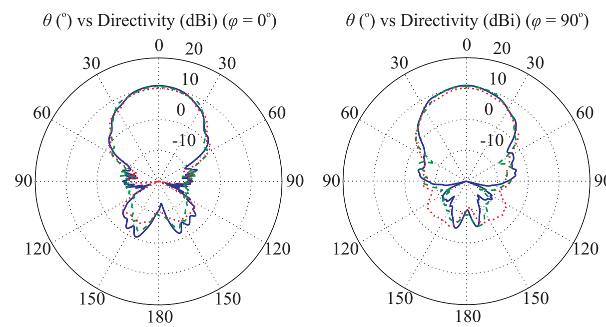

(c) (d)

Fig. 7. Radiation patterns of different PLPAs with $\tau_a = 20^o$ (blue continuous line), $\tau_a = 25^o$ (green dashed line), and $\tau_a = 30^o$ (red dotted line) at (a), (b) $f = 20$ GHz and (c), (d) $f = 100$ GHz.

So, the restriction for c_n is imposed by means of,

$$c_n < w_n - t_n . \qquad (8)$$

An effective way to increase the available space stems from the reduction of scale factor τ, as derived by equations (6) and (7); an issue that will be elaborately examined in the following paragraphs for large τ values. Furthermore, the presence of the central boom introduces a lower limit for a_n in order to evade possible element overlapping, as displayed in Fig. 10 (b). This constraint is satisfied via

$$a_1 > l_{\max} \frac{\tan(\tau_b / 2)}{\tan(\tau_{oa} / 2)}, \tag{9}$$

regarding the first tooth only. Observe however that the fulfillment of equation (9) is, also, applicable to the rest of the teeth, due to the scaling properties of LPAs. Hence, considering the prior analysis, meander elements are, herein, formed through the design of Fig. 10 (a) to enhance the competence of our method.

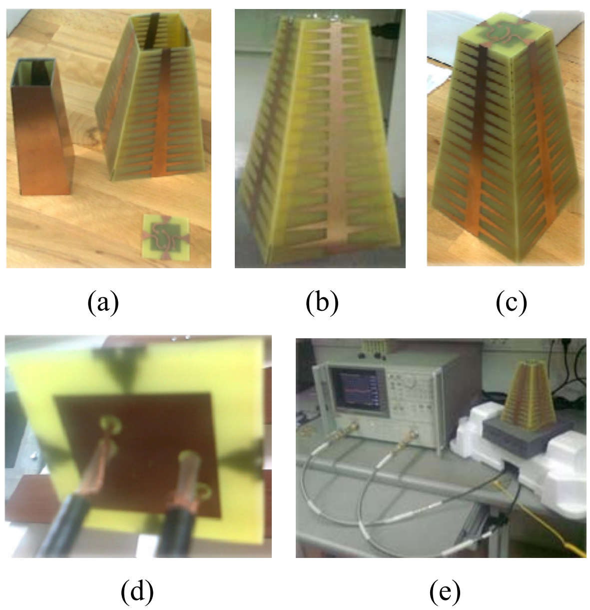

Fig. 8. The volume-confined PLPAs; (a) parts: four -arm radiator, conductive shield, and planar feeding circuit, (b), (c) views of the fabricated prototypes, (d) transmission line cables of the feeding system (internal side), and (e) measurement setup.

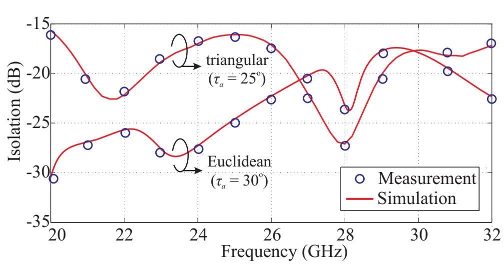

Fig. 9. Isolation of the fabricated triangular- and Euclidean-toothed volume-confined PLPAs.

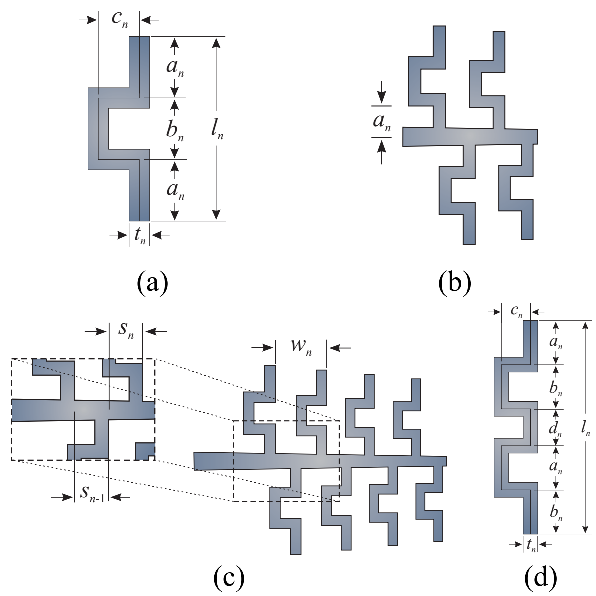

Fig. 10. (a) A 2nd-order meander element with (b), (c) its main design parameters, and (d) a 3rd-order meander element.

B. Applications and numerical validation

Next and after the specification of its upper limit through equation (8), let us concentrate on the effect of c_n variations. To this goal, three meander-toothed radiators of the proposed PLPA family are designed in which c_n is equal to the 50 %, 60 %, and 70 % of the maximum possible $w_n - t_n$ value. Thus, the grid consists of, (a) 323 × 323 × 359 ≈ 37.45 million cells (about 2.21 GB RAM and 6.92 hours of CPU time), for $c_n = 0.5\,(w_n - t_n)_{\max}$, (b) 310 × 310 × 359 ≈ 34.5 million cells (about 2.04 GB RAM and 6.38 hours of CPU time) for $c_n = 0.6\,(w_n - t_n)_{\max}$, and (c) 220 × 220 × 359 ≈ 17.3 million cells (about 1.03 GB RAM and 3.1 hours of CPU time) for $c_n = 0.7\,(w_n - t_n)_{\max}$. Note that the rest of the FDTD details are those described in subsection II. B. Furthermore, the thickness of the teeth is set to $t_n = 0.2 s_n$, whereas $a_n = b_n$ are evaluated using equation (6). The prior setups offer a notable decrease of the total volume and the FDTD lattice in comparison with those of the initial antenna, i.e., 41 %, 47.3 %, and 53 %, respectively. In order to realize this decrease, Fig. 11 presents the geometry of a Euclidean-toothed and a meander-toothed PLPA with the same properties. Obviously, the volume of the latter is proven to be much smaller and sufficiently more compact. On the other hand, directivity and HPBA results are shown in Fig. 12, while the corresponding radiation patterns are given in Fig. 13. Note that all volume-optimized antennas exhibit a very satisfactory performance in the preselected 20 GHz to 80 GHz spectrum. Nonetheless and as anticipated, these radiation characteristics start to deteriorate at higher frequencies, mainly due to the proximity of consecutive elements operating at the specific frequency region. This is attributed to the more prominent influence of parasitic capacitances, which change the electrical length of the elements and thus affects the device's behavior.

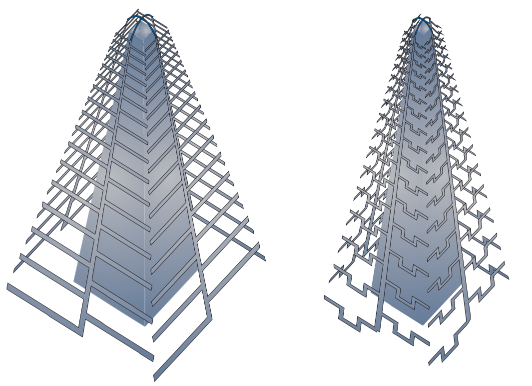

(a) (b)

Fig. 11. Geometry of (a) the Euclidean-element and (b) the proposed meander-element PLPA.

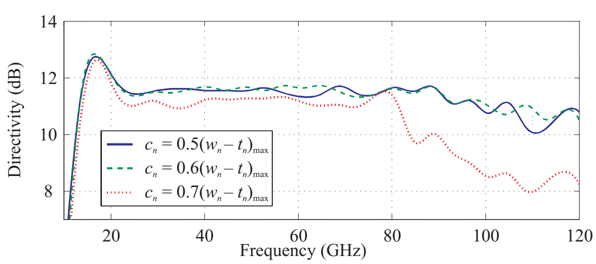

(a)

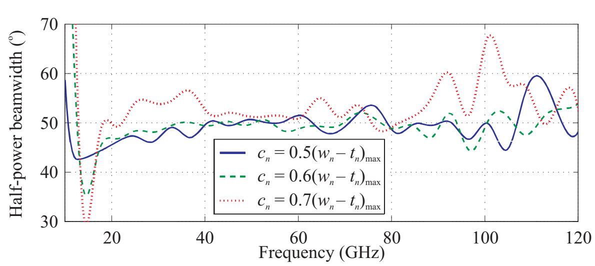

(b)

Fig. 12. Comparison between different meander-toothed PLPAs versus c_n, expressed as a percentage of the maximum $w_n - t_n$ value, (a) directivity and (b) half-power beamwidth angle.

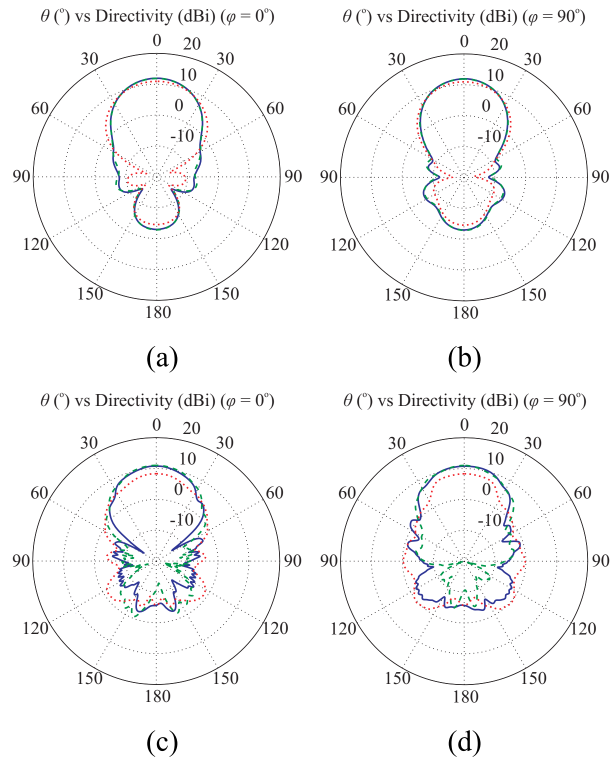

Fig. 13. Radiation patterns of diverse PLPAs with $c_n = 0.5\ (w_n - t_n)$ (blue continuous line), $c_n = 0.6\ (w_n - t_n)$ (green dashed line), and $c_n = 0.7\ (w_n - t_n)$ (red dotted line) at (a), (b) $f = 20$ GHz, and (c), (d) $f = 100$ GHz.

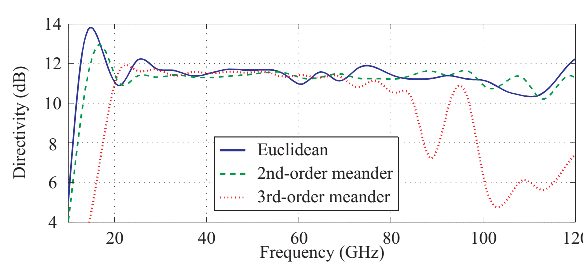

(a)

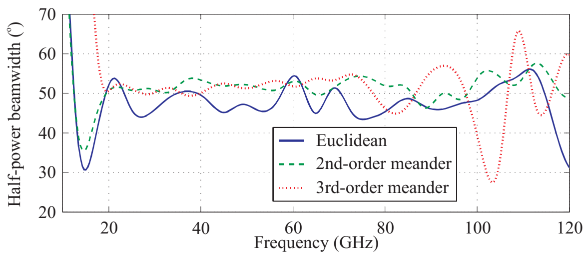

(b)

Fig. 14. Comparison between various PLPAs with different elements; (a) directivity and (b) half-power beamwidth.

The last PLPA arrangement involves the incorporation of the 3rd-order meander element of Fig. 10 (d). Its design is conducted by considering that

$$l_{en} = l_n + 4c_n = 2a_n + 2b_n + d_n + 4c_n \,. \qquad (10)$$

The rest of the constraints are identical to those introduced by equations (8) and (9) for the 2nd-order meander teeth. For our investigation, we compare a Euclidean-toothed PLPA ($\tau = 0.975$, $\tau_b = 0.67^{o}$, $\tau_{oa} = 20^{o}$) with two meander-toothed PLPAs based on 2nd- and 3rd-order elements. All τ, τ_b, and τ_{oa} values remain the same, except for $c_n = 0.6\,(w_n - t_n)$ and $t_n = 0.25 s_n$. Moreover, $a_n = b_n$ are computed using equation (5) for the 2nd-order meanders, whereas $a_n = b_n = d_n$ are derived using equation (10) for the 3rd-order case. It should be emphasized that the total volume reduction reaches the impressive level of 50 % for the second and 81.7 % for the third configuration.

To verify the proposed structures, numerical results, acquired by our FDTD simulations, are summarized in Figs. 14 and 15. Therefore, using the FDTD set-up of the previous example for the 2nd-order case, we discretize the 3rd-order meander element radiator by means of a 138 × 138 × 359 ≈ 6.83 million-cell grid (around 0.4 GB RAM and 1.26 hours of CPU time). Again, the properties of the meander-element PLPAs are very sufficient in the prefixed region of 20 GHz to 80 GHz, so indicating the efficiency of the volume-confinement concept. At high frequency regions, though, the operation of the 3rd-order meander-toothed device degrades owing to the presence of parasitic capacitances, which reveals a trade-off between compactness and high directivity beamwidth for these antennas. Nonetheless, the behavior of its 2nd-order counterpart resembles that of the conventional PLPA achieving a better compression ratio in UWB applications. Finally, the surface current distributions of the two meander-toothed PLPAs are visualized in Fig. 16, to indicate the smoothness in the propagation of the electromagnetic field energy. As a consequence and based on the aforementioned promising outcomes, it is deduced that the proposed miniaturization technique can be productively employed in several contemporary high-end communication appliances with a noteworthy performance.

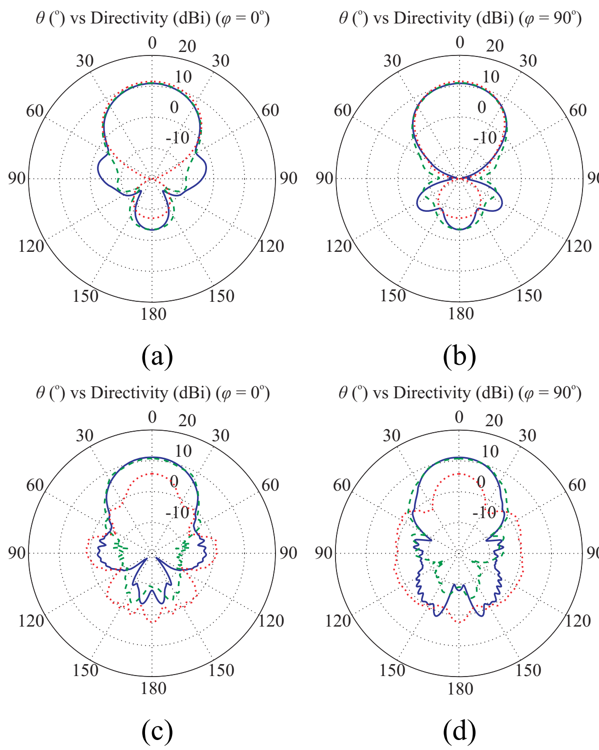

Fig. 15. Radiation patterns of diverse PLPAs with Euclidean (blue continuous line), 2nd-order meander (green dashed line), and 3rd-order meander (red dotted line) elements at (a), (b) f = 20 GHz, and (c), (d) f = 100 GHz.

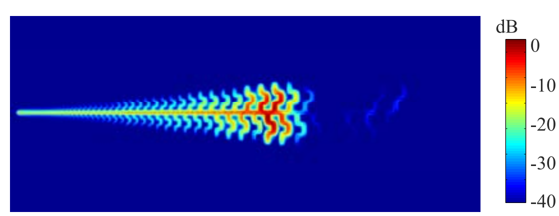

(a)

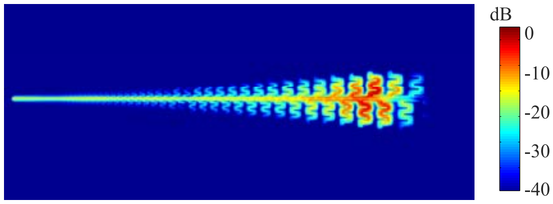

(b)

Fig. 16. Surface current density of two volume-optimized meander-toothed PLPAs; (a) 2nd-order at f = 40 GHz and (b) 3rd-order at f = 20 GHz.

IV. CONCLUSION

The optimal design and comprehensive characterization of a general PLPA class for modern UWB implementations have been presented in this paper. Focusing on the critical issue of overall volume reduction and the strict requirement for compact dimensions, a new meander-toothed configuration, occupying significantly less space than the conventional Euclidean-toothed structure, has been introduced. Essentially, the primary concept lies on the determination of certain constraints during the design of the meander elements. Aside from being fabricated and measured, the efficient devices have been successfully verified by means of a 3-D FDTD method. Extensive numerical simulations, addressing directivity, half-power beamwidth, and other instructive radiation characteristics, confirm that the specific PLPAs can suitably satisfy the UWB application standards, while the decreased volume does not influence their useful operational behavior.

ACKNOWLEDGMENT

This research has been co-financed by the EU (European Social Fund − ESF) and Greek national funds through the Operational Program "Education and Lifelong Learning" of the National Strategic Reference Framework (NSRF) − Research Funding Program: ARISTEIA I. Investing in knowledge society through the European Social Fund.

REFERENCES

[1] D. Anagnostou, J. Papapolymerou, M. Tent-zeris, and C. Christodoulou, "A printed log-periodic Koch-dipole array (LPKDA)," *IEEE Antennas Wireless Propag. Lett.*, vol. 7, pp. 456-460, 2008.

[2] C. de J. van Coevorden, A. Bretones, M. Pantoja, S. García, A. Monorchio, and R. Martín, "A new implementation of the hybrid Taguchi GA: Application to the design of a miniaturized log-periodic thin-wire antenna," *ACES Journal*, vol. 24, no. 1, pp. 21-31, 2009.

[3] S. Kurokawa, M. Hirose, and K. Komiyama, "Measurement and uncertainty analysis of free-space antenna factors of log-periodic antenna using time-domain techniques," *IEEE Trans. Instrum. Meas.*, vol. 58, no. 4, pp. 1120-1125, 2009.

[4] J. Yang and P. Kildal, "Optimization of reflection coefficient of large log-periodic array by computing only a small part of it," *IEEE Trans. Antennas Propag.*, vol. 59, no. 6, pp. 1790-1797, 2011.

[5] H. Nouri, J. Nourinia, and C. Ghobadi, "Multi-band printed dipole antenna with log-periodic toothed structure for WLAN/WiMAX applications," *Microw. Opt. Technol. Lett.*, vol. 53, no. 3, pp. 536-539, 2011.

[6] J. Yeo and J.-I. Lee, "Planar log-periodic bow-tie dipole array antenna with reduced size and enhanced front-back ratio," *Microw. Opt. Technol. Lett.*, vol. 54, no. 6, pp. 1435-1441, 2012.

[7] O. Ergül and L. Gürel, "Non-planar trapezoidal tooth log-periodic antennas: design and electromagnetic modeling," *Radio Sci.*, vol. 40, no. RS5010, pp. 1-14, 2005.

[8] G. Engargiola and W. Welch, "Log-periodic antenna," US Patent 6.677.913 B2, 2004.

[9] N. Haridas, A. El-Rayis, A. Erdogan, and T. Arslan, "Multi-frequency antenna design for space-based reconfigurable satellite sensor node," *Proc. 2nd NASA/ESA Conf. Adaptive Hardware Systems*, pp. 1-6, 2007.

[10] S. Kim, S. Lee, and Y. Kim, "Multi-band monopole antenna using meander structure for handheld terminals," *Electron. Lett.*, vol. 44, no. 5, pp. 331-332, 2008.

[11] P. Izdebski, H. Rajagopalan, and Y. Rahmat-Samii, "Conformal ingestible capsule: A novel chandelier meandered design," *IEEE Trans. Antennas Propag.*, vol. 57, no. 4, pp. 900-909, 2009.

[12] Y. Zhang, N. Nikolova, and M. Bakr, "Input impedance sensitivity analysis of patch antenna with discrete perturbations on method-of-moment grids," *ACES Journal*, vol. 25, no. 10, pp. 867-876, 2010.

[13] B. Devireddy, A. Yu, F. Yang, and A. Elsherbeni, "Gain and bandwidth limitations of reflectarrays," *ACES Journal*, vol. 26, no. 2, pp. 170-178, 2011.

[14] W. -T. Hsieh and J. -F. Kiang, "Small broadband antenna composed of dual-meander folded loop and disk-loaded monopole," *IEEE Trans. Antennas Propag.*, vol. 59, no. 5, pp. 1716-1720, 2011.

[15] M. Mohammadirad, N. Komjani, A. Sebak, and M. Chaharmir, "A broadband reflectarray antenna using the triangular array configuration," *ACES Journal*, vol. 26, no. 8, pp. 640-650, 2011.

[16] Y. Watanabe, K. Watanabe, and H. Igarashi, "Optimization of meander line antenna considering coupling between nonlinear circuit and electromagnetic waves for UHF-band RFID," *IEEE Trans. Magn.*, vol. 47, no. 5, pp. 1506-1509, 2011.

[17] M. Zoppi, C. Dedeban, C. Pichot, S. Selleri, and G. Pelosi, "Optimal location of multi-antenna systems - Influence of noise-corrupted data," *ACES Journal*, vol. 27, no. 2, pp. 198-205, 2012.

[18] W. Weng, "Optimal design of an ultra-wide-band antenna with the irregular shape on radiator using particle swarm optimization," *ACES Journal*, vol. 27, no. 5, pp. 427-434, 2012.

[19] J. -P. Berenger, "A perfectly matched layer for the absorption of electromagnetic waves," *J. Comp. Phys.*, vol. 114, pp. 185-200, 1994.

[20] A. Taflove and S. Hagness, *Computational Electrodynamics: The Finite-Difference Time-Domain Method*, Artech House, 2005.

[21] Y. Zhang, A. Kishk, A. Yakovlev, and A. Glisson, "FDTD analysis of a probe-fed dielectric resonator antenna in rectangular waveguide," *ACES Journal*, vol. 21, no. 1, pp. 37-44, 2006.

[22] M. Hadi, "Wide-angle absorbing boundary conditions for low and high-order FDTD algorithms," *ACES Journal*, vol. 24, no. 1, pp. 9-15, 2009.

Stamatios A. Amanatiadis received the Diploma degree in Electrical and Computer Engineering from the Aristotle University of Thessaloniki, Greece, in 2010, where he is currently pursuing his Ph.D. degree. His research focuses on modern antenna design, analysis of graphene structures, and computational electromagnetics.

Antonios X. Lalas received the Diploma and the Ph.D. degrees in Electrical and Computer Engineering from the Aristotle University of Thessaloniki, Greece, in 2006 and 2011, respectively. His research interests include numerical methods, antenna and MEMS modeling, with an emphasis on EBGs and metamaterials.

Nikolaos V. Kantartzis received the Diploma and Ph.D. degrees from the Department of Electrical and Computer Engineering, Aristotle University of Thessaloniki, Greece, in 1994 and 1999, respectively. In 2001, he joined the same department, as a Postdoctoral Research Fellow, where, currently, he serves as an Assistant Professor. He has authored/co-authored 3 books, more than 70 refereed journal and over 90 conference papers. His main research interests focus on EMC modeling, computational electromagnetics, antenna analysis, higher-order time- and frequency-domain methods, metamaterials, and advanced microwave structures. Dr. Kantartzis is a member of diverse societies and associations.

Theodoros D. Tsiboukis received the Diploma degree in Electrical and Mechanical Engineering from the National Technical University of Athens, Athens, Greece, in 1971, and the Doctor Eng. Degree from the Aristotle University of Thessaloniki (AUTH), Greece, in 1981. From 1981 to 1982, he was with the Electrical Engineering Department, University of Southampton, U.K., as a Senior Research Fellow. Since 1982, he has been with the Department of Electrical and Computer Engineering, AUTH, where he is currently a Professor. He has served in numerous administrative posts and as a chairman of many conference committees. He is the author of 8 books and over 280 refereed journal and conference papers. His research areas, primarily, include frequency- and time-domain computational electromagnetics, metamaterials, graphene, and EMC problems. Prof. Tsiboukis is a member of various societies, associations, and institutions, and has received several awards and distinctions.

Solving Inverse Scattering for a Partially Immersed Metallic Cylinder Using Steady-State Genetic Algorithm and Asynchronous Particle Swarm Optimization by TE waves

Ching-Lieh Li [1], Chi Hsien Sun [2], Chien-Ching Chiu [1], and Lung-Fai Tuen [1]

[1] Electrical Engineering Department, Tamkang University
Tamsui, Taiwan, R.O.C

[2] Department of Electronic and Computer Engineering, National Taiwan University of Science and Technology, Taipei City, Taiwan, R.O.C.

Abstract **─** The transverse electric (TE) polarization for shape reconstruction of a metallic cylinder by asynchronous particle swarm optimization (APSO) and steady-state genetic algorithm (SSGA) is presented. These approaches are applied to two-dimensional configurations. After an integral formulation, a discretization using the method of moment (MoM) is applied. Considering that the microwave imaging is recast as a nonlinear optimization problem, an objective function is defined by the norm of a difference between the measured scattered electric field and that calculated for an estimated shape of metallic cylinder. Thus, the shape of metallic cylinder can be obtained by minimizing the objective function. In order to solve this inverse scattering problem, two techniques are employed. The first is asynchronous particle swarm optimization. The second is steady-state genetic algorithm. Both techniques have been tested in the case of simulated measurements contaminated by additive white Gaussian noise. Numerical results indicate that the asynchronous particle swarm optimization outperforms steady-state genetic algorithm in terms of reconstruction accuracy and convergence speed.

Index Terms - Asynchronous particle swarm optimization, inverse scattering, partially immersed conductor, and transverse electric wave.

I. INTRODUCTION

Microwave imaging is an application of electromagnetic inverse scattering that is capable of performing noninvasive evaluation on a test object and determining its shape and/or material properties. The application of electromagnetic scattering to retrieve the shape, location, and the property of an unknown scatterer embedded in a homogeneous space or buried underground has shown great potential in several application areas such as medical tomography, geophysics, non-destructive testing, and object detection [1-11]. The reconstruction of the location, shape and/or size of metallic cylinders in a two-layer material medium may find its application for detection of landmine.

From a mathematical point of view, inverse problems are intrinsically ill-posed and nonlinear [12]. Hence, only a finite number of parameters can be accurately retrieved. To stabilize the inverse problems against ill-posedness, usually various kinds of regularizations are used, which are based on a priori information about desired parameters. On the other hand, due to the multiple scattering phenomena, the inverse-scattering problem is nonlinear in nature. Therefore, when multiple scattering effects are not negligible, the use of nonlinear methodologies is mandatory [13]. Recently, inverse scattering problems are usually considered in optimization-based procedures, such as adjoint-field scheme [14], Gauss–Newton method [15] genetic algorithms (GAs) [16-19], differential evolution (DE) [20-23], particle swarm

Submitted On: July 16, 2012
Accepted On: May 16, 2013

optimization (PSO) [23-28], and level-set algorithm [29]. However, these papers only focus on transverse magnetic (TM) cases.

It has been recognized that the 2D TE problems include two orthogonal electric field components in the transverse plane and thus leads to a vectorial mathematical formulation. Therefore, the computational load for exploiting such positive features is unavoidably increased as compared to the TM case with only one electric field component. In other words, the TE-polarized case includes polarization charges at dielectric discontinuities, which are more difficult to model numerically. However, there are advantages of utilizing the TE-polarized data (as compared to the TM-polarized ones) since they may contain more useful information about the object of interest data. It should be noted that these two polarizations are physically uncoupled and they provide independent information about the object being imaged [29, 30], although this may not be "practically" true when the curvature radius of the perfectly conducting cylinder is larger than the wavelength [31, 32].

Although particle swarm optimization and genetic algorithms have been confronted to numerical analysis and electromagnetic optimization problem [33-36], to the best of our knowledge, a comparative study about the performances of APSO and SSGA when applied to inverse scattering problems has not yet been investigated. Recently, there are a few reports on subject of 2D object about shape reconstruction problems by TE experimental data, such as genetic algorithms (GAs) [37-40] and level-set algorithm [29].

In this paper, the inverse scattering problem of the partially immersed perfectly conducting cylinder by TE wave illumination is investigated. We use the APSO to recover the shape of a partially immersed perfectly conducting cylinder. In section II, the theoretical formulation for the inverse scattering is derived. The numerical results for various objects of different shapes are presented in section III. Section IV gives the conclusions.

II. THEORETICAL FORMOLATION

A. Direct problem

Let us consider a perfectly conducting cylinder, which is partially immersed in a lossy homogeneous half-space, as shown in Fig. 1. Media in regions 1 and 2 are characterized by permittivities and conductivities (ε_1, σ_1) and (ε_2, σ_2), respectively. In our simulation, a priori information is assuming that scatterer is a metallic cylinder. A perfectly conducting cylinder is illuminated by a TE plane wave. The cylinder is of an infinite extent in the z-direction, and its cross-section is described in polar coordinates in the x, y plane by the equation $\rho = F(\theta)$. We assume that the time dependence of the field is harmonic with the factor $e^{j\omega t}$. Let $\vec{H}^{inc}$ denote the incidence field from region 1 with incident angle ϕ_1 as follow,

$$\vec{H}^{inc} = e^{-jk_1(y\cos\phi_1 + x\sin\phi_1)}\hat{z}\,. \qquad (1)$$

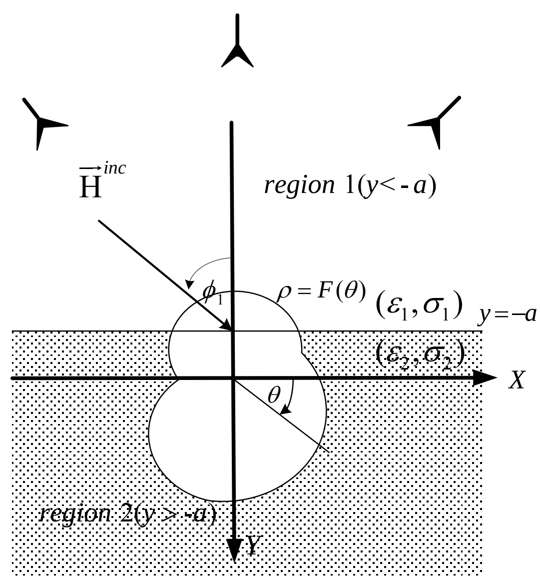

Fig. 1. Geometry of the problem in the (x,y) plane.

Owing to the interface between regions 1 and 2, the incident plane wave generates two waves that would exist in the absence of the conducting object. Since the cylinder is partially immersed, the equivalent current exists both in the upper half space and the lower half space. As a result, the details of Green's function are given first as follows:

(1) When the equivalent current exists in the upper half space, the Green's function for the line source in the region 1 can be expressed as,

$$G_1(x,y;x',y') = \begin{cases} G_{21}(x,y;x',y') & ,y > -a \\ G_{11}(x,y;x',y') = \\ G_{f11}(x,y;x',y') + G_{s11}(x,y;x',y') & ,y \le -a \end{cases}$$

$$G_{21}(x,y;x',y') = \frac{1}{2\pi}\int_{-\infty}^{\infty} \frac{j}{\gamma_1+\gamma_2} e^{-j\gamma_2(y+a)} e^{j\gamma_1(y'+a)} e^{-j\alpha(x-x')} d\alpha$$

$$G_{f11}(x,y;x',y') = \frac{j}{4} H_0^{(2)}[k_1\sqrt{(x-x')^2+(y-y')^2}] \,, \tag{2.2}$$

$$G_{s11}(x,y;x',y') = \frac{1}{2\pi}\int_{-\infty}^{\infty} \frac{j}{2\gamma_1}\left(\frac{\gamma_1-\gamma_2}{\gamma_1+\gamma_2}\right) e^{j\gamma_1(y+2a+y')} e^{-j\alpha(x-x')} d\alpha \,, \tag{2.3}$$

$\gamma_i^2 = k_i^2 - \alpha^2$, $i = 1, 2$, $\mathrm{Im}(\gamma_i) \le 0$, $y' < -a$.

(2) When the equivalent current exists in the lower half space, the Green's function for the line source in the region 2, is

$$G_2(x,y;x',y') = \begin{cases} G_{12}(x,y;x',y') & ,y \le -a \\ G_{22}(x,y;x',y') = \\ G_{f22}(x,y;x',y') + G_{s22}(x,y;x',y'), & y > -a \end{cases} \,, \tag{3}$$

where

$$G_{12}(x,y;x',y') = \frac{1}{2\pi}\int_{-\infty}^{\infty} \frac{j}{\gamma_1+\gamma_2} e^{j\gamma_1(y+a)} e^{-j\gamma_2(y'+a)} e^{-j\alpha(x-x')} d\alpha \,, \tag{3.1}$$

$$G_{f22}(x,y;x',y') = \frac{j}{4} H_0^{(2)}[k_2\sqrt{(x-x')^2+(y-y')^2}] \,, \tag{3.2}$$

$$G_{s22}(x,y;x',y') = \frac{1}{2\pi}\int_{-\infty}^{\infty} \frac{j}{2\gamma_2}\left(\frac{\gamma_2-\gamma_1}{\gamma_2+\gamma_1}\right) e^{-j\gamma_2(y+y'+2a)} e^{-j\alpha(x-x')} d\alpha \,, \tag{3.3}$$

$\gamma_i^2 = k_i^2 - \alpha^2$, $i = 1, 2$, $\mathrm{Im}(\gamma_i) \le 0$, $y' > -a$.

For programming purposes, the scattered magnetic field can be expressed according to the following two cases,

[case 1] if $a > 0$ ($\theta_1 > \theta_2$)

$$H^S(\bar{r}) = \begin{cases} H_1^S(\bar{r}) = \int_{\theta_1-2\pi}^{\theta_2} G_{12}(x,y;x',y') J_m(\theta') d\theta' + \int_{\theta_2}^{\theta_1} G_{11}(x,y;x',y') J_m(\theta') d\theta', & y \le -a \\ H_2^S(\bar{r}) = \int_{\theta_1-2\pi}^{\theta_2} G_{22}(x,y;x',y') J_m(\theta') d\theta' + \int_{\theta_2}^{\theta_1} G_{21}(x,y;x',y') J_m(\theta') d\theta', & y > -a \end{cases} \tag{4}$$

[case 2] if $a < 0$ ($\theta_1 < \theta_2$)

$$H^s(\bar{r}) = \begin{cases} H_1^S(\bar{r}) = \int_{\theta_1}^{\theta_2} G_{12}(x,y;x',y') J_m(\theta') d\theta' + \int_{\theta_2}^{2\pi-\theta_1} G_{11}(x,y;x',y') J_m(\theta') d\theta', & y \le -a \\ H_2^S(\bar{r}) = \int_{\theta_1}^{\theta_2} G_{22}(x,y;x',y') J_m(\theta') d\theta' + \int_{\theta_2}^{2\pi-\theta_1} G_{21}(x,y;x',y') J_m(\theta') d\theta', & y > -a \end{cases} \tag{5}$$

with

$$J_m(\theta) = -j\omega\varepsilon\sqrt{F^2(\theta) + F'^2(\theta)}\, J_{sm}(\theta) \,.$$

Here, $J_{sm}(\theta)$ is the induced surface magnetic current density, which is proportional to the normal derivative of the magnetic field on the conductor surface. $G_1(x, y; x', y')$ and $G_2(x, y; x', y')$ denote the Green's function for the line source in regions 1 and 2, respectively. $H_0^{(2)}$ is the Hankel function of the second kind of order zero. We might face some difficulties in calculating the Green's function. The Green's function, given by equation (2), is in the form of an improper integral, which must be evaluated numerically. However, the integral converges very slowly when r and r' approach the interface $y = -a$. Fortunately, we find that the integral in G_1 or G_2 may be rewritten as a closed-form term plus a rapidly converging integral. Thus the whole integral in the Green's function can be calculated efficiently.

For a perfectly conducting scatterer, the total tangential electric field at the surface of the scatterer is equal to zero,

$$\hat{n} \times \left(\frac{1}{j\omega\varepsilon} \nabla \times \vec{H}^{tot}\right) = 0 \quad (6)$$

with $\vec{H}^{tot} = \vec{H}^{i} + \vec{H}^{s}$, where $\hat{n}$ is the outward unit vector normal to the surface of the scatterer and $\vec{H}^{s}$ is the scattered field. For the direct scattering problem, the scattered field $\vec{H}^{s}$ is calculated by assuming that the shape is known. For the inverse problem, assume the approximate center of scatterer, which in fact can be any point inside the scatterer, is known. Then the shape function $F(\theta)$ can be expanded as,

$$F(\theta) = \sum_{n=0}^{N/2} B_n \cos(n\theta) + \sum_{n=1}^{N/2} C_n \sin(n\theta) \quad (7)$$

where B_n and C_n are real coefficients to be determined, and N+1 is the number of unknowns for the shape function. In the inversion procedure, the asynchronous particle swarm optimization is used to minimize the following cost function [36],

$$CF = \left\{\frac{1}{M_t} \sum_{m=1}^{M_t} \left|\vec{H}^{s}_{exp}(\vec{r}_m) - \vec{H}^{s}_{cal}(\vec{r}_m)\right|^2 / \left|\vec{H}^{s}_{exp}(\vec{r}_m)\right|^2\right\}^{1/2} \quad (8)$$

where M_t is the total number of measurement points. $\vec{H}^{s}_{exp}(\vec{r}_m)$ and $\vec{H}^{s}_{cal}(\vec{r}_m)$ are the measured and calculated scattered fields, respectively.

B. Asynchronous particle swarm optimization (APSO)

APSO starts with an initial population of potential solutions that is composed by a group of randomly generated individuals. Each individual is a D-dimensional vector consisting of D optimization parameters. The initial population may be expressed by $\{X_j: j = 1, 2, ..., N_p\}$, where N_p is the population size. Clerc [41] suggested the use of a different velocity update rule, which introduced a parameter ξ called constriction factor. The role of the constriction factor is to ensure convergence when all the particles tend to stop their movement. The flow chart of the APSO algorithm is shown in Fig. 2. The velocity update rule is then given by,

$$v_j^{k+1} = \xi \cdot \left(v_j^k + c_1 \cdot \phi_1 \cdot \left(x_{pbest_j}^k - x_j^k\right) + c_2 \cdot \phi_2 \cdot \left(x_{gbest}^k - x_j^k\right)\right), \quad (9)$$

$$x_j^{k+1} = x_j^k + v_j^{k+1},\ j = 0 \sim N_p - 1, \quad (10)$$

where $\xi = \dfrac{2}{\left|2 - \phi - \sqrt{\phi^2 - 4\phi}\right|}$, $\phi = c_1 + c_2 \geq 4$.

The symbols c_1 and c_2 are the learning coefficients used to control the impact of the local and global component in the velocity term of equation (9), ξ is the constriction factor, ϕ_1 and ϕ_2 are both random numbers between 0 and 1.

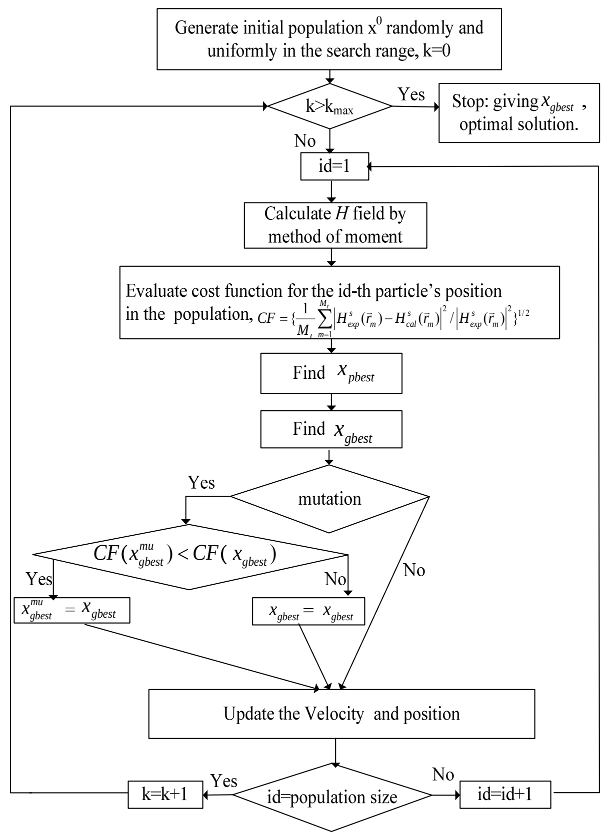

Fig. 2. The flowchart of the modified asynchronous PSO (APSO).

The key distinction between a particle swarm optimization (PSO) and the asynchronous particle swarm optimization (APSO) is on the updating mechanism, damping boundary condition and mutation scheme. The current updating mechanism of asynchronous PSO use the following rule: just after the update of equation (9) for each particle the best positions x_{pbest} and x_{gbest} will be replaced if the new position is better than the current best ones such that they can be used immediately for the next particle. In this way, the swarm reacts more quickly to speed up the convergence.

Boundary conditions in PSO play a key role as it is pointed out in [42]. In this paper we have applied the damping boundary condition and mutation scheme. The mutation scheme plays a role in avoiding premature convergences for the searching procedure and helps the x_{gbest} escape from the local optimal position. More details about the APSO algorithm can be found in [28].

III. Numerical Results

We illustrate the performance of the proposed inversion algorithm and its sensitivity to random noise in the scattered field. Let us consider a perfectly conducting cylinder buried in a lossless half-space ($\sigma_1 = \sigma_2 = 0$). The permittivity in each region is characterized by $\varepsilon_1 = \varepsilon_0$ and $\varepsilon_2 = 2.7\ \varepsilon_0$, respectively. The frequency of the incident wave is chosen to be 3 GHz with incident angles ϕ_1 equals to - 45^0, 0^0, and 45^0, respectively. The wavelength λ_0 is 0.5 m. The purpose of this study is to reconstruct the shape of the partially immersed perfectly conducting cylinder by using the scattered fields at different incident angles. To reconstruct the shape of the cylinder, the object is illuminated by incident waves from three different directions and 8 measurements are made for each incident angle at the points equally separated on a semi-circle with the radius of 3 m in region 1 along the interface $y = -a$, which is considered here as a test configuration for future application of landmine detection. To save computing time, the number of unknowns is set to be 7. Moreover, to avoid inverse crime, the discretization number for the direct problem is two times that for the inverse problem in the simulation. In forward problem, the shape function $F(\theta)$ is discretized to 60. The related coefficients of the APSO are set below. The learning coefficients c_1 and c_2 are set to 2.8 and 1.3, respectively [43]. The mutation probability is 0.1 and the population size is set to 70. The operations coefficients for the NU-SSGA algorithm are set as below: The crossover probability and the mutation probability are set to be 0.02 and 0.05, respectively [19]. The population size N_p is the same with APSO. The searching range for the unknown coefficients is chosen from 0 to 1.0. The relative error of shape function (RE) of the reconstructed shape is defined as,

$$RE = \{\frac{1}{N'}\sum_{i=1}^{N'}[\vec{F}^{cal}(\theta_i) - \vec{F}(\theta_i)]^2 / \vec{F}^2(\theta_i)\}^{1/2} . \tag{11}$$

where N' is cutting number of the object. $F^{cal}(\theta_i)$ and $F(\theta_i)$ are calculated shape function and is given the shape function.

In the first example, the shape function is chosen to be $F(\theta) = (0.1 + 0.04\cos 2\theta)$ m. In this case, the final reconstructed shapes by NU-SSGA algorithm and APSO scheme at the 1000 th generation are compared to the exact shape in Fig. 3. Figure 4 shows that the reconstruction relative error versus the number of iterations by NU-SSGA algorithm and APSO, respectively. It is clear that the APSO outperforms NU-SSGA.

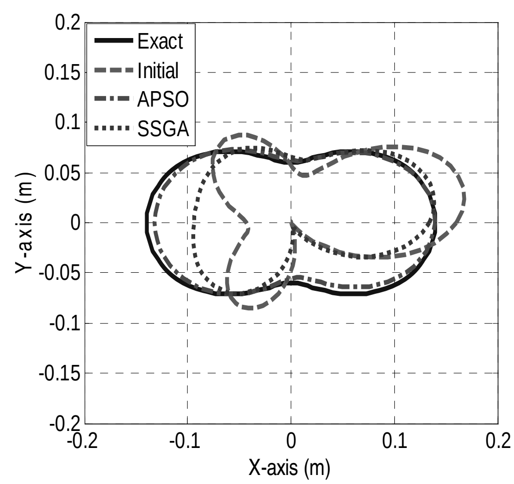

Fig. 3. The reconstructed shape of the cylinder for example 1.

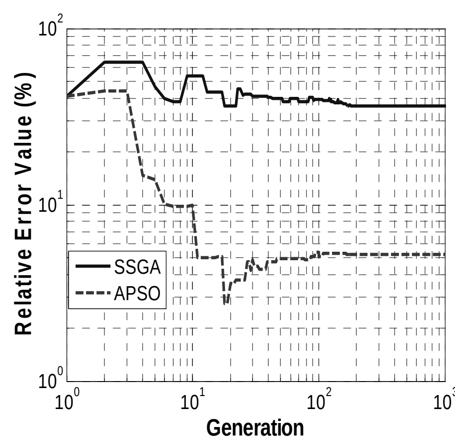

Fig. 4. Shape function error in each generation.

In the second example, the shape function is chosen to be $F(\theta) = (0.1 + 0.03\cos2\theta + 0.025\sin2\theta + 0.015\sin3\theta)$ m. The reconstructed shape function for the best population member is plotted in Fig. 5 with the shape error shown in Fig. 6. The reconstructed shape error is 5.3 % by APSO and it is seen that the error comes from the bottom of the shape. It is noted that the APSO still outperforms NU-SSGA in term of reconstruction accuracy and convergence speed.

For investigating the effect of noise, we add to each complex scattered field a quantity $b+cj$, where b and c are independent random numbers having a Gaussian distribution with zero mean, each random number is multiplied by the noise level times the rms value of the scattered field. The SNR applied include 40 dB, 30 dB, 20 dB, 10 dB, and 5 dB in the simulations. The numerical results for examples 1 and 2 are plotted in Fig. 7. They show that the effect of the noise is tolerable for noise levels below 10 dB.

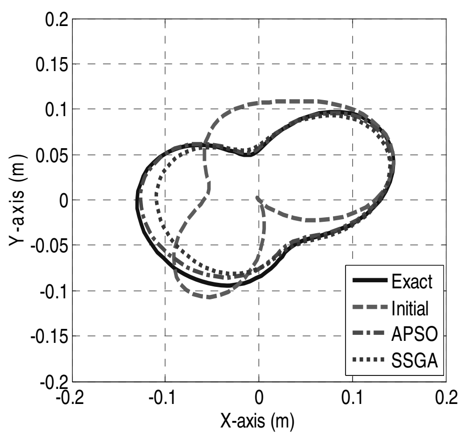

Fig. 5. The reconstructed shape of the cylinder for example 2.

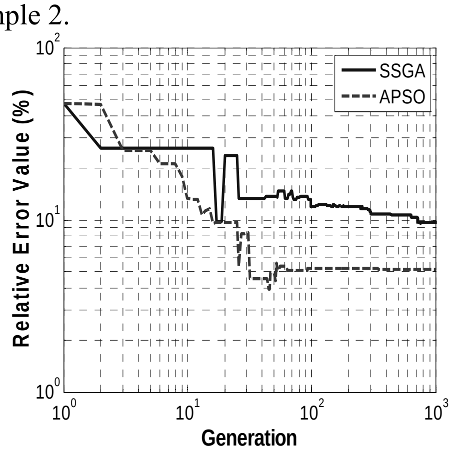

Fig. 6. Shape function error in each generation.

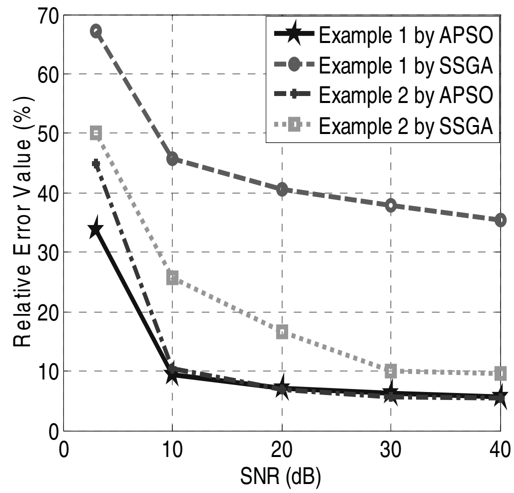

Fig. 7. Shape function error as a function of SNR for all examples.

IV. CONCLUSION

We have presented a study of applying the APSO and NU-SSGA to reconstruct the shapes of a partially immersed conducting cylinder illuminated by TE waves. The inverse problem is reformulated into an optimization one. Numerical results show that the APSO has better reconstructed results compared with NU-SSGA when the same number of iterations is applied.

Some numerical examples have been given, and good agreement between the exact and the reconstructed profiles is achieved by APSO in each case. The effect of noise on the overall reconstruction has also been investigated, and it is observed that the proposed method is able to provide good shape reconstruction as long as the normalized SNR is > 10 dB.

ACKNOWLEDGEMENT

This work was supported by the National Science Council, Republic of China, under Grant NSC 101-2221-E-032-029.

REFERENCES

[1] T. Takenaka and T. Moriyama, "Inverse scattering approach based on the field equivalence principle: inversion without a priori information on incident fields," *Optics Letters*, vol. 37, pp. 3432-3434, Aug. 2012.

[2] F. Soldovieri, F. Ahmad, and R. Solimene, "Validation of microwave tomographic inverse scattering approach via through-the-wall experiments in semi controlled conditions," *IEEE*

Transactions Geoscience and Remote Sensing, vol. 8, no. 1, pp. 123-127, Jan. 2011.

[3] C. H. Sun, C. L. Li, C. C. Chiu, and C. H. Huang, "Time domain image reconstruction for a buried 2D homogeneous dielectric cylinder using NU-SSGA," *Research in Nondestructive Evaluation,* vol. 22, no.1, pp. 1-15, Jan. 2011.

[4] C. C. Chiu, C. H. Sun, C. L. Li, and C. H. Huang, "Comparative study of some population-based optimization algorithms on inverse scattering of a two-dimensional perfectly conducting cylinder in slab medium," *IEEE Transactions on Geoscience and Remote Sensing*, vol. 51, pp. 2302-2315, Apr. 2013.

[5] M. Benedetti, D. Lesselier, M. Lambert, and A. Massa, "Multiple-shape reconstruction by means of multiregion level sets," *IEEE Transactions Geoscience and Remote Sensing*, vol. 48, no. 5, pp. 2330-2342, May 2010.

[6] C. L. Li, C. H. Huang, C. C. Chiu, and C. H. Sun, "Comparison of dynamic differential evolution and asynchronous particle swarm optimization for inverse scattering of a two-dimensional perfectly conducting cylinder," *Applied Computational Electromagnetics Society (ACES) Journal*, vol. 27, no. 10, pp. 850-865, October 2012.

[7] Z. Zhang, Z. Zhu, Q. Xin, X. Xie, J. Lei, and S. Huang, "Analysis and application of inverse detecting method based on local electric field," *Applied Computational Electromagnetics Society (ACES) Journal*, vol. 27, no. 7, pp. 566-573, July 2012.

[8] C. Huang, C. Chen, C. Chiu, and C. Li, "Reconstruction of the buried homogenous dielectric cylinder by FDTD and asynchronous particle swarm optimization," *Applied Computational Electromagnetics Society (ACES) Journal*, vol. 25, no. 8, pp. 672-681, August 2010.

[9] C. H. Sun, C. C. Chiu, and C. H. Chen "Time domain microwave imaging for a metallic cylinder by using evolutionary algorithms," *Imaging Science Journal*, vol. 61, pp. 3-12, Jan. 2013.

[10] M. Farmahini-Farahani, R. Faraji-Dana, and M. Shahabadi, "Fast and accurate cascaded particle swarm gradient optimization method for solving 2-D inverse scattering problems," *Applied Computational Electromagnetics Society (ACES) Journal*, vol. 24, no. 5, pp. 511-517, October 2009.

[11] C. H. Huang, C. C. Chiu, C. J. Lin, and Y. F. Chen, "Inverse scattering of inhomogeneous dielectric cylinders buried in a slab medium by TE wave illumination," *Applied Computational Electromagnetics Society (ACES) Journal*, vol. 22, no. 2, pp. 295-301, July 2007.

[12] P. C. Sabatier, "Theoretical considerations for inverse scattering," *Radio Science*, vol. 18, pp. 629-631, 1983.

[13] A. M. Denisov, *Elements of Theory of Inverse Problems*, VSP, Utrecht, The Netherlands, 1999.

[14] M. El-Shenawee, O. Dorn, and M. Moscoso, "An adjoint-field technique for shape reconstruction of 3-D penetrable object immersed in lossy medium," *IEEE Trans. Antennas Propag*., vol. 57, no. 2, pp. 520-534, 2009.

[15] T. Rubaek, P. M. Meaney, P. Meincke, and K. D. Paulsen, "Nonlinear microwave imaging for breast-cancer screening using Gauss-Newton's method and the CGLS inversion algorithm," *IEEE Trans. Antennas Propag*., vol. 55, no. 8, pp. 2320-2331, 2007.

[16] C. H. Sun, C. L. Li, C. C. Chiu, and C. H. Huang, "Time domain image reconstruction for a buried 2D homogeneous dielectric cylinder using NU-SSGA," *Research in Nondestructive Evaluation,* vol. 22, no.1, pp. 1-15, Jan. 2011.

[17] W. Chien, C. H. Sun, and C. C. Chiu, "Image reconstruction for a partially immersed imperfectly conducting cylinder by genetic algorithm," *International Journal of Imaging Systems and Technology*, vol. 19, pp. 299-305, 2009.

[18] X. M. Zhong, C Liao, and W. Chen, "Image reconstruction of arbitrary cross section conducting cylinder using UWB pulse," *Journal of Electromagnetic Waves Application*, vol. 21, no. 1, pp. 25-34, 2007.

[19] W. Chien and C. C. Chiu, "Using NU-SSGA to reduce the searching time in inverse problem of a buried metallic object," *IEEE Transactions on Antennas and Propagation*, vol. 53, no. 10, pp. 3128-3134, 2005.

[20] K. A. Michalski, "Electromagnetic imaging of circular-cylindrical conductors and tunnels using a differential evolution algorithm," *Microwave and Optical Technology Letters*, vol. 27, no. 5, pp. 330-334, Dec. 2000.

[21] A. Semnani, I. T. Rekanos, M. Kamyab, and M. Moghaddam, "Solving inverse scattering problems based on truncated cosine Fourier and cubic B-spline expansions," *IEEE Transactions on Antenna Propagation*, vol. 60, pp. 5914-5923, Dec. 2012.

[22] C. H. Sun, C. C. Chiu, C. L. Li, and C. H. Huang, "Time domain image reconstruction for homogenous dielectric objects by dynamic differential evolution," *Electromagnetics*, vol. 30, no. 4, pp. 309-323, May 2010.

[23] A. Semnani, I. T. Rekanos, M. Kamyab, and T. G. Papadopoulos, "Two-dimensional microwave imaging based on hybrid scatterer representation and differential evolution," *IEEE Trans. Antennas*

Propag., vol. 58, no. 10, pp. 3289-3298, Oct. 2010.

[24] I. T. Rekanos, "Shape reconstruction of a perfectly conducting scatterer using differential evolution and particle swarm optimization," *IEEE Transactions on Geoscience and Remote Sensing*, vol. 46, no. 7, pp. 1967-1974, 2008.

[25] A. Semnani and M. Kamyab, "An enhanced hybrid method for solving inverse scattering problems," *IEEE Transactions on Magnetics*, vol. 45, no. 3, pp. 1534-1537, March 2009.

[26] C. H. Chen, C. C. Chiu, C. H. Sun, and W. L. Chang, "Two-dimensional finite-difference time domain inverse scattering scheme for a perfectly conducting cylinder," *Journal of Applied Remote Sensing,* vol. 5, 053522, May 2011.

[27] M. Donelli and A. Massa, "Computational approach based on a particle swarm optimizer for microwave imaging of two-dimensional dielectric scatterers," *IEEE Transactions on Microwave Theory and Techniques*, vol. 53, no. 5, pp. 1761-1776, May 2005.

[28] C. C. Chiu, C. H. Sun, and W. L. Chang "Comparison of particle swarm optimization and asynchronous particle swarm optimization for inverse scattering of a two-dimensional perfectly conducting cylinder," *International Journal of Applied Electromagnetics and Mechanics*, vol. 35, no. 4, pp. 249-261, April 2011.

[29] M. R. Hajihashemi and M. E. Shenawee, "TE versus TM for the shape reconstruction of 2-D PEC targets using the level-set algorithm," *IEEE Transactions on Geoscience and Remote Sensing*, vol. 48, no. 3, pp. 1159-1168, 2010.

[30] A. Litman, "Reconstruction by level sets of n-array scattering obstacles," *Inverse Probl.*, vol. 21, no. 6, pp. S131-S152, Dec. 2005.

[31] A. Liseno, R. Pierri, and F. Soldovieri, "Shape identification by physical-optics: the two-dimensional TE case," *J. Opt. Soc. Am. A*, vol. 20, no. 9, pp. 1827-1830, Sept. 2003.

[32] C. L. Li, S. H. Chen, C. M. Yang, and C. C. Chiu, "Electromagnetic imaging for a partially immersed perfectly conducting cylinder by the genetic algorithm," *Radio Science*, vol. 39, no. 2, RS2016, April 2004.

[33] R. C. Eberhart and Y. Shi, "Comparison between genetic algorithms and particle swarm optimization," *Proc. 7th Annu. Conf. Evol. Program (EP-98)*, vol. 1447, pp. 611-616, Lecture Notes in Computer Science, March 1998.

[34] R. J. W. Hodgson, "Particle swarm optimization applied to the atomic cluster optimization problem," *Proc. Genetic and Evol. Comp. Conf.* (GECCO-2002), pp. 68-73, 2002.

[35] R. Hassan, B. Cohanim, and O. de Weck, "A comparison of particle swarm optimization and the genetic algorithm," *Proc. of the 46th AIAA/ASME/ASCE/AHS/ASC Structures, Structural Dynamics, and Materials Conference*, pp. 1-13, 2005.

[36] D. W. Boeringer and D. H. Werner, "Particle swarm optimization versus genetic algorithms for phased array synthesis," *IEEE Transactions on Antenna Propagation*, vol. 52, pp. 771-779, March 2004.

[37] J. Ma, W. C. Chew, C. C. Lu, and J. Song, "Image reconstruction from TE scattering data using equation of strong permittivity fluctuation," *IEEE Trans. Antennas Propag*. vol. 48, no. 6, pp. 860-867, 2000.

[38] C. H. Sun, C. L. Liu, K. C. Chen, C. C. Chiu, C. L. Li, and C. C. Tasi, "Electromagnetic transverse electric wave inverse scattering of a partially immersed conductor by steady-state genetic algorithm," *Electromagnetics*, vol. 28, no. 6, pp. 389-400, Aug. 2008.

[39] Y. C. Chen, Y. F. Chen, C. C. Chiu, and C. Y Chang, "Image reconstruction of buried perfectly cylinder illuminated by transverse electric waves," *International Journal of Imaging Systems and Technology*, vol. 15, pp. 261-265, 2006.

[40] Y. S. Lin and C. C. Chiu, "Image reconstruction for a perfectly conducting cylinder buried in slab medium by a TE wave illumination," *Electromagnetics*, vol. 25, no. 3, pp. 203-216, 2005.

[41] M. Clerc, "The swarm and the queen: towards a deterministic and adaptive particle swarm optimization," *Proceedings of Congress on Evolutionary Computation*, pp. 1951 - 1957, 1999.

[42] T. Huang and A. S. Mohan, "A hybrid boundary condition for robust particle swarm optimization," *IEEE Antennas and Wireless Propagation Letters*, vol. 4, pp. 112 - 117, 2005.

[43] A. Carlisle and G. Dozier, "An off-the-shelf PSO," *Proceedings of the 2001 Workshop on Particle Swarm Optimization*, pp. 1-6, 2001.

Ching-Lieh Li was born November 24, 1963, in Pingtun, Taiwan. He received the B.Sc. degree from National Taiwan University, Taipei, Taiwan, in 1985, and the M.Sc. and Ph.D. degrees from Michigan State University, East Lansing, in 1990 and 1993, respectively, all in

Electrical Engineering.

From 1989 to 1993, he was a Research Assistant in the Electrical Engineering Department, Michigan State University, where he worked on the measurement techniques for determining the electromagnetic properties of materials. In 1993, he joined the Electrical Engineering Faculty at Tamkang University, Taipei, Taiwan, where now he is a professor. Currently, his research activities involve inverse scattering problem, and microstrip antenna design and dielectric material characterization, etc. His areas of special interest include theoretical and computational electromagnetics, and application of various optimization schemes such as SSGA, PSO, DE, and Taguchi method to electromagnetics.

Chi-Hsien Sun received MSEE and PhD degrees in Electrical Engineering from Tamkang University, Taipei, Taiwan, in 2008 and 2012, respectively. Since 2012, he has been a postdoctoral with the Department of Electronic and Computer Engineering,National Taiwan University of Science and Technology. His special interests include radio over fiber (ROF), WDM-PON and computational electromagnetics, and application of various optimization schemes such as the steady state genetic algorithm (SSGA), particle swarm optimization (PSO), dynamic differential evolution (DDE), self-adaptive dynamic differential evolution (SADDE), and the Taguchi method in electromagnetics

Chien-Ching Chiu received his B.Sc. degree from National Chiao Tung University, Hsinchu, Taiwan, in 1985 and his M.Sc. and PhD degrees from National Taiwan University, Taipei, in 1987 and 1991, respectively. From 1987 to 1989, he was a communication officer with the ROC Army Force. In 1992 he joined the faculty of the Department of Electrical Engineering, Tamkang University, where he is now a professor. From 1998 to 1999, he was a visiting scholar at the Massachusetts Institute of Technology, Cambridge, and the University of Illinois at Urbana-Champaign. He is a visiting professor with the University of Wollongong, Australia, in 2006. Moreover, he was a visiting professor with the University of London, United Kingdom, in 2011. His current research interests include microwave imaging, numerical techniques in electromagnetics, indoor wireless communications, and ultra wideband communication systems. He has published more than 90 journal papers on inverse scattering problems, communication systems and optimization algorithms.

Lung-Fai Tuen received the B.Sc. degree from Jinwen University of Science and Technology, Taipei, Taiwan, in 2006, and the M.Sc. degree and Ph.D. student from Tamkang University, in 2009 and 2013, respectively, all in Electrical Engineering. From 2007 to 2009, he was a Research Assistant in the Electrical Engineering Department, Tamkang University, where he worked on the development techniques for array antenna design.

A Method-of-Moments Model for Determination of Radiated Magnetic Field from Switch-Mode Power Supplies Components using Near-Field Measurement Data

S. M. M. Mirtalaei [1, 2], S. H. H. Sadeghi [1], and R. Moini [1]

[1] Department of Electrical Engineering
Amirkabir University of Technology, Tehran, 4413-15875, Iran
mirtalaei@aut.ac.ir, sadeghi@aut.ac.ir, moini@aut.ac.ir

[2] Department of Electrical Engineering
Islamic Azad University – Najafabad Branch, Najafabad, 8514143131, Iran

Abstract **─** Electromagnetic interference due to switching-mode power supplies (SMPSs) is a great concern for the designers of electrical and electronic equipment. In this paper, we propose a method-of-moments model for efficient determination of radiated magnetic field due to SMPSs mounted on printed circuit boards (PCBs). This model involves three stages. First, the magnetic field distribution on a given rectangular plan in the vicinity of the board is measured. The measured data are then used to identify the equivalent source currents on the surface of the radiating board by the method-of-moments. Having determined the radiating sources, the magnetic field distribution at a desired distance from the PCB can be computed. The main feature of the proposed model is its direct approach for reconstruction of the radiating current sources, which makes it much faster than the conventional techniques, involving heuristic optimization algorithms. The validity of the proposed technique is demonstrated by comparing the actual and predicted far-field magnetic field radiations due to a small electrical loop, a high frequency inductor as a typical radiating magnetic field component of SMPSs, and a microstrip transmission line, which simulating conduction paths on the PCB.

Index Terms **─** Electromagnetic compatibility, method-of-moments, near-field measurement, and switch-mode power supply.

I. INTRODUCTION

Switching mode power supplies (SMPSs) are commonly used in electronic and electric equipment as their input power source. The development of fast power semiconductor devices (MOSFET, IGBT, etc.) has increased the switching frequency of SMPSs, improving their power-volume ratio. However, the designers of SMPSs are greatly concerned about the resultant fast voltage and current variations, which can cause related elements to radiate, including PCB conduction paths, inductors, transformers, and heat sinks [1-7].

SMPSs have thus become important sources of electromagnetic interference (EMI). On the other hand, increasing integration of power electronic circuit modules together with the continuing growth in power density and switching frequency have resulted in a close interaction between SMPS components.

In order to design an SMPS system, which satisfies the requirements of electromagnetic compatibility (EMC) standards; designers typically use a set of established EMC rules to control various electromagnetic parameters [8]. SMPSs are commonly tested in a semi-anechoic chamber (SAC) or open area test site (OATS) to assess compatibility with EMC standards. If the EMC test fails, designers must modify their design and repeat the test. This process is very time-consuming and expensive, and thus, designers seek more efficient methods to predict radiated

Submitted On: Nov.13, 2012
Accepted On: June 23, 2013

emission form SMPSs and their related components in the early design stages. It is worth noting that SMPSs require high frequency inductors, transformers, and current loops, radiating strong magnetic and electric fields.

However, there is little work on the determination of radiated electric field form SMPSs [9] but determination of radiated magnetic field is more popular [10, 11]. Modeling approaches for determination of radiated magnetic field from SMPSs can be summarized in three categories. The first approach is based on a simplified analytical model for radiating components of SMPSs [1]. In this model, the transmission line theory is used for computing the electromagnetic field radiations in low frequency while a number of electrical dipoles are used for modeling the high frequency range radiations. These simplified analytical expressions are very crude approximations of radiated emission.

The second approach is based on the use of numerical methods. In [2], the system is simulated by a 3D finite element tool for modeling the governing equations, with source current or voltage extracted by measurement or standard circuit analysis. In [3], the finite-difference time-domain method is adopted to examine the electromagnetic resonant effects of various types of heat sinks, which are commonly used in SMPSs. Recommendations are proposed for optimal selection of heat sinks and the placement of components to mitigate potential EMC effects. Identification of source current and voltage and modeling all SMPS components in this approach is relatively complicated and cumbersome, making it unattractive for treating a complex SMPS. The third approach is based on the reconstruction of radiating sources on the respective PCB [4, 5]. This approach can be summarized in three distinct stages. First, the near-field data are measured. The measured data are then used to identify a set of equivalent radiating sources that generate the same field data as the original radiating sources. Finally, the field value at any point outside the board is computed by adding the contributions from all sources. Radiating sources in this method can be modeled as a current distribution on the PCB plane [4] or a set of electric and magnetic dipoles [5]. The determination of the equivalent radiating source from the near-field measured data in this method is based on the application of the electromagnetic equivalence principle [12], which involves optimization methods. Since the optimization process is time consuming, these methods are time-consuming and thus inappropriate for treating complex SMPSs [11].

In this paper, we adopt the source reconstruction approach described above for predicting radiated magnetic field from a typical SMPS and its related components. Here, we use the method-of-moments (MOM) to solve the governing integral equations, relating measured near magnetic fields with the equivalent surface electrical currents on the PCB plane. The proposed method offers several advantages. It is a direct method, and hence, is faster than those involve heuristic optimization techniques. Because of using analytic free-space Green's function, the stability of the computations in the proposed method is guaranteed and is not influenced by the sampling criteria for the fields [13].

The manuscript is organized as follows. In section II, the theory and basic formulation of the proposed method are presented. The validity of the proposed technique is demonstrated in section III where the actual and predicted far-field magnetic field radiations are compared, using simulation and experimental data.

II. THEORY

The geometry of the problem is shown in Fig. 1. As shown in this figure, a typical PCB is represented by radiating current sources located at z = 0. It is assumed that the PCB contains an SMPS together with related components, including several inductors, transformers, heat sinks, and PCB conduction paths among other electronic devices. The SMPS is operating at frequency f large enough to cause related components to radiate.

To determine the far-field ($z = h_2$ in Fig. 1) magnetic field distribution in the problem posed above, we adopt the electromagnetic equivalence principle [12]. According to this principle, a given set of sources (Fig. 2) bounded within a closed surface S can be characterized by equivalent electric currents (J) and magnetic currents (M) distributed on the surface S that encloses the original sources such that the generated fields outside the surface containing the sources are the same in both the original and the equivalent problem.

As a first step to determine the far-field radiations, we measure the tangential magnetic fields, H_x and H_y, on a rectangular plane ($z = h_1$ in Fig. 1) parallel to the plane of the PCB. The measurement plane, placed at a close vicinity of the PCB is assumed to be large enough to encompass all measurable values of magnetic field, resembling plane S in Fig. 2. It is worth noting that the number of measurement points is restricted by the probe structure and its sensitivity to field variations.

The measured magnetic field data are then used to identify the unknown equivalent current density ($\vec{J}_{eq} = J_{xeq}\hat{x} + J_{yeq}\hat{y}$) on the PCB plane ($z = 0$ in Fig. 1). This is done by ensuring that the measured data are the same as those obtained theoretically by the current sources.

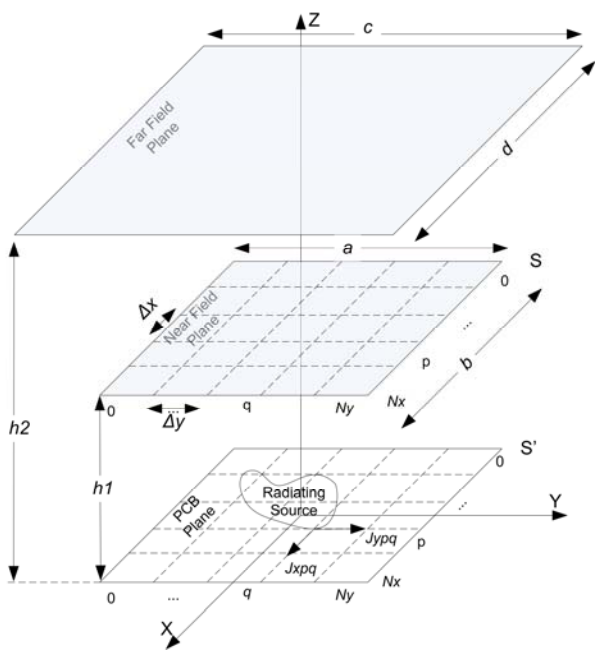

Fig. 1. Geometry of the problem, comprising the plane of radiating current sources at the location of PCB ($z = 0$), the measurement plane in the near filed zone ($z = h_1$) and the far-field plane ($z = h_2$) with unknown magnetic field distribution.

The magnetic field $\vec{H}$ in free space due to an arbitrary distribution of electric current J_{eq} is given as follows [14],

$$\vec{H} = \frac{1}{\mu_0}\nabla \times \vec{A}, \tag{1}$$

where μ_0 is the permeability of free space and $\vec{A}$ is the auxiliary magnetic vector potential,

$$\vec{A} = \frac{\mu_0}{4\pi}\iint_{S'} \vec{J}_{eq}\frac{e^{-jkR}}{R}ds'. \tag{2}$$

Here, R is the distance between source point (x',y',z') and observation point (x,y,z), k is the propagation constant and S' is the source surface.

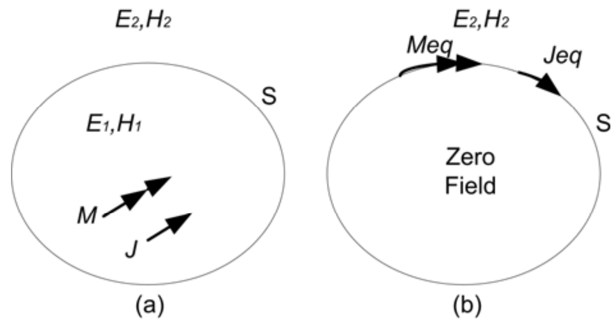

Fig. 2. The electromagnetic equivalence principle; (a) the original problem and (b) the equivalent problem.

By expanding equations (1) and (2) in the Cartesian coordinates, the values of the tangential magnetic field on the near-field plane, H_x and H_y, can be determined as follow,

$$H_x = \frac{1}{4\pi}\iint_{S'}[(z)J_y]\frac{1+jkR}{R^3}e^{-jkR}dx'dy' \tag{3}$$

$$H_y = \frac{1}{4\pi}\iint_{S'}-[(z)J_x]\frac{1+jkR}{R^3}e^{-jkR}dx'dy', \tag{4}$$

where J_x and J_y represent, respectively, the x- and y- components of the unknown equivalent current density (J_{eq}) on the PCB plane, S'.

To determine J_x and J_y in equations (3) and (4), we use the method-of-moments [15]. This is done by expanding $\vec{J}_{eq}$ in terms of the appropriate basis functions in sub-domains formed by discrediting S' in N_x and N_y segments along the x- and y-axes, respectively. The use of pulse basis function with constant amplitude and phase, we have,

$$\vec{J}_{eq} = \sum_{p=1}^{N_x}\sum_{q=1}^{N_y}(J_{pqx}\hat{x} + J_{pqy}\hat{y})\Pi(x-x_p, y-y_q) \tag{5}$$

where

$$\Pi(x,y)=\begin{cases}1 & |x|<\dfrac{\Delta x}{2},|y|<\dfrac{\Delta y}{2}\\ 0 & |x|>\dfrac{\Delta x}{2},|y|>\dfrac{\Delta y}{2}\end{cases}, \quad (6)$$

$$x_p = p\Delta x - \frac{\Delta x}{2}, \quad (7)$$

$$y_q = q\Delta y - \frac{\Delta y}{2}, \quad (8)$$

and J_{pqx} and J_{pqy} are, respectively, the unknown coefficients associated with the *x*- and *y*-components of $\vec{J}_{\text{eq}}$ on sub-domain pq.

Substituting equation (5) into equations (3) and (4), the integral equations relating the magnetic fields to their equivalent electrical currents lead to a system of linear equations where the number of equations is equal to the number of measurement points, i.e.,

$$H_x = \sum_{i=0}^{N_x}\sum_{j=0}^{N_y}\frac{1}{4\pi}[(z)\,J_{yij}]\frac{1+jkR_{ij}}{R_{ij}^{\,3}}e^{-jkR_{ij}}\Delta x\Delta y, \quad (9)$$

$$H_y = \sum_{i=0}^{N_x}\sum_{j=0}^{N_y}\frac{1}{4\pi}[(-z)J_{xij}]\,\frac{1+jkR_{ij}}{R_{ij}^{\,3}}e^{-jkR_{ij}}\Delta x\,\Delta y, \quad (10)$$

or, in matrix form,

$$[H_x] = \left[Z_{H_x,J_y}\right]\left[J_y\right], \quad (11)$$

$$\left[H_y\right] = \left[Z_{H_y,J_x}\right][J_x], \quad (12)$$

where

$$Z_{H_x,J_y}(i,j) = \frac{1}{4\pi}(z)\frac{1+jkR_{ij}}{R_{ij}^{\,3}}e^{-jkR_{ij}}\Delta x\,\Delta y, \quad (13)$$

$$Z_{H_y,J_x}(i,j) = -\frac{1}{4\pi}(z)\frac{1+jkR_{ij}}{R_{ij}^{\,3}}e^{-jkR_{ij}}\Delta x\Delta y. \quad (14)$$

Since Z_{H_x,J_y} and Z_{H_y,J_x} are large and sparse, the factorization methods are generally not efficient for solving equations (11) and (12). Instead, we use an iterative method such as the least square residual (LSQR) method to treat the problem in [16]. Having determined the unknown current sources on the PCB, the radiated far-field magnetic field can be readily obtained, using equations (3) and (4).

III. MODEL VERIFICATION AND RESULTS

To demonstrate the validity of the solution technique, we first consider the special case of a small electrical loop for which the results are available in the literature. We then present the theoretical and experimental results for a high frequency inductor, which is a typical component of an SMPS, radiating strong magnetic field and a microstrip transmission line, which simulating conduction paths on the PCB.

The setup shown in Fig. 3 is used to prepare the experimental results supporting the theoretical modeling. The setup consists of a Rohde & Schwarz Hz-11 EMI probe set, a three-dimensional motorized computer controlled scanner, and a Rohde & Schwarz ZVK-4GHz vector network analyzer. The probe is an H-field loop probe with 10 mm diameter [17].

A. Small electrical loop

In order to demonstrate the robustness of the model, simulated results are presented. In these simulations, the source is a small electrical loop of radius r = 10 mm placed at the location of the PCB (h = 0 in Fig. 1) as a radiating source. The loop is excited with a 1A sinusoidal current source of frequency 30 MHz. Figure 4 shows variations of the tangential magnetic field (H_x and H_y) produced by the small electrical loop on the near-field plane (h_1 = 10 mm, a = 100 mm, and b = 100 mm in Fig. 1.) [8]. To show the effect of the measurement noise on the simulated data, the values of H_x and H_y on the near-field plane are superposed by Gaussian noise with various signal-to-noise ratios (SNRs). The noisy data are then used as input measurement entries to the proposed model, producing equivalent electrical current distribution on the PCB. The equivalent current distribution is then used to compute the field distribution on the far-field plane (h_2 = 50 mm, c = 400 mm and d = 400 mm). A comparison of the actual and reconstructed results for the SNR = 30 dB shown in Figs. 6 (a) and (b), respectively, demonstrates the validity of the proposed model. The results indicate that the model is capable of accurately reconstructing magnetic field distributions at far-field regions. A quantitative comparison of these results can also be found in Table I where the mean-square deviation, *MSD*, between the actual tangential magnetic field

$H_{tn}(n=1,2,...,N)=\sqrt{H_{xn}{}^2+H_{yn}{}^2}$, and its reconstructed counterpart, $\hat{H}_{tn}(n=1,2,...,N)$ in all cases are given by,

$$MSD=\frac{\sum_{n=1}^{N}\left(H_n-\widehat{H}_n\right)^2}{\sum_{n=1}^{N}H_n^2}. \tag{15}$$

To study the effect of sampling distance (Δx and Δy in Fig. 1) on the accuracy of the proposed technique, we have used several simulated field data on the measurement plane (i.e., $z = h_1$ in Fig. 1) with various degrees of coarseness. A quantitative comparison between the actual and reconstructed field distributions on the far-field plane (h_2 = 50 mm, c = 400 mm, and d = 400 mm) can be found in Table II. From the results illustrated in this table, it is revealed that the proposed technique is readily converged for a wide range of sampling distances on the field measurement plane. However, the number of measurement data should be large enough to achieve accurate results.

Fig. 3. Experimental setup for magnetic field measurements.

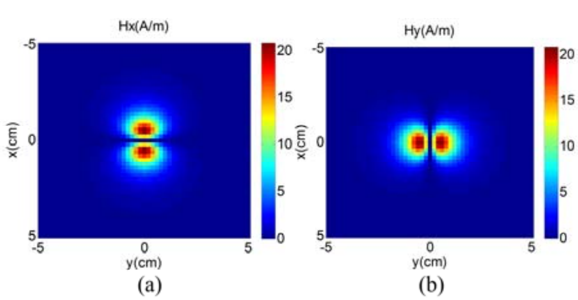

Fig. 4. Variations of the tangential magnetic field produced by the electrical loop on the near-field plane (h_1 =10 mm); (a) H_x and (b) H_y.

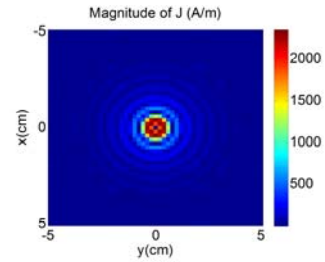

Fig. 5. Variations of the equivalent current ($|J|$) on the PCB plane (h = 0) predicted by the proposed model, using the data shown in Fig. 4.

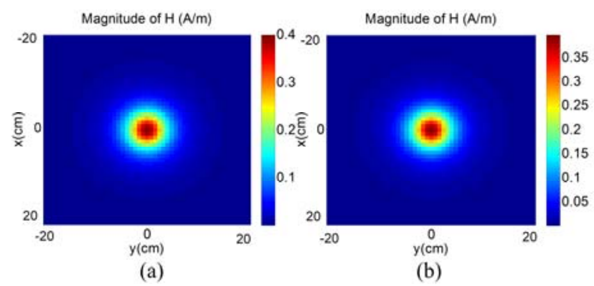

Fig. 6. Variations of the tangential magnetic field ($\sqrt{H_x^2+H_y^2}$) produced by the electrical loop on the far-field plane (h_2 = 50 mm); (a) theoretical and (b) reconstructed results.

Table I: Values of the MSD for several SNRs.

	SNR=30dB	SNR=20dB	SNR=10dB
MSD	0.0451	0.1698	0.4992

Table II: Values of the MSD and computation time for various sampling distances on the field measurement plane.

Δx =Δy	**2mm**	**5mm**	**10mm**	**20mm**
MSD	0.04	0.15	0.22	0.63
Time (sec)	279.24	1.78	0.281	0.16

B. High frequency inductor

To further examine the validity of the proposed inversion method, we analyze the experimental data obtained from a high-frequency inductor when measuring the tangential magnetic field distribution at a close distance. The inductor (Fig. 7) is a 60 turn copper wire wound on a ferromagnetic core of relative permeability 1200.

The results shown in Fig. 8 illustrate variations of the measured tangential magnetic field at frequency f = 48 MHz on the near-field plane (h_1 = 10 mm). Using the measured data, the equivalent current distribution on the PCB is reconstructed, as shown in Fig. 9. To examine the accuracy of the proposed method for computing the equivalent current, we compute the the predicted tangential magnetic field on a far-field plane (h_2 = 50 mm). A comparison of the results shown in Fig. 10 with those obtained experimentally confirms the validy of the proposed method.

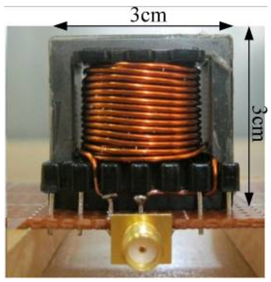

Fig. 7. High frequency inductor.

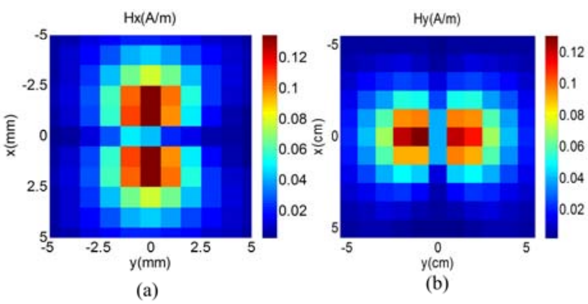

Fig. 8. Variations of the measured tangential magnetic field produced by the high frequency inductor on the near-field plane (h_1 =10 mm); (a) H_x and (b) H_y.

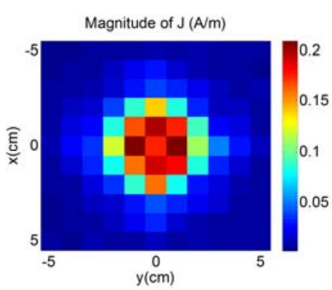

Fig. 9. Variations of the equivalent current ($|J|$) on the PCB plane (z = 0) predicted by the proposed model, using the data shown in Fig. 8.

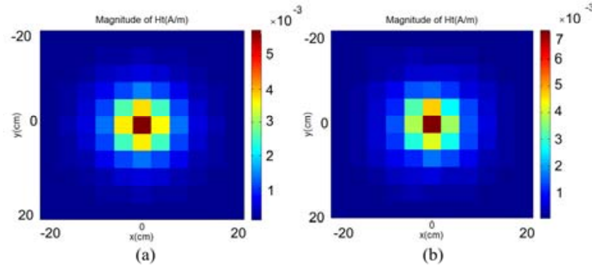

Fig. 10. Variations of the tangential magnetic field ($\sqrt{H_x^2+H_y^2}$) produced by high frequency inductor on the far-field plane (h_2 = 50 mm); (a) reconstructed and (b) measured results.

C. Microstrip transmission line

Another case used for validation of the proposed method, is microstrip transmission line. Figure 11 shows the structure of the microstrip transmission line. Microstrip fed by a sinusoidal source and terminated with a 50 Ω load. The results shown in Fig. 12 illustrate variations of the measured tangential magnetic field at frequency f = 30 MHz on the near-field plane (h_1 = 10 mm). Using the measured data, the equivalent current distribution on the PCB is reconstructed, as shown in Fig. 13. Using calculated equivalent current, we compute the predicted tangential magnetic field on a far-field plane (h_2 = 50 mm). A comparison of the results shown in Fig. 14 with those obtained experimentally confirms the validity of the proposed method.

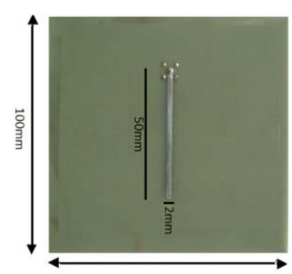

Fig. 11. Microstrip transmission line.

VI. CONCLUSION

In this paper we proposed a modeling technique, based on the electromagnetic equivalence principle, for prediction of radiated magnetic field from switch-mode power supply components. In this approach we substitute the radiating source by equivalent currents that produce same field as original radiating source. These equivalent currents are calculated based on near field measurements. It is shown that the proposed model is readily converged for a wide range of sampling distances on the field measurement plane. However, the number of measurement data should be large enough to achieve accurate results. Theoretical results supported by experiments have confirmed the accuracy of the proposed technique.

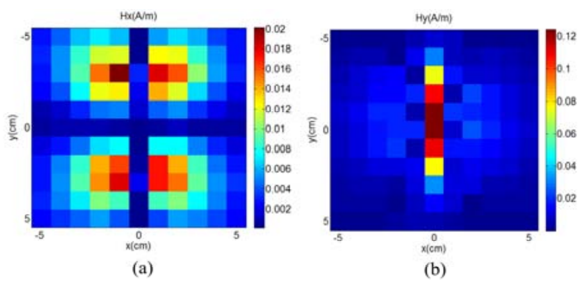

Fig. 12. Variations of the measured tangential magnetic field produced by the microstrip transmission line on the near-field plane (h_1 = 10 mm); (a) H_x and (b) H_y.

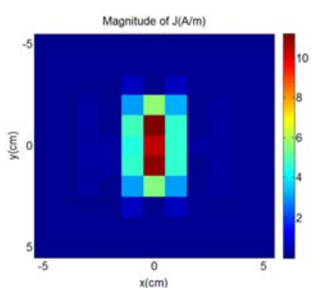

Fig. 13. Variations of the equivalent current ($|J|$) on the PCB plane (z = 0) predicted by the proposed model, using the data shown in Fig. 12.

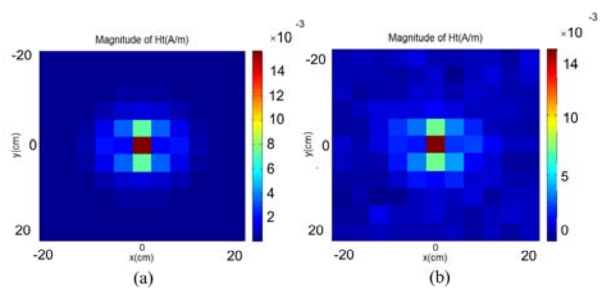

Fig.14. Variations of the tangential magnetic field ($\sqrt{H_x^2+H_y^2}$) produced by micro strip transmission line on the far-field plane (h_2=50mm); (a) reconstructed and (b) measured results.

REFERENCES

[1] G. Antonini, S. Cristina, and A. Orlandi, "EMC characterization of SMPS device circuit and radiated emission model," *IEEE Trans. Electromagn. Compat.*, vol. 38, no. 3, pp. 300-309, 1996.

[2] A. M. Sitzia, A. E. Baker, T. W. Preston, A. Puzo, and A. Pons, "Finite element analysis for power electronics EMC applications," *IEEE Trans. Magn.*, vol. 32, no. 3, pp. 1517-1520, 1996.

[3] N. J. Ryan, B. Chambers, and D. A. Stone, "FDTD modeling of heat sink RF characteristics for EMC mitigation," *IEEE Trans. Electromagn. Compat.*, vol. 44, no. 3, pp. 458-465, Aug. 2002.

[4] M. M. Hernando, A. Fernandez, M. Arias, M. Rodriguez, Y. Alvarez, and F. Las-Heras, "EMI radiated noise measurement system using the source reconstruction technique," *IEEE Trans. Ind. Electron.*, vol. 55, no. 9, pp. 3258-3265, 2008.

[5] L. Beghou, B. Liu, L. Pichon, and F. Costa, "Synthesis of equivalent 3-D models from near field measurements-application to the EMC of power printed circuit boards," *IEEE Trans. Magn.*, vol. 45, no. 3, pp. 1650-1653, Mar. 2009.

[6] M. Barzegaran and O. Mohammed, "Near field evaluation of electromagnetic signatures from wound rotor synchronous generators using wire modeling by finite elements," *28th Annual Review of Progress in Applied Computational Electromagnetics (ACES)*, pp. 774-779, Columbus, Ohio, April 2012.

[7] A. Nejadpak, M. R. Barzegaran, and O. A. Mohammed, "Evaluation of high frequency electromagnetic behavior of planar inductor designs for resonant circuits in switching power converters," *Applied Computational Electromagnetics Society (ACES) Journal*, vol. 26, no. 9, pp. 737-748, September 2011.

[8] K. Mainali and R. Oruganti, "Conducted EMI mitigation techniques for switch-mode power converters: A survey," *IEEE Trans. Power Electron.*, vol. 25, no. 9, pp. 2344 -2356, 2010.

[9] S. M. M. Mirtalaei, S. H. H. Sadeghi, and R. Moini, "Modeling the electric field emission of switch mode Power supplies using magnetic near-field measurement and method of moments," *Journal of Basic and Applied Science (JBASR)*, vol. 3, no. 2, pp. 597-602, February 2013.

[10] S. M. M. Mirtalaei, S. H. H. Sadeghi, and R. Moini, "Radiated emission determination from near field measurements for EMI evaluation of switch mode power supplies components by method of moments," *Power Electronics, Drive Systems and Technologies Conference (PEDSTC)*, pp. 421-425, Tehran, Iran, February 2013.

[11] S. M. M. Mirtalaei, S. H. H. Sadeghi, and R. Moini, "A combined method-of-moments and near field measurements for EMI evaluation of switch-mode power supplies," *Accepted for Publication in IEEE Trans. Ind. Electron,* 2013.

[12] R. F. Harrington, *Time-Harmonic Electromagnetic Fields*, McGraw-Hill, New York, 1961.

[13] Y. A. Lopez, F. L. Andrs, M. R. Pino, and T. K. Sarkar, "An improved super-resolution source reconstruction method," *IEEE Trans. Instrum. and Meas.*, vol. 58, no. 11, pp. 3855-3866, 2009.

[14] A. Balanis, *Antenna Theory: Analysis and Design*, John Wiley & Sons, 2005.

[15] Roger F. Harrington, *Field Computation by Moment Methods*, Macmillan, 1968.

[16] C. Paige and M. A. Saunders, "LSQR: An algorithm for sparse linear equations and sparse least squares," *ACM Trans. Math. Soft.*, vol. 8, pp. 43-71, 1981.

[17] K. Srinivasan, H. Sasaki, M. Swaminathan, and R. Tummala , "Calibration of near field measurements using microstrip line for noise predictions," *Proceedings of 54th Electronic Components and Technology Conference,* 2004.

Sayyed Mohammad Mehdi Mirtalaei received the B.Sc. degree in Electrical Engineering from Isfahan University of Technology (IUT), Isfahan, Iran, in 2005. He received the M.Sc. and Ph.D. degrees in Electrical Engineering from Amirkabir University of Technology (AUT), Tehran, Iran, in 2007 and 2013, respectively. Dr. Mirtalaei is Assistant Professor of Electrical Engineering at Islamic Azad University – Najafabad Branch, Isfahan, Iran. His research interest is power electronics, EMI/EMC and numerical method in electromagnetics.

Seyed Hossein H. Sadeghi received the B.Sc. degree in Electrical Engineering from Sharif University of Technology, Tehran, Iran, the M.Sc. degree in Power Engineering from the University of Manchester Institute of Science and Technology, Manchester, England, and the Ph.D. degree in Electronic Systems Engineering from Essex University, Colchester, U.K., in 1980, 1984, and 1991, respectively.

In 1992, he was appointed as a Research Assistant Professor at Vanderbilt University, Nashville, TN. During 1996-1997, and 2005-2006 he was a Visiting Professor at the University of Wisconsin, Milwaukee. Dr. Sadeghi is a Professor of Electrical Engineering at Amirkabir University of Technology, Tehran, Iran. He holds 3 patents and is the author or coauthor of one book and over 250 scientific papers published in reviewed journals and presented at international conferences. His current research interests include electromagnetic non-destructive evaluation of materials and electromagnetic compatibility issues in power engineering. He is currently a visiting professor with the University of Wisconsin, Milwaukee.

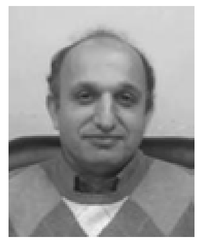

Rouzbeh Moini received the B.Sc., M.Sc., and Ph.D. degrees in Electronics from Limoges University, Limoges, France in 1984, 1985, and 1988, respectively. In 1988, he joined the department of Electrical Engineering, Amirkabir University of Technology, Tehran, Iran. From 1995 to 1996, he was a visiting Professor with the University of Florida, Gainesville. Dr. Moini is a professor of Electrical Engineering with Amirkabir University of Technology. He is the author or coauthor of more than 200 scientific publications in reviewed journals and international conferences. His current research interests include numerical methods in electromagnetics, electromagnetic compatibility, and antenna theory. He is currently a visiting Professor with the University of Toronto, Canada.

Convolutional Perfectly Matched Layer (CPML) for the Pseudospectral Time-Domain (PSTD) Method

Juan Chen [1] and Jianguo Wang [1, 2]

[1] Key Laboratory for Physical Electronics and Devices of the Ministry of Education,
Xi'an Jiaotong University, 710049, Xi'an, China
chenjuan0306@yahoo.com.cn

[2] Northwest Institute of Nuclear Technology; P. O. Box 69-15, Xi'an 710024, China

Abstract **─** In this paper, a perfectly matched layer (PML) medium with complex frequency shifted (CFS) constitutive parameters is introduced into the two-dimensional pseudospectral time-domain (PSTD) algorithm. The absorbing performance and computational efficiency of the method are illustrated by comparing with the PML method. It shows that no matter what spatial discretization is used, the reflection relative error of convolutional perfectly matched layer (CPML) is almost the same as that of the PML method. The total flops counts of the PSTD-CPML method are reduced from 49 to 34 compared with that of the PSTD-PML method. This corresponds to an efficiency gain of 1.44 in flops count reduction for the PSTD-CPML method.

Index Terms - Convolutional perfectly matched layer (CPML) and pseudospectral time-domain (PSTD) algorithm.

I. INTRODUCTION

Recently, the pseudospectral time-domain (PSTD) method has been introduced for solving Maxwell's equation [1-5]. In this method, the spatial discretization only needs two cells per wavelength. This method is extremely useful for problems with electrically large structure. For solving these problems the PSTD method is more efficient than the finite-difference time-domain method (FDTD) method in terms of computer memory. Due to the important impact of PSTD method on the electromagnetic computation, an accurate and efficient absorbing boundary condition must be developed to simulate electromagnetic interaction in an unbounded space.

In the initial implementation of the PSTD method in [1, 2], a split-step perfectly matched layer (PML) is used due to its broad band absorption characteristics and application to general media. Nevertheless, a split-field PML based on Berenger's original formulation [5-7] needed to split the field components and the implementation is complex compared with the original PSTD method.

Roden *et al.* [8] have demonstrated that the complex frequency shifted (CFS) constitutive PML parameters originally introduced by Kuzuoglu and Mittra [9] result in a PML that is highly effective at absorbing low-frequency evanescent waves. Their implementation, referred to as the convolutional-PML (CPML) method, allows the PML medium to be placed directly in the near field of geometric aberrations and can accurately absorb low-frequency waves.

In this paper, the CPML technique is introduced into the PSTD method. It is not needed to split the field components. The effectiveness of the method is illustrated through numerical examples. It is demonstrated that the reflection relative error of the CPML can reach to -70 dB, which shows good absorbing performance of the CPML method. Besides, compared with the PSTD-PML method, the PSTD-CPML method can reduce the total flops counts from 49 to 34. This corresponds to a gain of 1.44 in the computation time reduction for the PSTD-CPML method.

Submitted On: Nov. 21, 2012
Accepted On: May 13, 2013

II. FORMULATIONS

The formulations of PSTD method inclusion of CPML are presented in equations (1) to (3),

$$H_y^{n+1/2}(m,p) = H_y^{n-1/2}(m,p) + \frac{\Delta t}{\mu}\left[\frac{\partial E_z^n(m,p)}{k_x(m)\partial x} + \Phi_{Hyx}^n(m,p)\right] \quad (1)$$

$$H_x^{n+1/2}(m,p) = H_x^{n-1/2}(m,p) - \frac{\Delta t}{\mu}\left[\frac{\partial E_z^n(m,p)}{k_y(p)\partial y} - \Phi_{Hxy}^n(m,p)\right], \quad (2)$$

$$E_z^{n+1}(m,p) = E_z^n(m,p) + \frac{\Delta t}{\varepsilon}\left[\begin{array}{l}\frac{\partial H_y^{n+1/2}(m,p)}{k_x(m)\partial x} - \frac{\partial H_x^{n+1/2}(m,p)}{k_y(p)\partial y} \\ +\Phi_{Ezx}^{n+1/2}(m,p) - \Phi_{Ezy}^{n+1/2}(m,p)\end{array}\right]. \quad (3)$$

Convolutional perfectly matched layer is introduced by the variables Φ and k_s. The symbol k_s is the spatially scaled in the PML layer. Its expression is,

$$k_s(s) = 1 + (k_{\max} - 1)\frac{|s-s_0|^r}{d^r} \qquad s = x, y \quad (4)$$

where s_0 is the CPML interface, d is the depth of the CPML, r is the order of the polynomial, $k_{\max}$ is the maximum values of k_s at the exterior boundary. The expressions of Φ are as follows,

$$\Phi_{Hyx}^{n+1}(m,p) = b_x(m)\Phi_{Hyx}^n(m,p) + a_x(m)\frac{\partial E_z^{n+1}(m,p)}{\partial x} \quad (5)$$

$$\Phi_{Hxy}^{n+1}(m,p) = b_y(p)\Phi_{Hxy}^n(m,p) + a_y(p)\frac{\partial E_z^{n+1}(m,p)}{\partial y}, \quad (6)$$

$$\Phi_{Ezx}^{n+1/2}(m,p) = b_x(m)\Phi_{Ezx}^{n-1/2}(m,p) + a_x(m)\frac{\partial H_y^{n+1/2}(m,p)}{\partial x}, \quad (7)$$

$$\Phi_{Ezy}^{n+1/2}(m,p) = b_y(p)\Phi_{Ezy}^{n-1/2}(m,p) + a_y(p)\frac{\partial H_x^{n+1/2}(m,p)}{\partial y}, \quad (8)$$

where

$$b_s(s) = e^{-((\sigma_s(s)/k_s(s))+\alpha_s)(\Delta t/\varepsilon_0)}$$

$$a_s(s) = \frac{\sigma_s(s)}{k_s(s)(\sigma_s(s)+k_s(s)\alpha_s)}(b_s(s)-1).$$

The symbol σ_s are the conductivity in the PML. Within the host medium, the values of k_s are equal to 1, and all the variables Φ become zeros, then equations (1) to (3) are the standard formulations of the PSTD method [1].

The spatial derivatives in equations (1) to (7) should be replaced with the PS scheme, for example,

$$\begin{aligned}\left.\frac{\partial E_z^n(x,y)}{\partial x}\right|_{x=m\Delta x, y=p\Delta y} &= FFT_x^{-1}\left\{jk_x FFT_x\left[E_z^n(x,p\Delta y)\right]\right\}\Big|_{x=m\Delta x} \\ &= \frac{1}{2\pi}\sum_{l=0}^{M-1} jk_{x,l}\tilde{E}_z^n(k_{x,l},p\Delta y)e^{jk_{x,l}(m\Delta x)}\Delta k_x\end{aligned} \quad (9)$$

where FFT and FFT^{-1} stand for the fast Fourier transform and its inverse transform. $\tilde{E}_z^n(k_{x,l},p\Delta y) = \sum_{m=0}^{M-1} E_z^n(m\Delta x,p\Delta y)e^{-jk_{x,l}(m\Delta x)}\Delta x$ is the Fourier transforms of $E_z^n(x,p\Delta y)$. The symbol j is a complex symbol. Δx and Δy are the spatial increments in x and y directions; m and p denote the indices of the spatial increments; M is the total mesh cell in the x direction. The range of spectral domain k_x is in the form of $-2\pi/2\Delta x$ to $2\pi/2\Delta x$, so, $k_{x,l} = -\frac{2\pi}{2\Delta x} + l\Delta k_x$, $\Delta k_x = \frac{2\pi}{M\Delta x}$.

Unlike the previous PSTD-PML formula [1, 2], the PSTD-CPML formula is not needed to split the field components and the implementation is convenient.

III. THE COMPUTATIONAL EFFICIENCY OF THE CPML-PSTD COMPARED WITH PML-PSTD

To compare the computational efficiency of the PSTD-CPML method with that of the PSTD-PML method, we recall the updating equation of the PSTD-PML method as follows,

$$H_y^{n+1/2}(m,p) = \exp(-\sigma_{my}(p)\Delta t/\mu_0) H_y^{n-1/2}(m,p) + \frac{1-\exp(-\sigma_{my}(p)\Delta t/\mu_0)}{\sigma_{my}(p)} FFT^{-1}\left[jk_x \tilde{E}_z^n(m,p) \right] \tag{10}$$

$$H_x^{n+1/2}(m,p) = \exp(-\sigma_{mx}(m)\Delta t/\mu_0) H_x^{n-1/2}(m,p) - \frac{1-\exp(-\sigma_{mx}(m)\Delta t/\mu_0)}{\sigma_{mx}(m)} FFT^{-1}\left[jk_y \tilde{E}_z^n(m,p) \right], \tag{11}$$

$$E_{zx}^{n+1}(m,p) = \exp(-\sigma_x(m)\Delta t/\varepsilon_0) E_{zx}^n(m,p) + \frac{1-\exp(-\sigma_x(m)\Delta t/\varepsilon_0)}{\sigma_x(m)} FFT^{-1}\left[jk_x \tilde{H}_y^{n+1/2}(m,p) \right], \tag{12}$$

$$E_{zy}^{n+1}(m,p) = \exp(-\sigma_y(p)\Delta t/\varepsilon_0) E_{zy}^n(m,p) - \frac{1-\exp(-\sigma_y(p)\Delta t/\varepsilon_0)}{\sigma_y(p)} FFT^{-1}\left[jk_y \tilde{H}_x^{n+1/2}(m,p) \right], \tag{13}$$

$$E_z^{n+1}(m,p) = E_{zx}^{n+1}(m,p) + E_{zy}^{n+1}(m,p). \tag{14}$$

The floating point operations (flops) counts taking into account the number of multiplications /divisions (M/D), additions/subtractions (A/S), exponentiation and Fourier transform (FT) required for one complete time step for PSTD-CPML and PSTD-PML methods are listed in Table I, based on the right-hand sides of their respective updating equations. For simplicity, the number of electric and magnetic field components in all directions has been taken to be the same and assume that all multiplicative factors have been pre-computed and stored. From the table, it is clear that the total flops counts for the PSTD-CPML method are reduced from 49 to 34 compared with that of the PSTD-PML method. This corresponds to an efficiency gain of 1.44 in flops count reduction for the PSTD-CPML method.

Table I: Flops count for PSTD-CPML and PSTD-PML algorithms.

	A/S	M/D	FT	exponentiation
PSTD-CPML	12	18	4	0
PSTD-PML	9	28	4	8

IV. NUMERICAL RESULTS

To illustrate the CPML termination of the PSTD lattice, a simulation of a small current source radiating in free space is studied. A uniform mesh with cell spacing $\Delta x = \Delta y = 0.01$ *m* and lattice dimension of 200×200 is considered. The reflection error due to the CPML is studied by exciting a small current source at the center of the grid. The time dependence of the source is,

$$g(t) = \exp[\frac{-4\pi(t-t_0)^2}{t_1^2}] \tag{15}$$

where t_0 and t_1 are constants, and both equal to 1×10^{-9}. The highest frequency of the Gauss source is determined by the value $2/t_1$ = 2 GHz, thus the minimum wavelength of the source is about 0.15 *m*. The spatial discretization Δx is equal to 1/15 of the minimum wavelength. The reflection error is computed at the source point. A reference solution based on an extended lattice is computed in order to isolate the error due to the CPML from grid dispersion error. The relative error is computed as,

$$err(\text{dB}) = 20\log_{10}\frac{\left|E(t)-E^{std}(t)\right|}{\left|E^{std}(t)\right|} \tag{16}$$

where $E^{std}(t)$ is the value of the electric field at that point computed by the extended lattice PSTD. $E(t)$ is the electric field calculated by the PSTD truncated by the CPML.

CPML layers that are twenty cells thick terminate all four sides of the lattice. Within the CPML, the conductivity is selected as,

$$\sigma_s(s) = \frac{\sigma_{s\max}\left|s-s_0\right|^r}{d^r}\ . \tag{17}$$

A choice for $\sigma_{s\max}$ that will minimize the reflection is expressed as,

$$\sigma_{s\max} = \frac{(r+1)}{150\pi\Delta s} \tag{18}$$

where Δs is the grid spacing along the normal axis. The time step is selected as $\Delta t = 2\Big/\pi c\sqrt{(1/\Delta x)^2+(1/\Delta y)^2}$ = 15 ps, which is the maximum time step to satisfy time stability condition in the PSTD method, where c is the speed of light within the host medium. The reflection error with respect to time step is showed in Fig. 1. For the sake of comparison, the reflection error of the PSTD-PML method is also plotted in this figure. As can be seen from this figure, both the reflection relative error of CPML and PML are less than -70 dB. It means that the CPML has almost the same absorbing performance as the PML method.

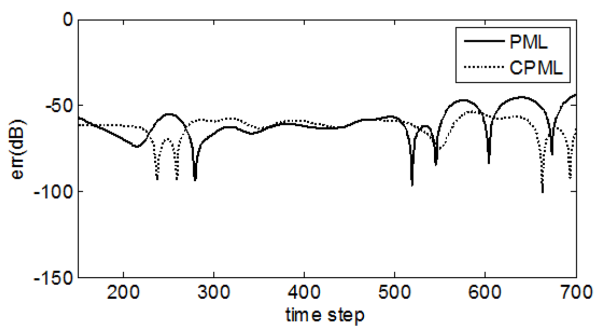

Fig. 1. The reflection relative error of CPML and PML with Δt = 15 ps.

The significant feature of the PSTD method is its spatial discretization, which only needs two cells per wavelength. So, we can increase the spatial increments of the PSTD method to $\Delta x = \Delta y = 0.075\ m$, corresponding to 1/2 of the wavelength. The reflection error with this spatial increment is plotted in Fig. 2. The time step size is selected as the maximum to satisfy the limitation of the stable condition in the PSTD method. It is $\Delta t = 2\big/\pi c\sqrt{\left(1/\Delta x\right)^2 + \left(1/\Delta y\right)^2}$ = 112.5 ps, which is seven times as that of the conventional FDTD method. It can be seen from Fig. 2 that the reflection relative error of the CPML method is also the same as that of the PML method, but due to very large time step size and spatial discretization used, both the reflection relative error of the CPML and PML become a little larger than the results in Fig. 1, especially in the late response. The reflection relative error reach to -50 dB after 400 time steps. However, it does not affect the application of the CPML method in the situation not with very stringent absorbing performance requirements.

It should be noted that when spatial increments of the PSTD method increase to 1/2 wavelength, some ripples appears in the reflection relative error of the CPML method, as shown in Fig. 2. This is duo to the wraparound effect of the PSTD method, which can be eliminated by using PML cells at the outer boundary.

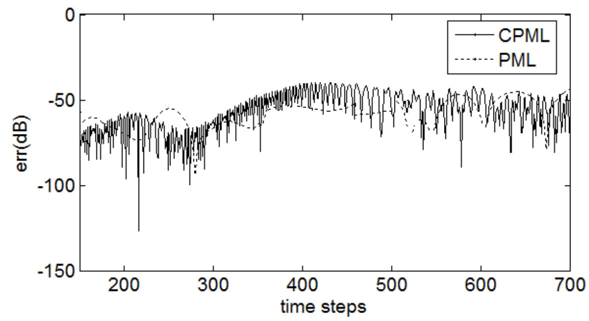

Fig. 2. The reflection relative error of the CPML with Δt = 112.5 ps.

One advantages of the CPML lies in its capability of dealing with the low frequency evanescent waves. Therefore, it is necessary to show the reflection relative error in the simulated frequency domain. The variation of the reflection relative error of the PSTD-CPML method with respect to frequency is plotted in Fig. 3. It can be seen from this figure that in the entire frequency range (including the low frequency band) the reflection relative error of CPML is less than -50 dB and it is highly effective at absorbing low-frequency evanescent waves. The CPML parameters r and $k_{\max}$ are selected by using the method in references [10] and [11].

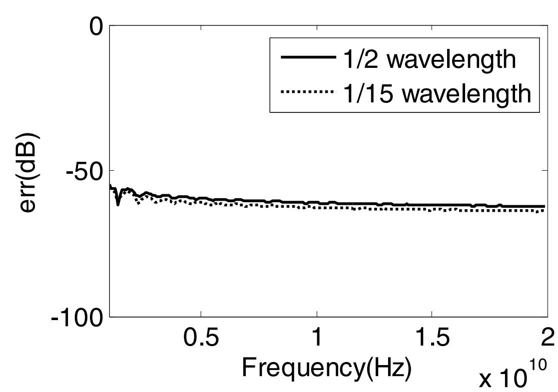

Fig. 3. Variation of the reflection relative error of the PSTD-CPML method with respect to frequency.

V. CONCLUSION

A pseudospectral time-domain method employing the CPML equations is presented. It is not needed to split the field components. Numerical example demonstrates that the reflection relative error of CPML is less than -70 dB and shows good absorbing performance of the convolutional perfectly matched layer.

ACKNOWLEDGMENT

This work was supported by the National Natural Science Foundations of China (No. 61001039 and 61231003), and also supported by the Fundamental Research Funds for the Central Universities.

REFERENCES

[1] Q. H. Liu, "The PSTD algorithm: A time-domain method requiring only two cells per wavelength," *Microwave Opt. Technol. Lett.*, vol. 15, pp. 158-165, 1997.

[2] Q. Li and Y. Chen, "Application of the PSTD for scattering analysis," *IEEE Trans. Antennas Propagat.*, vol. 50, pp. 1317-1319, 2002.

[3] Q. H. Liu and G. Fan, "A frequency-dependent PSTD algorithm for general dispersive media," *IEEE Microwave Guided Wave Lett.*, vol. 9, pp. 51-53, 1999.

[4] Z. Lin, Y. Jia, P. Ou, and C. Zhang, "A Full-spectrum numerical-dispersion compensation Technique for the Pseudospectral time-domain method," *IEEE Antennas and Wireless Propagation Lett.*, vol. 11, pp. 212-215, 2012.

[5] J. P. Berenger, "A perfectly matched layer for the absorption of electromagnetic waves," *J. Comput. Phys.*, vol. 114, pp. 185-200, 1994.

[6] J. P. Berenger, "Improved PML for the FDTD solution of wave-structure interaction problems," *IEEE Trans. Antennas Propagat.*, vol. 45, pp. 466-473, 1997.

[7] J. P. Berenger, "An effective PML for the absorption of evanescent waves in waveguides," *IEEE Microwave Guided Wave Lett.*, vol. 8, pp. 188-190, 1998.

[8] J. A. Roden and S. D. Gedney, "Convolutional PML (CPML): An efficient FDTD implementation of the CFS-PML for arbitrary media," *Microwave Opt. Technol. Lett.*, vol. 27, pp. 334-339, 2000.

[9] M. Kuzuoglu and R. Mittra, "Frequency dependence of the constitutive parameters of causal perfectly matched anisotropic absorbers," *IEEE Microwave Guided Wave Lett.*, vol. 6, pp. 447-449, 1996.

[10] J. P. Bérenger, "Application of the CFS PML to the absorption of evanescent waves in waveguides," *IEEE Microwave and Wireless Components Lett.*, vol. 12, pp. 218-220, 2002.

[11] M. F. Hadi, "Near-field PML optimization for low and high order FDTD algorithms using closed-form predictive equations," *IEEE Trans. Antennas Propagat.*, vol. 59, pp. 2933-2941, 2011.

Design and Improvement of Compact Half-Wavelength Band Pass Filter Employing Overlapped Slotted Ground Structure (SGS) and Multilayer Technique

A. Boutejdar [1], A. Darwish [2], and A. Omar [1]

[1]Institute for Signal Processing and Communications (IESK) University of Magdeburg, 39106, Magdeburg, Germany
ahmed.boutejdar@ovgu.de

[2] Faculty of Information Engineering and Technology, German University in Cairo, Cairo 11835, Egypt
abdulrahman.moustafa@gmail.com

Abstract **─** This paper deals with a compact Chebyschev 3rd hairpin band pass filter design, using the Richards-Kuroda transformation method. Afterwards, a combination of slotted ground structure (SGS) and multilayer technique is applied. Filters using quarter-wavelength stepped-impedance resonator without and with SGS technique are investigated. Finally, two band pass filters are designed, simulated, and partially measured. A compact SGS band pass filter operated at 4.35 GHz is demonstrated. The proposed band pass filter has low insertion loss, high rejection in both the stop bands and a compact size of (20 × 23) mm^2 (0.075 λg × 0.058 λg) with a guide wavelength λg = 0.359 m. Additionally, the structure has generated two transmission zeros on both sides of the pass band at 3.1 GHz and 4.9 GHz. The simulated results as well as the experimental results are satisfactory with the filter requirements. The introduced structure can be a good alternative to a conventional parallel-coupled half wavelength, as well as quarter-wavelength stepped-impedance resonator band pass filter.

Index Terms **─** Band pass filter, compactness, multilayer, and slotted ground structure.

I. INTRODUCTION

Modern personal communication systems require miniaturized high performance band pass filters having high selectivity in the pass band and low insertion loss in the stop band. This type of filter design is of key importance for the radio frequency engineer, since they are currently used in communication applications to reject spurious signal, and to separate different channels in multichannel communication systems. Microstrip line band pass filters with these characteristics should be designed with direct coupling in order to minimize the dispersion and radiation losses [1-5]. Other filters with λ/2 resonators may be used to realize the selectivity, but the disadvantage is that they are long and therefore cannot be used in all applications [6-9]. To eliminate this disadvantage and thus to manufacture a band pass filter, which is compact and useful in personal communication systems, we suggest a class of band pass filters, which consist of four coupled microstrip lines. Two are connected to a shorted ground inductive microstrip line. The two remaining ones are coupled together by means of a J-immitance inverter (see Fig. 1). This structure is improved and simplified through transformation of the short-circuit to the equivalent open end microstrip line, therefore, short-circuits are avoided. The proposed band pass filter employing Richards-Kuroda transformation method and short-open-circuit geometric trick is simulated, optimized, and finally fabricated. In order to improve the compactness of the structure, other ideas have been used so-called SGS and overlapped techniques. Good performance, low cost, and compact size are usually demanded in modern microwave communication systems. In order to alleviate these

Submitted On: Nov. 30, 2012
Accepted On: May 31, 2013

problems Karshenas et al. [10], Boutejdar et al. [11-13] proposed DGS or SGS, which is designed by connecting the middle thin channel slot with two identical defected areas. SGS bases on new ground plane hole (GPH) technique. GPH focuses not only on its application but also on its own proprieties. SGS can be designated as an etched periodic or non-periodic cascaded configuration holes in metallic ground plane of a microstrip structure, which causes a disturbed current distribution in the ground plane. This disturbance leads to an increase in the effective capacitance and inductance, thus unwanted second harmonic and circuit size reduction could be obtained [14-17]. SGS adds an extra degree of freedom in high frequency circuit design and opens a wide door to the RF, microwave, and millimeter-wave applications.

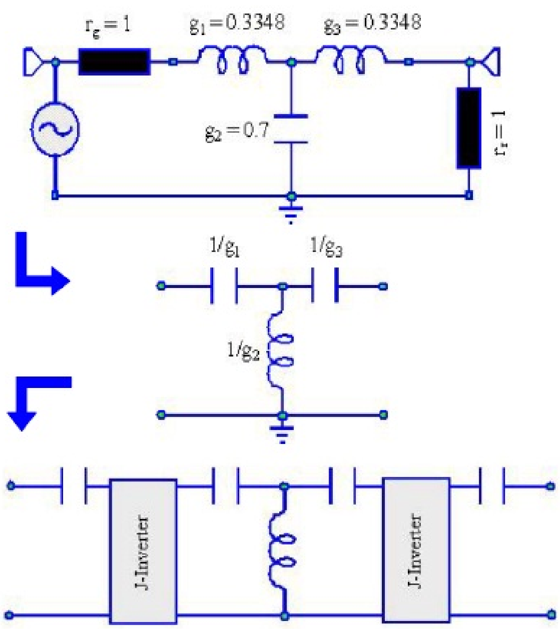

Fig. 1. LPF-HPF-BPF- transformation (first step, second step, and third step).

II. THE TRANSFORMATION FROM LPF TO BPF

In order to design a band pass filter cascaded coupled resonators, through inverters, have been used. An optimization process of filter dimensions will be carried out to get the desired filter parameters. In order to minimize the time outlay and to design a filter systematically, another method so-called LPF-HPF-BPF has been used in this work, where the low pass filter with known parameters has been first transformed to high pass filter. Moreover, the unit elements (inverter) and Kuroda transformation lead to realization of a band pass filter with desired properties [18].

In order to design a band pass filter with desired characteristics (f_c) using systematic and accurate process analysis, the cutoff frequency of a low pass filter must be nearly around $f_c/2$. Based on this idea a proposed low pass filter is a Chebyschev filter of 3rd order, with a cutoff frequency ($f_c/2$) of 2.1 GHz. The normalized element values for this low pass structure are $g_2 = 0.712$ and $g_1 = g_3 = 3.345$. In order to realize this LPF-BPF transformation (see Fig. 1), the lumped elements of the 3rd circuit have been calculated using normalized element values of lumped elements and characteristic impedance Z_0 [18, 19]. Using low-high pass transformation, Kuroda-identity and method of coupled line procedures (see Fig. 2), a required band pass circuit has been realized. Finally, the circuit is supplemented mutually with a unit-element (J-inverter), which represents the gap between the quarter length resonators (see Fig. 1).

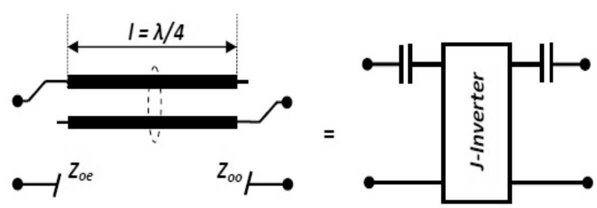

Fig. 2. Equivalent circuit to microstrip coupled lines transformation.

III. DESIGN OF THE COUPLED-LINE BANDPASS FILTER

The first proposed band pass filter (structure 1) is composed of two microstrip half-wavelength resonators and a shorted stub with metallic ground as shown in Fig. 3. All dimensions are shown in Table I, while the filter characteristics are shown in Table II. The response of the first structure is shown in Fig. 4. The second structure is proposed to avoid via holes short-circuits as shown in Fig. 5, this was done by extending the microstrip line by λ/2. The new length is then extended by means of the following length correction [2],

$$\Delta l = \frac{\xi_1 \cdot \xi_2 \cdot \xi_5}{\xi_4} h \tag{1}$$

$$\xi_1 \approx 0.44 \frac{\varepsilon_{r_{eff}}^{0.81} + 0.26 \cdot \eta^{0.85} + 0.24}{\varepsilon_{r_{eff}}^{0.81} - 0.19\eta^{0.85} + 0.87}, \quad (2)$$

$$\xi_2 \approx 1 + \frac{\eta^{0.37}}{2.35 \cdot \varepsilon_r + 1}, \quad (3)$$

$$\xi_3 \approx 1 + \frac{0.53 \tan^{-1}[0.1\eta^{\frac{1.94}{\xi_2}}]}{\varepsilon_{r_{eff}}^{0.924}}, \quad (4)$$

$$\xi_4 \approx 1 + 0.04 \tan^{-1}[0.07\eta^{1.46}] \times [6 - 5\exp[0.04(1-\varepsilon_r)]], \quad (5)$$

$$\xi_5 \approx 1 - 0.22\exp[-7.50\eta] \quad \text{with } \eta = \frac{W}{h}, \quad (6)$$

where h and W are the substrate thickness and microstrip width, successively.

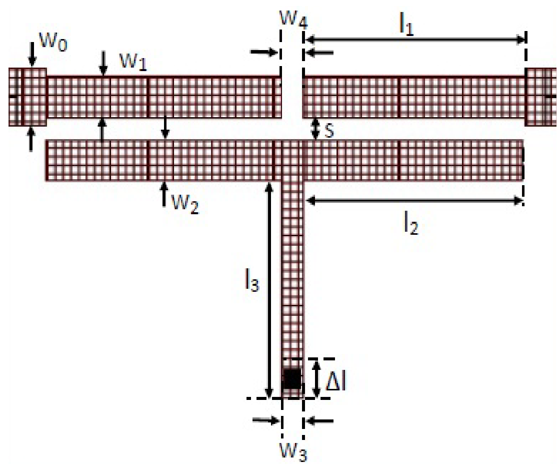

Fig. 3. Layout of the transformed band pass filter (structure 1).

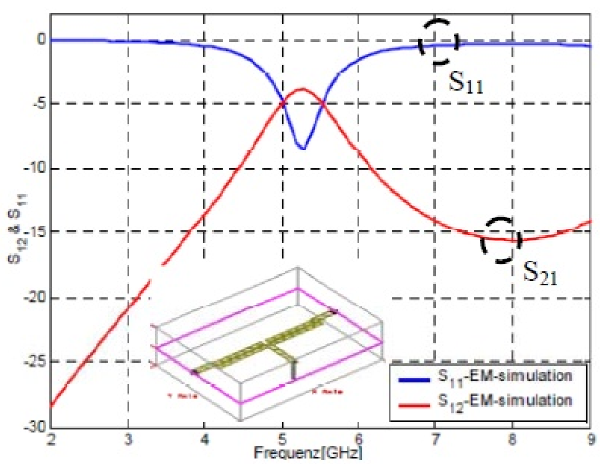

Fig. 4. Simulation results of the first proposed band pass filter (structure 1).

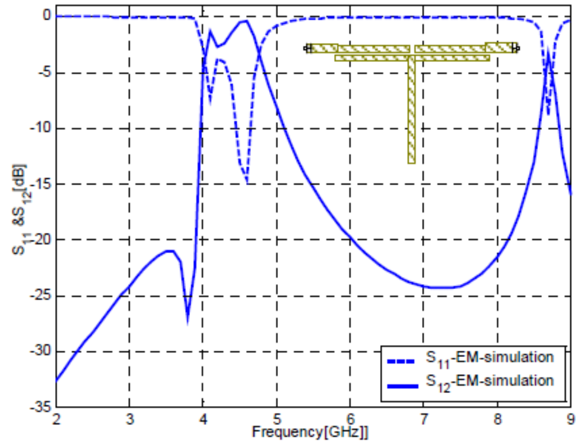

Fig. 5. Simulation results of the second proposed band pass filter (structure 2).

These corrections are applied simultaneously to the three microstrip lines l_1, l_2, and l_3. In structure 2, the open stub has several important characteristics. By changing the length of the open stub, the center frequency in the pass band can be controlled. In order to prove the validity of the proposed structure, the equivalent circuit network is provided as shown in Fig. 6. This network is valid for structures 2 and 3 (structure 3 is proposed in the next section) regardless the gap between the upper two microstrip lines. Comparison between the EM simulation and the circuit simulation is shown in the next section. In order to improve the filter characteristics, several structures have been designed and developed. The passage from structure 1 to structure 2 was carried out with the goal to avoid the shorting problem. Due to the loss in the pass band was non negligible, the coupling (gab = inverter) between the resonators has been changed to enhance the electrical coupling, and thus to minimize the losses in the pass band. For this purpose, structure 3 has been designed, simulated, and manufactured as shown in Fig. 7. The comparison between the simulation and measurement results are presented in Fig. 8. Structures 2 and 3 are similar to each other but with different coupling distances, which is determined using empirical method. The values of coupling distances (s) in structure 2 and 3 are 0.3 mm and 0.2 mm, respectively. In order to improve the filter characteristics a removing of the short circuit (via) (structure 3) and a minimizing of the filter structure, using the overlapping idea (structure 4) are used.

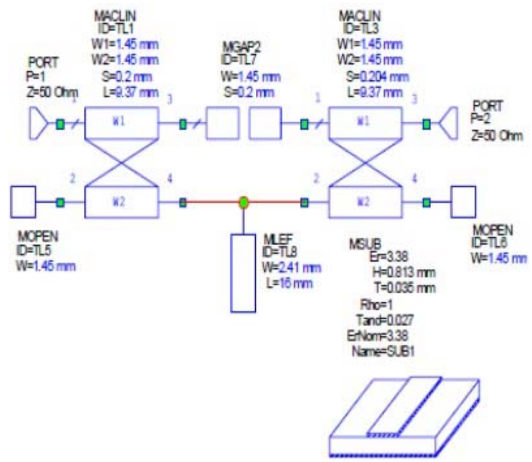

Fig. 6. Equivalent circuit model of the proposed band pass filter (structures 2 and 3).

IV. FABRICATION AND MEASUREMENT RESULTS

As shown in Fig. 7, the band pass filter (structure 3) has been designed, optimized, fabricated, and tested on a (20 × 23 mm^2) RO4003 microwave substrate with a relative dielectric constant ε_r of 3.38, a loss tangent tgδ of 0.0027, and a thickness h of 0.813 mm. The characteristic impedance of the microstrip lines used as resonators is Zoe = 74 Ω, Zoo = 70 Ω and that of the open stub is 64 Ω. The band pass filter was designed to have a center frequency of 4.5 GHz and a fractional bandwidth of 22.2 %. The detailed dimensions are shown in Table I. The EM and circuit simulations are carried out using the commercial microwave office software AWR. As Fig. 8 depicts, both simulation and experimental results show good agreement.

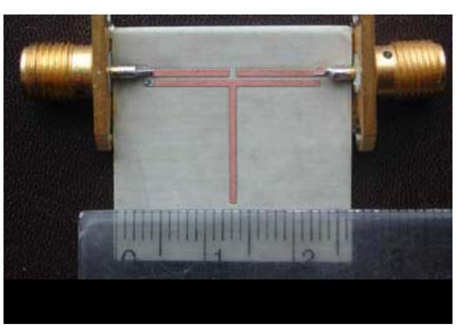

Fig. 7. Photograph of the fabricated optimized band pass filter.

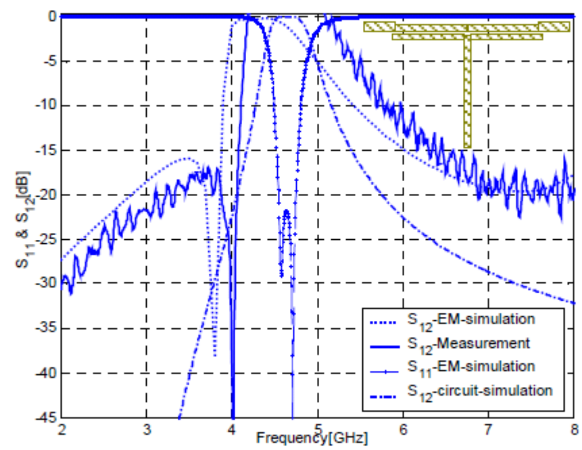

Fig. 8. The comparison of S-parameters of EM-, circuit simulations and measurement results of BPF (structure 3).

The observed deviation between both results is due to the mismatches and fabrication errors. Turning the filter arms around λ/2 reduces the dimension of the filter by approximately 49 %, which introduces the fifth structure. Moreover, the space of coupling becomes smaller, which causes good results and high compactness. In order to obtain the optimal coupling distance between the filter arms and thus to control the results in pass band, an empirical method [16, 18] is used instead of the procedures based on the coupling coefficient and the external quality factor [11, 20]. In our case, the insertion losses in the pass band reaches 1.2 dB resulted by an optimal gap width of 0.5 mm as shown in Fig. 9 for structure 4.

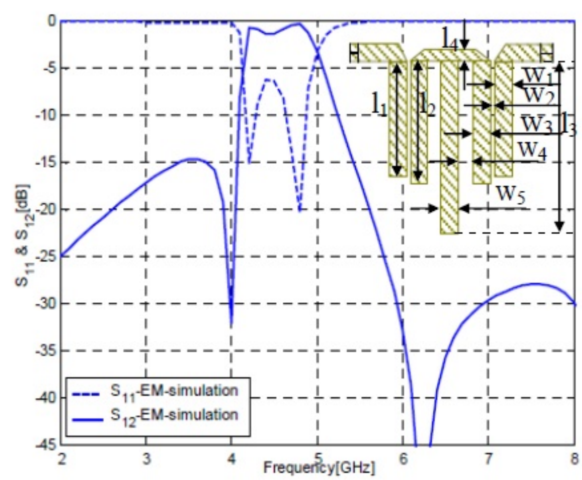

Fig. 9. S-parameters of the compact overlapped BPF (structure 4).

V. DESIGN AND IMPROVEMENT OF NEW OVERLAPPED SGS-BAND PASS FILTER

As the compactness of devices is an important characteristic, which is frequently considered in various technologies and particularly in wireless communication and microwave applications, a new structure topology has been designed and optimized employing defected slotted ground (SGS) and multilayer techniques (structure 5). The simulation results have been carried out using microwave studio^{TM} software under the same conditions as before. The filter structure of the proposed compact SGS band pass filter is shown in Figs. 10 and 11. It consists of two compensated coupled microstrip capacitors on the top layer, while three overlapped slot cannels presents a SGS resonator in the metallic ground plane. Through the substrate, the SGS is electromagnetic coupled with the top compensated capacitors. The gap between the microstrip capacitors corresponds to J-inverter and controls the inter-stage (w_2) coupling, which also determines the filter bandwidth.

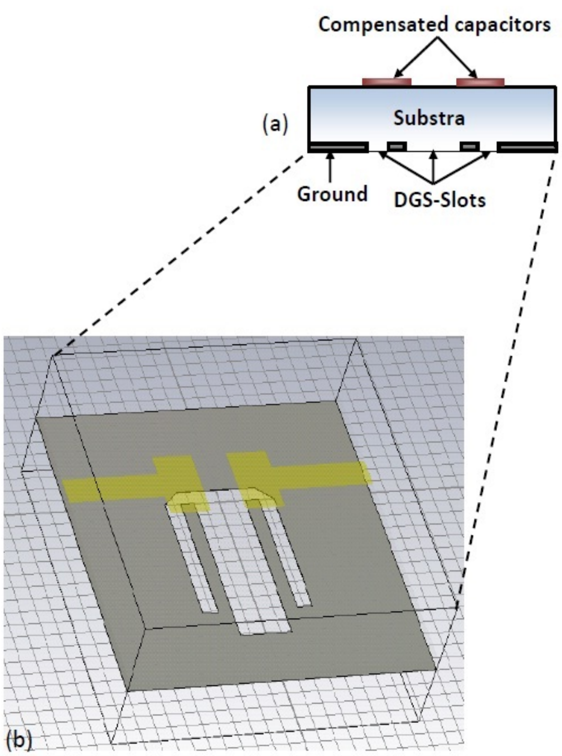

Fig. 10. 3D view of the new proposed SGS band pass filter (structure 5).

All dimensions of the new structure are depicted in Table I. In order to guarantee the matching between the ports (SMA) and the structure, the width of the feed lines (w_0 = 1.88 mm) has been computed using a microstrip line calculator [21]. This filter exhibits two transmission zeros at 3.1 GHz and 4.9 GHz, thus a relative response symmetric is achieved. From the simulated results shown in Fig. 12, it can be seen that the simulated overlapped structure has a pass band center frequency at 4.35 GHz as required. The insertion loss is as low as 0.24 dB in the pass band of the BPF, the upper stop band is using SGS and slow wave effect suppressed below 20 dB from 4.7 GHz to 8 GHz. Using overlapping and SGS techniques, the size of the new SGS BPF is 49 % less than conventional BPF (structure 3).

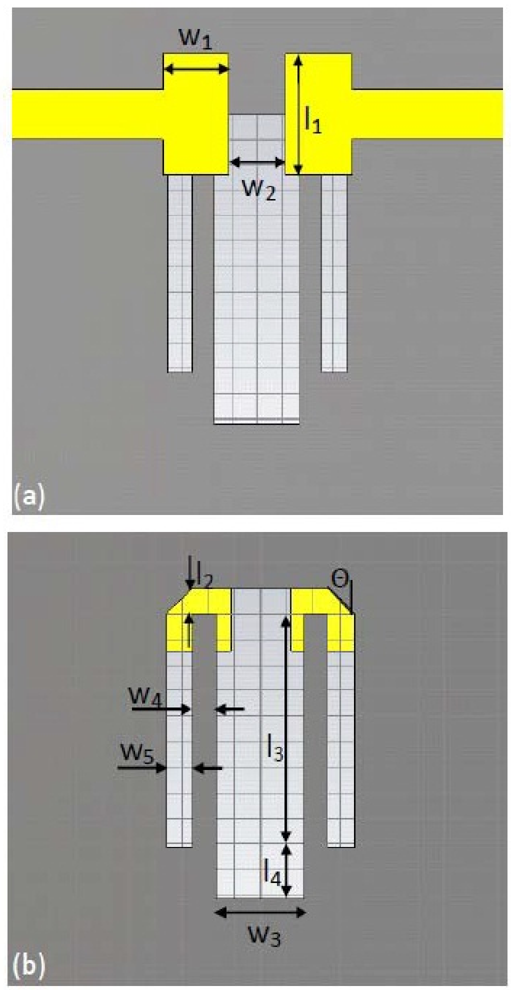

Fig. 11. 2D view of the new SGS BPF; (a) top and (b) bottom layers.

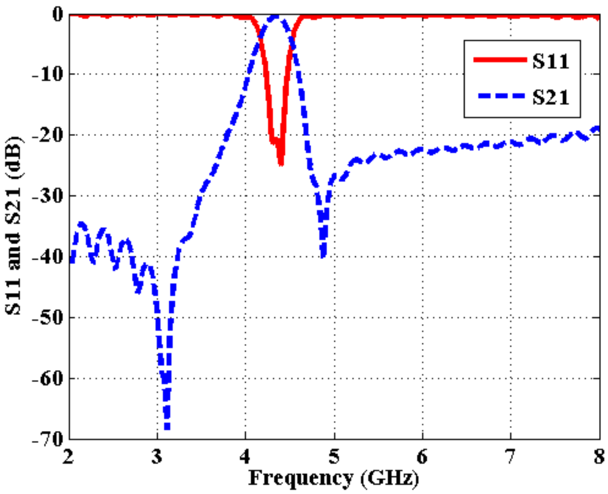

Fig. 12. Simulation results of the compact SGS BPF (Structure 5).

Table I: The dimensions (in mm) of the different proposed structures' topologies.

Structure 1	Structure 2	Structure 3	Structure 4	Structure 5
l_1= 9.37	l_1= 9.00	l_1= 9.00	l_1= 11.75	l_1= 4.75
l_2= 9.37	l_2= 9.00	l_2= 9.00	l_2= 12.66	l_2= 1.00
l_3= 5.37	l_3= 13.5	l_3= 13.5	l_3= 17.73	l_3= 9.15
w_1= 1.45	w_1= 0.80	w_1= 0.80	l_4= 1.250	l_4= 2.00
w_2= 1.25	w_2= 0.80	w_2= 0.80	w_1= 2.400	w_1= 2.60
w_3= 1.85	w_3= 0.80	w_3= 0.80	w_2= 0.500	w_2= 2.30
w_4= 0.8	w_4= 0.50	w_4= 0.50	w_3= 2.150	w_3= 3.35
			w_4= 1.650	w_4= 0.90
			w_5= 2.4	w_5= 1.00
				Θ= 45°

VI. CONCLUSION

In this work, the required λ/2–microstrip BPF and its equivalent circuit have been realized starting from a known low pass filter and using kurodas' and Richards' transformations. In order to show the validity of the proposed BPF and the derived equivalent circuit, the BPF have been designed, fabricated, and measured. Numerical simulations using microwave office AWR show a satisfactory agreement between simulated and measured responses. In order to minimize the size of the structure and to improve the filter responses, SGS and multilayer technique are used. The simulation results of the proposed compact SGS-overlapped BPF have demonstrated the optimum performances in pass band and stop band. This additional electric coupling between the compensated microstrip capacitors allows the generation of 2 finite transmission zeros instead of one near the pass band. Comparison between the proposed BPF and the enhanced filter show a significant size reduction up 49 %. Simulation results of the proposed compact structure show that the SGS and overlapping ideas work very well. It is expected that this proposed method and this filter topology can be applied to improve the compactness and stop band performances of other microwave filters, and thus could be used in mobile communication systems and RF/microwave applications.

Table II: The characteristics of the different investigated structures.

Structure	1	2	3	4	5
Characteristics					
fc_1, fc_2 (GHz)		4.05, 4.70	4.20, 4.95	4.10, 4.95	4.15, 4.50
f_0 (GHz)	5.20	4.60	4.50	4.52	4.35
S_{21},max.(dB)	15.5	24.0	35.0	50.0	41.5
S_{21},max.,losses(dB)	4.20	2.30	0.30	1.20	0.24
BW (GHz)		0.75	0.75	0.85	0.35
FBW (%)		16.0	16.6	18.8	8.00
SF_1, SF_2		0.88, 1.02	0.93, 1.10	0.90, 1.09	0.95, 1.03

ACKNOWLEDGMENT

The authors would like to thank the German Research Foundation (DFG) for financial support of this project. The authors are grateful to Mr.

Harald Dempewolf and Mr. Dennis Winkler for their supports and assistances for their cooperation in laboratory.

REFERENCES

[1] G. L. Matthaei, L. Young, and E. M. Jones, *Microwave Filters, Impedance-Matching Networks, and Coupling Structures*, Norwood, MA: Artech House, 1980.

[2] J.-S. Hong and M. J. Lancaster, *Microwave Filter for RF/Microwave Application*, New York: Wiley, 2001.

[3] W. Bächtold, *Mikrowellentechnik*, Vieweg Verlag, 1999.

[4] H. Yabuki, M. Sagawa, M. Matsuo, and M. Makimoto, “Stripline dual-mode ring resonators and their application to microwave devices,” *IEEE Trans. Microwave Theory Tech.*, vol. 44, pp. 723-728, May 1996.

[5] K. Wada, Y. Yamamoto, O. Hashimoto, and H. Harada, “A design method of a 2-pole tapped resonator BPF with multiple attenuation poles and its miniaturization,” *Proc. Asia-Pacific Microwave Conf.*, pp. 1111-1114, Nov. 2001.

[6] J. T. Kuo, S. P. Chen, and M. Jiang, “Parallel-coupled microstrip filters with over-coupled end stages for suppression of spurious responses,” *IEEE Microwave and Wirless Components Letters*, vol. 13, no. 10, Oct. 2003.

[7] B. Easter and K. A. Merza, “Parallel-coupled-line filters for inverted-microstrip and suspended-substrate MIC’s,” *11th Eur. Microwave Conf. Dig.*, pp. 164-167, 1981.

[8] A. Riddle, “High performance parallel coupled microstrip filters,” *IEEE MTT-S Symp. Dig.*, pp. 427-430, 1988.

[9] I. J. Bahl, “Capacitively compensated high performance parallel coupled microstrip filters,” *IEEE MTT-S Symp. Dig.*, pp. 679-682, 1989.

[10] F. Karshenas, A. R. Mallahzadeh, and J. R.-Mohassel, “Size reduction and harmonic suppression of parallel coupled-line bandpass filters using defected ground structure,” *Applied Computational Electromagnetics Society (ACES) Journal*, vol. 25, no. 2, pp. 149-155, Feb. 2010.

[11] A. Boutejdar, A. Batmanov, A. Elsherbini, A. Omar, and E. Burte, “A miniature 3.1 GHz microstrip bandpass filter with a suppression of spurious harmonic using multilayer-technique and defected ground structure open loop-ring (DGS),” *Proc. EUROEM European Electromagnetic 2008*, Lausanne, Switzerland, 21-25 July 2008.

[12] A. Boutejdar, A. Abdel-Rahman, A. Batmanov, et. al., “Miniaturized band stop filter based on multilayer-technique and new coupled octagonal defected ground structure with interdigital capacitor,” *Microwave and Optical Technology Letters*, vol. 52, no. 3, pp. 510-514, March 2010.

[13] A. Boutejdar, N. Mohamed, B. Edmund, O. Abbas, and S. Parui, “Design of novel 4-GHz bandpass filter using a combination of defected ground structure resonators and admittance J-inverter,” *Recent Patents on Electrical Engineering Journal, Bentham Science Publishers*, vol. 4, no. 1, pp. 42-49, Jan. 2011.

[14] G. Al-Omair, S. Mahmoud, and A. Al-Zayed, “Lowpass and bandpass filter designs based on DGS with complementary split ring resonators,” *Applied Computational Electromagnetics Society (ACES) Journal*, vol. 26, no. 11, pp. 907-914, Nov. 2011.

[15] S. Rehman, A. Sheta, and M. Alkanhal, “Compact bandpass filters with bandwidth control using defected ground structure (DGS),” *Applied Computational Electromagnetics Society (ACES) Journal*, vol. 26, no. 7, pp. 624-630, July 2011.

[16] M. Al Sharkawy, A. Boutejdar, F. Alhefnawi, and O. Luxor, “Improvement of compactness of lowpass / bandpass filter using a new electromagnetic coupled crescent defected ground structure resonators,” *Applied Computational Electromagnetics Society (ACES) Journal*, vol. 25, no. 7, pp. 570-577, July 2010.

[17] N. Garmjani and N. Komjani, “Improved microstrip folded tri-section stepped impedance resonator bandpass filter using defected ground structure,” *Applied Computational Electromagnetics Society (ACES) Journal*, vol. 25, no. 11, pp. 975-983, Nov. 2010.

[18] A. Boutejdar, “Design, development and optimization of compact microstrip RF filters using "Defected Ground Structure" (DGS) technology”, *PhD dissertation, University of Magdeburg, IESK, Magdeburg, Germany*.

[19] A. Boutejdar, A. Elsherbini, and A. Omar, “Design of a novel ultra-wide stop band low pass filter using H-defected ground structure,” *Microwave and Optical Technology Letters*, vol. 50, no. 3, pp. 771-775, March 2008.

[20] S. Amari, “Synthesis of cross-coupled resonator filters using an analytical gradient based optimization technique,” *IEEE Trans. Microwave Theory Tech.*, vol. 48, pp. 1559-1564, Sept. 2000.

[21] http://www.emtalk.com/

Ahmed Boutejdar was born in Souk El-Arbaa Gharb, Marocco. He received the Diplom (Licence) in Mathematics, Physics and Chemistry from Ibn Tofeil University, Kénitra, Morocco in 1994 and in Technische Hochschule Köthen in 1997. From 1995 to 1997 Preparatory Year of German language and Preparatory Year of Engineering high School in köthen, Germany. B.Sc. and Diplom-Eng degrees (Magna Cum Laude) in Electrical Engineering, Communication, and Microwave Engineering from Otto-von-Guericke University, Magdeburg, Germany in 2002 and 2004 respectively and he received his Ph.D. degree in 2009/2010 from the Department of Communication and High Frequency-Technique from the University of Magdeburg. He is currently working on a research project on "Entwurf, Optimierung, CMOS kompatible Herstellung und Charakterisierung von abstimmbaren planaren und koplanaren MEMS DGS-Filtern", which is one part of his Ph.D. thesis (Summa Cum Laude). His research interests include the design and analysis of microstrip filters, Defected Ground Structures devices, microstrip antennas, fractal DGS-filters, UWB-DGSfilters and tunable DGS-filters using MEMS-technology.

Dr. Boutejdar has authored over 125 papers in international journals and proceedings of international and national symposia and a book chapter in "Ultra-Wideband, Short Pulse Electromagnetics 9" Springer 2010", and these papers have been cited by other researchers more than 357 times (Scopus) and in three famous filter books: "Mirostrip and Printed Antennas: New Trends, Techniques and Applications (2011)" and "Microstrip Filters for RF/ Microwave Applications, 2nd Edition (2011)". Dr. Boutejdar is nominated for top 100 educators 2013, by International Biographical Center, Cambridge (IBC), England-Sep. 2013. He is reviewer of the IEE Microwave, Antennas & Propagation (IET). He is reviewer of the IEEE Microwave and Wireless Components Letters (MWCL). He is reviewer of the IEEE Electronics Letters. He is reviewer of the Hindawi Publishing Corporation/ International Journal of Microwave science and Technology (IJMST). He is reviewer of the Journal of Microwaves, Optoelectronics and Electromagnetic Applications (JMOe). He is reviewer of the Journal of Electromagnetic Analysis and Applications (JEMAA). He is reviewer of the Progress in Electromagnetics Research Symposium (PIERS). He is reviewer of the IEEE Transaction on Electromagnetic Compatibility (IEEE EMC). He is reviewer of International Journal of Circuit Theory and Applications and he is reviewer of the Recent Patents on Electrical Engineering-journal. He is reviewer of International Journal of Microwave and Optical Technology (IJMOT).

Abdulrahman Moustafa Darwish received his bachelor degree in communication and signal processing from the German University in Cairo (GUC), Egypt in 2011. He is currently a teaching and research assistant at the GUC, he is working towards his Master Degree in Microwave Engineering. Darwish previously carried his bachelor thesis at Ulm University, Germany and he is currently working on his master thesis at the University of Magdeburg, Germany (under the supervision of Assoc. Prof. Dr. A. Boutejdar). His main interests are microwave technology and signal processing.

A. Omar received the B.Sc. and M.Sc. degrees from Ain Shams University, Cairo, Egypt, in 1978 and 1982, respectively, and the Doktor-Ing. degree in Electrical Engineering from the Technical University of Hamburg, Hamburg–Harburg, Germany, in 1986. Since 1990, he has been a Professor of Electrical Engineering and Head of Chair at the University of Magdeburg, Magdeburg, Germany. He is an Editorial Board member of the Proceedings of the Institution of Electrical Engineers, Electronics Letters, and the Journal of Electromagnetics.

Dr. Omar is a member of the technical program committee of the IEEE Microwave Theory and Techniques Society (MTT-S) Symposium. He is an Editorial Board member of the IEEE Transactions on Microwave Theory and Techniques, the IEEE Transactions on Antennas and Propagation, and the IEEE Microwave and Wireless Letters. He is also the IEEE MTT-S financial coordinator for Region 8.

A Pattern Reconfigurable Antenna Based on TM_{10} and TM_{02} Modes of Rectangular Patch

Hai-Yan Huang, Bing-Zhong Wang, Xiao Ding, and Wei Shao

The Institute of Applied Physics
University of Electronic Science and Technology of China, Chengdu, 610054, China
haiyanhuang123@yahoo.com, bzwang@uestc.edu.cn, dx_000217@yahoo.com.cn, and weishao@uestc.edu.cn

Abstract ─ A pattern reconfigurable rectangular microstrip antenna is reported in this paper. A broadside radiation pattern and a conical pattern are obtained when it alternatively operates in the TM_{10} mode and TM_{02} mode of the rectangular patch. Suitable patch size parameters and feeding positions are selected so that these two modes share the same operating frequency. Two PIN diodes are employed to switch the operating modes. The configuration of the antenna is simple, which consists of a rectangular patch and a reconfigurable feeding network to excite expected mode. The feature of the proposed antenna is that the design method is explicit, based on different resonant modes with different radiation characteristics, and can be used to design other types of reconfigurable antennas.

Index Terms ─ Microstrip patch, modes characteristics, and reconfigurable antenna.

I. INTRODUCTION

Reconfigurability of an antenna refers to the capacity to adjust a radiator's characteristics in terms of resonant frequency, radiation pattern, or polarization. The dynamic tuning is achieved by manipulating a certain switching mechanism through controlling electronic, mechanical, or optical switches. Among them electronic switches are the most popular in constituting reconfigurable antennas due to their efficiency, reliability, and ease of integrating with microwave circuitry. The typical electronic switches are PIN diodes, FET transistors, and RF MEMS switches. Compared to RF MEMS switches and FET transistor, PIN diodes have acceptable performance and low price.

Pattern reconfigurable antennas are attractive in applications of surveillance and tracking, because they produce more than one radiation pattern with different directivity at the same operating frequency. In addition, manipulation of patterns is useful in avoiding noise source, mitigating electronic jamming, improving security, and increasing energy efficiency. For their attractive features, pattern reconfigurable antennas have received considerable attentions and a number of works have been demonstrated in the past years [1-3]. A typical example for pattern reconfigurable microstrip antennas is given in [4], where a Yagi–Uda antenna is selected to constitute a pattern reconfigurable antenna. By adjusting the lengths of two parasitic elements acting as the director and reflector, three reconfigurable patterns are achieved. The antenna in [5] can be regarded as a combination of a monopole and two Vivaldi slots, providing a broadside pattern and two opposite endfire patterns with a broad impedance bandwidth. The main methods to obtain a pattern reconfigurable antenna, to the authors' knowledge, are finding structures with the potential to produce pattern diversity, or reconfiguring the feeding configurations, which can be interpreted by the array theory [6].

In this paper, a new design method is presented to design reconfigurable antennas. The mode characteristics of rectangular microstrip patch are studied and applied to the pattern reconfigurable antenna design. First, the theoretical mode characteristics are analyzed. Then, a feeding network is designed according to

Submitted On: Dec. 25, 2012
Accepted On: Aug. 10, 2013

the mode characteristics. Last, a prototype antenna is fabricated and measured to verify the design concept.

II. ANTENNA DESIGN

A microstrip antenna can be regarded as a dielectric-loaded cavity with two perfect electric conducting surfaces (top and bottom) and four perfect magnetic conducting sidewalls along its perimeter. The radiation mainly takes place at the four sidewalls of the cavity, and can be calculated by using the aperture radiating theory through introducing equivalent currents [7]. Notice that different resonant modes within the cavity have different electric field distributions at the sidewalls of the cavity, which leads to different equivalent magnetic current distributions and finally results in different radiation patterns.

Here, the TM_{10} and TM_{02} modes are selected to design a pattern reconfigurable antenna. Figure 1 depicts the electric field distributions and the equivalent magnetic currents of these two modes within the cavity. As shown in Fig. 1 (a) the electric field distribution of the TM_{10} mode undergoes a phase reversal along the *x*-direction but is uniform along the *y*-direction. The equivalent magnetic currents along those two slots of length L and height H are of the same magnitude and the same phase. The far-zone electric fields radiated by each slot will add in phase and form a broadside pattern in the *y*-*z* plane. The same analysis procedure can be performed on the other two slots of width W and height H. Their far-zone electric fields are cancelled in the *y*-*z* plane and *x*-*z* plane. Therefore, for TM_{10} mode, it possesses a broadside pattern as shown in Fig. 1 (c). The same analysis process can also be carried out for the TM_{02} mode. The two slots of length L and height H are non-radiating slots. The radiating slots are those of width W and height H. Because their equivalent magnetic currents are of the same magnitude but 180° out of phase, the radiation pattern of TM_{02} mode is a conical pattern in the *y*-*z* plane. Figure 1 (d) shows the pattern of TM_{02} mode in the *y*-*z* plane.

Here, the TM_{10} and TM_{02} modes are chosen for developing a pattern reconfigurable antenna due to their attractive broadside and conical patterns. In fact, other higher modes of the rectangular patch also have similar patterns. For example, TM_{n0} and TM_{0n} modes, where n is an odd number, produce maximum radiations at broadside; on the other hand, TM_{0m} and TM_{m0} modes, where m is an even number, form nulls in the broadside direction. Theoretically, they can be used to design a pattern reconfigurable antenna. But the higher the mode, the larger the patch size will be, which goes against the antenna compactness. Except the modes mentioned above, there are other modes like TM_{11} mode, which possesses a conical pattern. But if those kinds of modes are picked, it is difficult to make the two different modes resonate at the same frequency. Therefore, the operating modes used in this paper are the TM_{10} and TM_{02} modes.

In order to excite the desired modes, not only the operating frequency should be set close to the resonant frequency of the modes, but also the feeding positions should be properly picked. The general principle is that: first, figure out the field distributions of the modes beneath the patch; next, find those positions where the magnitudes of fields are maximum of one mode and minimum of another mode; and then place the feed lines at positions with maximum field magnitude of the desired mode and with minimum filed magnitude of the undesired mode. Through these steps the corresponding mode is efficiently and exclusively excited.

According to the electrical field distributions shown in Fig. 1 (a) and (b), when the TM_{10} mode is desired, the microstrip feed lines should be placed at points B and C where the electric fields of TM_{10} mode are maximum while that of TM_{02} mode are minimum; when the operating mode is TM_{02}, the antenna is fed at point A where the electric fields of TM_{02} mode are maximum while that of TM_{10} mode are minimum. Figure 2 shows the simulated electric field amplitude distributions of TM_{10} and TM_{02} modes. It is apparent from Fig. 2 (a) that the TM_{10} mode is effectively excited when the patch is fed at points B and C. Figure 2 (b) shows that the TM_{02} mode is effectively excited when the patch is fed at point A.

The resonant frequency is easy to obtain by using the cavity model. The resonant frequencies of the TM_{nm} modes are given by

$$f_{TM_{nm}} = \frac{1}{2\pi\sqrt{\varepsilon\mu}}\sqrt{\left(\frac{n\pi}{W}\right)^2 + \left(\frac{m\pi}{L}\right)^2}\ , \tag{1}$$

where n and m are the order of modes, and W and

L are the width and the length of the rectangular patch. It is obvious that the resonant frequency is determined by the size of the patch and the order of the modes.

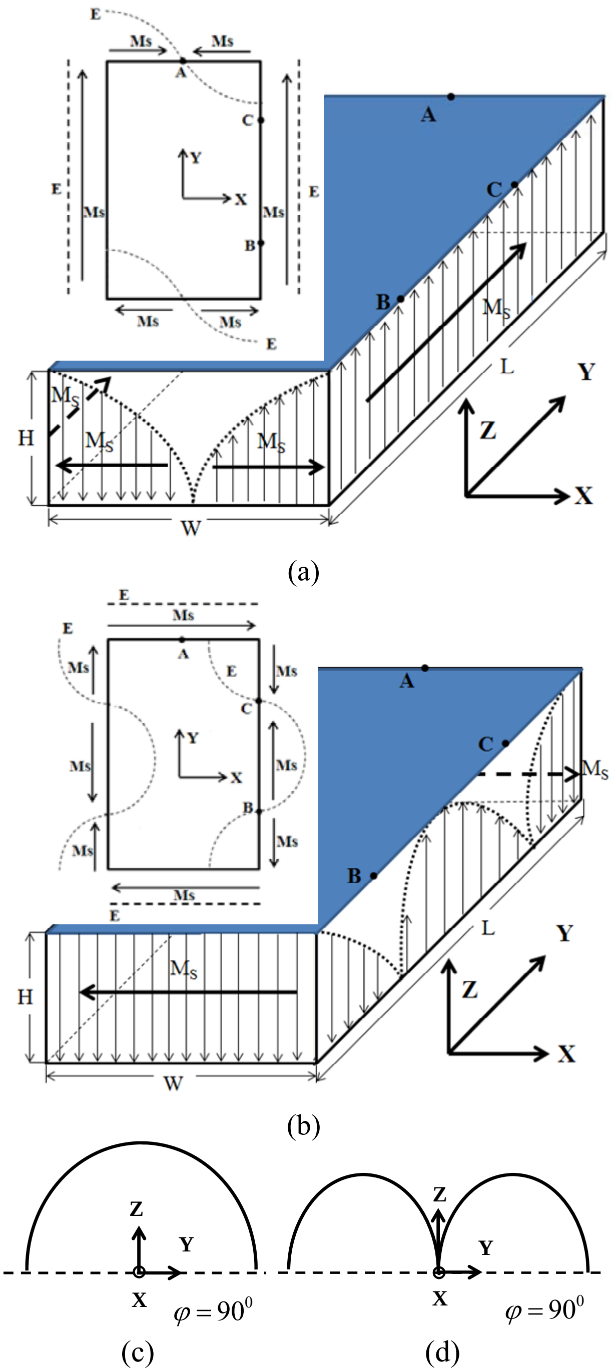

Fig. 1. Electrical field distributions: (a) TM_{10} mode and (b) TM_{02} mode. Radiation patterns in the *y*-*z* plane: (c) TM_{10} mode and (d) TM_{02} mode.

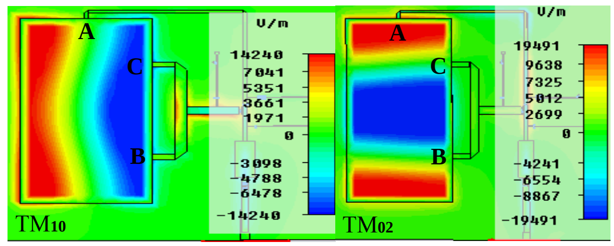

(a) (b)

Fig. 2. Simulated electrical field amplitude distributions: (a) TM_{10} mode and (b) TM_{02} mode.

By carefully choosing the ratio of the length to the width, two different modes with the same resonant frequency can be obtained. In this design the ratio is chosen to be 2, so that the TM_{10} and TM_{02} modes share the same resonant frequency. Thus, as long as the two modes are excited alternatively, the antenna gets the capacity to provide two different radiation patterns at the same frequency.

III. SIMULATED AND MEASURED RESULTS

To verify the reconfigurable ability of the proposed antenna, a prototype was simulated, fabricated, and measured. The antenna is printed on a substrate with a relative permittivity of 3 and a height of 1 mm. The structure of the proposed antenna is shown in Fig. 3 (a). It consists of a rectangular patch, a reconfigurable feeding network, two PIN diodes acting as switches and a simple bias network providing DC bias to the PIN diodes. There are two gaps of width 0.5 mm in the feeding network, across which the PIN diodes are mounted using electrically conductive silver epoxy. In this paper, the implemented diodes are beam lead PIN diodes (MA4AGBL912). According to the PIN diode datasheet [8], the diode has a forward resistance of typical value 4 Ω for the ON state while a parallel circuit with a capacitance of 0.025 pF and a resistance about 4 K Ω for the OFF state. The circuit schematic of the bias network for the antenna is shown in Fig. 3 (b), where capacitor C1 is the DC blocking capacitor, inductor L2 is the RF chock inductor, and capacitor C2 is the filter capacitor, which forms a low-pass filter with the inductor L1 for a better isolation from the RF signals.

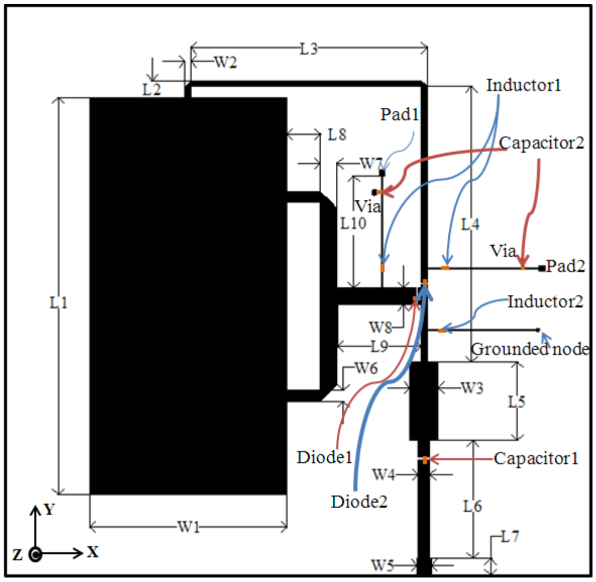

(a)

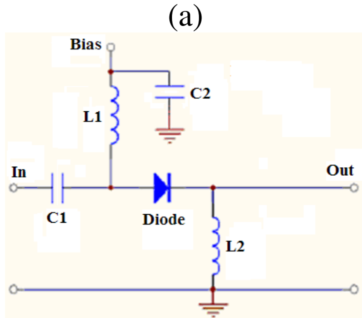

(b)

Fig. 3. (a) Structure of the reconfigurable rectangular patch and (b) circuit schematic of the DC bias network.

In the practical design, two chip capacitors of capacitance 20 pF labeled as Capacitor 2 in Fig. 3 (a) and two chip inductors of inductance 100 nH labeled as Inductor 1 in Fig. 3 (a) are employed to build the low-pass filters with a rejection band starting from 0.5 GHz, which is much lower than the operating frequency 2.45 GHz, to ensure the isolation from the RF signals. A chip inductor of inductance 100 nH, labeled as Inductor 2 in Fig. 3 (a), is mounted on the grounded high impedance line. A chip capacitor with capacitance 10 pF, labeled as Capacitor 1 in Fig. 3 (a), is employed to prevent the DC bias voltage flowing into RF source at the antenna terminal. Because the applied diodes (MA4AGBL912) can also work in the OFF state when the bias is 0 V according to its datasheet [8], there is only one grounded line required. When positive bias voltage is provided for Diode 1 and no bias voltage for Diode 2, Diode 1 is in the ON state and Diode 2 is in the OFF state, and vice versa. When Diode 1 is ON and Diode 2 is OFF, the patch is fed at points B and C as shown in Fig. 2 (a). The TM_{10} mode is excited and the antenna radiates a broadside pattern. On the contrary, when Diode 1 is OFF and Diode 2 is ON, the patch is fed at the point A and the TM_{02} mode is excited as shown in Fig. 2 (b). In this case the radiation pattern is conical.

The parameters of the antenna are provided in Table I. Since microstrip antennas are resonant antennas, the length and width of the patch are important design parameters, which greatly affect resonant frequency and input impedance. In this paper, the proposed antenna operates at 2.45 GHz. In order to make the two modes work at the same frequency, the length and the width of the patch are chosen to be 70.7 mm and 35.2 mm, respectively. The ratio of the length to the width is not exactly equal to 2. The slight deviation is due to the small adjustment of length for achieving a better impedance match.

Table I: Dimensions of the proposed antenna (in unit of millimeter).

W1	35.2	W2	1	W3	5
W4	2	W5	2.5	W6	2
W7	3	W8	3	L1	70.7
L2	3	L3	42.1	L4	49
L5	14	L6	21	L7	3
L8	6	L9	15	L10	20

The antenna is analyzed by the time domain solver of CST Microwave Studio. Figure 4 gives the simulated surface electric current distributions. As depicted in Fig. 4 (a), for the TM_{10} mode, the surface current vectors are in the *x*-direction and the maximum takes place along the *y*-direction center line of the patch. For the TM_{02} mode, as demonstrated in Fig. 4 (b), the surface current vectors are in the *y*-direction, and the two parts of the surface current distribution are 180° out of phase, which accounts for a radiation pattern with a null at broadside. Figure 5 exhibits the simulated 3-D radiation patterns of the proposed antenna. As shown in Fig. 5 (a), the pattern of mode TM_{10} is a typical broadside pattern in the *y*-*z* plane. It is obvious that the pattern of TM_{02} mode is a conical pattern with a null at broadside in the *y*-*z* plane.

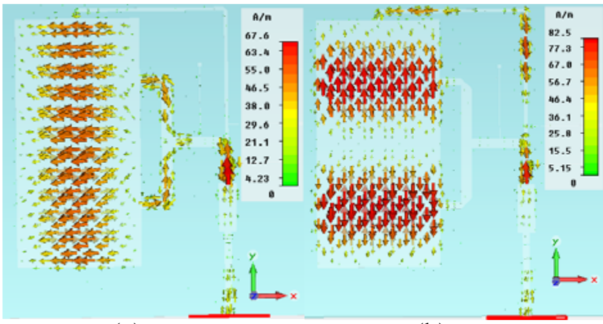

(a) (b)

Fig. 4. Surface current distributions of the proposed antenna: (a) TM_{10} mode when diode 1 is ON and diode 2 is OFF and (b) TM_{02} mode when diode 1 is OFF and diode 2 is ON.

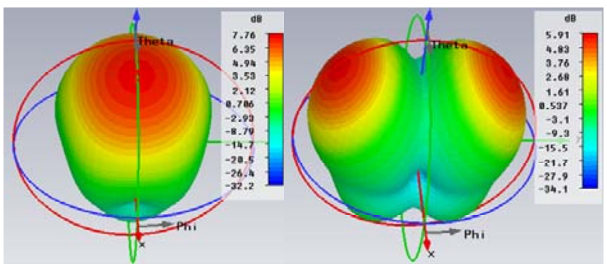

(a) (b)

Fig. 5. 3-D radiation patterns of the proposed antenna: (a) TM_{10} mode and (b) TM_{02} mode.

The input reflection coefficient measurements are done by using an Agilent's E8361A network analyzer. The simulated and measured reflection coefficients of the TM_{10} and TM_{02} modes are given in Fig. 6. The impedance bandwidths of the TM_{10} mode and the TM_{02} mode are relatively narrow compared to commonly used antennas. One reason is that the impedance bandwidth of a microstrip antenna is inherently narrow. This is due to the fact that microstrip antennas are resonant antennas. The input impedance of a microstrip antenna is found to vary fast with frequency, and this feature limits the frequency range over which it can be matched to its feed line. Although some bandwidth expanding techniques are widely used to enlarge its impedance bandwidth, such as cutting slots on the patch and using proximity coupling or aperture coupling, those bandwidth expanding methods can not be utilized here, because those approaches usually use more than one mode of the patch, which may cause distortion in the radiation pattern. Figure 6 (a) shows that the measured and simulated return losses are in an acceptable agreement, and the resonant frequencies are exactly at the designed 2.45 GHz. Figure 6 (b) shows that, for the TM_{02} mode, the measured resonant frequency shifts slightly to the higher frequency. This discrepancy between the measured and simulated results can be attributed to the inaccuracies in the fabrication process, the variation in discrete component parameters from values given in manufacturer's data sheet, and diode parasitic parameters, which are not considered in simulation procedure. The shift, since it is very small, does not considerably affect the performance of the antenna.

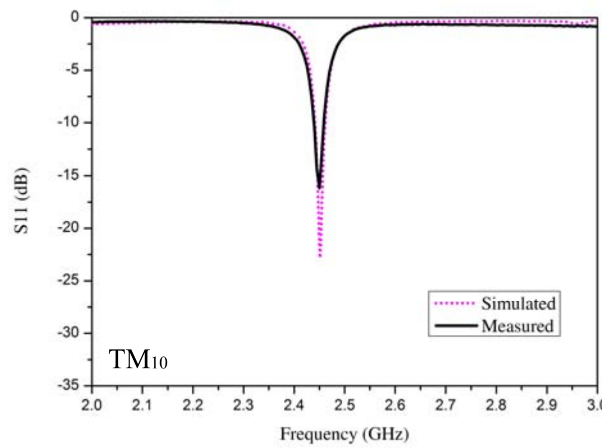

(a)

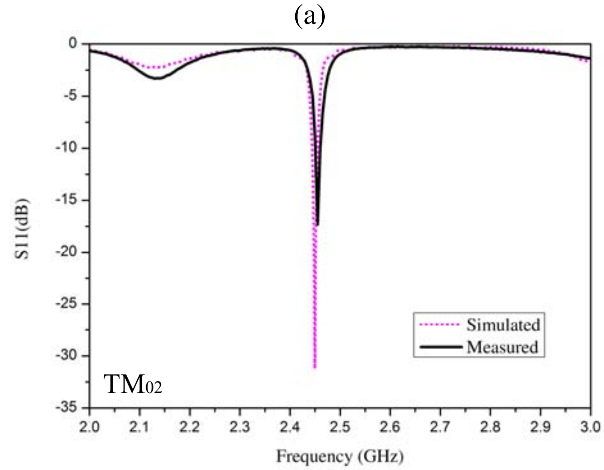

(b)

Fig. 6. Simulated and measured input reflection coefficients: (a) TM_{10} mode and (b) TM_{02} mode.

Figure 7 (a) is the photograph of the fabricated antenna with the mounted lump elements. Radiation patterns are measured for the TM_{10} and TM_{02} modes using a spherical near-field measurement system as shown in Fig. 7 (b). The orientations of the coordinate system used in all radiation pattern figures are the same as the one shown in Fig. 3 (a). Simulated and measured radiation patterns of the two modes are compared in the *y*-*z* and the *x*-*z* planes, and the *y*-*z* plane is the principle plane where pattern diversity takes place.

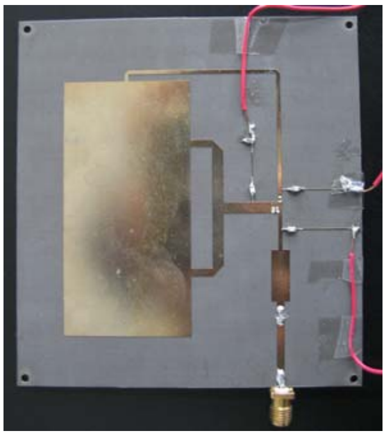

(a)

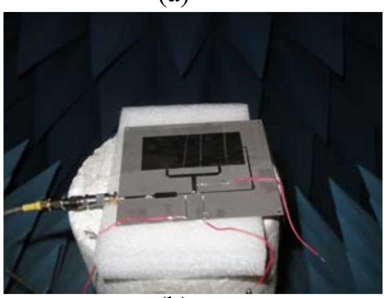

(b)

Fig. 7. (a) Photograph of the fabricated antenna and (b) photograph of the proposed antenna in a spherical near-field measurement system.

As shown in Fig. 8 (a), well-defined broad radiation pattern can be observed in the *y*-*z* plane for the TM_{10} mode. The simulated and measured maximum radiation gains are 6.6 dBi and 5.7 dBi, respectively. Both simulated and measured half-power beamwidths are 64^0. The cross polarization, which mainly comes from the TM_{02} mode, is lower than -12 dBi for the measured result.

Figure 8 (b) shows that it is a conical radiation pattern for the TM_{02} mode in the *y*-*z* plane. The beam peaks of the measured conical pattern point at $\pm 40^0$. The measured half-power beamwidth is 53^0. The maximum radiation gains are 5.7 dBi and 3.8 dBi for simulation and measurement, respectively. The measured maximum gain is 1.9 dBi smaller than the simulated result. One reason for this phenomenon is that the resonant frequency of the TM_{02} mode shifts a little bit from the designed 2.45 GHz to the higher frequency, which makes the reflection coefficient larger than -10 dB at the operating frequency and results in the degradation of the gain. The cross polarization, which mainly comes from the TM_{10}, is lower than -11 dBi for the measured result. By comparing Fig. 8 (a) with Fig. 8 (b), it can be found that the gain of the TM_{10} mode is higher than that of the TM_{02} mode. This is due to the fact that conical radiation pattern disperses radiation energy. It also can be found that the cross polarization of the TM_{02} mode is higher than that of the TM_{10} mode, which reveals that even though the designed resonant frequencies are the same, the TM_{10} mode is stronger than the TM_{02} mode and is harder to be suppressed.

Figure 8 (c) shows the radiation patterns of the TM_{10} mode in the *x*-*z* plane. From Fig. 8 (c) it can be seen that there is a tilt of the maximum radiation, which pushes the maximum radiation to the +*x*-direction. The main factor which accounts for this phenomenon is the spurious radiation of the feed lines. The 3-D radiation pattern in Fig. 5 (a) gives a more intuitive view. The feeding network placed beside the patch plays a role as a director, which drags the radiation pattern from the broadside to the +*x*-direction in the *x*-*z* plane. The distortion of the radiation pattern can be alleviated considerably by using other feeding techniques such as probe feeding and aperture coupling. However, those techniques are not used here, because for the probe feeding it is not convenient to integrate switches with the feeding networks; and for the aperture coupling, it usually excites multiple modes and it is hard to separate them. Furthermore, since the pattern reconfigurable ability is designed in the *y*-*z* plane, except for the maximum gain undergoing a 1.1 dBi decrease, the tilt of pattern in the *x*-*z* plane does not significantly influence the performance of the antenna.

Figure 8 (d) shows the radiation patterns of the TM_{02} mode in the *x*-*z* plane, which indicates that the radiation of TM_{02} mode in the *x*-*z* plane is small. This is due to the fact that the pattern of TM_{02} mode possesses a theoretical null in the broadside direction. It can be found clearly in the simulated 3-D pattern as shown in Fig. 5 (b). In general, the agreements between the simulated and the measured results are acceptable, and the performances of the proposed antenna confirm the feasibility of the design concept.

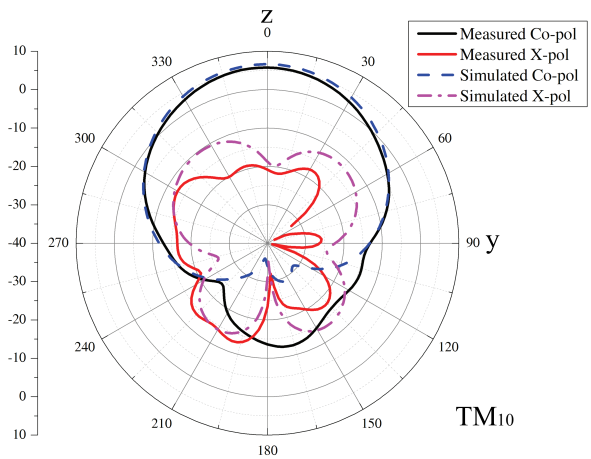

(a)

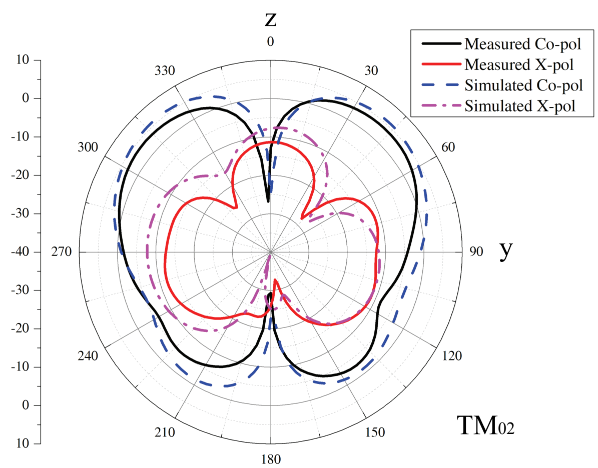

(b)

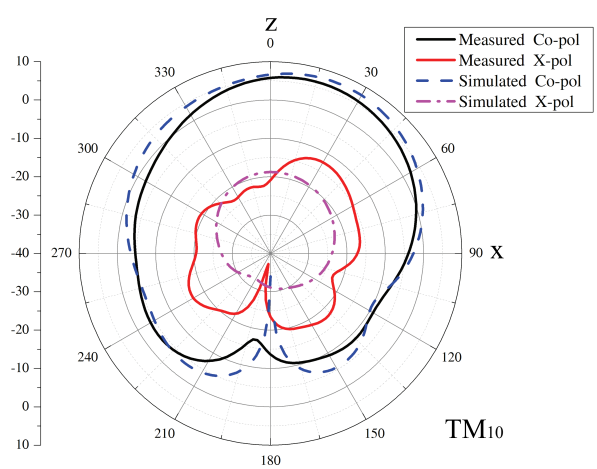

(c)

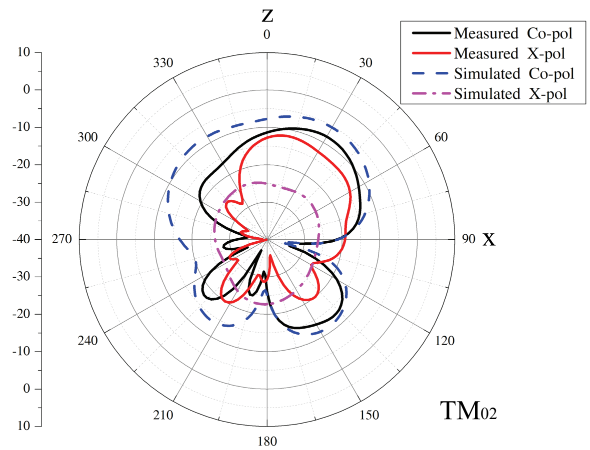

(d)

Fig. 8. Simulated and measured radiation patterns at 2.45 GHz: (a) TM_{10} mode in the *y-z* plane, (b) TM_{02} mode in the *y-z* plane, (c) TM_{10} mode in the *x-z* plane, and (d) TM_{02} mode in the *x-z* plane.

Figure 9 gives the simulated and measured gains of the proposed antenna versus frequency. The proposed antenna is a narrow-band antenna, which is due to the realization of operating in TM_{10} and TM_{02} modes at the same frequency. The frequency band for gain investigation is set from 2.43 GHz to 2.47 GHz. From Fig. 9, it can be seen that the measured gain varies from 4.9 dBi to 6.8 dBi for TM_{10} mode, while the simulated gain varies from 5.2 dBi to 7.6 dBi for TM_{10} mode; and that the measured gain varies from 0.3 dBi to 4.1 dBi for TM_{02} mode, while the simulated gain varies from 0.5 dBi to 5.7 dBi for TM_{02} mode. Owing to the narrow operating band, gain changes considerably with frequency especially for TM_{02} mode. The maximum measured gain of TM_{02} mode is at 2.46 GHz, just like the measured S_{11} of TM_{02} mode shifts slightly towards higher frequency as shown in Fig. 6 (b).

IV. CONCLUSION

A pattern reconfigurable rectangular patch antenna operating at the TM_{10} mode or the TM_{02} mode is presented in this paper. PIN diodes are used to alter the feeding positions, and to steer the operating modes. The theory and experiments presented in this work show that this simple rectangular patch antenna can provide a broadside pattern or a conical pattern at 2.45 GHz. The main limitation of this antenna is its narrow impedance bandwidth, which needs to be improved in the future. The design method can be used in other shapes of microstrip antennas for reconfigurable antenna designs. For example, circular patches and annular rings, the high order modes of which also possess conical patterns, can be used to design similar pattern reconfigurable antennas. This antenna can be used in wireless systems in which we are not much concerned about the polarization while the direction of arrival is a big concern.

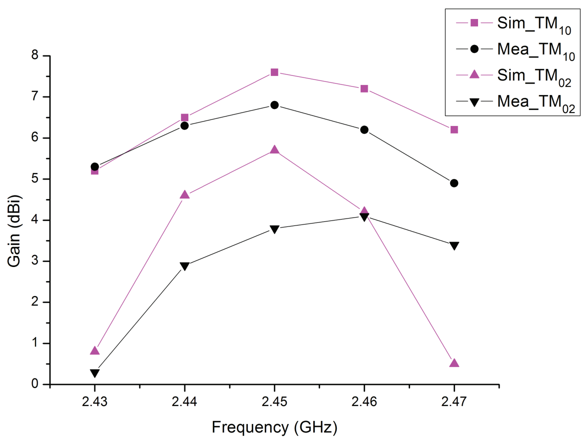

Fig. 9. Simulated and measured gains of the proposed antenna versus frequency.

REFERENCES

[1] X. -S. Yang, B. -Z. Wang, and W. Wu, "Yagi patch antenna with dual-band and pattern recofigurable characteristic," *IEEE Antennas Wireless Propagat. Lett.*, vol. 6, pp. 168-171, 2007.

[2] Y. -Y. Bai, S. Xiao, and B. -Z. Wang, "Two-dimensional pattern scanning by linear phased array with pattern reconfigurable elements," *Applied Computational Electromagnetics Society (ACES) Journal*, vol. 25, no. 2, pp. 144-148, Feb. 2010.

[3] S. Xiao, Y. -Y. Bai, and B. -Z. Wang, "Scan angle extension by array with pattern reconfigurable elements," *Applied Computational Electromagnetics Society (ACES) Journal*, vol. 24, no. 5, pp. 453-457, Oct. 2009.

[4] S. Zhang, G. H. Huff, J. Feng, and J. T. Bernhard, "A pattern reconfigurable microstrip parasitic array," *IEEE Trans. Antennas Propagat.*, vol. 52, pp. 2773-2776, 2004.

[5] G. M. Zhang, J. S. Hong, B. -Z. Wang, G. Song, and P. Li, "Design and time-domain analysis for a novel pattern reconfigurable antenna," *IEEE Antennas Wireless Propagat. Lett.*, vol. 10, pp. 365-368, 2011.

[6] W. Cao, B. Zhang, A. Liu, T. Yu, D. Guo, and K. Pan, "A reconfigurable microstrip antenna with radiation pattern selectivity and polarization diversity," *IEEE Antennas Wireless Propagat. Lett.*, vol. 11, pp. 453-456, 2012.

[7] C. A. Balanis, *Antenna Theory, Analysis and Design*, John Wiley and Sons, USA, 2005.

[8] MA4AGBLP912, M/A-COM Technology Solution Inc. www.macomtech.com

A Simple Design of UWB Small Microstrip Slot Antenna with Band-Notched Performance by using a T-Shaped Slit and a Pair of U-Shaped Conductor-Backed Plane

Mohammad Ojaroudi [1], Nasser Ojaroudi [2], and Noradin Ghadimi [1]

[1] Young Researchers Club
Ardabil Branch, Islamic Azad University, Ardabil, Iran
m.ojaroudi@iauardabil.ac.ir and noradin.ghadimi@gmail.com

[2] Department of Electrical Engineering,
Germi Branch, Islamic Azad University, Germi, Iran
n.ojaroudi@iaugermi.ac.ir

Abstract **─** In this paper, a simple and compact ultra wideband printed slot antenna with band-notch performance is designed and manufactured. In order to increase the impedance bandwidth of the square slot antenna, we use two U-shaped parasitic structures inside the rectangular slot on the ground plane that with this structure UWB frequency range can be achieved. Additionally, by using a T-shaped slit on the ground plane, a frequency notched band performance has been obtained. The designed antenna has a small size of 20×20 mm while showing the radiation performance in the frequency band of 3.05 GHz to over 12 GHz with a band rejection performance in the frequency band of 5.1 GHz to 6.05 GHz.

Index Terms **─** Square slot antenna, T-shaped slit, U-shaped parasitic structure, and ultra-wideband (UWB).

I. INTRODUCTION

In UWB communication systems, one of the key issues is the design of a compact antenna while providing wideband characteristic over the whole operating band. Consequently, a number of printed microstrip antennas with different geometries have been experimentally characterized [1, 2]. Moreover, other strategies to improve the impedance bandwidth have been investigated [3-5]. The Federal Communication Commission (FCC)'s allocation of the frequency range 3.1 GHz – 10.6 GHz for UWB systems and it will cause interference to the existing wireless communication systems, such as, the wireless local area network (WLAN) for operating in 5.15 GHz – 5.35 GHz and 5.725 GHz – 5.825 GHz bands), so the UWB antenna with a single band-stop performance is required [6, 7].

In this paper, we present a new design of compact wideband slot antenna with band rejection characteristics for UWB applications. In this antenna, two U-shaped parasitic structures inside the rectangular slot on the ground plane were used to enhance the bandwidth and a modified T-shaped slit in the square ground plane was applied to generate a band notch performance. In the slot antenna design, by reducing the antenna size, the impedance matching at lower frequencies becomes poor and the bandwidth is degraded [3, 4]. The distinctive point of the proposed antenna is that although it has small size respect to the antennas introduced in [2-5], (43 % smaller than the antenna in [1]), it has wider impedance bandwidth in the frequency band of 3.05 GHz to 12.06 GHz with a rejection bands around 5.1 GHz – 6.05 GHz, which has a frequency bandwidth increment of 13 % with respect to the previous similar antenna [7-9], and also, the impedance matching at lower frequencies is very well obtained. In [10], by using two parasitic structure in the ground plane and in [11], by using a V-shaped sleeve in the ground plane to achieve the

Submitted On: Oct. 1, 2012
Accepted On: June 9, 2013

band. Good return loss and radiation pattern characteristics are obtained in the frequency band of interest.

II. ANTENNA DESIGN

The proposed square slot antenna fed by a 50 Ω microstrip line is shown in Fig. 1, which is printed on an FR4 substrate of thickness 0.8 mm, and permittivity 4.4. In this proposed antenna, the U-shaped parasitic structures inside the rectangular slot on the ground plane are playing an important role in the broadband characteristics of this antenna. These parasitic structures improve the impedance bandwidth without any cost of size or expense [4]. In addition, using T-shaped slit with variable size generates the frequency band-notch function [3].

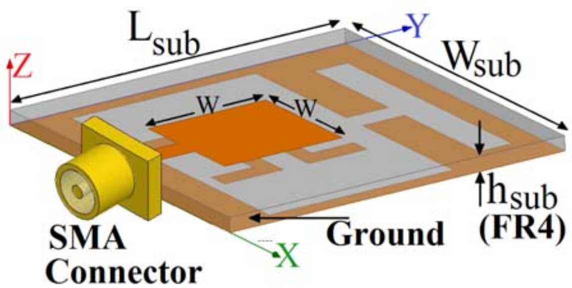

(a)

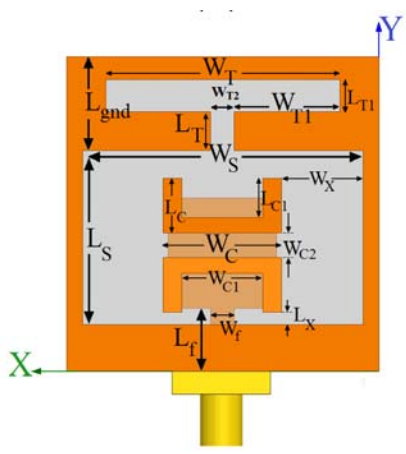

(b)

Fig. 1. Geometry of the proposed square slot antenna; (a) bottom view and (b) side view.

The final dimensions of the designed antenna are as follows: W_{sub} = 20 mm, L_{sub} = 20 mm, h_{sub} = 0.8 mm, W_f = 1.5 mm, L_f = 4 mm, W = 7 mm, W_s = 18 mm, L_s = 11 mm, W_c = 10 mm, L_c = 3 mm, W_{c1} = 8 mm, L_{c1} = 2 mm, W_{c2} = 1 mm, W_x = 4 mm, L_x = 1 mm, W_T = 18 mm, L_T = 1.5 mm, W_{T1} = 8.5 mm, L_{T1} = 2.5 mm, W_{T2} = 1 mm, and L_{gnd} = 6 mm.

III. RESULTS AND DISCUSSIONS

The proposed slot antenna with various design parameters were constructed, and the numerical and experimental results of the input impedance and radiation characteristics are presented and discussed. The Ansoft simulation software high-frequency structure simulator (HFSS) [12] is used to optimize the design.

The configuration of the presented slot antenna was shown in Fig. 1. Geometry for the ordinary square slot antenna (Fig. 2 (a)), with two U-shaped parasitic structures inside the rectangular slot on the ground plane (Fig. 2 (b)), and the proposed antenna (Fig. 2 (c)) structures are shown in Fig. 2. The return loss characteristics for the structures that are shown in Fig. 2 are compared in Fig. 3. As shown in Fig. 3, it is observed that the upper frequency bandwidth is affected by using the U-shaped parasitic structures inside the rectangular slot on the ground plane and the notch frequency bandwidth is sensitive to the T-shaped slit cut in the upper edge of the ground plane.

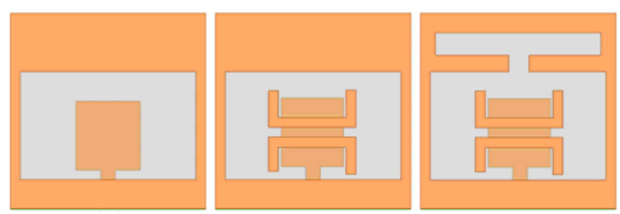

(a) (b) (c)

Fig. 2. (a) The ordinary square slot antenna, (b) antenna with a pair of U-shaped parasitic structures in the ground plane, and (c) the proposed square slot antenna.

Also the input impedance of the proposed slot antenna structure that was studied in Fig. 1, on a Smith chart is shown in Fig. 4. To understand the phenomenon behind this additional resonance performance, the simulated current distribution on the ground plane for the slot antenna with two U-shaped parasitic structures inside the rectangular slot on the ground plane at the new resonance frequency of 11.15 GHz is presented in Fig. 5 (a). It can be observed from Fig. 5 (a), that the current is concentrated on the edges of the interior and exterior of U-shaped parasitic structure inside the rectangular at 11.15 GHz. Therefore, the antenna impedance changes at this frequency due to the resonance properties of the proposed structure. Also, to understand the phenomenon behind this band-notch performance, the simulated current distribution on the ground plane for the proposed antenna at the notch frequency (5.5 GHz) is presented in Fig. 5 (b). It can be observed from Fig. 5 (b) that the current is concentrated on the edges of the interior and exterior of the T-shaped slit at 5.5 GHz. Therefore, the antenna impedance changes at this frequency due to the band-notch properties of the proposed structure.

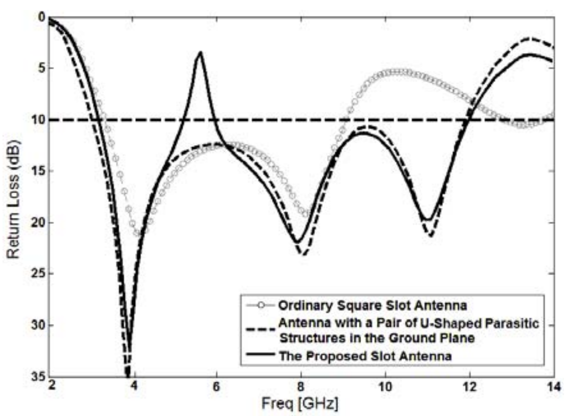

Fig. 3. Simulated VSWR characteristics for the various square slot antenna structures shown in Fig. 2.

The simulated VSWR curves with different values of W_{T2} are plotted in Fig. 6. As shown in Fig. 6, when the interior gap distance between the T-shaped slit edges increase from 0.25 mm to 4 mm, the center frequency of the notched band varies from 6.48 GHz to 4.85 GHz. From these results, we can conclude that the notch frequency is controllable by changing the gap distance between the T-shaped slit edges.

The proposed antenna with final design parameters, was built and tested. The measured and simulated VSWR characteristics of the proposed antenna is shown in Fig. 7. The fabricated antenna has the frequency band of 3.05 GHz to over 12 GHz with a rejection band around 5.1 GHz to 6.05 GHz. As shown in Fig. 7, there is a good agreement between the measured data and the simulated results. This discrepancy could be due to the effect of the SMA port, and also the accuracy of the simulation due to the wide range of simulation frequencies. To confirm the accurate VSWR characteristics for the designed antenna, it is recommended that the manufacturing and measurement process need to be performed carefully.

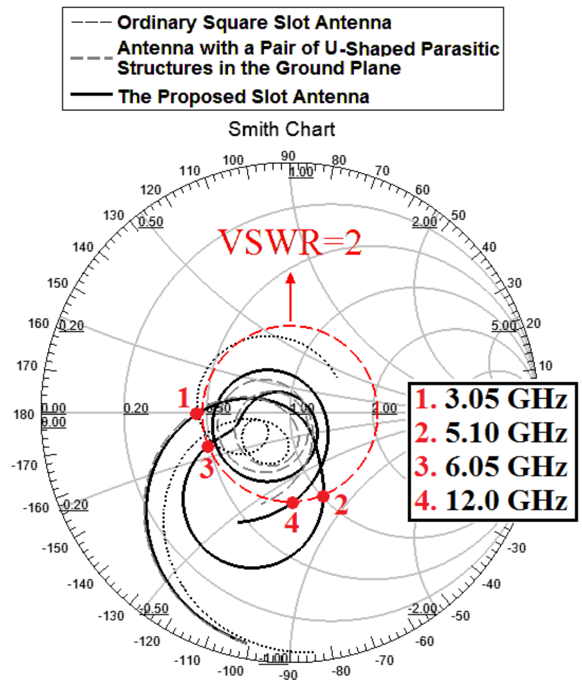

Fig. 4. The simulated input impedance on a Smith chart for the various slot antenna structures shown in Fig. 2.

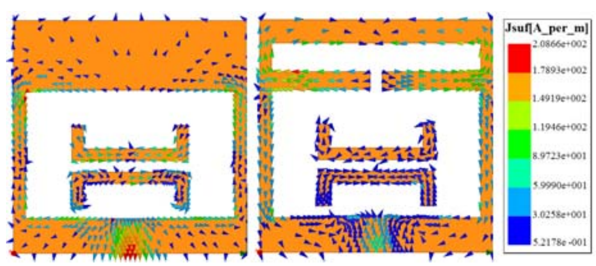

(a) (b)

Fig. 5. Simulated surface current distributions on the ground plane for (a) the square antenna with a pair of U-shaped parasitic structures in the ground plane at third resonance frequency (11.15 GHz) and (b) for the proposed antenna at the notch frequency (5.5 GHz).

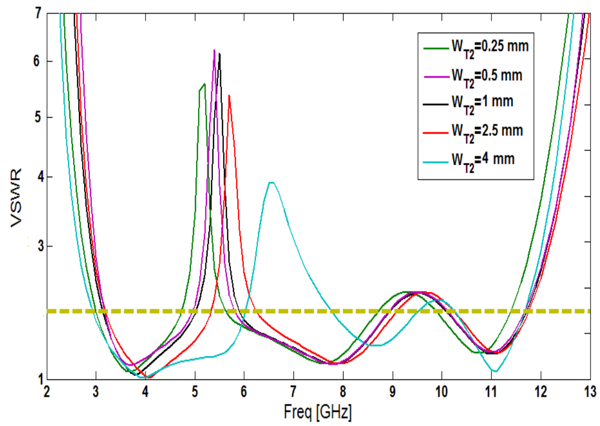

Fig. 6. Simulated VSWR characteristic for various values of W_{T2}.

Figure 8 shows the simulated and measured radiation patterns including the co-polarization and cross-polarization in the H-plane (x-z plane) and E-plane (y-z plane). The main purpose of the radiation patterns is to demonstrate that the antenna actually radiates over a wide frequency band. Reasonable agreement between simulations and measurements is demonstrated at 4 GHz, 7 GHz, and 10 GHz. It can be seen that the radiation patterns in x-z plane are nearly omni-directional for the 4 GHz and 7 GHz.

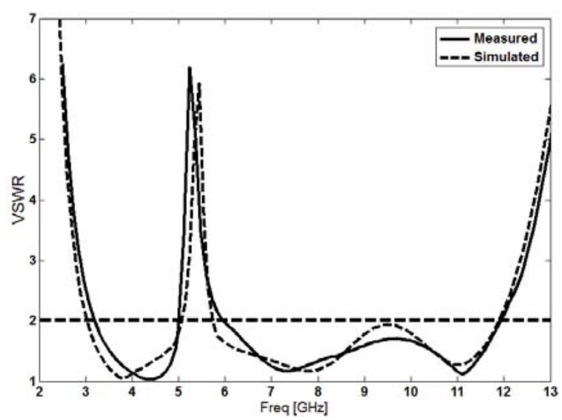

Fig. 7. Measured and simulated VSWR for the proposed antenna.

Figure 9 shows the effects of the T-shaped slit at the ground plane, on the maximum gain in comparison to the same antenna without it. As shown in Fig. 9, the basic structure (ordinary slot antenna) has a gain that is low at 2 GHz and increases with frequency [8]. It is found that the gain of the basic structure decreases with the use of the T-shaped slit in the ground plane. It can be observed in Fig. 9 that by using the T-shaped slit at the ground plane, a sharp decrease of maximum gain in the notched frequency band at 5.5 GHz is shown. For other frequencies outside the notched frequency band, the antenna gain with the filter is similar to those without it.

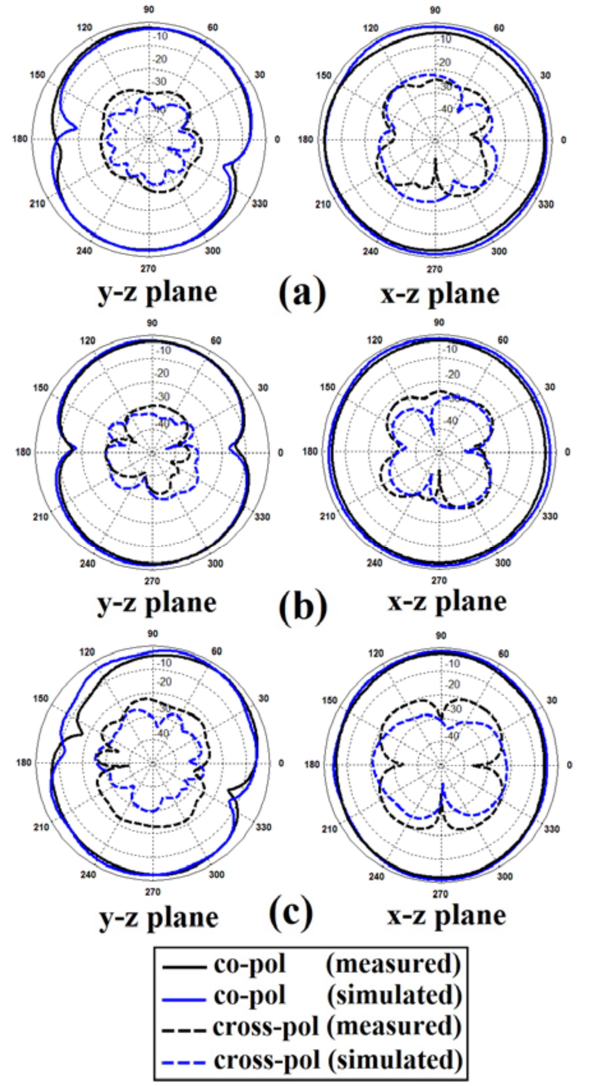

Fig. 8. Measured and simulated radiation patterns of the proposed antenna at (a) 4 GHz, (b) 7 GHz, and (c) 10 GHz.

IV. CONCLUSION

In this paper, a novel design of ultra wide band slot antenna with variable band notch function is proposed. The presented slot antenna can operate from 3.05 GHz to 12 GHz with VSWR < 2, and with a rejection band around 5.1

GHz to 6.05 GHz. By using two U-shaped parasitic structures inside the rectangular slot on the ground plane additional resonance at higher frequency range is excited and much wider impedance bandwidth can be produced. In order to generate a frequency band-stop performance we use a T-shaped slit in the ground plane. The designed antenna has a small size. The measured results show good agreement with the simulated and measured results.

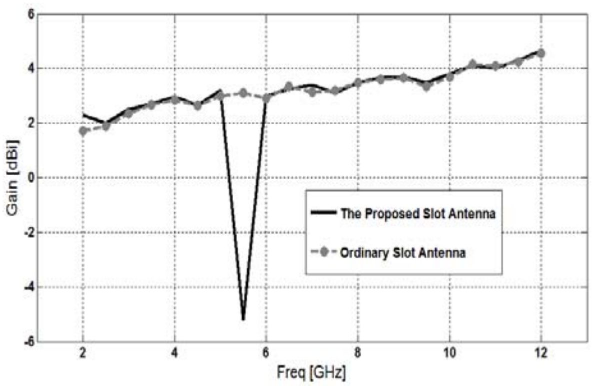

Fig. 9. Maximum gain comparisons for the ordinary slot antenna (simulated), and the proposed antenna (measured) in the z-direction (x-z plane).

ACKNOWLEDGMENT

The authors are thankful to Microwave Technology (MWT) company staff for their beneficial and professional help (www.microwave-technology.com).

REFERENCES

[1] M. Ojaroudi and A. Faramarzi, "Multi resonance small square slot antenna for ultra-wideband applications," *Microwave and Optical Tech. Letters*, vol. 53, no.9, pp. 2145-2149, September 2011.

[2] M. T. Partovi, N. Ojaroudi, and M. Ojaroudi, "Small slot antenna with enhanced bandwidth and band-notched performance for UWB applications," *Applied Computational Electromagnetics Society (ACES) Journal*, vol. 27, no. 9, pp. 772-778, September 2012.

[3] B. H. Siahkal-Mahalle, M. Ojaroudi, and N. Ojaroudi, "Enhanced bandwidth small square monopole antenna with band-notched functions for UWB wireless communications," *Applied Computational Electromagnetics Society (ACES) Journal*, vol. 27, no. 9, pp. 759-765, September 2012.

[4] M. Ojaroudi, N. Ojaroudi, and Y. Ebazadeh, "Dual band-notch small square monopole antenna with enhanced bandwidth characterestics for UWB applications," *Applied Computational Electromagnetics Society (ACES) Journal*, vol. 27, no. 5, pp. 420-426, May 2012.

[5] A. Valizade, Ch. Ghobadi, J. Nourinia, N. Ojaroudi, and M. Ojaroudi, "Band-notch slot antenna with enhanced bandwidth by using Ω-shaped strips protruded inside rectangular slots for UWB applications," *Applied Computational Electromagnetics Society (ACES) Journal*, vol. 27, no. 10, pp. 816-822, October 2012.

[6] G. Zhang, J. S. Hong, B. Z. Wang, and G. Song, "Switched band-notched UWB/ WLAN monopole antenna," *Applied Computational Electromagnetics Society (ACES) Journal*, vol. 27, no. 3, pp. 256-260, March 2012.

[7] M. Ojaroudi, S. Yzdanifard, N. Ojaroudi, and R. A. Sadeghzadeh, "Band-notched small square-ring antenna with a pair of T-shaped strips protruded inside the square ring for UWB applications," *IEEE Antennas Wireless Propag. Lett.*, vol. 10, pp. 227-230, 2011.

[8] X. L. Ma, W. Shao, and G. Q. He, "A novel dual narrow band-notched CPW-fed UWB slot antenna with parasitic strips," *Applied Computational Electromagnetics Society (ACES) Journal*, vol. 27, no. 7, pp. 581-586, July 2012.

[9] Z. L. Zhou, L. Li, and J. S. Hong, "A novel compact monopole antenna with triple high quality rejected bands for UWB applications," *Applied Computational Electromagnetics Society (ACES) Journal*, vol. 27, no. 8, pp. 654-659, August 2012.

[10] M. Rostamzade, S. Mohamadi, Ch. Ghobadi, J. Nourinia, and M. Ojaroudi, "Square monopole antenna for UWB applications with novel rod-shaped parasitic structures and novel V-shaped slots in the ground plane," *IEEE Antennas and Wireless Propag. Lett.*, vol. 11, pp. 446-449, 2012.

[11] M. Mehranpour, J. Nourinia, C. Ghobadi, and M. Ojaroudi, "Dual band-notched square monopole antenna for ultrawideband applications, " *IEEE Antennas and Wireless Propag. Lett.* , vol. 11, pp. 172-175, 2012.

[12] Ansoft High Frequency Structure Simulation (HFSS), Ver. 13, Ansoft Corporation, 2010.

Mohammad Ojaroudi was born on 1984 in Germi, Iran. He received his B.Sc. degree in Electrical Engineering from Azad University, Ardabil Branch and M.Sc. degree in Telecommunication Engineering from Urmia University. From 2010, he is working toward the Ph.D. degree at Shahid Beheshti University. From 2007 until now, he is a Teaching Assistant with the Department of Electrical Engineering, Islamic Azad University, Ardabil Branch, Iran.

Since March 2009, he has been a Research Fellow (Chief Executive Officer) in the Microwave Technology Company (MWT), Tehran, Iran. From 2012, Mr. Ojaroudi is a member of the IEEE Transaction on Antennas and Propagation (APS) reviewer group and the Applied Computational Electromagnetic Society (ACES). From 2013 he is a student member of the IEEE. His research interests include analysis and design of microstrip antennas, design and modeling of microwave structures, radar systems, and electromagnetic theory. He is author and coauthor of more than 100 journal and international conferences papers. His papers have more than 400 citations with 10 h-index.

Nasser Ojaroudi was born on 1986 in Germi, Iran. He received his B.Sc. degree in Electrical Engineering from Islamic Azad University, Ardabil Branch. From 2011, he is working toward the M.Sc. degree in Telecommunication Engineering at Shahid Rajaee Teacher Training University. Since March 2008, he has been a Research Fellow in the Microwave Technology (MWT) Company, Tehran, Iran. His research interests include ultra-wideband (UWB) microstrip antennas and band-pass filters (BPF), reconfigurable structure, design and modeling of microwave device, and electromagnetic wave propagation.

Noradin Ghadimi was born in ardabil-Iran in 1985, and received the B.Sc. degree in Electrical Engineering from the Islamic Azad University, Ardabil Branch, Ardabil, Iran, in 2009 and the M.Sc. degree in Electrical Engineering from the Islamic Azad University Ahar Branch, Ahar, Iran , in 2011. His research interests include power system protection, modeling and analysis of distributed generations, renewable energy and communications systems.

Design of a Two Bands Circularly Polarized Square Slot Antenna for UWB Application

N. Felegari [1], H. R. Dalili Oskouei [2], M. Akbari [1], M. Mighani [2]

[1] Young Researchers and Elite club, Central Tehran Branch,
Islamic Azad University, Tehran, Iran
N.felegari@gmail.com and Akbari.telecom@gmail.com

[2] Department of Electrical Engineering,
Shahid Sattari Aeronautical University of Science and Technology, Tehran, Iran.
H_oskouei@yahoo.com and Mojtaba.mighani@gmail.com

Abstract ─ A novel ultra-wideband slot antenna fed by a coplanar waveguide (CPW) is presented and experimentally investigated. The proposed antenna has capability of both the circular polarization and ultra wideband (UWB) performance. The designed antenna has a size of 40 × 40 × 0.8 mm^3. The experimental results show that the antenna has an impedance bandwidth of 142 % and axial-ratio (AR) bandwidths of 35 % for the lower band and 22.6 % for the upper band.

Index Terms ─ Antenna, CPW-fed, CPSSA, circularly-polarized square slot antenna, and UWB.

I. INTRODUCTION

The interest in UWB technology has increased after the U.S. Federal Communications Commission (FCC) allocation of the frequency band on 3.1 GHz – 10.6 GHz for commercial use. Recently, UWB technology has been widely used in various radars and has attracted much attention for communication systems. Although there are many antennas to cover the UWB systems [1-3], but there are few articles that designed UWB antennas with circular polarization (CP) [4-6]. By using the circular polarization in wireless communication systems, arranging the orientation of the antenna between transmitter and receiver is not needed any more. Circularly polarized (CP) antennas overcome the multipath fading problem and enhance system performance [6]. In this paper, we suggest a circularly polarized square slot antenna (CPSSA) for UWB systems with the combination of the techniques introduced in [7-8]. Two main characteristics have been used in the presented antenna: a fork-like feed line for improving impedance bandwidth, three T-shaped and one L-shaped grounded strips mainly for creating circular polarization operation. The measurements indicate that it has an impedance bandwidth of 1.95 GHz – 11.55 GHz (142 %) and also the CP bandwidth is from 2.38 GHz to 3.4 GHz (35 %) for lower band and from 5.1 GHz to 6.4 GHz (22.6 %) for upper bands, respectively.

II. ANTENNA DESIGN

The geometry of the proposed circularly-polarized square slot antenna (CPSSA) and a photograph of the fabricated antenna are depicted in Figs. 1 (a) and (b). The presented antenna consists of a square ground plane with length of 40 mm, three T-shape and one L-shape strips. The T-shape strips consist of a centre arm with fixed length of 4 mm and upper arm with length of L_t and the L-shape strip has a horizontal arm with fixed length of 10.5 mm and a vertical arm with length of L_1. The CPSSA has been printed on a commercially cheap FR4-epoxy substrate with relative permittivity 4.4, thickness 0.8 mm, and loss tangent 0.024 g^2. The width of the coplanar waveguide (CPW) feed line is 3.1 mm, and the width of the gap between the feed line and the ground plane is 0.3 mm (Fig. 1 (a)). To enhance the bandwidth the fork-like microstrip line has been used. Also, to generate circular polarization

Submitted On: Oct. 31, 2012
Accepted On: July 9, 2013

three T stubs and L strip were embedded in the ground plane. The T-Shaped grounded strip was first proposed in [9]. Also, Fig. 1 illustrate the structure of the CPSSA that will generate left and right-handed circularly-polarized (LHCP and RHCP) radiations in lower and upper bands, respectively with AR below 3 dB.

III. EXPERIMENTAL RESULTS AND DISCUSSION

The performance of the CPSSA at parametric studies has been investigated to find the optimized parameters using Ansoft high frequency structure simulator (HFSS ver. 13) based on the finite element method (FEM). To clarify the performance of the antenna, four prototypes of the proposed antenna are defined as follows (Fig. 1 (c)). Ant. I includes only a single strip and a ground plane, Ant. II contains fork-like feed line, Ant. III has a fork-like feed line, and L strip. The proposed antenna or Ant. IV contains T-shaped stubs and L strip embedded in the ground plane. The fabricated antenna has been measured using an Agilent 8722ES vector network analyzer in its full operational span (10 MHz – 20 GHz). Simulated and measured return loss and CP axial ratio are shown in Figs. 2 (a) and (b). The simulated results show that the variation in the feed line shape from straight to fork-like shape assists in creating additional resonances and thus enhances the bandwidth. It should be mentioned that the impedance bandwidth is greatly increased by tuning the fork like feed line while the polarization of antenna become linear. The CP operation of the proposed antenna is mostly related to the T- and L-shaped stubs embedded in the ground plane. Note that Ant. IV has already attained a dual band -3 dB ARBW (2.38 GHz – 3.4 GHz, 5.1 GHz – 6.4 GHz). As exhibited in Figs. 2 (a) and (b), the measured impedance bandwidth for Ant. IV has an operating frequency range from 1.95 (GHz) to 11.55 GHz (142 %) and 3 dB ARBW of 35 % on lower band and 22.6 % on upper band. As mentioned earlier, the T-shape and L-shape strips are used to obtain dual band CP performance of the proposed antenna. To more clarify, the role of these metallic strips in CP operation, the -3 dB axial ratio curves for different values of L_l and L_t are shown in Figs. 3 and 4, respectively. From the simulation results, it is seen that the small changes in the metallic strips lengths (T-shape and L-shape strips) has a significant effect on the CP operation. By increasing L_l, the -3 dB AR bandwidth is fine improved specially on the upper band, whilst the variations of the parameter L_t impress the CP performance, particularly on the lower band as shown in Fig. 4. From the results it is found that the optimum values for L_p and L_t are 8 mm. Usually in design of circularly polarized antennas, obtaining large CP bandwidth is very important (Table I). The size and simulated and measured characteristics of some CPSSA have been summarized in Table I. Meanwhile, all these antennas were fabricated on an FR4 substrate.

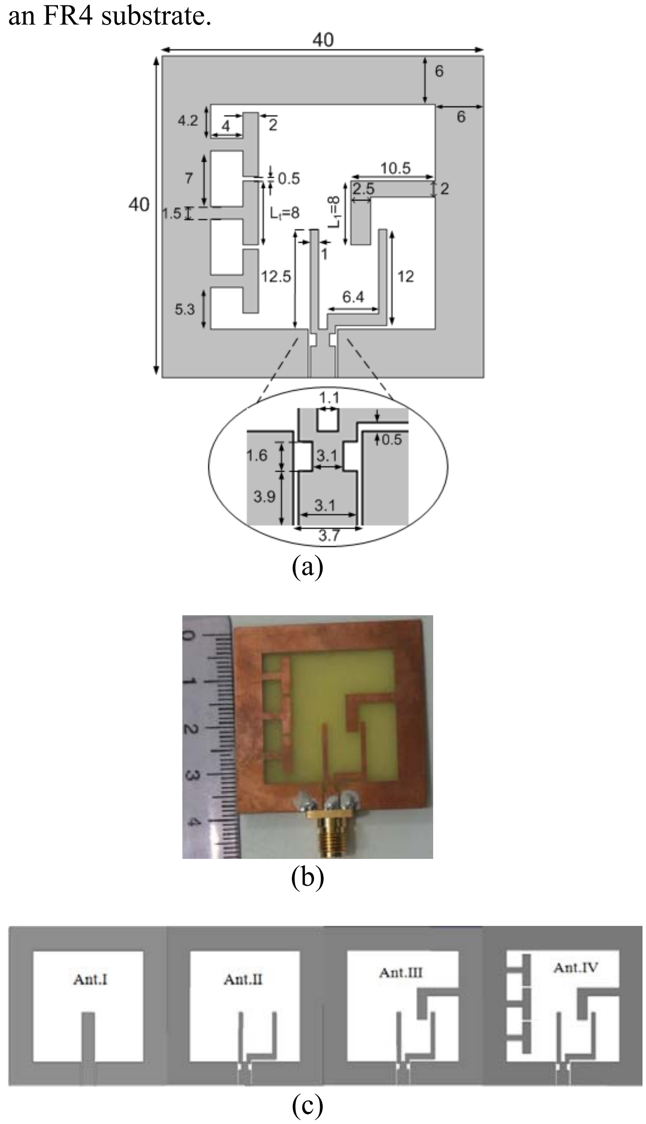

Fig. 1. Geometry of the proposed UWB antenna; (a) antenna configuration, (b) photo of the optimized antenna, and (c) four prototypes of the CPSSA under investigation.

Table I: Summary of the measured characteristics of some CPSSA.

Type	Size (mm^3)	Impedance bandwidth (GHz)	3dB ARBW (GHz, %)
Ant. I	40×40×0.8	2.85-4.25	0, (0%)
Ant. II	40×40×0.8	2.65-3.25 3.75-9.4 10.6-more than 12	0, (0%)
Ant. III	40×40×0.8	1.85-2.15 3.1-9.65 10.3-more than 12	5.65-6.05, (6.8%)
Ant. IV (Simulation)	40×40×0.8	1.85-more than 12	2.37-3.31, (33.1%) 5.2-6.66, (24.6%)
Ant. IV (Measurement)	40×40×0.8	1.95-11.55	2.38-3.4, (35%) 5.1-6.4, (22.6%)
Ref.[1]	60×60×0.8	2.67-13	4.9-6.9, (32.2%)
Ref.[2]	25×25×0.8	2.98-11.23	5.012-7.382, (38.2%)
Ref.[3]	60×60×0.8	2-7.07	2.03-5.12, (85%)

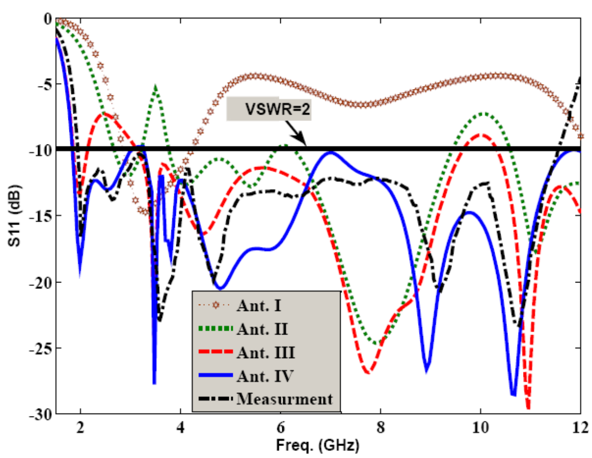

(a)

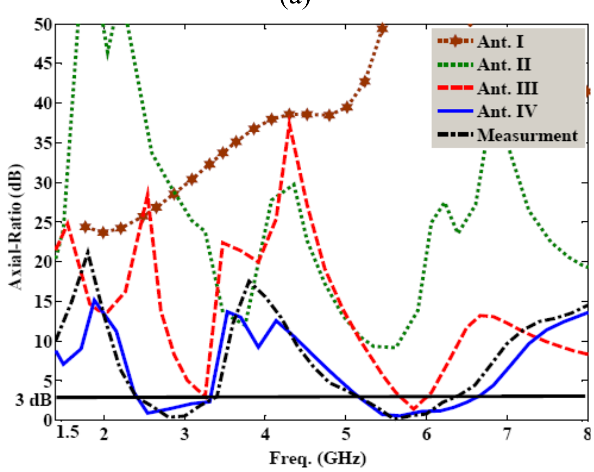

(b)

Fig. 2. Measured and simulated S_{11} and CP axial ratios for Ants. I to IV.

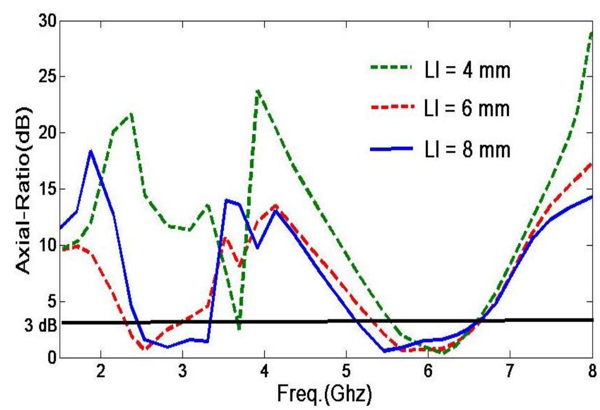

Fig. 3. Simulated AR curves of the proposed antenna with different values of L_l (L_t was fixed at 8 mm).

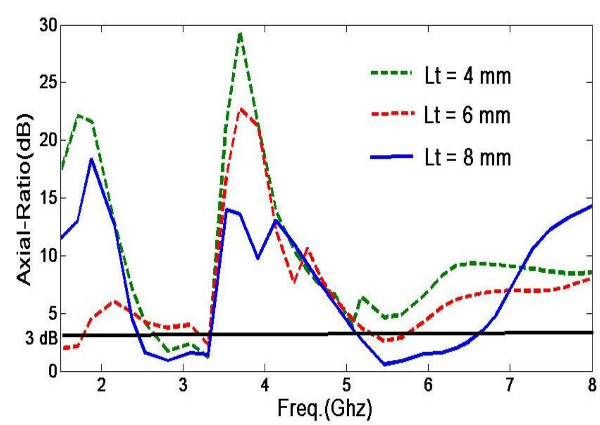

Fig. 4. Simulated AR curves of the proposed antenna with different values of L_t (L_l was fixed at 8 mm).

Figure 5 shows the measured normalized RHCP and LHCP radiation patterns of the proposed antenna at frequencies of 3 GHz, 5.5 GHz, and 8 GHz.

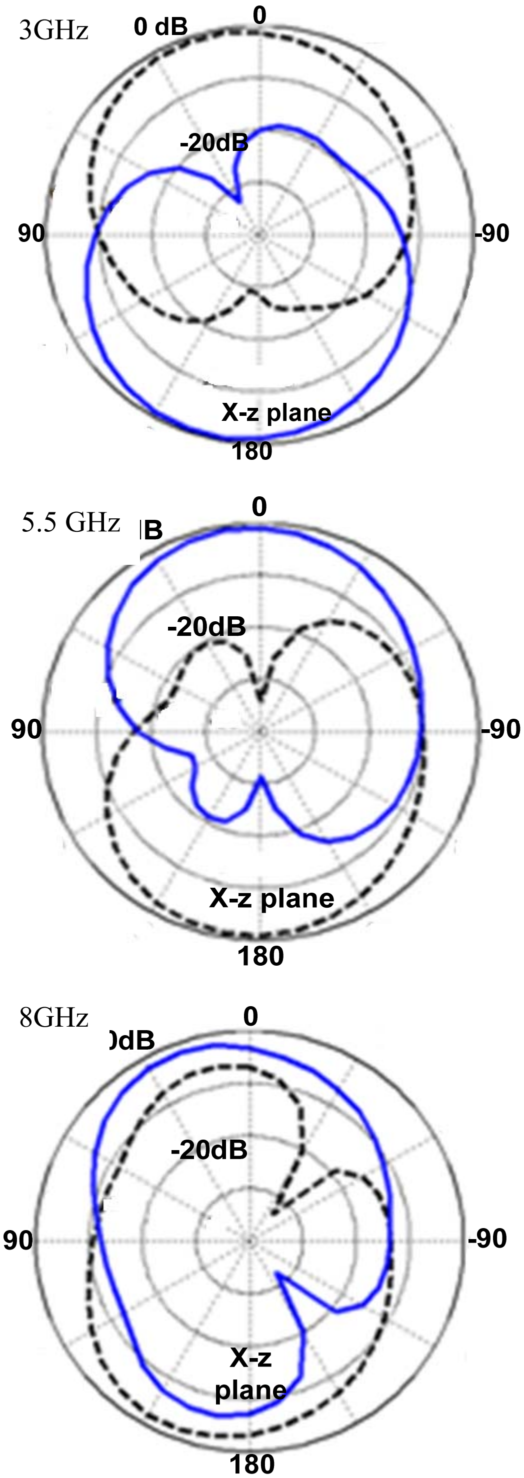

Fig. 5. Measured radiation patterns of the proposed antenna.

IV. CONCLUSION

A novel ultra-wideband antenna fed by a coplanar waveguide has been proposed. The novel structure helps to enlarge the 3 dB ARBW on both of the lower and upper bands to be greater than 35 % and 22.6 %, respectively. The designed antenna has a size of 40 × 40 × 0.8 mm^3. The measured results show that the antenna has a broad bandwidth of 142 %. According to the impedance bandwidth and -3 dB axial ratio bandwidth, the proposed antenna is a good candidate for various wireless systems and applications.

REFERENCES

[1] M. Mighani, M. Akbari, and N. Felegari, "A CPW dual band notched UWB antenna," *Applied Computational Electromagnetics Society (ACES) Journal*, vol. 27, no. 4, pp. 352-359, April 2012.

[2] M. Mighani, M. Akbari, and N. Felegari, "A novel SWB small rhombic microstrip antenna with parasitic rectangle into slot of the feed line," *Applied Computational Electromagnetics Society (ACES) Journal*, vol. 27, no. 1, pp. 74-79, January 2012.

[3] R. Azim, M. T. Islam, and N. Misran, "Design of a planar UWB antenna with new band enhancement technique," *Applied Computational Electromagnetics Society (ACES) Journal*, vol. 26, no. 10, pp. 856-862, October 2011.

[4] J. Pourahmadazar, C. Ghobadi, J. Nourinia, N. Felegari, and H. Shirzad, "Broadband CPW-fed circularly polarized square slot antenna with inverted-L strips for UWB applications," *IEEE Antennas Wirel. Propag. Lett.*, vol. 10, pp. 369-372, 2011.

[5] J. Pourahmadazar and S. Mohammadi, "Compact circularly-polarized slot antenna for UWB applications," *Electron. Lett.*, vol. 47, no. 15, pp. 837-838, 2011.

[6] N. Felegari, J. Nourinia, C. Ghobadi, and J. Pourahmadazar, "Broadband CPW-fed circularly polarized square slot antenna with three inverted-L-shape grounded strips," *IEEE Antennas Wirel. Propag. Lett.*, vol. 10, pp. 274-277, 2011.

[7] J. -Y. Sze and K. -L. Wong, "Bandwidth enhancement of a microstrip-line-fed printed wide-slot antenna," *IEEE Tran. Antennas Propag.*, vol. 49, no. 7, pp. 1020-1024, 2001.

[8] J. -Y. Sze, K. -L. Wong, and C. C. Huang, "Coplanar waveguide-fed square slot antenna for broadband circularly polarized radiation," *IEEE*

Trans. Antennas Propag., vol. 51, pp. 2141-2144, 2003.

Nader Felegari was born in Songhor, Iran 1984. He received his B.Sc. degree of Electrical Engineering and his M.Sc. degree of Communication Engineering from the Urmia University, Iran. His primary research interests are in antenna design.

Hamid Reza Dalili Oskouei received his B.Sc. and M.Sc. degrees in Electrical Engineering from the University of Aeronautical Science & Technology and the Trabiat Modares University, Iran in 2002 and 2004, respectively. He obtained his Ph.D. degree in Electrical Engineering from Trabiat Modares University, Tehran, Iran. He then joined the University of Aeronautical Science & Technology, Tehran, Iran, as an Assistant Professor in 2006, his research areas are communication, radar, microwave component, and antenna and wave propagation. Dr. Oskouei has served as a reviewer for a number of journals and conferences.

Mohammad Akbari was born on February 3, 1983 in Tehran, Iran; He received his B.Sc. degree in Electrical Engineering at Bahonar University of Kerman, Iran, in 2007 and M.Sc. degrees in Electrical Engineering at Urmia University, Urmia, Iran, in 2010. His research interests include analysis and design of antennas, design and modeling of microwave structures, radar systems, and electromagnetic theory. He has taught courses in microwave engineering, antenna theory, and fields & waves, and electromagnetic in Aeronautical University, Tehran, Iran. He is author and coauthor of approximately 30 journals and international conference papers.

Mojtaba Mighani was born in Mashhad, Iran, in September 23, 1983. He received B.Sc. degree in Electrical and Electronic Engineering from Aeronautical University, Tehran, Iran, in 2005 and M.Sc. degrees in Electrical and Telecommunication Engineering from K.N.Toosi University of Technology, Tehran, Iran. He is currently working toward the Ph.D. degree in communication Engineering. Since 2007 He has taught courses in communication circuits, microwave engineering, antenna theory, radar, and fields and waves in Aeronautical University, Tehran, Iran. Also he is working in some projects in PMS and RAMTEC Co. as a project manager and RF designer. His research interests include antenna theory, microwave active circuits and RF communication links.

Square Monopole Antenna with Band-Notched Characteristic for UWB Communications

Nasser Ojaroudi [1], Mohammad Ojaroudi [2], and Noradin Ghadimi [2]

[1] Department of Electrical Engineering,
Germi Branch, Islamic Azad University, Germi, Iran
n.ojaroudi@iaugermi.ac.ir

[2] Young Researchers Club
Ardabil Branch, Islamic Azad University, Ardabil, Iran
m.ojaroudi@iauardabil.ac.ir and noradin.ghadimi@gmail.com

Abstract **—** In this paper, a novel ultra wideband monopole antenna with frequency band-stop performance is designed and manufactured. The proposed antenna consists of a square radiating patch, and a ground plane with a cross-shaped slit and an inverted π-shaped conductor-backed plane. The cross-shaped slit, increases the bandwidth that provides a wide usable fractional bandwidth of more than 125 % (2.86 GHz – 12.91 GHz). In order to create band-notched function we use an inverted π-shaped parasitic structure in the ground plane, a frequency notch band of 5.11 GHz – 6.02 GHz has been achieved. Good VSWR and radiation pattern characteristics are obtained in the frequency band of interest. Simulated and measured results are presented to validate the usefulness of the proposed antenna structure for UWB applications.

Index Terms **—** Band-notched function, inverted π-shaped conductor-backed plane, printed monopole antenna (PMA), and ultra wideband (UWB).

I. INTRODUCTION

Communication systems usually require smaller antenna size in order to meet the miniaturization requirements of radio-frequency (RF) units [1]. It is a well-known fact that planar monopole antennas present really appealing physical features, such as simple structure, small size, and low cost. Due to all these interesting characteristics, planar monopoles are extremely attractive to be used in emerging UWB applications, and growing research activity is being focused on them. Consequently, a number of planar monopoles with different geometries have been experimentally characterized [2, 3].

The frequency range for UWB systems is between 3.1 GHz – 10.6 GHz, which will cause interference to the existing wireless communication systems for example the wireless local area network (WLAN) for IEEE 802.11a operating in 5.15 GHz – 5.35 GHz and 5.725 GHz – 5.825 GHz bands, so the UWB antenna with a band-notched function is required. Lately, to generate the frequency band-notched function, several modified planar antennas with band-notch characteristic have been reported [4-8]. In references [4-6], different shapes of the slots (i.e., square ring, W-shaped, and folded trapezoid) are used to obtain the desired band-notched characteristics. Also reconfigurable structures integrated with diodes can be used to generate band-notched performances [7]. In [8] single and multiple half-wavelength U-shaped is used to generate the frequency band-notched function, modified planar slits are embedded in the radiation patch to generate the band-notched functions.

All of the above methods are used for rejecting a single band of frequencies. However, to effectively utilize the UWB spectrum and to improve the performance of the UWB system, it is desirable to design the UWB antenna with dual band rejection. It will help to minimize the interference between the narrow band systems

Submitted On: Aug. 8, 2012
Accepted On: April 24, 2013

1054-4887 © 2013 ACES

with the UWB system. Some methods are used to obtain the dual band rejection in the literature [9-11].

In this paper, a simple method for designing a novel and compact microstrip-fed monopole antenna with band-notched characteristic for UWB applications has been presented. In the proposed antenna, for bandwidth enhancement we use cross-shaped slit in the ground plane and by using an inverted π-shaped parasitic structure with variable dimensions on the other side of the substrate a band-stop performance can be created. The presented monopole antenna has a small size of 12×18×1.6 mm^3. Good VSWR and radiation pattern characteristics are obtained in the frequency band of interest. Simulated and measured results are presented to validate the usefulness of the proposed antenna structure for UWB applications.

II. ANTENNA DESIGN

The presented small monopole antenna fed by a microstrip line is shown in Fig. 1, which is printed on an FR4 substrate of thickness 1.6 mm, permittivity 4.4, and loss tangent 0.018. The basic monopole antenna structure consists of a square patch, a feed line, and a ground plane. The square patch has a width W. The patch is connected to a feed line of width W_f and length $L_f + L_{gnd}$. The width of the microstrip feed line is fixed at 2 mm, as shown in Fig. 1. On the other side of the substrate, a conducting ground plane is placed. The proposed antenna is connected to a 50 Ω SMA connector for signal transmission.

In this study, based on defected ground structure (DGS), the cross-shaped slit in the ground plane is used to perturb an additional resonance at higher frequencies and increase the bandwidth [5]. Also, based on electromagnetic coupling theory (ECT), for generating band-stop performance we use an inverted π-shaped parasitic structure in the ground plane. In this structure, by inserting the inverted π-shaped parasitic structure, the desired high attenuation near the notch frequency can be produced.

In this work, we start by choosing the dimensions of the designed antenna. These parameters, including the substrate, are $W_{sub} \times L_{sub}$ = 12 mm × 18 mm or about 0.15 λ × 0.25 λ at 4.2 GHz (the first resonance frequency). We have a lot of flexibility in choosing the width of the radiating patch. This parameter mostly affects the antenna bandwidth. As W_X decreases, so does the antenna bandwidth, and vice versa. Next step, we have to determine the length of the radiating patch L_X. This parameter is approximately $\lambda_{lower}/4$, where λ_{lower} is the lower bandwidth frequency wavelength. λ_{lower} depends on a number of parameters such as the radiating patch width as well as the thickness and dielectric constant of the substrate on which the antenna is fabricated [9]. The important step in the design is to choose $L_{resonance}$ (the length of the resonator), L_{notch} (the length of the filter). $L_{resonance}$ is set to resonate at 0.25 λ_g, where $L_{resonance3} = 0.5\,(W_S\text{-}W_{S1}) + L_{S1} + L_{S2}$, corresponds to resonance frequency wavelength (12 GHz is the third resonance frequency). L_{notch} is set to band-stop resonate at 0.5 λ_g, where $L_{notch} = L_P + W_{P1}$, λ_g corresponds to the notched band frequency wavelength (5.5 GHz is the notched frequency).

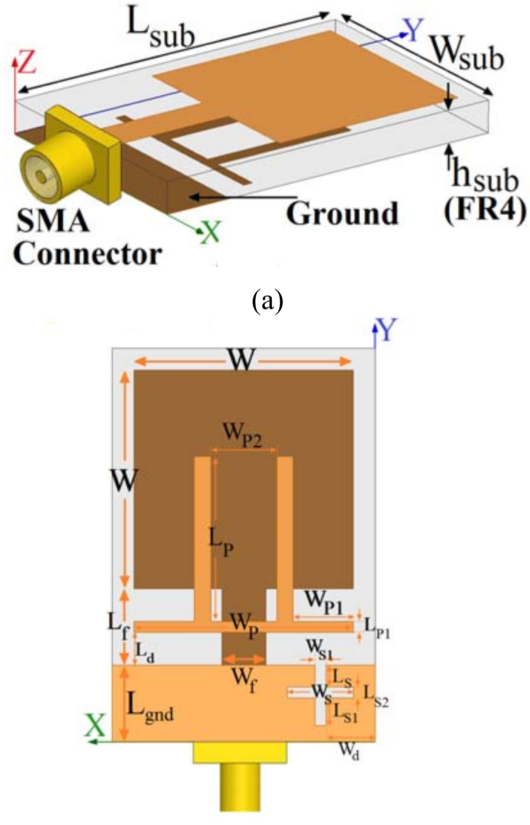

Fig. 1. Geometry of the proposed monopole antenna, (a) side view, (b) bottom view.

The optimized values of the proposed antenna design parameters are as follows: W_{sub} = 12 mm, L_{sub} = 18 mm, h_{sub} = 1.6 mm, W_f = 2 mm, L_f = 3.5 mm, W = 10 mm, W_s = 3.5 mm, L_s = 0.5 mm, W_{s1} = 0.5 mm, L_{s1} = 1 mm, L_{s2} = 0.5 mm, W_d = 2.25 mm, L_d = 1.5 mm, W_p = 8 mm, L_p = 9.5 mm, W_{p1} = 2.5 mm, L_{p1} = 0.5 mm, W_{p2} = 2 mm, and L_{gnd} = 3.5 mm.

III. RESULTS AND DISCUSSIONS

The proposed microstrip monopole antenna with various design parameters were constructed, and the numerical and experimental results of the input impedance and radiation characteristics are presented and discussed. The proposed microstrip-fed monopole antenna was fabricated and tested. The parameters of this proposed antenna are studied by changing one parameter at a time and fixing the others. Ansoft HFSS simulations are used to optimize the design and agreement between the simulation and measurement is obtained [12]. The configuration of the presented monopole antenna was shown in Fig. 1. The geometry of the ordinary square patch antenna (Fig. 2 (a)), with a cross-shaped slit in the ground plane (Fig. 2 (b)), and the proposed antenna (Fig. 2 (c)) structures are compared in Fig. 2.

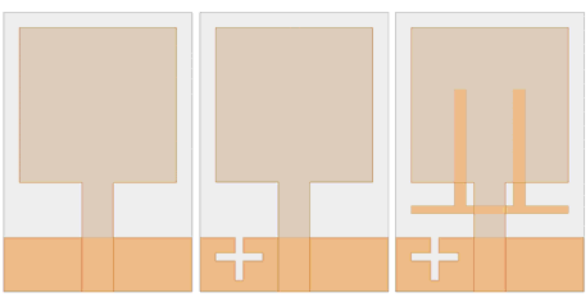

Fig. 2. (a) basic structure (ordinary monopole antenna), (b) antenna with a cross-shaped slit in the ground plane, and (c) the proposed antenna.

The VSWR characteristics of the structures that were shown in Fig. 2 are compared in Fig. 3. As shown in Fig. 3, it is observed that the upper frequency bandwidth is affected by using the cross-shaped slit in the ground plane and the notch frequency bandwidth is sensitive to the inverted π-shaped parasitic structure. Also the input impedance of the various monopole antenna structures that were studied in Fig. 3, are shown on a Smith chart in Fig. 4.

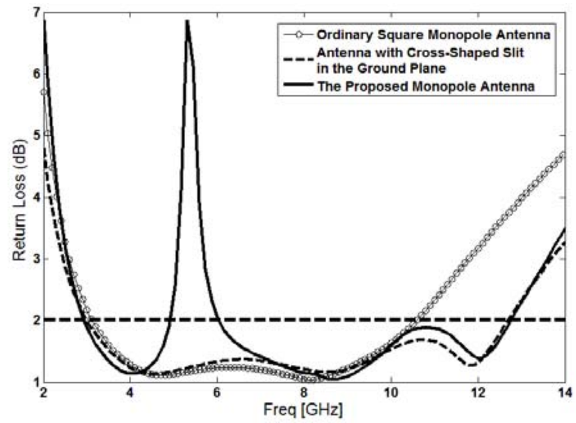

Fig. 3. Simulated VSWR characteristics for the antennas shown in Fig. 2.

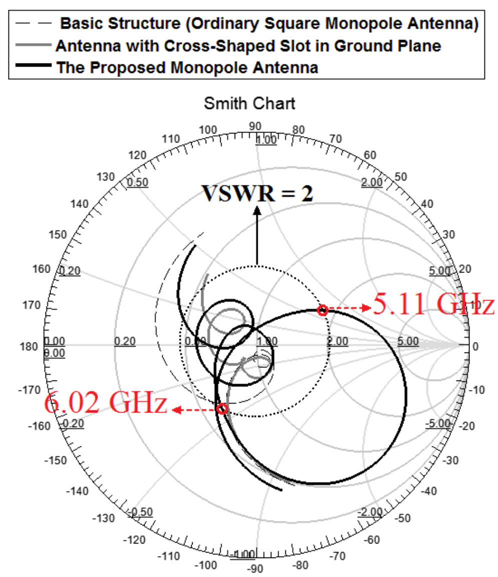

Fig. 4. The simulated input impedance on a Smith chart for the various antenna structures shown in Fig. 2.

In order to understand the phenomenon behind this additional resonance performance, the simulated current distributions on the ground plane for the square antenna with a cross-shaped slit in the ground plane at 12 GHz are presented in Fig. 5 (a). It is found that, based on the defected ground structure (DGS), by using the cross-shaped slit in the ground plane; third resonance at 12 GHz can be achieved. Other important design parameters of this structure is the use of an inverted π-shaped parasitic structure on the ground plane. Figure 5 (b) presents the simulated current distributions on the ground plane at the notch frequency (5.5 GHz). As shown in Fig. 5 (b), at the notch frequency the current flows are more dominant around the inverted π-shaped parasitic structure.

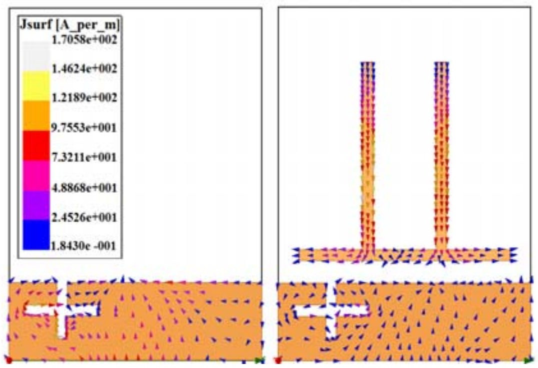

(a) (b)

Fig. 5. Simulated surface current distributions for the proposed antenna on the ground plane (a) at the extra resonance frequency at 12 GHz and (b) at the notch frequency at 5.5 GHz.

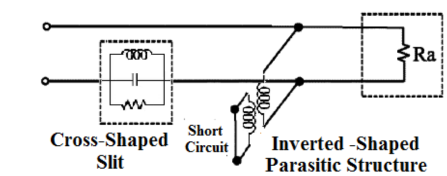

(a)

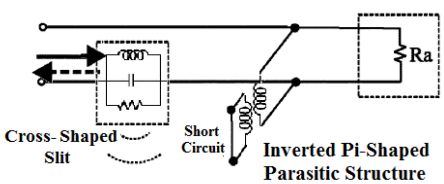

(b)

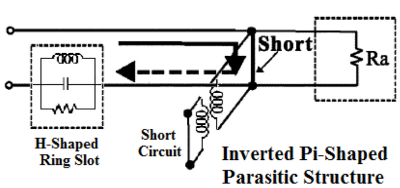

(c)

Fig. 6. (a) Conceptual equivalent-circuit model for the proposed antenna, and the equivalent circuits at (b) the new resonance frequency, and (c) at the first notch frequency.

Figure 6 shows the conceptual equivalent circuit model for the proposed antenna, which has an RLC resonator and a shunt stub. When the current path in the inverted π-shaped ring conductor backed plane is equal to a half-wavelength at 5.5 GHz in Fig. 6 (c), the input impedance at the feeding point is zero (short circuit). Figure 7 shows the simulated VSWR curves with different values of L_p. As shown in Fig. 7, when the exterior length of the inverted π-shaped parasitic structure increases from 9.5 mm to 12.25 mm, the center of the notch frequency decreases from 6.6 GHz to 4.8 GHz. From these results, we can conclude that the notch frequency is controllable by changing the exterior length of the inverted π-shaped parasitic structure [13].

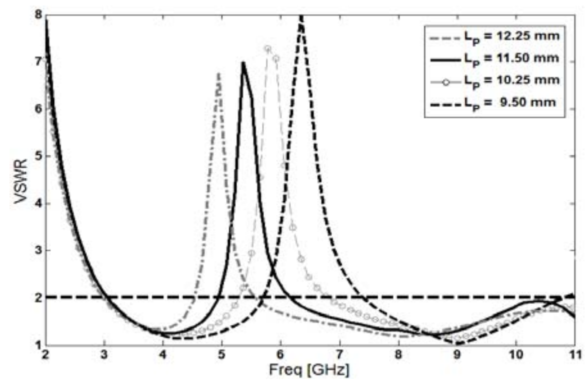

Fig. 7. Simulated VSWR characteristics for the proposed antenna with different values of W_X.

Another main effect of the inverted π-shaped conductor-backed plane occurs on the filter bandwidth. In this structure, the width W_{p2}, is the critical parameter to control the filter bandwidth. Figure 8 illustrates the simulated VSWR characteristics with various length of W_{p2}. As the interior width of the W_{p2} increases from 0.4 mm to 1.4 mm, the filter bandwidth varies from 0.7 GHz to 1.5 GHz. Therefore the bandwidth of the notch frequency is controllable by changing the width of W_{p2}.

The proposed antenna with optimal design was built and tested. The measured and simulated VSWR characteristic of the proposed antenna are shown in Fig. 9. The fabricated antenna has the frequency band of 2.86 GHz to 12.91 GHz with WLAN rejection band around 5.11 GHz – 6.02 GHz.

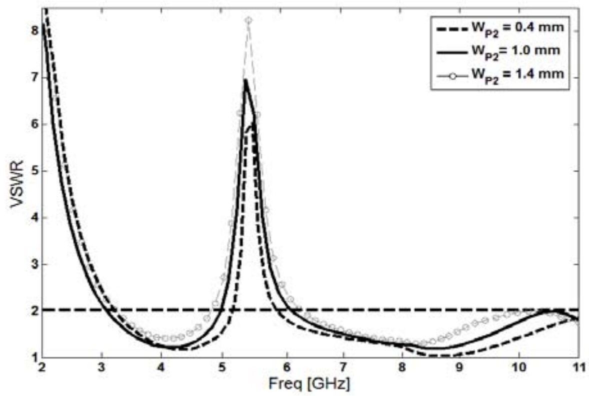

Fig. 8. Simulated VSWR characteristics for the proposed antenna with different values of W_{X1}.

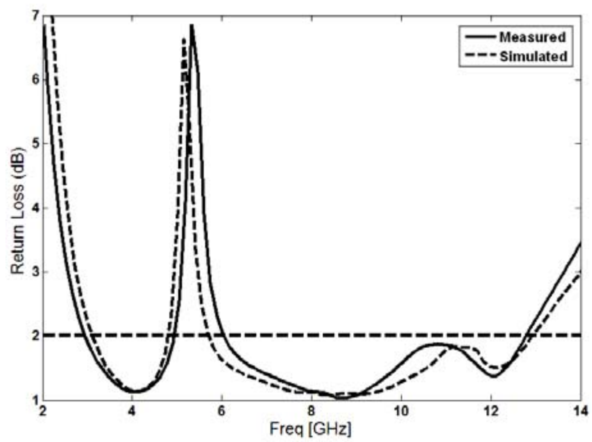

Fig. 9. Measured and simulated VSWR for the proposed antenna.

Figure 10 illustrates the measured radiation patterns, including the co–polarization and cross–polarization, in the H– (x–z plane) and E–planes (y–z plane). It can be seen that the radiation patterns in x–z plane are nearly omni-directional for the three frequencies. Figure 11 shows the effects of the cross-shaped slit and the inverted π-shaped parasitic structure, on the maximum gain in comparison to the same antenna without them. As shown in Fig. 11, the ordinary square antenna has a gain that is low at 3 GHz and increases with frequency. It can be observed in Fig. 11 that by using a cross-shaped slit and the inverted π-shaped parasitic structure, a sharp decrease of maximum gain in the notched frequency band at 5.5 GHz is shown. For other frequencies outside the notched frequency band, the antenna gain with the filter is similar to those without it.

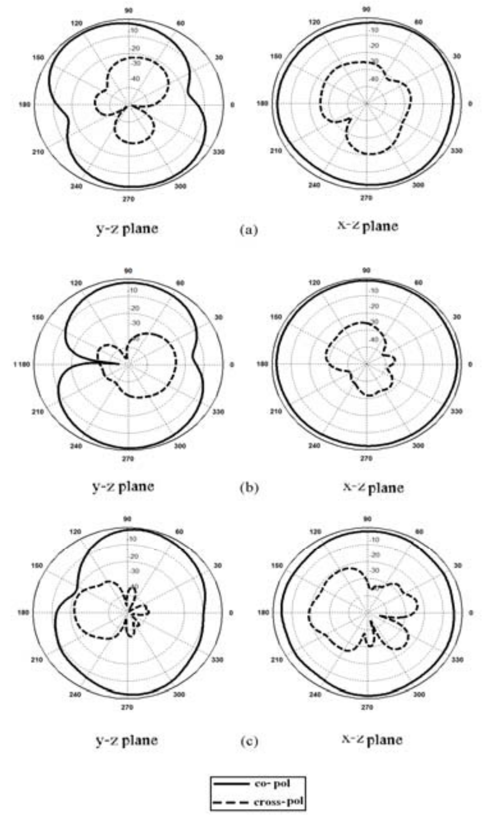

Fig. 10. Measured radiation patterns of the proposed antenna at (a) 4 GHz, (b) 7 GHz, and (c) 10 GHz.

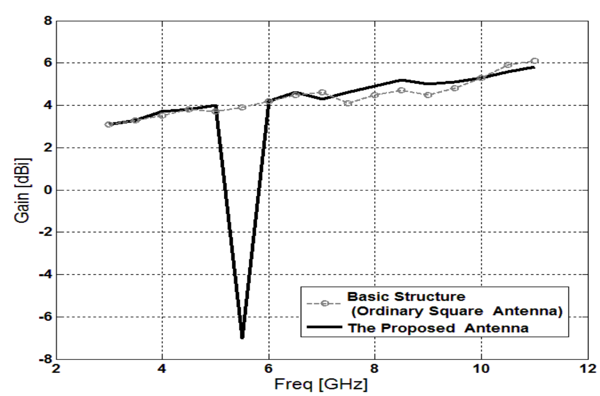

Fig. 11. Measured maximum gain comparisons for the ordinary square antenna and the proposed antenna.

IV. CONCLUSION

A new small monopole antenna with band-notched function for UWB applications is presented in this paper. The proposed antenna can operate from 2.86 GHz to 12.91 GHz with WLAN rejection band around 5.11 GHz – 6.02 GHz. In order to enhance the bandwidth we cut a cross-shaped slit in the ground plane, and also by using an inverted π-shaped parasitic structure at the ground plane, a frequency band-notched function can be achieved and improved. The designed antenna has a small size of 12×18 mm^2. Simulated and experimental results show that the proposed antenna could be a good candidate for UWB applications.

ACKNOWLEDGMENT

The authors are thankful to Microwave Technology (MWT) Company staff for their beneficial and professional help (www.microwave-technology.com).

REFERENCES

[1] H. Schantz, "The art and science of ultra wideband antennas," *Artech House* 2005.

[2] M. Ojaroudi, Sh. Yzdanifard, N. Ojaroudi, and M. Nasser-Moghaddasi, "Small square monopole antenna enhanced by using inverted T-shaped slot and conductor-backed plane," *IEEE Transactions on Antenna and Propagation*, vol. 59, no. 2, pp. 670-674, February 2011.

[3] A. Ghazi, M. N. Azarmanesh, and M. Ojaroudi, "Muti-resonance square monopole antenna for ultra-wideband applications," *Progress In Electromagnetics Research C*, vol. 14, pp. 103-113, 2010.

[4] M. Ojaroudi, Sh. Yzdanifard, N. Ojaroudi, and R. A. Sadeghzadeh, "Band-notched small square-ring antenna with a pair of T-shaped strips protruded inside the square ring for UWB applications," *IEEE Antennas and Wireless Propagation Letters*, vol. 10, pp. 227-230, 2011.

[5] M. Ojaroudi, "Printed monopole antenna with a novel band-notched folded trapezoid for ultra-wideband applications," *Journal of Electromagnetic Waves and Application (JEMWA)*, vol. 23, pp. 2513–2522, 2009.

[6] Sh. Yazdanifard, R. A. Sadeghzadeh, and M. Ojaroudi, "Ultra-wideband small square monopole antenna with variable frequency band-notch," *Progress In Electromagnetics Research C*, vol. 15, pp. 133-144, 2010.

[7] G. Zhang, J. S. Hong, B. Z. Wang, and G. Song, "Switched band-notched UWB/WLAN monopole antenna," *Applied Computational Electromagnetics Society (ACES) Journal*, vol. 27, no. 3, pp. 256-260, March 2012.

[8] M. Ojaroudi, Gh. Ghanbari, N. Ojaroudi, and Ch. Ghobadi, "Small square monopole antenna for UWB Applications with variable frequency band-notch function," *IEEE Antennas and Wireless Propagation Letters*, vol. 8, pp. 1061-1064, 2009.

[9] M. Ojaroudi, N. Ojaroudi, and Y. Ebazadeh, "Dual band-notch small square monopole antenna with enhanced bandwidth characteristics for UWB applications," *Applied Computational Electromagnetics Society (ACES) Journal*, vol. 27, no. 5, pp. 420-426, May 2012.

[10] M. Mighani, M. Akbari, and N. Felegari, "A CPW dual band notched UWB antenna," *Applied Computational Electromagnetics Society (ACES) Journal*, vol. 27, no. 4, pp. 352-359, April 2012.

[11] J. William and R. Nakkeeran, "A new UWB slot antenna with rejection of WiMax and WLAN bands," *Applied Computational Electromagnetics Society (ACES) Journal*, vol. 25, no. 9, pp. 787-793, September 2010.

[12] Ansoft High Frequency Structure Simulation (HFSS), ver. 13, Ansoft Corporation, 2010.

[13] Y. Li, W. Li, and W. Yu, "A switchable UWB slot antenna using SIS-HSIR and SIS-SIR for multi-mode wireless communications applications," *Applied Computational Electromagnetics Society (ACES) Journal*, vol. 27, no. 4, pp. 340-351, April 2012.

Nasser Ojaroudi was born on 1986 in Germi, Iran. He received his B.Sc. degree in Electrical Engineering from Islamic Azad University, Ardabil Branch. From 2011, he is working toward the M.Sc. degree in Telecommunication Engineering at Shahid Rajaee Teacher Training University. Since March 2008, he has been a Research Fellow in the Microwave Technology (MWT) Company, Tehran, Iran. His research interests include ultra-wideband (UWB) microstrip antennas and band-pass filters (BPF), reconfigurable structure, design and modeling of microwave device, and electromagnetic wave propagation.

Mohammad Ojaroudi was born on 1984 in Germi, Iran. He received his B.Sc. degree in Electrical Engineering from Azad University, Ardabil Branch and M.Sc. degree in Telecommunication Engineering from Urmia University. From 2010, he is working toward the Ph.D. degree at Shahid Beheshti University. From 2007 until now, he is a Teaching Assistant with the Department of Electrical Engineering, Islamic Azad University, Ardabil Branch, Iran. Since March 2009, he has been a Research Fellow (Chief Executive Officer) in the Microwave Technology Company (MWT), Tehran, Iran. From 2012, Mr. Ojaroudi is a member of the IEEE Transaction on Antennas and Propagation (APS) reviewer group and the Applied Computational Electromagnetic Society (ACES). From 2013 he is a student member of the IEEE. His research interests include analysis and design of microstrip antennas, design and modeling of microwave structures, radar systems, and electromagnetic theory. He is author and coauthor of more than 100 journal and international conferences papers. His papers have more than 400 citations with 10 h-index.

Noradin Ghadimi was born in ardabil-Iran in 1985, and received the B.Sc. degree in Electrical Engineering from the Islamic Azad University, Ardabil Branch, Ardabil, Iran, in 2009 and the M.Sc. degree in Electrical Engineering from the Islamic Azad University Ahar Branch, Ahar, Iran , in 2011. His research interests include power system protection, modeling and analysis of distributed generations, renewable energy and communications systems.

A Planar UWB Monopole Antenna with On-Ground Slot Band-Notch Performance

M. Mirmozafari [1], Ch. Ghobadi [1], H. Mirhedayati [2], and A. Rezaee[3]

[1] Department of Electrical Engineering
University of Urmia, Urmia, Iran
m.mirmozafari@yahoo.com and ch.ghobadi@urmia.ac.ir

[2] Department of Electrical and computer Engineering
Shahid Beheshti University, Tehran, Iran
Mirhedayati@gmail.com

[3] Department of Mechatronics Engineering, Faculty of New Sciences and Technologies
University of Tehran, Tehran, Iran
arrezaee@yahoo.com

Abstract **─** A planar monopole antenna with variable frequency band-notch characteristic for ultra wideband applications is presented. The proposed antenna consists of a truncated ground plane and a radiating rectangular patch. By employing two L-shaped strips on the top edge of the ground plane, the ultra wideband property is achieved. Electromagnetic interference (EMI) from IEEE 802.11a can be avoided for a wideband antenna with a stop-band. For a notched frequency band, two L-shaped slits are embedded on the ground plane. The designed antenna has a stop-band of 5 GHz to 5.9 GHz while maintaining wideband performance from 3.1 GHz to 10.6 GHz for VSWR < 2.

Index Terms **─** Band-notched, slot, slit, and ultra wideband.

I. INTRODUCTION

In the last few years, UWB technology has attracted a great interest for use in the industry and academia especially since Federal Communication Commission (FCC) allowed using the (3.1 GHz ─ 10.6 GHz) band for commercial applications. The antenna is one of the important components in UWB systems and it affects their overall performance. It is of a particular interest to design an antenna with simple structure, low profile, easy manufacturing, and low cost. Moreover, the UWB antenna should have good impedance matching characteristics over the whole UWB frequency range. Also, it should have a flat gain, linear phase, and constant group delay to minimize distortion of transmitted pulses waveforms. Different types of planar wideband monopoles using various bandwidth enhancement techniques have been proposed for UWB applications [1-8]. However, there exist narrow band for other communication systems over the designated frequency band, such as: the wireless local area network (WLAN) for IEEE802.11a operating at 5.15 GHz ─ 5.35 GHz, which may cause severe electromagnetic interference to the UWB system. Therefore, it is desirable to design UWB antennas with band-notched performance in this frequency band to avoid potential interference. In this way a number of different techniques have been reported recently [9-12]. The commonly used approach is to insert different shapes of slot in the main radiator [9-10]. In reference [11] it is shown that parasitic elements can be utilized to implement the desired band-rejection at a particular frequency and by embedding a slit in the feeding strip band-notched performance was achieved [12]. For most of the work mentioned above, the band-notched structures are designed on the main radiator. It is demonstrated in [13] by inserting simple slits in antenna ground plane, a band-notched performance can also be achieved.

Submitted On: May 12, 2012
Accepted On: Aug. 10, 2013

The main idea in this article is the deviation of the current on the ground plane. Instead of changing the patch or the feed line shapes, by using two L-shaped strips on the ground plane, a pair of additional current paths are introduced and much wider bandwidth is produced. Also the notched band, covering the 5 GHz ─ 5.9 GHz WLAN band, is provided by a pair of folded slits inserted on the ground plane. As a different method we apply both slits and slots on the ground plane that provides a simple structure. In comparison with previous works the proposed antenna has a small size and simple structure. In this study, antenna design is experimentally investigated; its characteristics and radiation patterns are analyzed and discussed. By adopting different source signals, the influence of the frequency notch as well as the antenna's propagation characteristics is clearly presented giving the reader a thorough understanding about the antenna performance.

II. ANTENNA CONFIGURATION

Figure 1 shows the geometry of the proposed antenna, which is symmetrical with respect to the longitudinal direction. It consists of a main patch and a conductor truncated ground plane in the back, a pair of folded strips, and a pair of L-shaped slits on the ground plane. The L-shaped strip with width of 0.4 mm is printed on the top edge of the ground plane at a distance of 0.93 mm (= 0.5 W_F) from the feed line. It consists of a vertical arm of length L_Y and a horizontal arm of length L_X. In this study the length L_Y of the strip is fixed at 1.2 mm. The L-shaped slits are embedded on the ground plane at a distance of 3.2 mm from the feed line. The proposed slits comprise of a vertical arm (along y-axis) of length L_V and a horizontal arm (along x-axis) of length L_H connected at their ends, where the two arms are of the same width (g). In this study L_V is fixed at 0.4 mm.

The antenna is fed with a 50 Ω microstrip line and is printed on a 22 × 22 mm^2 FR4 substrate with dielectric constant of 4.4 and substrate thickness of 1 mm. The rectangular patch with size of 10 × 13 mm^2 is attached to a feed line of width (W_F = 1.86 mm) and length 7.5 mm on the front surface of the substrate. A conducting ground plane with size of 22 × 4.5 mm^2 is also printed on the other side of the substrate. The gap distance between the radiating patch and ground plane is fixed at 3 mm.

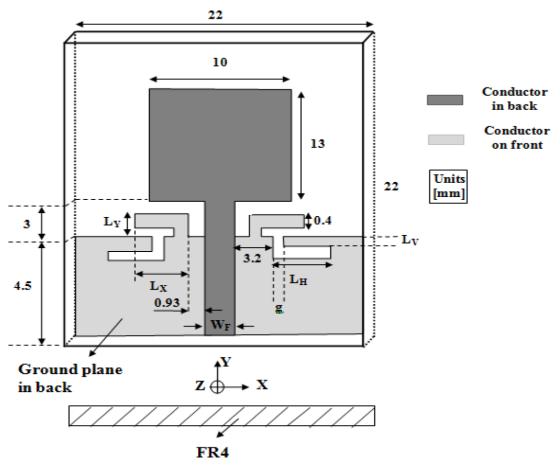

Fig. 1. Geometry of the proposed antenna.

III. RESULTS AND DISCUSSIONS

The proposed antenna is designed using Ansoft's HFSS and its simulated results in terms of bandwidth are presented and compared with that of the measured ones. As mentioned, the main idea in the design of this antenna is the deviation of the current path on the ground plane. By inserting two L-shaped strips a pair of current paths are presented that influence current distribution on the ground plane. The proposed folded strips served as an impedance-matching circuit at higher frequencies and an additional coupling is introduced between the lower edge of the rectangular patch and the folded strips [14].

In order to have a good insight, Fig. 2 shows the difference of current distributions on the ground plane with and without the strips. By adjusting the length L_X the strip, the third resonance occurs at f_t and much more enhanced impedance bandwidth can be achieved. As shown in Fig. 3 by fine-adjusting from experiments for the desired center frequency at 10 GHz, the dimensions of the folded strip are selected. The figure shows as L_X increases, the upper frequency limit is shifted downward. It can be observed that, by fine-adjusting L_X, the antenna bandwidth increases leading to the third resonance. On the other hand, the lower edge frequency of the band is insensitive to the changes of L_X.

To achieve the band-notched characteristic, the lengths of both slits are close to λ/4 at the desired center frequency of the rejection. Regarding the defected ground structure (DGS), the creating slits on the ground plane provide an additional current path, which greatly increases the small VSWR observed at the λ/4 mode for the antenna without slits. The successful excitation of the λ/4 mode is mainly due to the length L of the slit, $L = L_V + L_H$. The center frequency of the stop-band f_r is varied by adjusting the length of L_H. In Fig. 4 the simulated VSWR curves for different values of L_H are considered. As illustrated, with an increase in the length L_H of the slit from 5.2 mm to 7.2 mm, the center frequency of the rejection shifts downward from 7.2 GHz to 5.5 GHz.

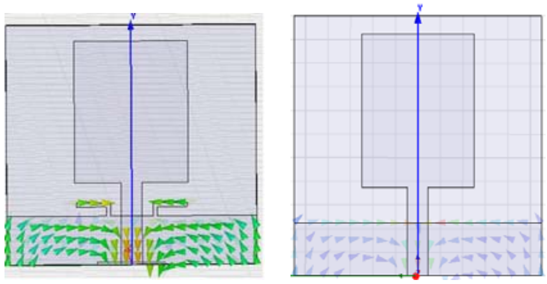

(a) (b)

Fig. 2. Current distribution on the ground at 10 GHz; (a) with and (b) without strips.

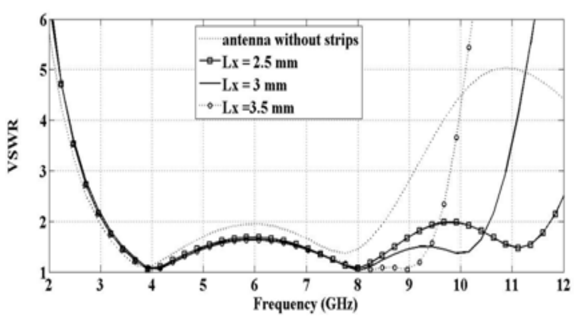

Fig. 3. Simulated VSWR characteristics for different values of L_X (L_Y = 1.2 mm).

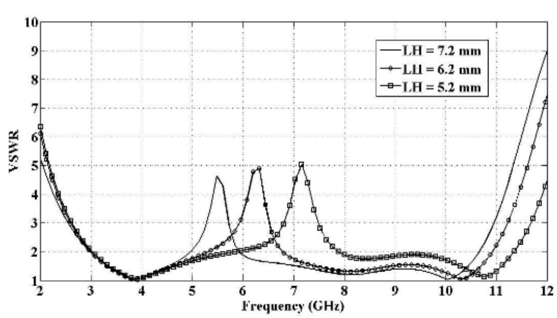

Fig. 4. Simulated VSWR characteristics for different values of L_H (g = 0.2 mm).

The notched center frequency f_r can be empirically approximated. To provide desired bandwidth of the rejection at f_r, the width of the slit, "g", is an important parameter. By carefully adjusting this parameter suitable band-notch width can be obtained. The band-rejection characteristics of the proposed antenna influenced by the "g" size are investigated in Fig. 5 (L_H = 7.2 mm). It is observed that the bandwidth of the rejection increases monotonically with an increase in "g". The antenna has been fabricated and its photo is shown in Fig. 6. The measured results for the fabricated prototype of the proposed antenna based on the optimized simulated design parameters are presented. Figure 7 shows the measured and simulated VSWR curve for the fabricated antenna.

The measured far-field radiation patterns of the proposed antenna in the x-z and y-z planes at sampling frequencies 3.5 GHz and 9.5 GHz are investigated in Figs. 8 (a) and (b). The proposed antenna has relatively omni-directional radiation pattern in the x-z plane (H-plane) at these frequencies. For comparison, the measured antennas gain in the y-z plane at θ = 180˚, for the two antennas (with and without slits) is presented in Fig. 9. As expected, the gain decreases sharply at the notched frequency band for the antenna with slits respect to the same antenna without them.

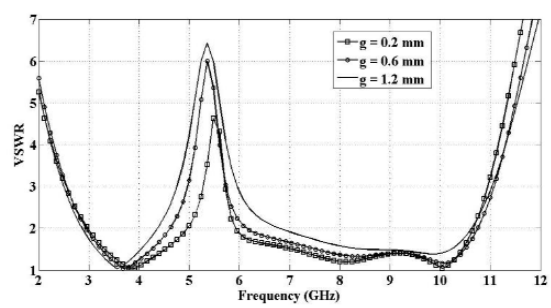

Fig. 5. Simulated VSWR characteristics for different values of g (L_H = 7.2 mm).

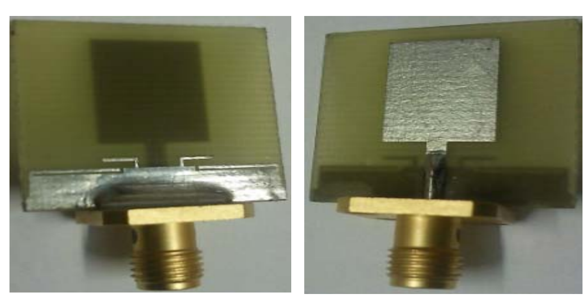

Fig. 6. Photographs of the manufactured antenna.

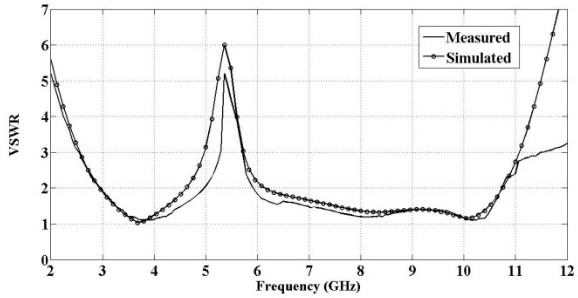

Fig. 7. Simuated and measured VSWR characteristics for the fabricated antenna.

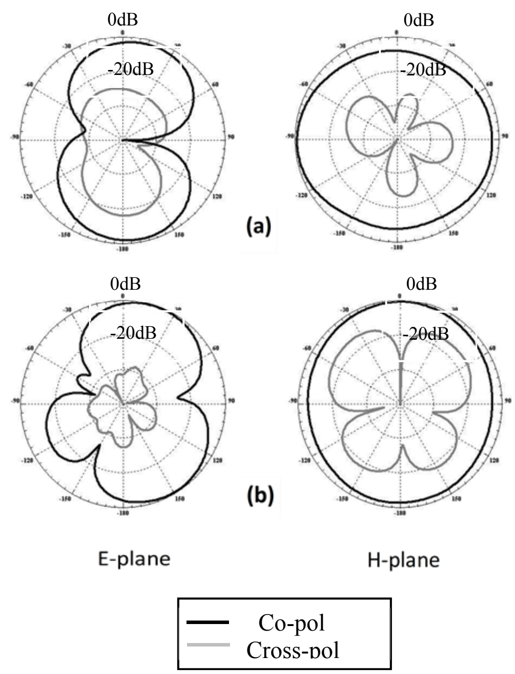

Fig. 8. Measured E-plane and H-plane radiation patterns for the proposed antenna at (a) 3.5 GHz and (b) 9.5 GHz.

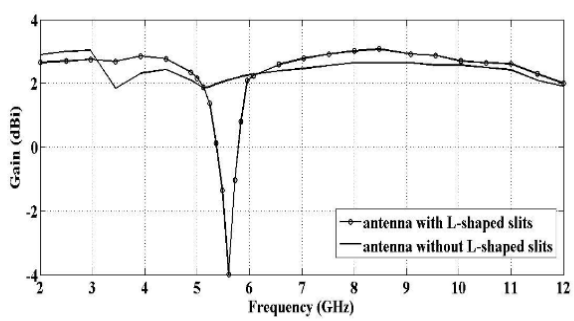

Fig. 9. Measured antennas gain (with and without L-shaped slits).

IV. TIME DOMAIN PERFORMANCE

In ultra wideband systems, the information is transmitted using short pulses. Hence, the temporal behavior of the transmitted pulse is important. The communication system for UWB pulse transmission must provide as minimum as possible distortion, spreading, and disturbance. Here different input signals are introduced to fully examine the influence of the frequency notch as well as the antenna abilities in transceiving signals. In our communication setup, two identical antennas have been used that were aligned side-by-side at a distance of 50 cm (antennas are in the far field of the each other). Two bipolar signals with different waveform widths were employed (Figs. 10 (a) and (b)). Since the antennas have a notch from 5 GHz ─ 6 GHz, considerable spectral information loss is expected to take place when transmitting the 170 ps bipolar signal. Figures 11 (a) and (b) present the received transient responses for the 170 ps and 280 ps bipolar signals, respectively. It is seen that the detected signal for the 170 ps bipolar pulse is quite weak and suffers distinct distortion. Compared with the 170 ps pulse, the received signal for the 280 ps pulse has larger magnitude and undergoes less distortion. The observed late time ringing is caused by the frequency notch.

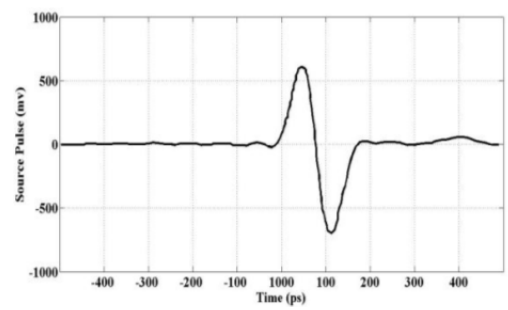

(a)

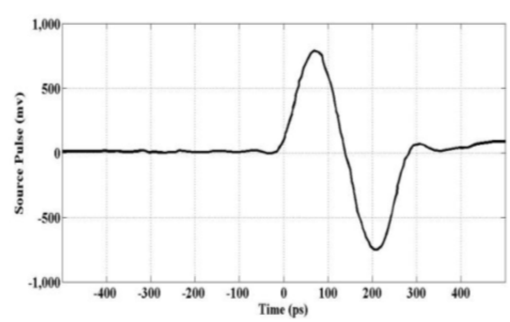

(b)

Fig. 10. Input bipolar signals for (a) 170 ps and (b) 280 ps.

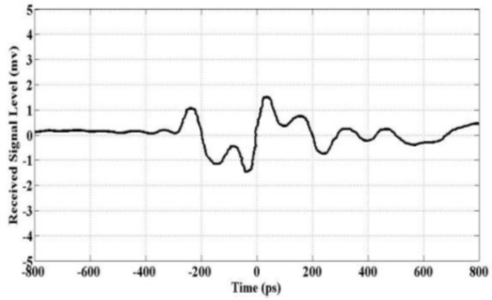

(a)

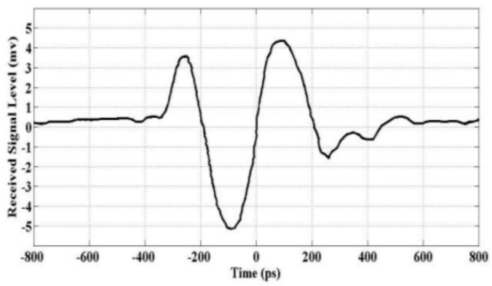

(b)

Fig. 11. Output signal waveforms for (a) 170 ps and (b) 280 ps input pulses.

To examine the time-domain performance of the antenna, Gaussian pulses are selected to be the source waveforms and applied to the proposed antenna. The time domain characteristics of the proposed antenna are studied using CST Microwave Studio and presented in Fig. 12. the correlation between the transmitting antenna's input signal and the receiving antenna's output signal shows approximately 83 % antipodal resemblance that is clearly acceptable among the other UWB antennas. So it can preserve signal shape by a little distortion that makes it suitable for UWB applications.

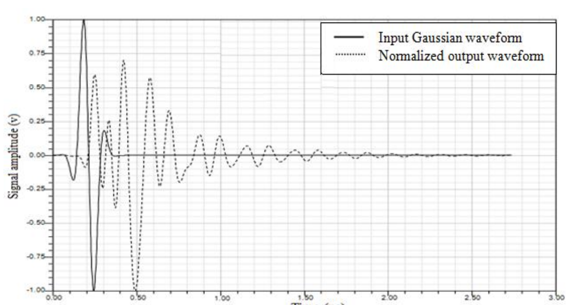

Fig. 12. Simulated time domain analysis: input and output pulse waveforms.

V. CONCLUSION

A printed monopole antenna with controllable band-notched configuration for ultra wideband applications is presented. A pair of L-shaped strips is used to satisfy the desired characteristics of the antenna. By embedding a pair of L-shaped slits on the ground plane, the frequency band-stop performance is achieved. The designed antenna has a stop-band of 5 GHz to 5.9 GHz while maintaining wideband performance from 3.1 GHz to 10.6 GHz for VSWR < 2. The antenna is fabricated and tested. A good agreement is achieved between the simulated and measured results.

REFERENCES

[1] M. Mighani, M. Akbari, and N. Felegari, "A CPW dual band notched UWB antenna," *Applied Computational Electromagnetics Society (ACES) Journal*, vol. 27, no. 4, pp. 352-359, April 2012.

[2] R. Azim, M. T. Islam, and N. Misran, "Design of a planar UWB antenna with new band enhancement technique," *Applied Computational Electromagnetics Society (ACES) Journal*, vol. 26, no. 10, pp. 856-862, October 2011.

[3] J. William and R. Nakkeeran, "A new UWB slot antenna with rejection of WiMax and WLAN bands," *Applied Computational Electromagnetics Society (ACES) Journal*, vol. 25, no. 9, pp. 787-793, September 2010.

[4] D. S. Javan and O. H. Ghouchani, "Cross slot antenna with U-shaped tuning stub for ultra wideband applications," *Applied Computational Electromagnetics Society (ACES) Journal*, vol. 24, no. 4, pp. 427-432, August 2009.

[5] H. Jalali, Ch. Ghobadi, and J. Nourinia, "A novel ultra wideband monopole antenna with band-stop characteristic," *Wireless Engineering and Technology*, vol. 2, pp. 235-239, 2011.

[6] Q. X. Chu and Y. Y. Yang, "A compact ultra wideband antenna with 3.4/5.5 GHz dual band-notched characteristics," *IEEE Transactions on Antennas and Propagation*, vol. 56, pp. 3637-3644, 2008.

[7] D. Chen and C.-H. Cheng, "A novel compact ultra-wideband (UWB) wide slot antenna with via holes," *Progress In Electromagnetics Research*, vol. 94, pp. 343-349, 2009.

[8] R. Danesfahani, L. Asadpor, and S. Soltani, "A small UWB CPW-fed monopole antenna with variable notched bandwidth," *Journal of Electromagnetic Waves and Applications*, vol. 23, pp. 1067-1076, 2009.

[9] R. Fallahi, A. A. Kalteh, and M. G. Roozbahani, “A novel UWB elliptical slot antenna with band-notched characteristics,” *Progress In Electromagnetics Research*, vol. 82, pp. 127-136, 2008.
[10] A. M. Abbosh, M. E. Bialkowski, J. Mazierska, and M. V. Jacob, “A planar UWB antenna with signal rejection capability in the 4–6 GHz band,” *IEEE Microwave Wireless and Component Letters*, vol. 16, pp. 278-280, 2006.
[11] L. Peng, C. -L. Ruan, Y. -L. Chen, and G. -M. Zhang, “A novel band-notched elliptical ring monopole antenna with a coplanar parasitic elliptical patch for UWB applications,” *Journal of Electromagnetic Waves and Applications*, vol. 22, pp. 517-528, 2008.
[12] L. N. Zhang, S. S. Zhong, C. Z. Du, and J. H. Chen, “Compact UWB planar monopole antenna with band-notch function,” *Microwave Optical and Technology Letters*, vol. 51, pp.1908-1911 2009.
[13] J. Jung, H. Lee, and Y. Lim, “Compact band-notched ultra wideband antenna,” *Electronics Letters*, vol. 44, pp. 391–392, 2008.
[14] R. Eshtiaghi, J. Nourinia and Ch. Ghobadi, “Electromagnetically coupled band-notched elliptical monopole antenna for UWB applications,” *IEEE Transactions on Antennas and Propagation*, vol. 58, pp. 1397-1402, 2010.

Mirhamed Mirmozafari received the M.Sc. degree in Telecommunication Engineering from the University of Urmia, Iran in 2011. He participated in many projects inside and outside the university between 2009 and 2012. He is author of many papers concerning UWB antennas, Dual-band antennas, MEMS and EMC problems.

Changiz Ghobadi received his B.Sc. degree in Electrical Engineering-Electronic and M.Sc. degree in Electrical Engineering-Telecommunication from Isfahan University of Technology, Isfahan, Iran. He received Ph.D. degree in Electrical-Telecommunication from University of Bath, Bath, UK in 1998. From 1998 he was an assistant professor and now he is an associated professor in the Department of Electrical Engineering of Urmia University, Urmia, Iran. His primary research interests are in antenna design, radar and adaptive filters.

Habib Mirhedayati received his B.Sc. in Telecommunication Engineering from Shahid Beheshti University. His research interests include microwave, millimeter-wave circuit design and power line communication.

Alireza Rezaee received his B.Sc. degree in Control Engineering from Sharif University of Technology, Iran 2002 and M.Sc. and Ph.D. degrees in Electrical Engineering from Amirkabir University of Technology, Iran (2005 and 2011, respectively). From 2013 till now he is an Assistance Professor in the Department of Mechatronics Engineering in new sciences and technologies faculty at Tehran University. His research interests are in intelligent robotics, mobile robot navigation, machine learning, Bayesian networks and cognitive science.

Compact Dual Band-Reject Monopole Antenna for UWB Applications

Ping Wang

College of Electronic and Information Engineering, Chongqing Three Gorges University, Chongqing 404000, China
wangpingcqz@163.com

***Abstract* ─** In this letter, a compact planar ultra-wideband (UWB) monopole antenna with excellent band-rejection characteristics is proposed for UWB communications applications. To achieve band-rejection filter property at the WiFi / WiMAX bands, two different types of slots: sloped open-ended Z-shaped slot and split rectangle ring slot on radiation patch, are introduced to form two stop-bands. The measured and simulated results show that the band-notched characteristics not only bring good rejection frequency, but also improved the skirt area in the band-notched frequency, and the proposed antenna has nearly omni-directional radiation pattern, moderate gain, and low cross-polarization level, which is suitable for UWB communication applications.

***Index Terms* -** Coplanar waveguide (CPW) feeding, dual notched bands, open-ended Z-shaped slot, split rectangle ring slot, and ultra-wideband (UWB) antenna.

I. INTRODUCTION

It is a well-known fact that monopole antennas have been a highly competitive topic in wireless communication systems in recent years, since they have many attractive advantages, such as simple structure, low profile, light weight, small size, easy fabrication, omni-directional radiation pattern, and so on. On the other hand, coplanar waveguide (CPW)-fed mechanism has many irreplaceable advantages over microstrip-fed manner [1], such as low dispersion, lower loss, the ability to effectively eliminate the alignment errors, and the antenna can be printed on a single side of the printed circuit board for alleviating the problem of space restrictions in a device, thus it often is introduced to design ultra-wideband (UWB) monopole antennas [1-7], which operate in the United States federal communication commission (FCC) frequency defined from 3.1 GHz to 10.6 GHz for high data rate and short range ultra-wideband communication systems [8].

However, it is generally known that UWB transmitters should not cause any electromagnetic interference on nearly communication system, such as the existing wireless local area network (WLAN) and the worldwide interoperability for microwave access (WiMAX) covering the 3.3 GHz - 3.7 GHz, 5.15 GHz - 5.35 GHz, and 5.725 GHz - 5.825 GHz. Therefore, UWB antenna with notched characteristics in these frequency bands is desired. Recently, various methods were reported to design band-notched antenna. The universal method is cutting slots on the radiation patch or ground plane, i.e., slot-type split ring resonators (SRRs), W-shaped slots, semicircular slots, L-shaped slots, U/C-shaped slots, E-shaped slot, H-shaped slot in [3, 9-16], and so on. Others main approaches are the use of parasitic elements [17-19], quarter-wavelength stub connected to radiation patch [19, 20] or ground plane [21] by metallic vias on the opposing plane, and electromagnetic-band-gap (EBG) structures [22]. However, most of the antennas mentioned above can not provide satisfactory skirt area and sufficient rejection bandwidth, which reveals that lower performance of potential interference suppression from skirt bands may still exist in such antennas.

In this work, a novel design of UWB monopole antenna is designed, which presents

Submitted On: July 10, 2012
Accepted On: Aug. 29, 2013

desired band-rejection features by embedding two different types of resonant slots. Experimental results demonstrate that the proposed antenna have very sharp, fully wide, and deep band-notched characteristics.

II. ANTENNA CONFIGURATION

The geometrical configuration of the proposed UWB band-rejected antenna is shown in Fig. 1. The antenna has a single-layer metallic structure and is printed on an inexpensive FR-4 substrate of thickness 0.8 mm, with a dielectric constant of 4.6 and a loss tangent of 0.02. A 50 Ω CPW transmission line of strip width 2.1 mm, and gap 0.3 mm is used for feeding the antenna. The overall dimension of the antenna is only 30 mm (L) × 25 mm (w). The radiation patch is composed of a trapezoid patch and a rectangle patch, and then loaded by arbitrary hexagon-shaped slot on the edge of the radiating patch. The ground plane is modified by truncating two triangle-shaped patches in both sides of the ground plane. To achieve notched bands, a pair of sloped open-ended Z-shaped slots and two split rectangle ring slots on the radiating patch are adopted to generate two notched bands in the center frequency of 3.5 GHz and 5.5 GHz, respectively. In this design, the Z-shaped slots (ZSS) act as a quarter-guided-wavelength resonator, which the length may be empirically approximated by,

$$L_{ZSS} = n_2 + n_3 + n_4 = \lambda/4 . \quad (1)$$

The split rectangle ring slot (SRRS) is a half-guided-wavelength resonator, and can be deduced by

$$L_{SRRS} = 2(d_1 + d_2) + d_3 = \lambda/2, \quad (2)$$

where $\lambda = c \Big/ f\sqrt{\frac{\varepsilon_r + 1}{2}}$, c is the speed of light in free space, ε_r is the dielectric constant, and f is the center notched frequency. At the beginning of the design, and by using equations (1) and (2), one may estimate the notched dimensions of the sloped Z-shaped slots and split rectangle ring slot approximately. Moreover, by adjusting the width and length of the slots, the stop-band property of the antenna can be controlled desirably. The proper parameters can be obtained with the aid of the commercially available software Ansoft HFSS13 (high-frequency structure simulator), and a 50 Ω-SMA connector is connected to the end of the CPW-feed mechanism, which serves as the antenna port. Parameter values of the proposed antenna are summarized in Table I. Moreover, a photograph of the fabricated antenna with dual-band notched characteristic is shown in Fig. 1 (b).

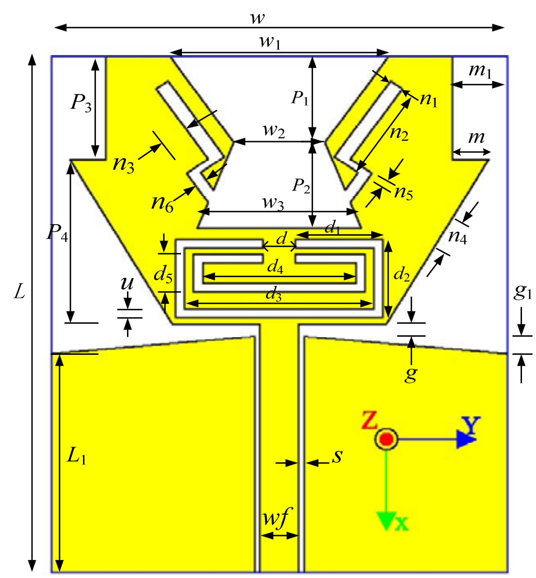

(a)

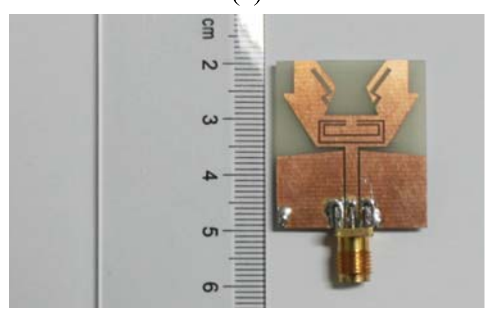

(b)

Fig. 1. (a) Geometry of the proposed antenna and (b) photograph of the proposed antenna.

Table I: Parameter values of the fabricated antenna (dimensions are in mm).

Parameter	*u*	*L1*	*w1*	*w2*	*w3*	*wf*
Value	0.3	12.7	12	5	9	2.1
Parameter	P_1	P_2	P_3	P_4	g	g_1
Value	5	5	6	9.6	0.7	1
Parameter	d	d_1	d_2	d_3	d_4	d_5
Value	1.8	4.6	4.15	10.4	8.8	2.2
Parameter	n_1	n_2	n_3	n_4	n_5	n_6
Value	0.8	5.4	1.45	2.06	0.4	0.65
Parameter	s	m	m1			
Value	0.3	1.98	3			

III. RESULTS AND DISCUSSIONS

A. Compact UWB Planar antenna with single notched slot

To further comprehend the band-rejection characteristic, a Z-shaped slot or rectangle split ring slot is embedded in the radiation patch as shown in Figs. 2 (a) and (b), respectively. At the notch frequency, the current flows are more dominant around the filter structures, and are concentrated on the edges of these slots with opposite direction. Therefore, the resultant radiation fields cancel out, and high attenuation near the notch frequency is produced. Namely, the antenna does not radiate efficiently in the notched frequency ranges. It is also seen that unlike Fig. 2 (b), in Fig. 2 (a) the main current not only flows around the Z-shaped slot, but also a small quantity of currents appear in CPW, which show that rectangle split ring slot have better band-rejection character than open-ended slot.

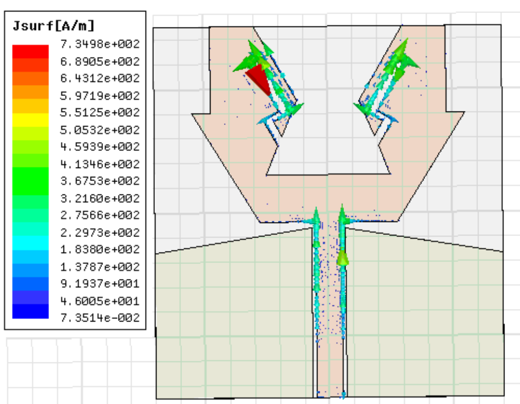

(a)

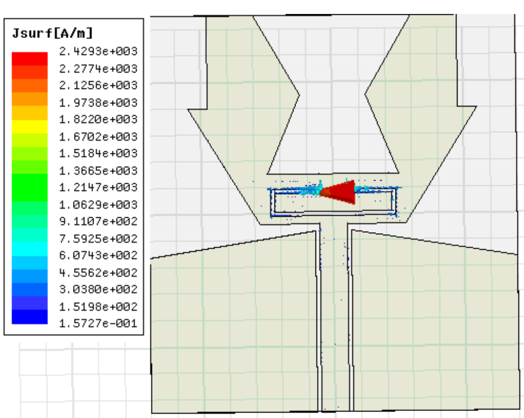

(b)

Fig. 2. Current distributions at the notched frequency.

Figure 3 shows the simulated filter characteristic with single notched slot. The figure clarifies that the maximum values of the reflection coefficient curve in the Z-shaped slot filter frequency band is closer to the high edge band-rejection frequency, which is in contrast to the low edge band-rejection frequency. Nevertheless, the split ring slot filter mechanism has opposite property. It is shown that the Z-shaped slot filter mechanism may control the high edge band-notched frequency. The spilt ring slot notched mechanism may master the low edge notched frequency, which lead to improve the skirt area in the band-notched frequency.

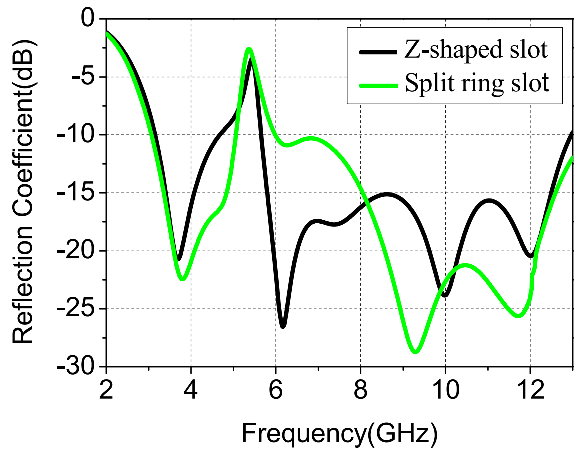

Fig. 3. Simulated reflection coefficient of a single notched slot.

B. Compact UWB planar antenna with united notched frequency characteristics

The proposed antenna was implemented and tested using an Agilent N5230A series vector network analyzer. Figure 4 shows the simulated and measured reflection coefficient against frequency for the proposed united dual band-notched antenna, which shows good agreement. There exists a discrepancy between the simulated results and the measured data owing to the error of the substrate parameters of the FR-4 substrate and the tolerance in manufacturing [22]. The simulated notched frequency bandwidth of the proposed antenna is achieved from 3.34 GHz to 3.74 GHz and 5.15 GHz to 5.9 GHz, and the measured stop-band frequency ranges are from 3.35 GHz - 3.72 GHz and 5.17 GHz - 6.14 GHz for S11 > -10dB with maximum reflection coefficient of -2.47 dB.

Obviously, the achieved notched bandwidths can suppress dispensable WLAN/WiMAX bands for UWB applications completely. Table II presents performance comparison with other works [5, 10, 15, 17], which shows that the proposed antenna not only has small size, but also good band-reject characteristics.

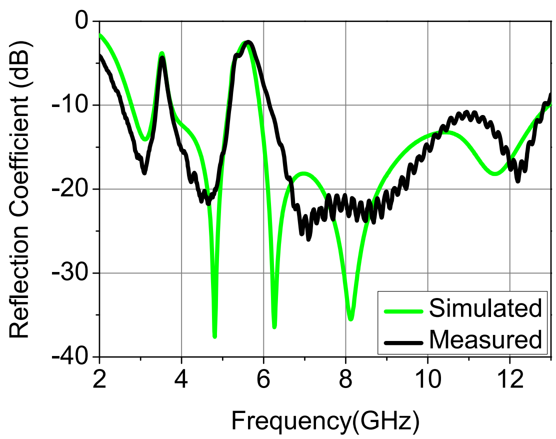

Fig. 4. Simulated and measured reflection coefficient of the proposed antenna.

Table II: Performance comparison.

Works	ε_r	Dimensions (mm^3)	Notched band ranges (GHz) (<-10dB)
Ref.[5]	4.4	21×28×1.6	3.2-3.8 and 5.1-5.9
Ref.[10]	4.4	20×30×1.5	3.4-3.8 and 4.8-6.2
Ref.[15]	2.65	14×35×0.8	3.49-4.12 and 5.66-6.43
Ref.[17]	4.4	30×35×1.6	5.12-6.08
This paper	4.4	30×25×0.8	3.35-3.72 and 5.17-6.14

Radiation characteristics are also considered. To examine the design validity, a comparison in the radiation pattern, in the *xz*- and *yz*-planes for both E_Φ and E_θ at 4 GHz, 8 GHz, and 10 GHz, by using the simulator HFSS and time-domain finite integration technique (CST Microwave Studio) is shown in Fig. 5, which shows very good agreement. From the results, it demonstrates that all the operating frequencies have the same polarization plane, similar radiation patterns, and very small cross-polarization levels throughout the UWB range of frequencies (less than -20 dB). The radiation pattern is found to be figure of eight shape along the *xz*-plane and nearly omni-directional pattern in the *yz*-plane. It is observed that at the *yz*-plane radiation pattern of the antenna shows relatively larger cross-polarization level than that at the *xz*-plane. This behavior is largely due to the strong horizontal components of the surface current and electric field. Because the vertical component of the surface current is the main contribution to the co-polarization radiation and the horizontal component contributes to the cross-polarization radiation.

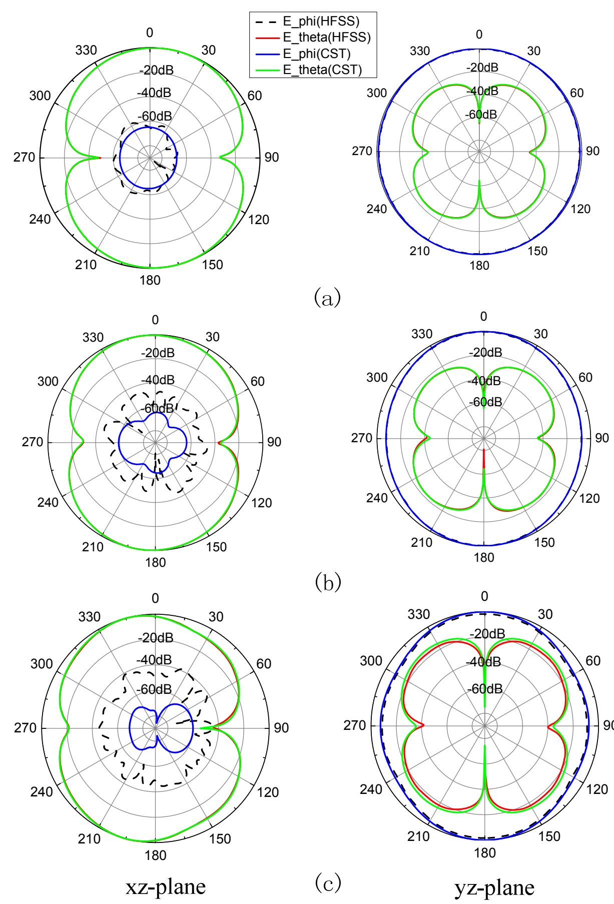

Fig. 5. Radiation patterns for the proposed antenna at (a) 4 GHz, (b) 8 GHz, and (c) 10 GHz in the *xz*- and *yz*-planes, respectively.

For the sake of further describing excellent filter performance, the simulated peak gain for the proposed antenna from 2 GHz to 13 GHz is presented in Fig. 6. As expected, the gain decreases sharply at the notched frequency bands for the antenna with band-notched filter and the band-notched characteristic is improved in the shirt area of the notched frequency. The simulated radiation efficiency is also provided in Fig. 7 and varies from 78.5 % to 94 % in the operating bands. Whereas it is low as 19.5 % and 20 %, within the band-rejection frequency (3.3 GHz - 3.7 GHz, 5.15 GHz - 5.85 GHz, respectively).

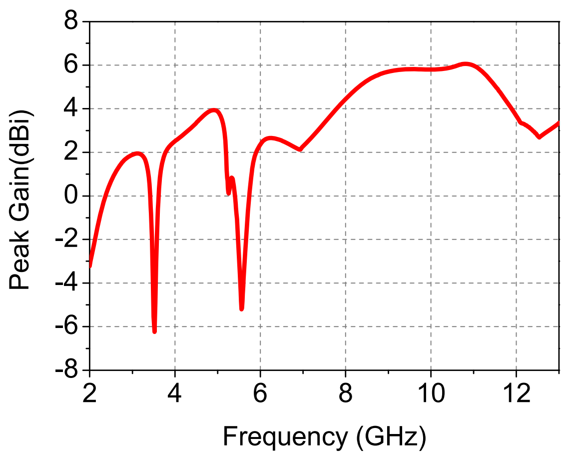

Fig. 6. Simulated gain curve of the proposed band-notched antenna.

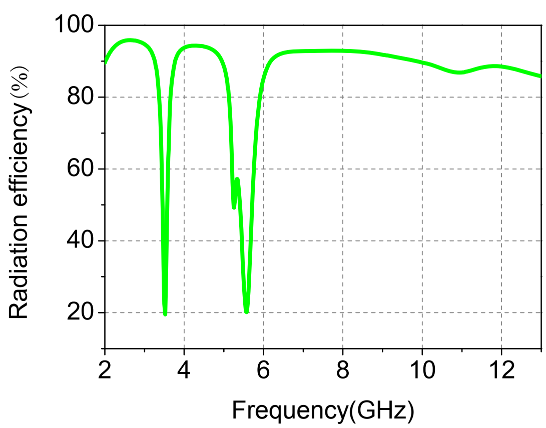

Fig. 7. Simulated radiation efficiency of the proposed band-notched antenna.

IV. CONCLUSION

In this paper, a novel planar UWB monopole antenna with excellent band-rejected characteristics is achieved by embedding two different types of slots on the radiating patch, i.e., sloped open-ended Z-shaped slot and split rectangle ring slot. The measured results show that the notched frequency of the proposed antenna has very sharp form, fully wide, and deep band-notched characteristics. This antenna also presents good omni-direction pattern in the entire UWB frequency, and keeps a stable gain and high radiation efficiency in the UWB frequency ranges expect for the notched frequency ranges. Furthermore, the proposed antenna exhibits compact and small dimensions of 30 × 25mm^2. These features make it a good candidate for ultra-wideband wireless applications.

ACKNOWLEDGMENT

This work is supported by Chongqing University Innovation Team Founding under Grant No. KJTD201320.

REFERENCES

[1] C. Deng, Y. J. Xie, and P. Li, “CPW-fed planar printed monopole antenna with impedance bandwidth enhanced,” *IEEE Antenna Wireless Propag. Lett.*, vol. 8, pp. 1394-1397, 2009.

[2] W. C. Weng, “Optimal design of an ultra-wideband antenna with the irregular shape on radiator using particle swarm optimization,” *Applied Computational Electromagnetics Society (ACES) Journal*, vol. 27, no. 5, pp. 427-434, May 2012.

[3] Y. Zhang, W. Hong, C. Yu, Z.-Q. Kuai, Y.-D. Dong, and J.-Y. Zhou, “Planar ultra-wideband antennas with multiple notched bands based on etched slots on the patch and/or split ring resonators on the feed line,” *IEEE Trans. Antennas Propag.*, vol. 56, no. 9, pp. 3063-3068, 2008.

[4] P. Wang, G. J. Wen, and H. Y. Jin, “A compact cross-shaped slot antenna with a coplanar waveguide fed rotated patch for UWB applications,” *Frequency Journal of RF-Engineering and Telecommunications*, vol. 66, no. 7, pp. 171-175, July 2012.

[5] J. William and R. Nakkeeran, “A new UWB slot antenna with rejection of WiMAX and WLAN bands,” *Applied Computational Electromagnetics Society (ACES) Journal*, vol. 25, no. 9, pp. 787-793, Sep. 2010.

[6] M. Mighani, M. Akbari, and N. Felegari, “A CPW dual band notched UWB antenna,” *Applied Computational Electromagnetics Society (ACES) Journal*, vol. 27, no. 4, pp. 352-359, April 2012.

[7] Y. S. Li, W. X. Li, and W. H. Yu, “A switchable

UWB slot antenna using SIS-HSIR and SIS-SIR for multi-mode wireless communications applications," *Applied Computational Electromagnetics Society (ACES) Journal*, vol. 27, no. 4, pp. 340-351, April 2012.

[8] Federal communications commission, First report and order, Revision of Part 15 of commission's rule regarding UWB transmission system FCC 02-48, Washington, DC, April 2002.

[9] M.-C. Tang, S. Q. Xiao, T. W. Deng, D. Wang, J. Guan, B. Z. Wang, and G. D. Ge, "Compact UWB antenna with multiple band-notches for WiMAX and WLAN," *IEEE Trans. Antennas Propag.*, vol. 59, no. 4, pp. 1372-1376, 2011.

[10] L. Y. Cai, Y. Li, G. Zeng, and H. C. Yang, "Compact wideband antenna with double-fed structure having band-notched characteristics," *Electron. Lett.*, vol. 46, no. 23, pp. 1534-1536, 2010.

[11] N. D. Trang, D. H. Lee, and H. C. Park, "Compact printed CPW-fed monopole ultra-wideband antenna with triple sub-band notched characteristics," *Electron. Lett.*, vol. 46, no. 17, pp. 1177-1179, 2010.

[12] K. Shambavi and Z. C. Alex, "Printed dipole antenna with band rejection characteristics for UWB applications," *IEEE Antenna Wireless Propag. Lett.*, vol. 9, pp. 1029-1032, 2010.

[13] Y. S. Li, X. D. Yang, C. Y. Liu, and T. Jiang, "Compact CPW-fed ultra-wideband antenna with dual band-notched characteristics," *Electron. Lett.*, vol. 46, no. 14, pp. 967-968, 2010.

[14] Q. X. Chu and Y. Y. Yang, "A compact ultrawideband antenna with 3.4/5.5GHz dual band-notched characteristics," *IEEE Trans. Antennas Propag.*, vol. 56, no. 12, pp. 3637-3644, 2008.

[15] L. Luo, Z. Cui, J. P. Xiong, X. M. Zhang, and Y. C. Jiao, "Compact printed ultra-wideband monopole antenna with dual band-notch characteristic," *Electron. Lett.*, vol. 44, no. 19, pp. 1106-1107, 2008.

[16] J. Y. Deng, Y. Z. Yin, S. G. Zhou, and Q. Z. Liu, "Compact ultra-wideband antenna with tri-band notched characteristic," *Electron. Lett.*, vol. 44, no. 21, pp. 1231-1233, 2008.

[17] H.-W. Liu, C.-H. Ku, T.-S. Wang, and C.-F. Yang, "Compact monopole antenna with band-notched characteristic for UWB applications," *IEEE Antenna Wireless Propag. Lett.*, vol. 9, pp. 397-400, 2010.

[18] G. M. Zhang, J. S. Hong, B. Z. Wang, and G. B. Song, "Switched band-notched UWB/WLAN monopole antenna," *Applied Computational Electromagnetics Society (ACES) Journal*, vol. 27, no. 3, pp. 256-260, March 2012.

[19] M. Ojaroudi, N. Ojaroudi, and Y. Ebazadeh, "Dual band-notch small square monopole antenna with enhanced bandwidth characterestics for UWB applications," *Applied Computational Electromagnetics Society (ACES) Journal*, vol. 27, no. 5, pp. 420-426, May 2012.

[20] H. Mardani, C. Ghobadi, and J. Nourinia, "A simple compact monopole antenna with variable single- and double-filtering function for UWB applications," *IEEE Antenna Wireless Propag. Lett.*, vol. 9, pp. 1076-1079, 2010.

[21] A. Ghobadi, C.Ghobadi, and J. Nourinia, "A novel band-notched planar monopole antenna for ultrawideband applications," *IEEE Antenna Wireless Propag. Lett.*, vol. 9, pp. 608-611, 2010.

[22] L. Peng and C. L. Ruan, "UWB band-notched monopole antenna design using electromagnetic-bandgap structures," *IEEE Trans. Microw. Theory Tech.*, vol. 59, no. 4, pp. 1074-1081, 2011.

Ping Wang was born in Chongqing, China, in 1981. He received his B.Sc. in physics from Western Chongqing University of China in 2005 and the M.Sc. degree in theoretical physics from Chongqing University, Chongqing, in 2008. Currently, he is working toward the Ph.D. degree in University of Electronic Science and Technology of China (UESTC). Since July 2008, he has been working in College of Electronic and Information Engineering, Chongqing three Gorges University, China. His current research interests include patch antennas, wideband antennas, and arrays, and RF/Microwave components and circuits.

A New Design of Printed Monopole Antenna with Multi-Resonance Characteristics for DCS/WLAN/WiMAX Applications

Nasser Ojaroudi [1], Mohammad Ojaroudi [2], and Noradin Ghadimi [2]

[1] Department of Electrical Engineering,
Germi Branch, Islamic Azad University, Germi, Iran
n.ojaroudi@iaugermi.ac.ir

[2] Young Researchers Club
Ardabil Branch, Islamic Azad University, Ardabil, Iran
m.ojaroudi@iauardabil.ac.ir and noradin.ghadimi@gmail.com

Abstract **─** In this paper, a new printed monopole antenna is presented for simultaneously satisfying DCS, wireless local area network (WLAN) and worldwide interoperability for microwave access (WiMAX) applications. The operating frequencies of the proposed antenna are 1.8 GHz, which covers DCS operations, 2.4/5.2/5.8 GHz for WLAN system and 2.5/3.5/5.5 GHz for WiMAX system. The desired first and second resonant frequencies are obtained by adjusting the length of the L-shaped slits. Also by cutting an inverted Γ-shaped slot in the radiating patch; multi band performance can be produced. Prototypes of the proposed antenna have been constructed and studied experimentally. The measured results show good agreement with the numerical prediction and good multiband operation.

Index Terms **─** L-shaped structure, monopole antenna, and multi-resonance characteristics.

I. INTRODUCTION

The evolution of the mobile communication system has required simple configuration, light and easy integration with monolithic microwave integrated circuits (MMICs) and multiband antennas for the widespread system application. For such reasons, numerous designs of multiple-band microstrip antenna have been developed for DCS applications [1-3]. Also in the last few years, there have been rapid developments WLAN/WiMAX applications, thus there are various antenna designs, which enable antennas with low-profile, lightweight, flush mounted, and WLAN/WiMAX devices. These antennas include the planar inverted-F antennas [4], the chip antennas [5, 6], and the planar slot antennas [7, 8].

In this paper, a compact wideband microstrip-fed monopole antenna is designed to satisfy all the system requirements for DCS1800 (1.71 GHz – 1.88 GHz), DCS1900 (1.85 GHz – 1.99 GHz), WiBro (2.3 GHz – 2.39 GHz), WLAN (2.4 GHz – 2.483 GHz), and WiMAX (2.5 GHz, 3.5 GHz, and 5.5 GHz), simultaneously. By cutting two L-shaped slits in the square radiating patch, we can tune frequency bands for 1.8/2.4/5.2/5.8 GHz. Also by cutting an inverted Γ-shaped in the radiating patch, a new resonance at 3.5 GHz can be created. Details of the antenna design are described, and prototypes of the proposed antenna have been constructed and tested. The size of the designed antenna is smaller than the antennas for DCS/WLAN/WiMAX applications that reported recently [1-8].

II. ANTENNA DESIGN

The current design (Fig. 1) was performed for FR4 substrate of thickness 1.6 mm, permittivity 4.4, and loss tangent 0.018. The antenna comprises a pair of L-shaped slits and an inverted Γ-shaped cut on the square radiating patch. The basic monopole antenna structure consists of a square patch, a feed line, and a ground plane. In this study, two L-shaped slits in the radiating patch are

Submitted On: July 13, 2012
Accepted On: April 24, 2013

used to perturb a new resonance. In the proposed configuration the inverted Γ-shaped is playing an important role in the multi band characteristics of this antenna, because it can creates additional surface current paths in the antenna therefore additional resonance is excited [5, 6].

The optimal dimensions of the designed printed monopole antenna are as follows: W_{sub} = 14 mm, L_{sub} = 22 mm, h_{sub} = 1.6 mm, W = 12 mm, L = 13 mm, W_f = 2 mm, L_f = 3 mm, W_S = 3 mm, L_S = 12 mm, W_{S1} = 6 mm, L_{S1} = 5 mm, W_1 = 7.5 mm, L_1 = 10 mm, W_2 = 6.5 mm, L_2 = 9.25 mm, W_3 = 0.5 mm, and L_{gnd} = 5 mm. It is found that the designed antenna satisfies all the requirements in the desired frequency band.

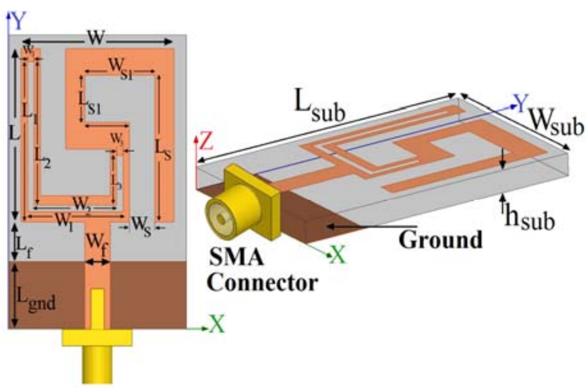

(a) (b)

Fig. 1. Geometry of the proposed antenna, (a) top view and (b) side view.

III. RESULTS AND DISCUSSIONS

In this section, the printed monopole antenna was constructed. Both numerical and experimental results of the input impedance and the radiation characteristics are presented and discussed. The simulated results are obtained using the Ansoft simulation software high-frequency structure simulator (HFSS) [9].

The configuration of the presented monopole antenna was shown in Fig .1. The return loss characteristics for the ordinary square antenna with an L-shaped slit in the radiating patch (Fig. 2 (a)), with two L-shaped slits in the radiating patch (Fig. 2 (b)), and the proposed antenna structure (Fig. 2 (c)) are compared in Fig 3. As shown in Fig. 3, it is observed that the lower frequency bandwidth is affected by using two L-shaped slits and by cutting an inverted Γ-shaped in the radiating patch, a new resonance at 3.5 GHz can be created. Also the input impedance of the proposed antenna, on a Smith chart is shown in Fig. 4.

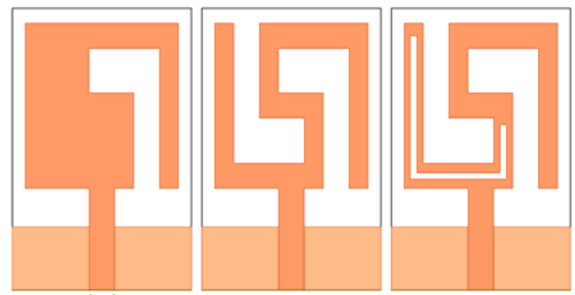

(a) (b) (c)

Fig. 2. (a) The ordinary square antenna with an L-shaped slit in the radiating patch, (b) the antenna with a pair of L-shaped slits in the radiating patch, and (c) the proposed antenna.

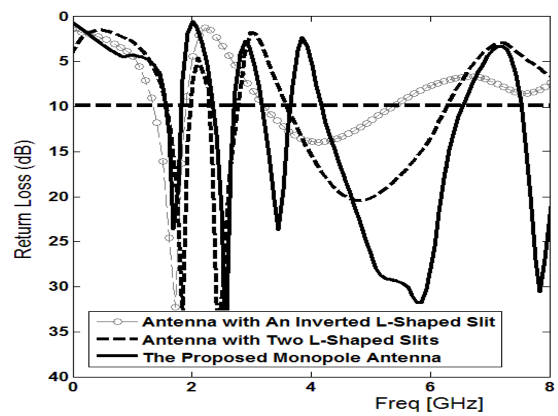

Fig. 3. Simulated return loss characteristics for the antennas shown in Fig. 2.

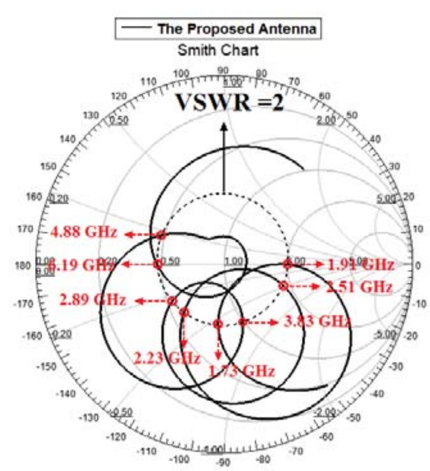

Fig. 4. Smith chart demonstration of the simulated input impedance for various monopole antenna structures, shown in Fig. 2.

Moreover, the input impedance of the proposed antenna, on a Smith chart is shown in Fig. 4. In order to understand the phenomenon behind this multi-resonance performance, the simulated current distributions for various square slot antenna structures shown in Fig. 2, at new resonances frequencies 1.8 GHz, 2.4 GHz, and 3.5 GHz are presented in Fig. 5, respectively.

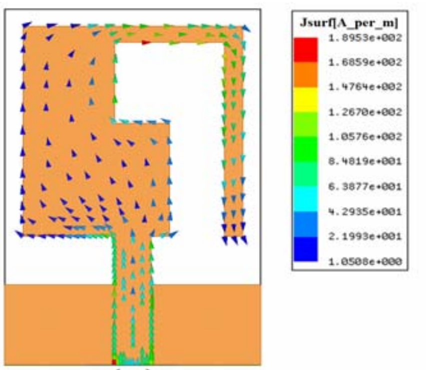

(a)

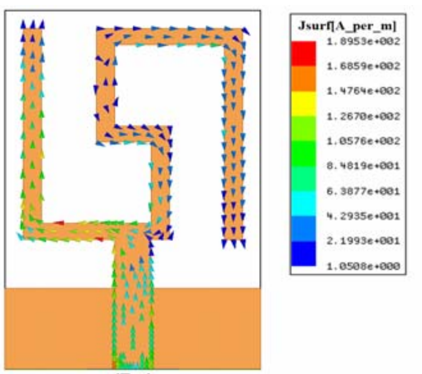

(b)

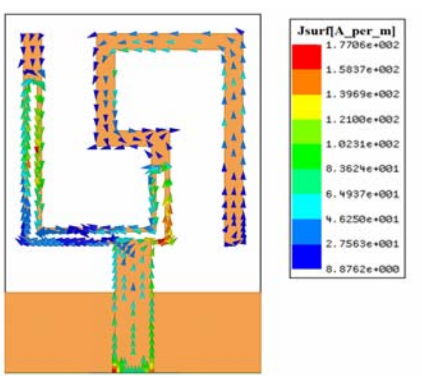

(c)

Fig. 5. Simulated surface current distributions on the radiating patch for antennas shown in Fig. 2 at (a) first resonance frequency (1.8 GHz), (b) second resonance frequency (2.4 GHz), and (c) third resonance frequency (3.5 GHz).

It can be observed that in Fig. 5 (a) and (b), that the current concentrated on the edges of the interior and exterior of the L-shaped slits at 1.8 GHz and 2.4 GHz. Therefore, the antenna impedance changes at these frequencies due to the resonant properties of the L-shaped slits [8]. Another important design parameter of this structure is the inverted Γ-shaped slot used in the radiating patch. Figure 5 (c) presents the simulated current distributions on the radiating patch of the proposed antenna at 3.5 GHz. As shown in Fig. 5 (c), at the third resonance frequency the current flows are more dominant around of the inverted Γ-shaped slot structure.

The proposed antenna with optimal design was built and tested. The measured and simulated return loss characteristics of the proposed antenna are shown on Fig. 6. The fabricated antenna has the frequency band from 1.73 GHz – 1.91 GHz, 2.23 GHz – 2.51 GHz, 2.89 GHz – 3.83 GHz, and 4.88 GHz – 6.19 GHz, that satisfy all the system requirements for DCS1800 (1.71 GHz – 1.88 GHz), DCS1900 (1.85 GHz – 1.99 GHz), WiBro (2.3 GHz – 2.39 GHz), WLAN (2.4 GHz – 2.483 GHz), and WiMAX (2.5 GHz, 3.5 GHz, and 5.5 GHz), simultaneously. As shown in Fig. 6, there exists a discrepancy between the measured and simulated results. In order to confirm the accurate return loss characteristics of the designed antenna, it is recommended that the manufacturing and measurement process need to be performed carefully. In conclusion, as the monopole is a short radiator, the SMA connector can modify its impedance matching.

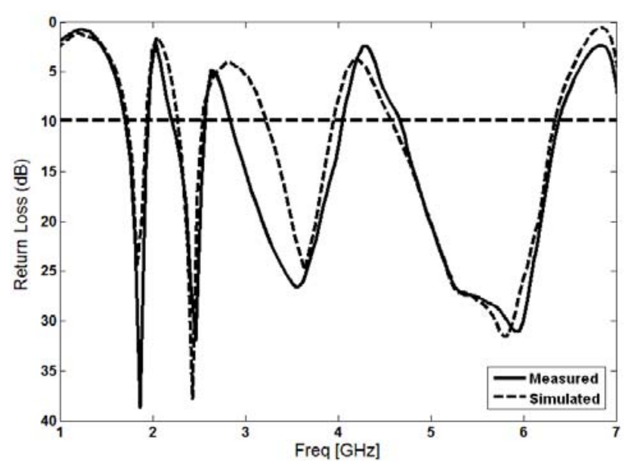

Fig. 6. Measured and simulated return loss for the proposed antenna.

The simulated radiation efficiencies and the measured maximum gains of the proposed antenna are shown in Figs. 7 and 8, respectively. Results of the calculations using the software HFSS indicated that the proposed antenna features a good efficiency, being greater than 62 % across the entire radiating band, as shown in Fig. 7. Also, the measured maximum gains of the proposed antenna are presented in Fig. 8. As shown in Fig. 8, the proposed antenna has a gain that is low at 1 GHz and increases with frequency.

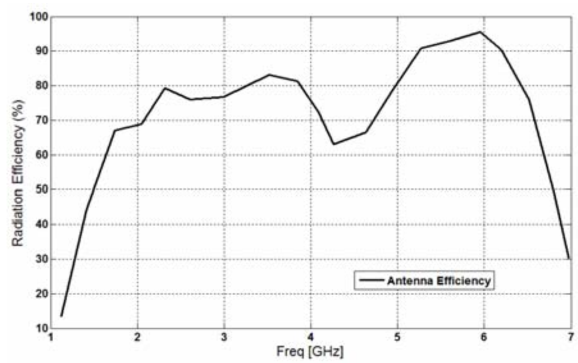

Fig. 7. Simulated radiation efficiency values of the proposed monopole antenna.

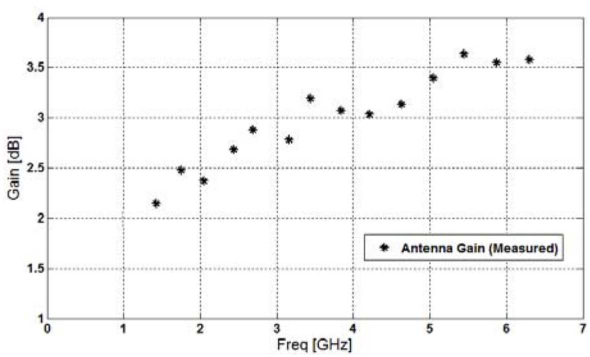

Fig. 8. Measured maximum gain and simulated radiation efficiency values of the proposed monopole antenna.

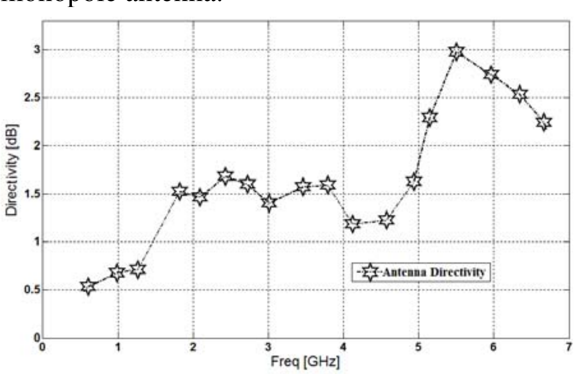

Fig. 9. Simulated directivity characteristics of the proposed monopole antenna.

The simulated directivity characteristic for the proposed antenna is shown in Fig. 9. As shown in Fig. 9, the directivity characteristics of the proposed monopole antenna have a variation similar to other monopole antennas directivity at DCS/WLAN/ WiMAX frequencies bands [7]. Figures 10 and 11 show the measured radiation patterns at resonance frequencies including the co–polarization and cross–polarization, in the H–plane (x–z plane) and E–plane (y–z plane). The main purpose of the radiation patterns is to demonstrate that the antenna actually radiates over a multi frequency band. It can be seen that the radiation patterns in *x*–*z* plane are nearly omni–directional even at higher frequencies, and also the cross–polarization level is low for the five frequencies.

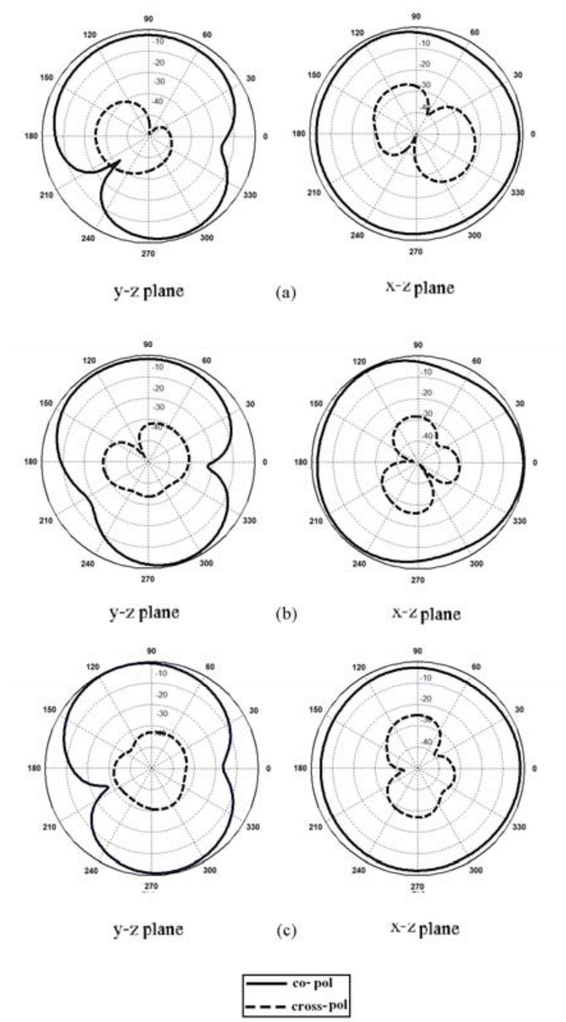

Fig. 10. Measured radiation patterns of the proposed antenna at (a) 1.8 GHz, (b) 2.4 GHz, and (c) 3.5 GHz.

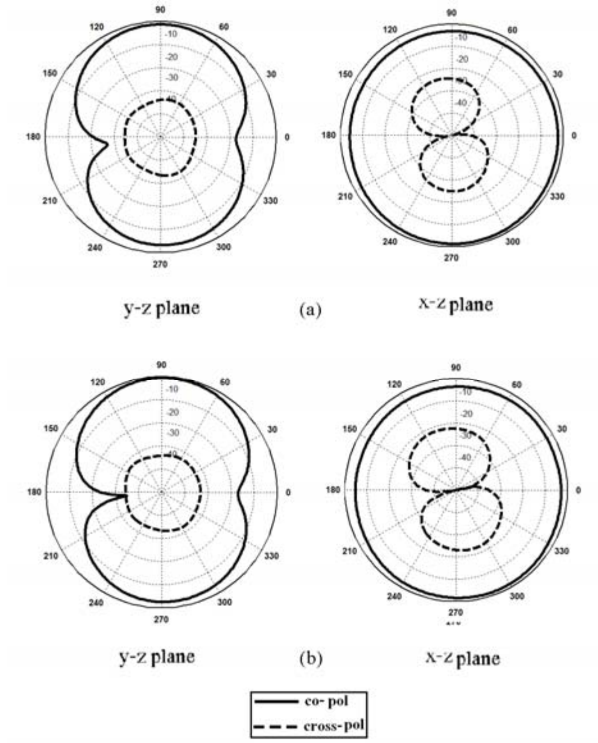

Fig. 11. Measured radiation patterns of the proposed antenna at (a) 5.2 GHz and (b) 5.8 GHz.

IV. CONCLUSION

In this paper, a new multi-resonances printed monopole antenna by using a pair of L-shaped slits and an inverted Γ-shaped is presented for satisfying DCS operations at the 1.8 GHz frequency, WLAN operations at the 2.4 GHz, 5.2 GHz, and 5.8 GHz frequencies and also for WiMAX operations at the 2.5 GHz, 3.5 GHz, and 5.5 GHZ frequencies. Prototypes of the proposed antenna have been constructed and studied experimentally. The measured results showed good agreement with the numerical prediction. By adjusting the L-shaped slits the desired first and second resonant frequencies are obtained by adjusting the length of L-shaped slits. Also by cutting an inverted Γ-shaped slot in the radiating patch, a new resonance at 3.5 GHz can be created. Prototypes of the proposed antenna have been constructed and studied experimentally

ACKNOWLEDGMENT

The authors are thankful to Microwave Technology (MWT) Company staff for their beneficial and professional help (www. microwave-technology.com).

REFERENCES

[1] M. Ojaroudi, N. Ojaroudi, and N. Ghadimi "Enhanced bandwidth small square slot antenna with circular polarization characteristics for WLAN/WiMAX and C-band applications," *Applied Computational Electromagnetics Society (ACES) Journal*, vol. 28, no. 2, pp. 156-161, February 2013.

[2] B. Li, J. S. Hong, and B. Z. Wang, "A novel circular disc monopole antenna for dual- band WLAN applications," *Applied Computational Electromagnetics Society (ACES) Journal*, vol. 27, no. 5, pp. 441-448, May 2012.

[3] G. Zhang, J. S. Hong, B. Z. Wang, and G. Song, "Switched band-notched UWB/WLAN monopole antenna," *Applied Computational Electromagnetics Society (ACES) Journal*, vol. 27, no. 3, pp. 256-260, March 2012.

[4] M. Ojaroudi, M. Hassanpour, Ch. Ghobadi, and J. Nourinia, "A novel planar inverted-F antenna (PIFA) for WLAN/WiMAX applications," *Microwave and Optical Tech. Letters*, vol. 52, no. 8, August 2010.

[5] N. Ojaroudi and M. Ojaroudi, "Small monopole antenna with multi-resonance characteristic by using rotated T-shaped slit and parasitic structure for UWB systems, " *Microwave and Optical Tech. Letters*, vol. 55, pp. 482-485, March 2013.

[6] M. Ojaroudi, N. Ojaroudi, and Y. Ebazadeh, "Dual band-notch small square monopole antenna with enhanced bandwidth characterestics for UWB applications," *Applied Computational Electromagnetics Society (ACES) Journal*, vol. 27, no. 5, pp. 420-426, May 2012.

[7] A. Ghazi, M. N. Azarmanesh, and M. Ojaroudi, "Multi-resonance square monopole antenna for ultra-wideband applications," *Progress In Electromagnetics Research C*, vol. 14, pp. 103-113, 2010.

[8] Gh. Beigmohammadi, Ch. Ghobadi, J. Nourinia, and M. Ojaroudi, "Small square slot antenna with circular polarization characteristics for WLAN/WiMAX applications, " *Electronic Letters*, vol. 46, no. 10, pp. 672-673, 2010.

[9] Ansoft High Frequency Structure Simulation (HFSS), Ver. 13, Ansoft Corporation, 2010.

Nasser Ojaroudi was born on 1986 in Germi, Iran. He received his B.Sc. degree in Electrical Engineering from Azad University, Ardabil Branch. From 2011, he is working toward the M.Sc. degree in Telecommunication Engineering at Shahid Rajaee Teacher Training University. Since March 2008, he has been a Research Fellow in the Microwave Technology Company (MWT), Tehran, Iran. His research interests include microstrip antennas for radar systems, ultra-wideband (UWB) and small antennas for wireless communications, microwave passive devices and circuits, and microwave/millimeter systems.

Mohammad Ojaroudi was born on 1984 in Germi, Iran. He received his B.Sc. degree in Electrical Engineering from Azad University, Ardabil Branch and M.Sc. degree in Telecommunication Engineering from Urmia University. From 2010, he is working toward the Ph.D. degree at Shahid Beheshti University. From 2007 until now, he is a Teaching Assistant with the Department of Electrical Engineering, Islamic Azad University, Ardabil Branch, Iran.

Since March 2009, he has been a Research Fellow (Chief Executive Officer) in the Microwave Technology Company (MWT), Tehran, Iran. From 2012, Mr. Ojaroudi is a member of the IEEE Transaction on Antennas and Propagation (APS) reviewer group and the Applied Computational Electromagnetic Society (ACES). From 2013 he is a student member of the IEEE. His research interests include analysis and design of microstrip antennas, design and modeling of microwave structures, radar systems, and electromagnetic theory. He is author and coauthor of more than 100 journal and international conferences papers. His papers have more than 400 citations with 10 h-index.

Noradin Ghadimi was born in Ardabil-Iran in 1985, and received the B.Sc. degree in electrical engineering from the Islamic Azad University, Ardabil branch, Ardabil, Iran, in 2009 and the M.Sc. degree in electrical engineering from the Islamic Azad University Ahar Branch, Ahar, Iran , in 2011.

His research interests include power system protection, modeling and analysis of distributed generations, renewable energy, and communications systems.

Magnetic Charge and Magnetic Field Distributions in Ferromagnetic Pipe

Huang Xinjing, Chen Shili, Guo Shixu, Zhao Wei, and Jin Shijiu

State Key Laboratory of Precision Measurement Technology and Instrument
Tianjin University, Tianjin, 86-300072, China
1207571368@qq.com, huangxinjing@tju.edu.cn, and shjjin@tju.edu.cn

Abstract **—** This paper proposes the equivalent magnetic charge (EMC) method, to analyze the magnetic field presented in ferromagnetic pipe. Distributions of the magnetic charge density on pipes' surface are calculated, and the magnetic field on several measurement lines is predicted using numerical calculation with several different directions of magnetization. The correctness of the analysis results is then validated by the comparison between the results of the ANSOFT and measurement of the magnetic field inside several actual pipes. With the EMC method, it is of great interest to found that when the magnetization direction changes, the radial and axial magnetic field components inside the pipe will shift accordingly. Moreover, the variation law of magnetic field along the axial retains substantially unaltered, and the magnetic field distribution in the pipe is obviously symmetrical with a plurality of extreme points. As a result, the magnetic field distributes evenly if the pipe is long enough.

Index Terms - Magnetization, magnetostatics, magnetic charge, magnetic field, and pipe.

I. INTRODUCTION

In-pipe, pipelines inspection gauge (PIG) represents one of the most popular techniques to detect the pipelines' integrity in oil and gas storage and transportation departments, enabling the early identification of corrosion and early restoration of pipelines before any leak occurs [1]. PIG or other methods as well usually utilize the magnetic field inside or outside the pipelines to discover pipelines' defects and assist in positioning and calculating pipelines' routes [2-4]. Ignoring the distributions of the background magnetic field in the pipelines often leads to inconsistencies between the analysis results of PIG's detection based on the magnetic field inside pipelines and actual pipe disfigurement conditions, inducing additional error to cause great inconvenience to maintain pipelines. Therefore, it is very important to ascertain the distributions of the magnetic field inside the pipelines that serves for the magnetic field measurement and data analyses for PIG, and thus improving the detection accuracy of PIG.

A number of literatures had reported the characteristics of axial uniform magnetization to non ellipsoid using the numerical method, achieving a lot of meaningful results [5-12]. Nakamura et al. [5] gave a detailed description of scalar magnetic potential method for three dimensional analyses of the distributions of the magnetic charge density on the surface of the ferromagnetic material, and analyzed the distributions of the magnetic field around the magnetic poles of the motor. Kobayashi et al. [6] adopted the method proposed in reference [5] to make abundant analyses for cylindrical tubular model applied an axial uniform magnetization, discussing in detail the distribution characteristics of the magnetic charge density on the surface of the ferromagnetic body in cases of different diameter ratios, different aspect ratios, and different magnetic susceptibilities. However, the authors did not involve the distribution characteristics of the magnetic field inside the pipe when applied different directions of magnetization. Chen et al. [13], indicated conversely the distributions of the magnetic charge density on ships' surfaces using the measured magnetic field values at finite points near the ship

Submitted On: Nov. 24, 2012
Accepted On: June 14, 2013

according to the scalar magnetic potential theory, thus predicting the magnetic field generated by the ship at any point in the space accurately. However, this method is affected by the condition number of the calculation matrix and the distribution of the measurement points drastically, making it unreliable and inaccurate in practice. It is therefore very important to develop new methods for accurate magnetic field analyses.

In this regard, this paper presents the equivalent magnetic charge (EMC) method to the magnetic field analyses for pipes to improve the calculation accuracy. With different directions of magnetization of the pipes, we calculate the distributions of the magnetic charge density on the surface of non-axially magnetized cylindrical tubular body and the magnetic field distributions inside the pipe. Simultaneously discrete calculation method used in this paper does not depend on the distribution of measurement points, and the condition number of the calculation matrix is very small. Both of the improvements make the calculation result rather reliable. The present work demonstrates this methodology by comparison between the results of ANSOFT and measurement results of the magnetic field distributions in several actual pipes. The results indicate the correctness of the proposed EMC method, producing a reliable and accurate calculation result for magnetic field analyses.

II. METHOD OF ANALYZING

A. Equivalent magnetic charge theory

For the relative permeability μ, which is finite and homogeneous in the magnetic body, we express the magnetic flux density $\boldsymbol{B}$ in terms of the magnetic field $\boldsymbol{H}$ and the magnetization $\boldsymbol{M}$ as follows,

$$\boldsymbol{B} = \mu_0(\boldsymbol{H}+\boldsymbol{M}) = \mu_0\mu\boldsymbol{H}\ , \tag{1}$$

where

$$\boldsymbol{M} = (\mu-1)\boldsymbol{H}\ . \tag{2}$$

In three-dimensional magnetostatic problems, usually resultant intensity of magnetic field $\boldsymbol{H}$ at an arbitrary point in space can be expressed by summation of the applied magnetic field $\boldsymbol{H_0}$ and the demagnetizing field $\boldsymbol{H_d}$ as follows,

$$\boldsymbol{H}(\boldsymbol{r}) = \boldsymbol{H}_0(\boldsymbol{r}) + \boldsymbol{H}_d(\boldsymbol{r})\,. \tag{3}$$

The magnetic field intensity at a point ($\boldsymbol{r}$) in space can be expressed as the gradient of the scalar magnetic potential U,

$$\boldsymbol{H}_d(\boldsymbol{r}) = -grad\,U(\boldsymbol{r}) \tag{4}$$

where

$$\begin{aligned} U(\boldsymbol{r}) = \frac{1}{4\pi}\int_V \frac{-\nabla\cdot\boldsymbol{M}(\boldsymbol{r}')}{|\boldsymbol{r}-\boldsymbol{r}'|}dV' + \\ \frac{1}{4\pi}\int_S \frac{\boldsymbol{M}(\boldsymbol{r}')\cdot\boldsymbol{n}}{|\boldsymbol{r}-\boldsymbol{r}'|}dS' \end{aligned}\,. \tag{5}$$

Wherein V represents an occupied space of the ferromagnetic material, S represents the surface of the ferromagnetic material, and $\boldsymbol{n}$ represents the unit outer normal vector at a point $\boldsymbol{r}'$ on the surface of the ferromagnetic material. $\boldsymbol{M}$ is the bulk density of the magnetic dipole moment, i.e., the magnetic polarization intensity.

For uniformly magnetized magnetic media, $\boldsymbol{M}$ is constant, the first term in equation (5) vanishes because of $\nabla\bullet\boldsymbol{M} = 0$ and only the second term remains. Then, the $\boldsymbol{H_d}$ can be expressed in terms of the surface magnetic charge density $\sigma(\boldsymbol{r})$ as the following integration,

$$\boldsymbol{H}_d(\boldsymbol{r}) = -\frac{1}{4\pi}\int_S grad\frac{\sigma(\boldsymbol{r}')}{|\boldsymbol{r}-\boldsymbol{r}'|}dS'\,, \tag{6}$$

where

$$\sigma(\boldsymbol{r}) = \boldsymbol{M}(\boldsymbol{r})\cdot\boldsymbol{n}\ . \tag{7}$$

When the observation point $\boldsymbol{r}$ is taken on the surface of the ferromagnetic material $\boldsymbol{r_s}$, integral equation can be expressed in terms of the integration on the small finite area ΔS including the observation point $\boldsymbol{r_s}$ and the one on the remaining area S' excluding $\boldsymbol{r_s}$, as shown in Fig. 1. Therefore, $\boldsymbol{H_d}(\boldsymbol{r_s})$ can be expressed as follow,

$$\boldsymbol{H}_d(\boldsymbol{r}_s) = \boldsymbol{H}_{d_s}(\boldsymbol{r}_s) + \boldsymbol{H}_{d_o}(\boldsymbol{r}_s) \tag{8}$$

where

$$\boldsymbol{H}_{d_o}(\boldsymbol{r}_s) = -\frac{1}{4\pi}\int_{S'} grad\frac{\sigma(\boldsymbol{r}')}{|\boldsymbol{r}_s-\boldsymbol{r}'|}dS'\,. \tag{9}$$

Considering the discontinuity of $\boldsymbol{H_d}(\boldsymbol{r_s})$ at $\boldsymbol{r_s}$ on the interface of the air and the magnetic body, we can get,

$$\left\{\boldsymbol{H}^{(a)}(\boldsymbol{r}_s) - \boldsymbol{H}^{(m)}(\boldsymbol{r}_s)\right\}\cdot\boldsymbol{n} = \sigma(\boldsymbol{r}_s) \tag{10}$$

where

$$\boldsymbol{H}^{(a)}(\boldsymbol{r}_s) = \boldsymbol{H}_0^{(a)}(\boldsymbol{r}_s) + \boldsymbol{H}_{d_s}^{(a)}(\boldsymbol{r}_s) + \boldsymbol{H}_{d_o}^{(a)}(\boldsymbol{r}_s)\,, \tag{11}$$

$$\boldsymbol{H}^{(m)}(\boldsymbol{r}_s) = \boldsymbol{H}_0^{(m)}(\boldsymbol{r}_s) + \boldsymbol{H}_{d_s}^{(m)}(\boldsymbol{r}_s) + \boldsymbol{H}_{d_o}^{(m)}(\boldsymbol{r}_s)\,. \tag{12}$$

Wherein the superscripts (a), (m) denote the air side and the magnetic body side, respectively. Using $\boldsymbol{H}_0^{(a)}(\boldsymbol{r}_s)=\boldsymbol{H}_0^{(m)}(\boldsymbol{r}_s)$, $\boldsymbol{H}_{d_s}^{(a)}(\boldsymbol{r}_s)=\boldsymbol{H}_{d_s}^{(m)}(\boldsymbol{r}_s)$, $\boldsymbol{H}_{d_o}^{(a)}(\boldsymbol{r}_s)=-\boldsymbol{H}_{d_o}^{(m)}(\boldsymbol{r}_s)$, we can get,

$$\boldsymbol{H}_{d_s}^{(m)}(\boldsymbol{r}_s)=-\boldsymbol{H}_{d_s}^{(a)}(\boldsymbol{r}_s)=-\frac{\sigma(\boldsymbol{r}_s)}{2}\boldsymbol{n}. \qquad (13)$$

Taking the inner product of equation (12) and $\boldsymbol{n}$, and using equations (2), (7), and (13) we can get,

$$\frac{\sigma(\boldsymbol{r}_s)}{\mu_0(\mu-1)}=\boldsymbol{H}_0(\boldsymbol{r}_s)\cdot\boldsymbol{n}-\frac{\sigma(\boldsymbol{r}_s)}{2\mu_0}+\boldsymbol{H}_{d_o}(\boldsymbol{r}_s)\cdot\boldsymbol{n}. \quad (14)$$

Finally, we can get

$$\begin{aligned}&\frac{1}{4\pi}\left(\int_{S'} grad\frac{\sigma(\boldsymbol{r}')}{|\boldsymbol{r}_s-\boldsymbol{r}'|}dS'\right)\cdot\boldsymbol{n}+\\&\left(\frac{1}{2}+\frac{1}{\mu-1}\right)\sigma(\boldsymbol{r}_s)=\mu_0\boldsymbol{H}_0(\boldsymbol{r}_s)\cdot\boldsymbol{n}\end{aligned}. \qquad (15)$$

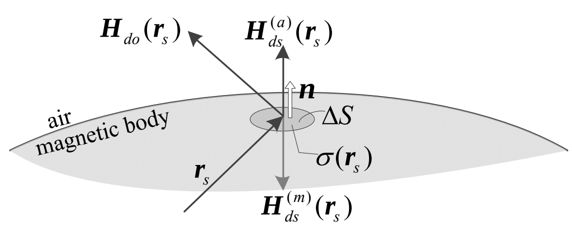

Fig. 1. Magnetic field at a point on the surface of the magnetic body.

B. Discretizing approach

Let us consider the pipe model as shown in Fig. 2. $\boldsymbol{M}$ is the magnetization intensity, $\boldsymbol{M}$ // XOZ plane. The angle between $\boldsymbol{M}$ and OZ axis is α. Inner and outer surfaces and two end surfaces of the ferromagnetic material are divided into N surface elements S_i, i = 1,2,3,…,N, assuming that the magnetic charge density σ_i within each surface element is constant, and then equation (9) can be expressed as equations (16) and (17).

Pipeline is usually made of alloy steel, whose permeability is relatively big [15]. Based on the results from Sakurai et al. [11], we can learn that, when permeability gets larger, the distribution law of the magnetic charge density on the surface of the ferromagnetic material tends to a limit soon in the same mode, but the distribution law keeps consistent. Solving equation (16) we can obtain the distribution of the magnetic charge density on each surface element. For different pipe models, the condition number of the coefficient matrix $\boldsymbol{A}$ of equation (16) is very small, cond ($\boldsymbol{A}$)≈1.

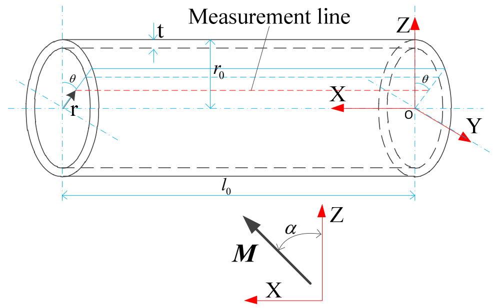

Fig. 2. Pipe model diagram.

$$\begin{pmatrix}\frac{1}{2}+\frac{1}{\mu\text{-}1} & A_{12} & A_{13} & \cdots & A_{1N}\\ A_{21} & \frac{1}{2}+\frac{1}{\mu\text{-}1} & A_{23} & \cdots & A_{2N}\\ A_{31} & A_{32} & \frac{1}{2}+\frac{1}{\mu\text{-}1} & \cdots & A_{3N}\\ \cdots & \cdots & \cdots & \cdots & A_{4N}\\ A_{N1} & A_{N2} & \cdots & A_{N4} & \frac{1}{2}+\frac{1}{\mu\text{-}1}\end{pmatrix}$$

$$\times\begin{pmatrix}\sigma_1\\ \sigma_2\\ \sigma_3\\ \cdots\\ \sigma_N\end{pmatrix}=\begin{pmatrix}\mu_0\boldsymbol{H}_0\cdot\boldsymbol{n}_1\\ \mu_0\boldsymbol{H}_0\cdot\boldsymbol{n}_2\\ \mu_0\boldsymbol{H}_0\cdot\boldsymbol{n}_3\\ \cdots\\ \mu_0\boldsymbol{H}_0\cdot\boldsymbol{n}_N\end{pmatrix}, \qquad (16)$$

where

$$A_{ji,i\neq j}=\int_{S_i}\frac{1}{4\pi}\frac{\boldsymbol{r}_j-\boldsymbol{r}_i}{|\boldsymbol{r}_j-\boldsymbol{r}_i|^3}dS\cdot\boldsymbol{n}_j. \qquad (17)$$

C. Calculation method of magnetic field in pipeline

We select a group of measurement points, marked as P={$\boldsymbol{r}_i$|i=1，2，…，M}. Foregoing divided surface elements here are denoted as S={S_j|j=1，2，…，N}. And then we calculate the magnetic field at each point using equations (18) and (19),

$$\begin{pmatrix} \boldsymbol{H}_1/H_0 \\ \boldsymbol{H}_2/H_0 \\ \cdots \\ \boldsymbol{H}_N/H_0 \end{pmatrix} = \begin{pmatrix} \boldsymbol{C}_{11} & \boldsymbol{C}_{12} & \cdots & \boldsymbol{C}_{1N} \\ \boldsymbol{C}_{21} & \boldsymbol{C}_{22} & \cdots & \boldsymbol{C}_{2N} \\ \cdots & \cdots & \cdots & \cdots \\ \boldsymbol{C}_{M1} & \boldsymbol{C}_{M2} & \cdots & \boldsymbol{C}_{MN} \end{pmatrix} \times \begin{pmatrix} \sigma_1 \\ \sigma_2 \\ \cdots \\ \sigma_N \end{pmatrix} \quad (18)$$

where

$$\boldsymbol{C}_{\mathrm{ij}} = \int_{S_j} \frac{1}{4\pi} \frac{\boldsymbol{r}_j - \boldsymbol{r}_i}{\left|\boldsymbol{r}_j - \boldsymbol{r}_i\right|^3} dS \ . \quad (19)$$

III. RESULTS AND DISCUSSIONS

A. Distributions of magnetic charge density on pipes' surfaces

We apply a series of different directions of magnetization to the pipes and calculate the distributions of the magnetic charge density on the surface of the ferromagnetic pipes. The magnetic charge density on each surface element is denoted as σ_{osi}, σ_{isi}, σ_{1ej}, σ_{2ej}, for the outer side, the inner side, the end side1, and the end side2. The mean and standard deviation of $\{\sigma_{osi}/\sigma_{isi}\}$is calculated and shown in Fig. 3. We can learn that each mean of $\{\sigma_{osi}/\sigma_{isi}\}$ is very close to -1 according to the corresponding directions of magnetization, and the standard deviation is very small. Especially, when the magnetization angle α is less than 80°, the standard deviation of $\{\sigma_{osi}/\sigma_{isi}\}$ is smaller. So it is clear that the magnetic charge density inside and outside pipe is equivalent but opposite for the pipe model. What should be stressed is that pipe cannot be equivalent to a thin model when we analyze its surface's magnetic charge density distribution. We have to calculate all sides of the magnetic charge density of the pipe.

The means of $\{\sigma_{osi},\sigma_{isi}\}$ and $\{\sigma_{1ej},\sigma_{2ej}\}$ are calculated and shown in Fig. 4, using equations (20) and (21). With the magnetization angle α varying from 0° to 90°, the magnetic charge density on the side surfaces becomes larger and larger gradually, while the magnetic charge density on the end surfaces becomes smaller and smaller gradually,

$$\bar{\sigma}_s = \sum_{i=1}^{N_1} \left(\left|\sigma_{osi}\right| + \left|\sigma_{isi}\right|\right) \Big/ 2N_1 \ , \quad (20)$$

$$\bar{\sigma}_e = \sum_{j=1}^{N_2} \left(\left|\sigma_{1ej}\right| + \left|\sigma_{2ej}\right|\right) \Big/ 2N_2 \ , \quad (21)$$

$$\bar{\sigma}_s = k_1 cos\alpha, \bar{\sigma}_e = k_2 sin\alpha, k_2/k_1 \approx 1.5 \ . \quad (22)$$

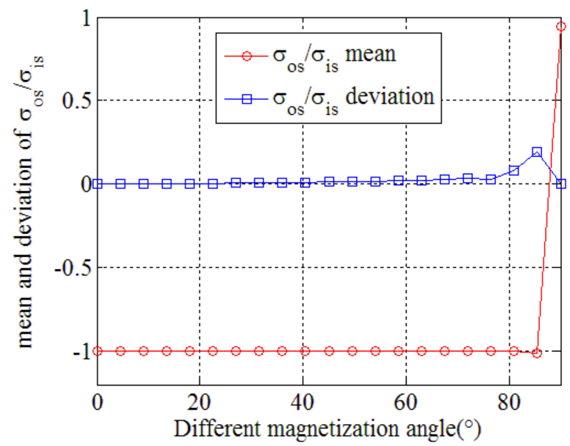

Fig. 3. Inner and outer magnetic charge density contrast on pipe's side surfaces under different directions of magnetization.

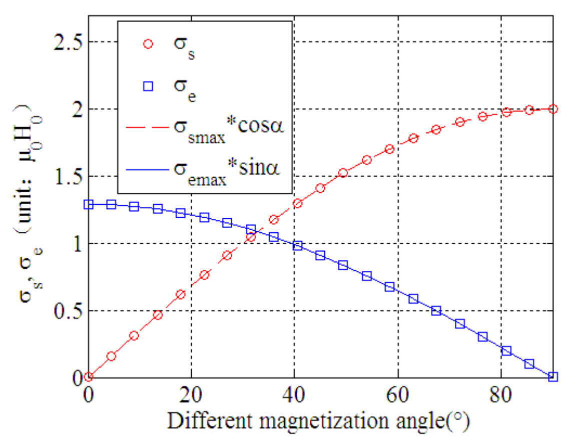

Fig. 4. Contrast of the magnetic charge density on pipe's side and end surfaces under different directions of magnetization.

Some representative results of the foregoing magnetization angles are shown in Figs. 5 (a) - (f) in the form of color intensity maps, which denote the magnetic charge density on the outer surface. As shown in Fig. 5 (a) - (f), when the magnetization direction changes, the distribution of the magnetic charge density changes significantly. However, the magnetic charge density on the outer side surface decreases after the magnetization angle increases. When the magnetization angle α is close to 90°, the circumferential distribution of the magnetic charge density along the pipe has no significant changes, but the axial distribution along the pipe changes significantly, obtaining extremes at the ends of the pipe. When the magnetization angle α is less than 86°, the circumferential distribution of the magnetic charge density along the pipe changes significantly and shows an obvious periodic variation, obtaining extremes at θ = 0° (+z) and θ = 180° (-z), respectively, but the axial distribution has no significant change.

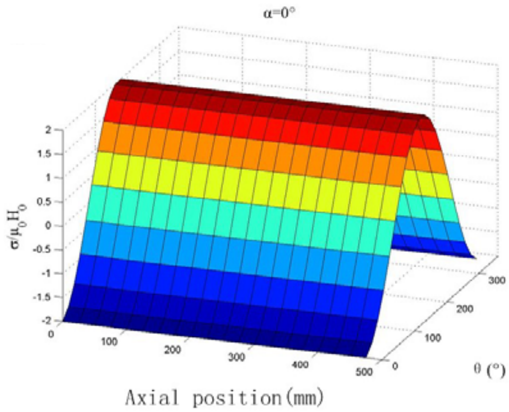

(a)

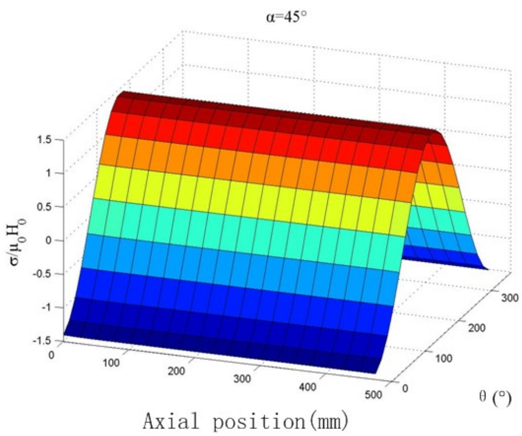

(b)

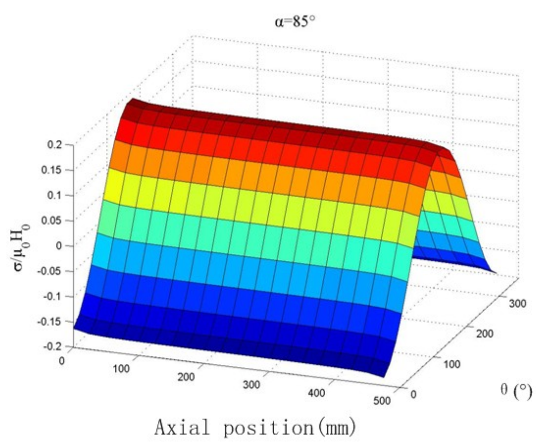

(c)

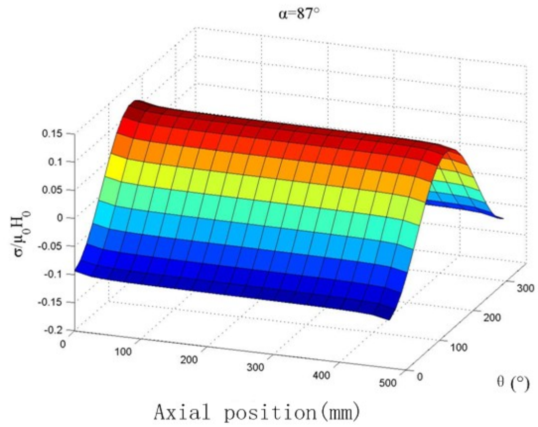

(d)

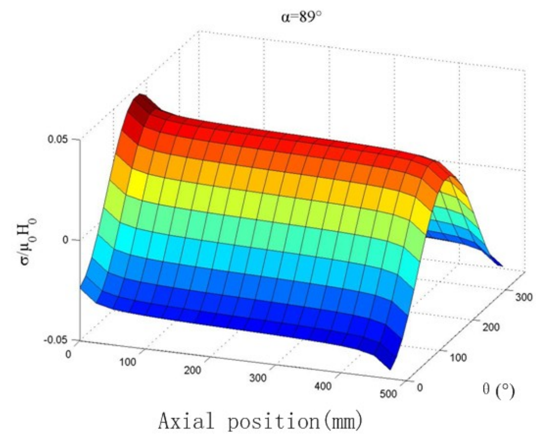

(e)

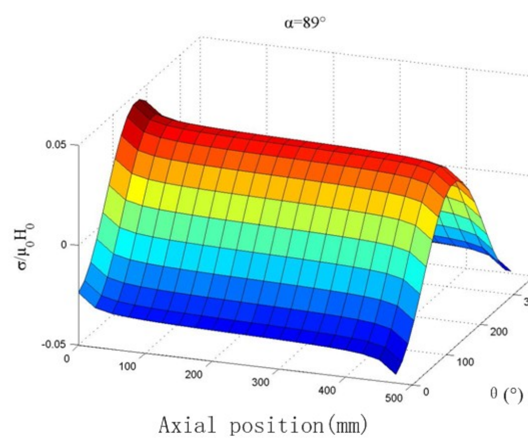

(f)

Fig. 5. Magnetic charge density distributions on pipe's outer side surface under different directions of magnetization.

B. Magnetic field distribution law inside the pipe

The position of the measuring line has no important impact on the magnetic field distribution characteristics as shown in Figs. 6 (a) - (d). For the pipe of l_0= 500 mm, t = 7 mm, r_0 = 100 mm, we take the measuring lines, respectively at $r = 0$, $\theta = 0°$, $r = 0.2\,r_0$, $\theta = 0°$, $r = 0.2r_0$, $\theta = 72°$, $r = 0.2r_0$, $\theta = 144°$. From each graph of Figs. 6 (a) - (d), it is clear that for each magnetization direction, the magnetic field intensity at different measuring lines inside the pipe has no obvious variation either the amplitude or the fluctuation. When the magnetizing angle α increases gradually from 0° to 90°, the axial component H_x of the magnetic field at each measuring line increases gradually, the radial component H_z reduces gradually, but H_y is always very small. The distribution of the magnetic field inside the pipe is obviously symmetrical. H_z shows an even symmetrical distribution all along the axis of the pipe around the median normal plane of the axis of the pipe with only one extreme. When α is very small, H_x shows an odd symmetrical distribution all along the axis of the pipe around the median normal plane of the axis of the pipe with several extremes. When α is big, H_x shows an even symmetrical distribution all along the axis of the pipe around the median normal plane of the axis of the pipe. The distribution of the magnetic field at measuring line $r = 0$, $\theta = 0°$ in the pipe of l_0 = 1500 mm, t = 7 mm, r_0 = 100 mm, is shown in Fig. 6 (e). The results indicate that the magnetic field distribution in the long pipe is similar to that of the short pipe, only with a longer flat portion of the axial and radial magnetic field component. It can be thus expected that the magnetic field will be uniform if the pipeline is very long.

C. Comparison with ANSOFT

In order to confirm the validity of the results above, we perform the finite element analyses for the 500 mm long pipe with the same specification using ANSOFT, a commercial software for electromagnetic simulation. With different magnetization angles of 90°, 45°, and 0°, we analyze the magnetic field distribution inside and outside the pipe, and the simulation results are displayed in the form of magnetic field vector graphic, as shown in Figs. 7 (a) - (c). It can be seen that when the magnetization angle varies, the magnitude and direction of the magnetic field in the XOZ plane inside the pipe obviously changes accordingly. The magnitude and direction of the magnetic field do not change almost inside and outside the pipe far away from both ends of the pipe, basically consistent with the applied magnetization direction. The direction of the magnet field inside the pipe is opposite to the magnetization direction, while the direction of the magnet field outside and far away from the pipe is identical with the magnetization direction. The magnetic field can be approximately assumed uniform inside the pipe far away from the ends and the wall of the pipe, but the magnitude and direction of the magnetic field near to both ends of the pipe has very dramatic changes. We can build a scene in our brain from the magnetic field vector graphic, which presents the distribution of the magnitude and direction of the magnetic field in the axial measurement lines: the direction of B_x changes twice, while the direction of B_z never changes. It can be very easily inferred that all these distribution characteristics are consistent with the analysis results using our method.

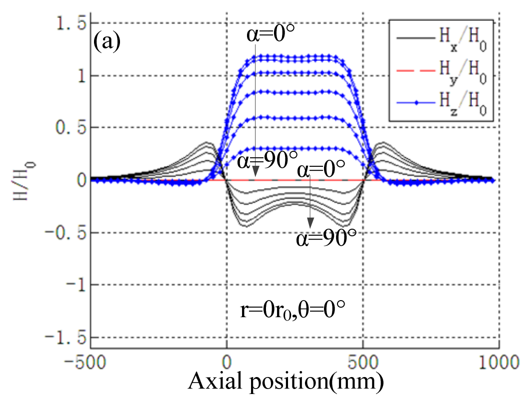

(a)

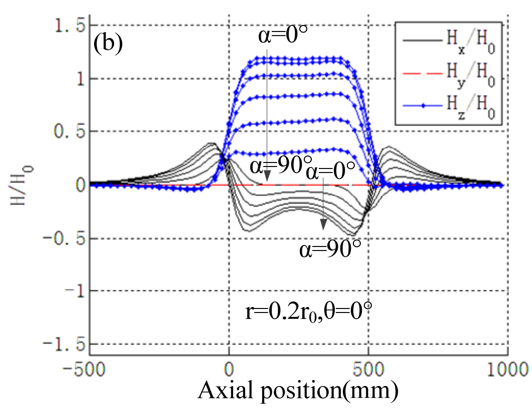

(b)

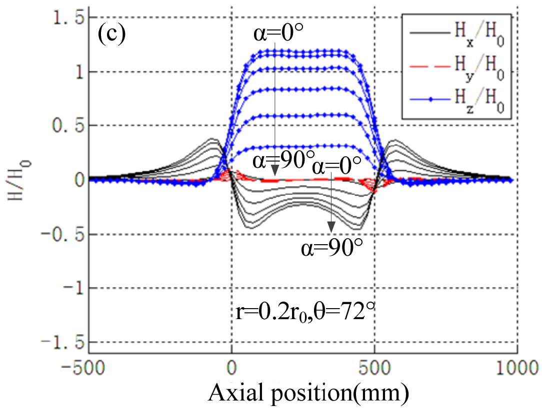

(c)

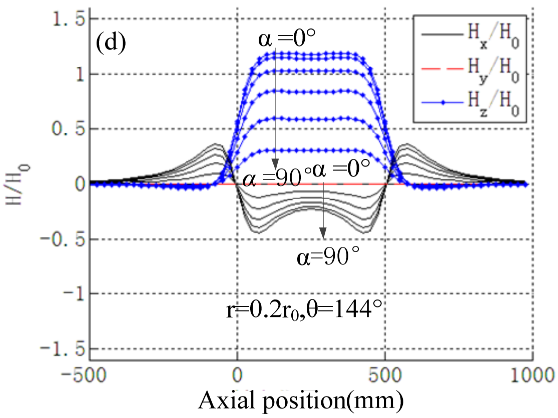

(d)

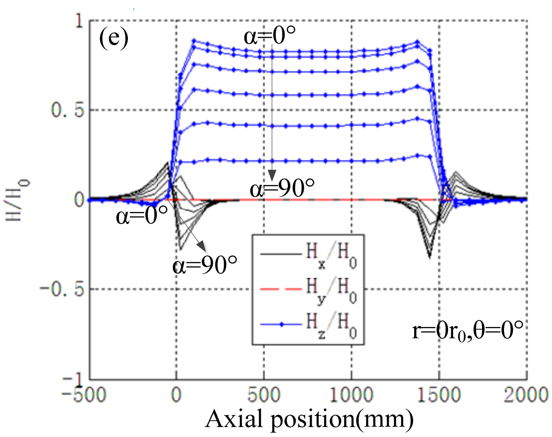

(e)

Fig. 6. Magnetic field distributions in different pipes under different directions of magnetization; $\alpha = 0°, 15°, 30°, 45°, 60°, 75°, 90°$; $r_0 = 100$ mm, $t = 7$ mm, (a)-(d) $l_0 = 500$ mm and (e) $l_0 = 1500$ mm.

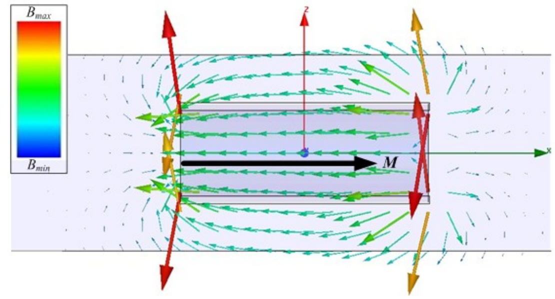

(a)

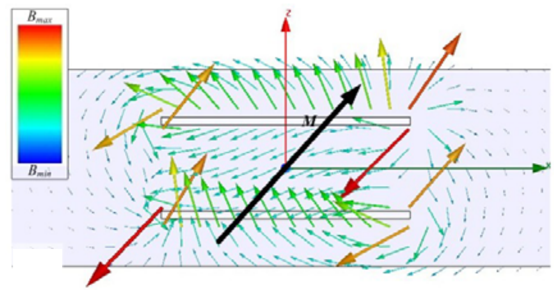

(b)

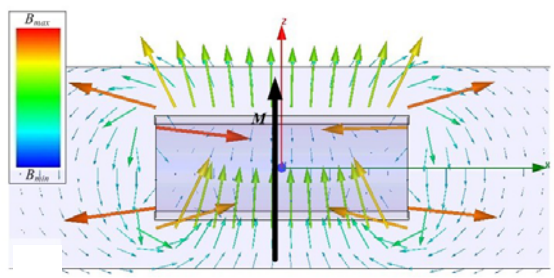

(c)

Fig. 7. Simulation results of ANSOFT.

D. Experiments

For the purpose of verifying the correctness of the analyses above, we measure the magnetic field distribution in several sections of the pipes using the experimental apparatus shown in Fig. 8. Guide rail is parallel to the pipe's axis and goes through the pipe. The slider moves along the pipe's axis as uniform as possible, carrying the magnetic sensor HMC2003. The magnetic induction intensity ***B*** output by the magnetic sensor is collected in real time by the USB4431 data acquisition card. The sensor HMC2003 is a magneto-resistive sensor, which is produced by the Honeywell Company. It has the following features: three-axis sensing, 4nT resolution, 1V/100uT sensitivity, and 0.5V-4.5V voltage output. The data acquisition card

USB4431 is produced by the national instruments (NI) company. It has the following features: four analog inputs, 24 bits resolution, 102.4 ksps synchronous sampling rate, and input range of ± 10 V, one analog output. The data acquisition software LabView is also developed by the NI Company. The pipe's specifications are shown in Table I. The experiment data is shown in Figs. 9 (a)-(d).

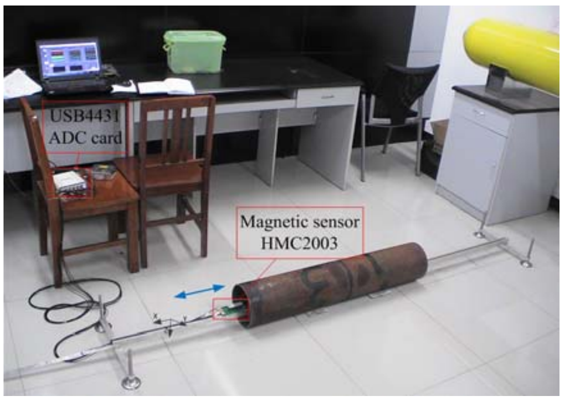

Fig. 8. Experiment equipment.

Table I: Specifications of experimental pipes.

Parameters	Pipes 1, 2	Pipe 3
Length l_0/mm	500	1500
Radius r_0/mm	100	100
Thickness t/mm	7	7
Material	20#	20#

The intensity of the magnetization has little impact on the distribution characteristics of each magnet field component along the axial measurement lines inside the pipe. When the intensity of the magnetization changes with the magnetization direction kept constant, all components of the magnet field are only multiplied by the same scale factor. Therefore, we do not care much about the intensity of the magnetization, and we have not normalized the measured magnetic field inside the pipe to the magnetization magnetic field. There is only a difference of a coefficient between the magnetic induction density $\boldsymbol{B}$ and the magnetic field $\boldsymbol{H}$. Anyway, it can also confirm the correctness of our analyses above by comparing the relative amplitude of the measured magnetic induction density with that of the theoretical analyses above.

For short pipes, we can learn that the measured three-dimensional magnetic field is very consistent with the theoretical analysis results by the comparison of Fig. 9 (a) and Figs. 6 (a)-(d) (when α = 60°). In comparison of the results presented in Fig. 9 (b) and Figs. 6 (a)-(d), it is clear that the actual measured B_x component and B_z component are basically consistent with that of theoretical analysis results. But B_y is not zero, this is due to the inconsistent thing between sensor's sensitive axes y, z and reference axes y, z in the coordinate system as shown in Fig. 2. Therefore, we integrate radial components B_y and B_z into one component, as shown in Fig. 9 (c). The composited magnetic field is very consistent with the results as shown in Figs. 6 (a)-(d) (when α = 30°). In comparison of Fig. 9 (d) and Fig. 6 (e) (when α = 45°), we can learn that the measured B_x component is basically consistent with the theoretical analysis results, and the B_y component and B_z component are very consistent with the theoretical analysis results.

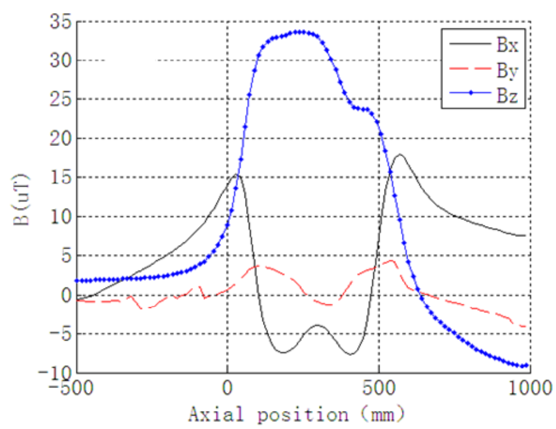

(a)

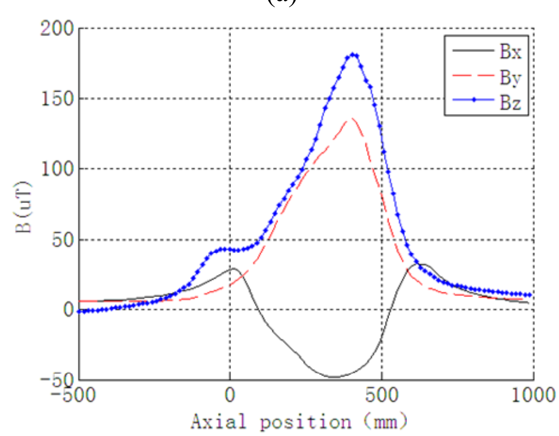

(b)

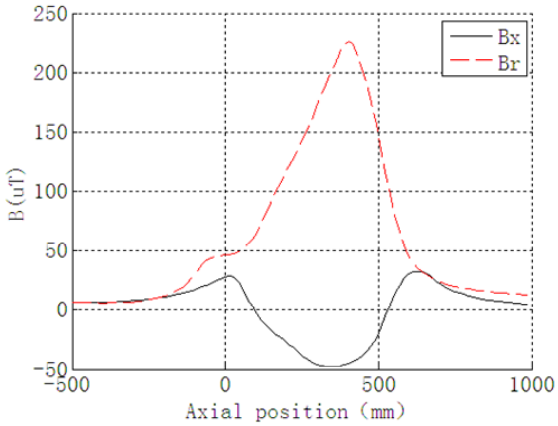

(c)

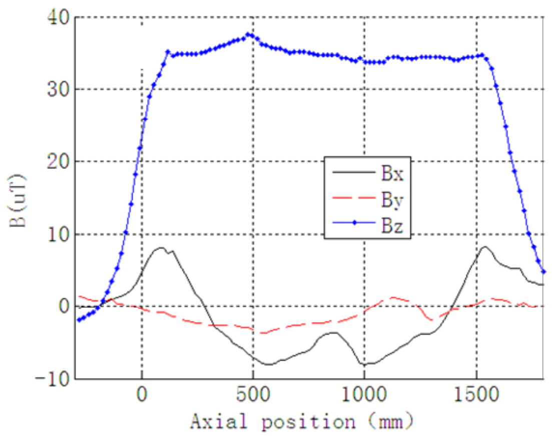

(d)

Fig. 9. Measured magnetic induction intensity inside pipes; (a)-(c) $l_0 = 500$ mm and (d) $l_0 = 1500$ mm.

IV. CONCLUSION

In this paper, the EMC method is used to analyze the magnetic field inside pipes. We calculate the distributions of the magnetic charge density on the surface of a non-axially magnetized cylindrical tubular body and the inner magnetic field distributions with different directions of magnetization applied to the pipe. By comparison with the simulation results of ANSOFT and measurement of the magnetic field distributions within several actual pipes, we validate the correctness of the analyses in this paper. Theoretical analyses and experimental results show that: the axial magnetic field distribution in the pipe is obviously symmetrical and with a plurality of extreme points; when the magnetization direction varies, the axial component and radial components of the magnetic field inside the pipeline will shift, but the magnetic field variation law along the axial retains substantially unchanged; the magnetic field will be uniform if the pipe is long enough.

The research results can be used to evaluate the background magnetic field distribution in the pipelines, and contribute to the magnetic field measurement strategies and the data analyses for PIG. For example, if we know the distribution characteristics of the background magnetic field inside the pipelines, we can make use of the mutation of the magnetic field near the girth weld to identify the weld to correct the mileage measurement error of the in-pipe detector, utilize the abnormal magnetic field to estimate the pipeline damage, or adopt the magnetic field in the pipelines to calculate the angle between the geomagnetic field and pipeline to determine the pipeline route. It is also obvious that considering the background magnetic field distributions in the pipelines can make it closer between PIG's detection analysis results based on the magnetic field inside the pipelines and the actual pipelines' disfigurement conditions, thus reducing calculation error and improving the detection precision.

REFERENCES

[1] Y. Zhou, H. R. Dong, Z. G. Zhou, and H. Xie, "The development of in-line inspection technology of oil and gas pipeline," *China Petroleum Machinery*, vol. 39, no. 3, pp. 74-77, 2011.

[2] W. Zhao, Z. M. Zeng, S. L. Chen, Y. Zhang, and S. J. Jin, "Analysis and experimental study of the characteristic of geomagnetic field inside pipeline," *Chinese Journal of Scientific Instrument*, vol. 33, no. 7, pp. 1556-1560, July 2012.

[3] S. I. Sheikh, H. A. Ragheb, K. Y. Alqurashi, and I. Babelli, "A microwave technique for detecting water deposits in an air flow pipelines," *Applied Computational Electromagnetics Society Journal*, vol. 25, no. 7, pp. 647-651, July 2010.

[4] F. Deek and M. El-Shenawee, "Microwave detection of cracks in buried pipes using the complex frequency technique," *Applied Computational Electromagnetics Society Journal*, vol. 25, no. 10, pp. 894-902, Oct. 2010.

[5] S. Nakamura, T. Nomura, and M. Iwamoto, "Three dimensional analysis of leakage field in a power transformer," *IEE Trans. Japan*, vol. 96, no.

5, pp. 443-450, 1976.

[6] M. Kobayashi and H. Iijima, "Surface magnetic charge distributions of cylindrical tubes," *IEEE Transactions on Magnetics*, vol. 32, no. 1, pp. 270-273, Jan. 1996.

[7] M. Kobayashi and Y. Ishikawa, "Surface magnetic charge distributions and demagnetizing factors of circular cylinders," *IEEE Transactions on Magnetics*, vol. 28, no. 3, pp. 1810-1814, May 1992.

[8] K. Ozaki, M. Kobayashi, and G. Rowlands, "Surface magnetic charge distribution of a long, thin cylinder and its edge singularity," *IEEE Transactions on Magnetics*, vol. 34, no. 4, pp. 2185-2191, July 1998.

[9] M. Kobayashi, Y. Ishikawa, and S. Kato, "Magnetizing characteristics of circular cylinders in perpendicularly applied magnetic field," *IEEE Transactions on Magnetics*, vol. 32, no. 1, pp. 254-258, Jan. 1996.

[10] S. Kato and M. Kobayashi, "Magnetic charge densities around edges of circular cylinders," *IEEE Transactions on Magnetics*, vol. 32, no. 3, pp. 1880-1887, May 1996.

[11] S. Sakurai, N. Soda, M. Kobayashi, and G. Rowlands, "Geometries with the demagnetizing energy independent of the direction of magnetization," *IEEE Transactions on Magnetics*, vol. 43, no. 3, pp. 982-991, March 2007.

[12] N. Soda, M. Kobayashi, and G. Rowlands, "Charge densities and inclination angles of magnetization on various surfaces of rotational symmetry," *IEEE Transactions on Magnetics*, vol. 40, no. 4, pp. 1763-1768, July 2004.

[13] J. Chen and X. W. Lu, "A method for magnetic field prediction caused by naval vessels using magnetic charge distribution," *ACTA Physica Sinica*, vol. 58, no. 6, pp. 3839-3843, June 2009.

[14] S. X. Wang and Y. X. Jia, "Equivalent magnetic monopoles model for calculation of magnetic field," *Journal of Taiyuan Heavy Machinery Institute*, vol. 11, no. 3, pp.85-87, 1990.

[15] Q. Bing, "Quick reference of commonly used steel's magnetic characteristic curve," *Beijing: China Machine Press*, pp. 17-18, 2004.

Huang Xinjing was born on April 13, 1987, in the Henan province of China. He received his B.Sc. degree in the Tianjin University where he is currently working toward his Ph.D. degree. His current research interests involve the distribution characteristics of the magnetic field in the pipeline and its application in the detection and location of pipeline damage.

Chen Shili, was born in the Hubei province, China, in 1973. He received his B.Sc. and Ph.D. degrees both from the College of the Precision Instrument & Opto-electronics Engineering of Tianjin University, in 1997 and 2003, respectively. Here he is currently an Associate Professor. His research interests include ultrasonic phased array inspection, novel online in-pipe detector, pipeline safety warning, etc.

Jin Shijiu received his B.Sc. and M.Sc. degrees in 1970 and 1981, respectively, both from the College of Precision Instrument & Opto-electronics Engineering of the Tianjin University, where he is now a Professor, and a doctoral supervisor. His main research area covers detection technology and equipment, automatic measurement and control system, system integration and optimization, etc.

Shore to Ship Steerable Electromagnetic Beam System Based Ship Communication and Navigation

P. R. P. Hoole [1], S. T. Ong [2], and S. R. H. Hoole [3]

[1] Department of Electrical and Electronic Engineering
Papua New Guinea University of Technology, Lae, Papua New Guinea
prphoole@gmail.com

[2] Motorola Malaysia Sdn Bhd
47300 Petaling Jaya, Selangor, Malaysia
syinthon@gmail.com

[3] Department of Electrical and Computer Engineering
Michigan State University, East Lansing, MI 48824, USA
srhhoole@gmail.com

Abstract **─** Electromagnetic waves prove to be a common ground for producing integrated systems that use a single transmitter, receiver, and computer system to perform communication, navigation, and surveillance activities. A steerable beam array antenna serves to communicate from shore to a moving ship close to the harbor. In this paper, the communication system parameters are used also to navigate the ship to a predetermined harbor dock. Knowledge of the electromagnetic radiation pattern of the beam steering array antenna, the position of the ship, and the predetermined trajectory for the ship are used to create an on-line navigational system that is driven by the received communication signal power. The discrepancies in signal power measured and the expected received power are used as an indicator that the ship is not properly aligned to the transmitter beam peak point. This discrepancy that is obtained by a signal processor is used to reset the rudder angle through a PID controller. It is shown that this system successfully keeps the ship within the border lines of the trajectory that had been marked out to guide the ship to its harbor dock. Moreover, the antenna electromagnetic beam, like a torch, moves a step ahead of the ship along the trajectory, allowing for automatic navigation of the ship as the ship's rudder is activated to move the ship to keep within the antenna beam's half-power points.

Index Terms **─** Antennas, electromagnetic signal processing, controls, and ship steering.

I. INTRODUCTION

Major ports over the world, including the port Klang in Malaysia, are undergoing restructuring to increase ship handling capacity, merging separate and distant berthing docks for different operators into a single large housing of multiple berths, and to tighten security both underwater and on sea surface. In each one of these futuristic changes, electromagnetic-based systems are expected to play a major role from satellite or aircraft based surveillance to narrow beam antennas to track, communicate, and navigate ships and fast boats within a limited space of waters close to the port [1]. In this paper, we report an integrated system for communication and navigation of a ship using a single spectrum, array antenna radiated electromagnetic waves to carry information and to provide the required parameters to estimate the position of the ship, the direction of its travel, and the speed required by the ship controller to navigate the ship along a path to the dock, determined by the port control officers.

Submitted On: G^k+. .)/-. /
Accepted On: J ^v 0.)/-. 0

Ship communication stations may communicate with other ship stations or coast stations primarily for safety, and secondarily for navigation, and operational efficiency. However, wireless communication is in general subject to phenomena such as electromagnetic interference, unintended wave reflections, and atmospheric effects, which may deteriorate the electromagnetic signal quality, leading to lower possible bandwidth and errors in the transmitted signal. Hence, analysis and comparison of the communication carriers that are used for ship-shore communication are necessary to expose strengths and weaknesses in the geographical areas where the electromagnetic carriers may be used, how they fulfill different communication needs, and so on [2, 3].

The skill and knowledge required to navigate a ship close to a harbor versus at sea is significantly different [4, 5]. In the middle of the sea, the ship may be guided by the satellite signal using super high frequency bands. However, a shore based system usually involves a harbor base station (BS) for ship-to-shore communication. The very-high frequency bands and ultra-high frequency bands are commonly known as line-of-sight transmission bands and can be used for land-to-ship communication [5-8]. These also lend themselves well to signal processing the mathematically well defined electromagnetic radiation to get narrow, steerable beams which may be used to estimate the parameters of ship motion needed for navigation. The computation of the line-of-sight electromagnetic communication beam strength at the ship's receiver antenna is used as the basis for automatic ship navigation.

II. DESIGN CONSIDERATIONS FOR SHORE-TO-SHIP COMMUNICATION

An array antenna is usually chosen for shore to ship communication [1, 9, 10] as we did here. The more the elements an array antenna has, the better the gain and quality of the received signal; nevertheless, in order to keep the cost to a minimum and to make the signal processor fast and less heavy on digital memory, a two- element array antenna has been chosen as the transmitter antenna. An analytical solution for the electromagnetic power radiated is assumed to be known, which is the case for a two element array antenna. There are several types of radiation pattern that can be formed using different phase excitations between adjacent elements such as broadside, end-fire, and even scanning phase radiation patterns. Since the communication between ship station and shore station focuses only in the front direction, the end-fire radiation pattern is a good choice as it gives no radiation towards the back (landside) of the antenna, causing no waste of energy or interference with land systems. As in wireless mobile communications [11, 12], the position of the mobile station, and hence the position of the ship itself, could be determined by the communication signal when appropriately processed using a mathematical model of electric field strength and the actual electric field (corrupted by noise) received on board the ship. This feature has not yet been incorporated into the communication-navigation system reported in this paper.

III. THE SCENARIO OF THE ELECTROMAGNETIC ENVIRONMENT

Figure 1 shows the ship moving close to the coast and being guided by the antenna radiation pattern from the shore to its destination. Beam-forming at the shore base station antenna is done to maximize the signal-to-noise ratio of the communication link, as well as guide the ship along the pre-planned trajectory towards the dock. The study on ship dynamics is compulsory in order to control the motion of the ship. A mathematical ship model is necessary when designing an adaptive autopilot ship steering controller. A mathematical model is developed based on Fig. 2. The ship's path is sketched out by the moving antenna beam, like a torch lighting the path ahead. The ship is moving in the same direction as the steered antenna beam and eventually it is guided by the antenna beam to the dock.

The ship is kept moving within the half-power beam-width of the base station antenna's radiation pattern so that the received signal strength is always within the 500 km and 1500 km track. The radiation energy outside the half-power region is assumed to be negligible. Thus, successive beam-forming is needed to assure that the ship is kept moving within the half-power region and successfully navigated to its destination. The fluctuations in the electromagnetic signal are used to control the rudder of the ship through a PID controller [13, 14]. Assumptions made to develop this basic integrated electromagnetic system included ignoring signal noise and disturbances caused by other ships and boats to navigation. The ship's propeller system, and hence the speed of the ship, are not taken into account. Further refined development of this new system to make it implementable in a busy harbor should take these factors into account.

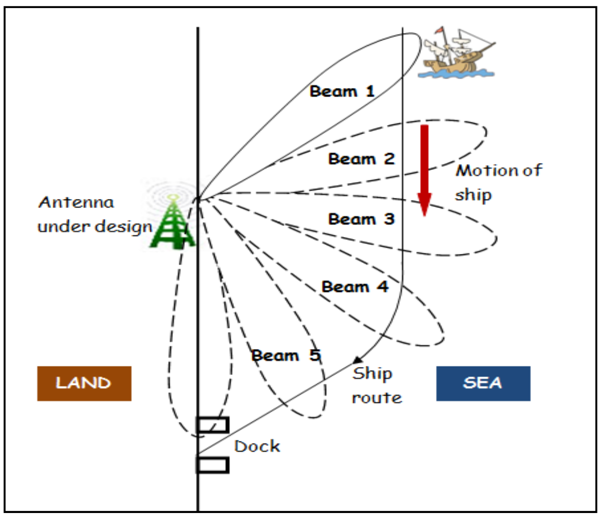

Fig. 1. Illustration of ship navigation system using antenna radiation pattern.

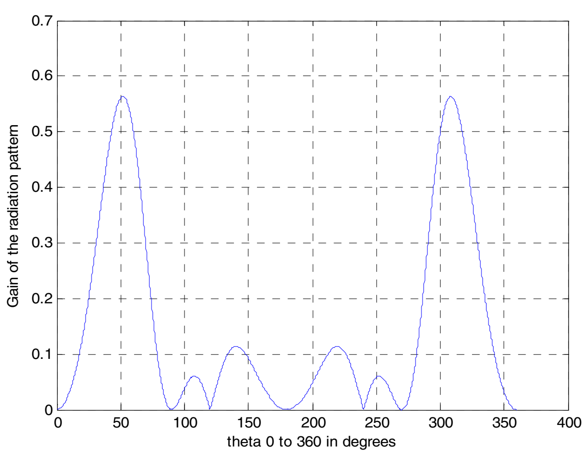

(a) Rectangular plot of the phase scanning array pattern.

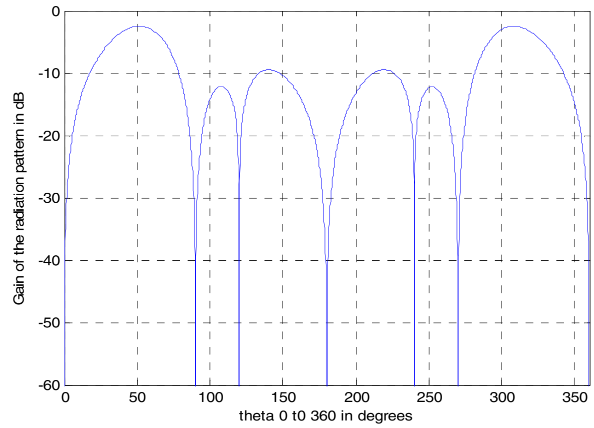

(b) Rectangular plot of the phase scanning array in dB.

Fig. 2. Radiation plot of the phase scanning array in polar and rectangular forms.

In Fig. 2 the radiation pattern is given for the two element antenna when pointed 50^{o} away from the end fire axis. Although the beam-width is wide and side-lobes significant, for the specific scenario we considered without other interferers and signal noise, in the absence of other ships, the two element array was found adequate to steer the ship to its dock, keeping the ship within the specified track. The three tracks for which the integrated communication-navigation system was tested are shown in Fig. 3. In the first two cases the ship is initially outside the specified track, and the communication system must drive the ship control system to navigate it into the track, and then to the dock.

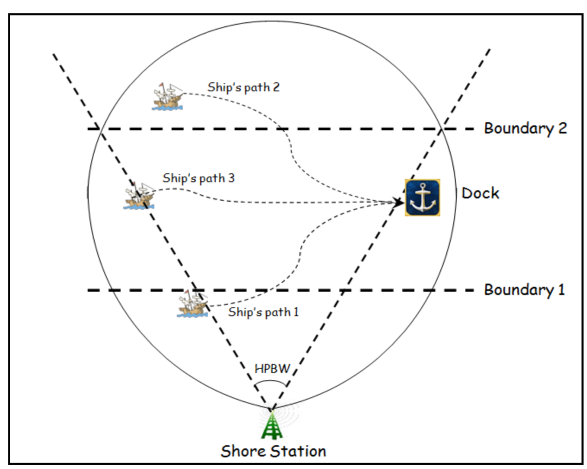

Fig. 3. Ship motion within the half-power beam-width.

In Fig. 3 we may also see the initial complex navigation, using the communication antenna, required to bring the ship to the straight forward trajectory once inside the two boundaries. The direction or turning angle of the ship will be different in order to guide the ship to the dock. The ship is being correctly guided as long as the ship is inside the half-power beam-width region. Two element end-fire array beam-forming is used as the shore-based base station guiding beam for the ship. There are two assumptions made: (a) The radiation energy outside the half-power beam-width is very low and is thus negligible; and (b) the radiation pattern is assumed to be uniform over the angle of the half-power beam-width.

IV. DYNAMICS OF SHIP NAVIGATION

The study on ship dynamics is compulsory in order to control the motion of the ship. A mathematical ship model is necessary when designing an adaptive autopilot ship steering controller. A mathematical model is developed based on Fig. 4, where (x_0, y_0) is the starting point of the ship, $\delta(t)$ is the instantaneous rudder angle, $(x(t), y(t))$ is the instantaneous position of the ship with respect to the coordinate system (X, Y), $\psi(t)$ is the heading angle at instant "t" with respect to the Y-axis, (x_G, y_G) is the heading position, $\psi_G(t)$ is the desired heading angle at instant "t" with respect to the Y-axis and V is the forward speed of the ship. The state of ship is defined by x(t), y(t), and $\psi(t)$ and its time derivative $\psi(t)$.

Now let r(t) be the desired turning rate of the ship. In this paper we have only considered the control of the rudder, and not that of the propeller [13]. Moreover, we have not considered collision avoidance in an environment in which other ships or boats may prove a threat to the ship [4]. The equations of motion in the discrete form are given by [13],

$$x(t+1) = x(t) + \Delta V \sin\psi(t) \tag{1}$$

$$y(t+1) = y(t) + \Delta V \cos\psi(t)\,, \tag{2}$$

$$\psi(t+1) = \psi(t) + \Delta\dot{\psi}(t), \tag{3}$$

and

$$\dot{\psi}(t+1) = \dot{\psi}(t) + \frac{\Delta\left(\mathrm{r(t)}-\psi(\mathrm{t})\right)}{\mathrm{T}}. \tag{4}$$

V. CONTROL SYSTEM FOR SHIP STEERING

The control system block diagram for a conventional controller is shown in Fig. 5. In the conventional ship steering controllers, the whole control system is developed for one set point. Hence, the controller is based on a linear model. In the PID controller design presented herein, the controller is developed using a varying set-point generator as indicated in Fig. 5. The set-point generator determines the desired heading angle at each state of the ship. At each point in the state space, the generator finds the desired heading with reference to the target point (destination). The controller input is the error obtained by comparing the present heading of the ship with the desired heading. With the variation of ship position coordinates (Fig. 4), the desired heading varies. Therefore, a desired heading generator is introduced into the system, which will determine the desired heading by looking at the target point.

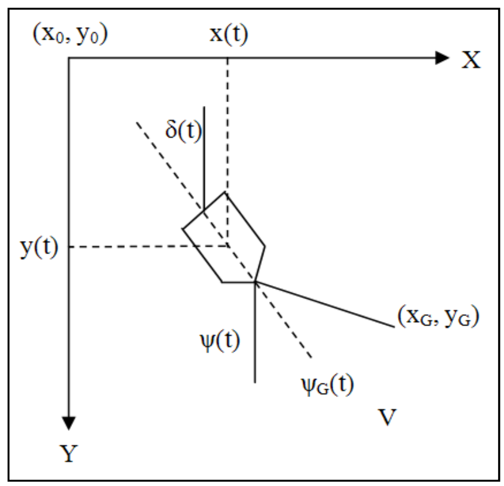

Fig. 4. Coordinates and notation used to describe the motion of a ship.

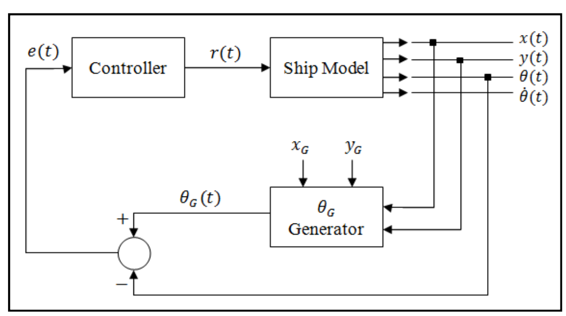

Fig. 5. Block diagram of the PID control system.

The design interface for a PID controller is determined by the following equations,

$$\theta_G = \tan^{-1}\frac{X_G - x(t)}{Y_G - y(t)} \quad (5)$$

$$e(t+1) = \theta_G - \theta(t+1)\ , \quad (6)$$

$$u(t+1) = \frac{k_I \times (e(t+1) + e(t)) \times \Delta}{2} \quad (7)$$

and

$$r = k_P \times e(t+1) + u(t+1) + \frac{k_D \times (e(t+1) - e(t))}{\Delta} \quad (8)$$

where θ_G is the set point generator output, and e(t) is the error of turning rate compared to the desired turning rate, θ_G. The PID controller output at instant t is given by,

$$r(t) = U_p(t) + U_I(t) + U_D(t), \quad (9)$$

where,

$$U_P(t) = K_P e(t) \quad (10)$$

$$U_I(t) = U_I(t-1) + K_I e(t), \quad (11)$$

and

$$U_D(t) = K_D \frac{(e(t) - e(t-1))}{\Delta}. \quad (12)$$

The large changes in the heading angle over the initial distances are due to the communication signal driving the ship back into its lane. Once inside the lane, it gradually settles at an angle of about 1^0 to keep it moving along the track as the moving transmission beam guides the ship smoothly along the track towards the dock.

Figure 6 shows the ship navigation for the ship path 2 shown in Fig. 3, where the position of the ship is initially beyond the second predefined boundary. The communication signals have to navigate the ship back into the path within which the ship needs to be kept and guided towards the dock. The ship control system will constantly adjust the heading angle of the ship by suitable turning. It is seen from Figs. 6 and 7 that the ship has been guided to its dock successfully.

Figure 7 shows the instantaneous heading angle with respect to the position of the ship for case 2. The heading angle in case 2 is always negative, thus the ship moves on in the downward direction until it reaches the dock. It can be seen that the heading angle of the ship changes significantly at the beginning. The changes in the heading angle get smaller and smaller until the desired heading angle is found for smooth guidance once the ship is back inside the predefined lane between 500 km and 1500 km; the changes in heading angle then become insignificant.

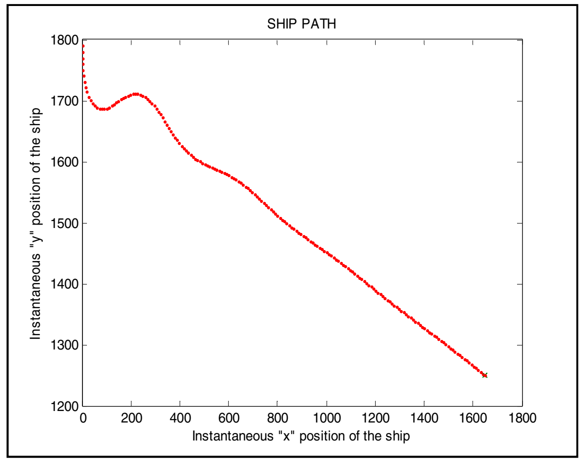

Fig. 6. Instantaneous position of the ship in km (Case 2 - ship on path 2).

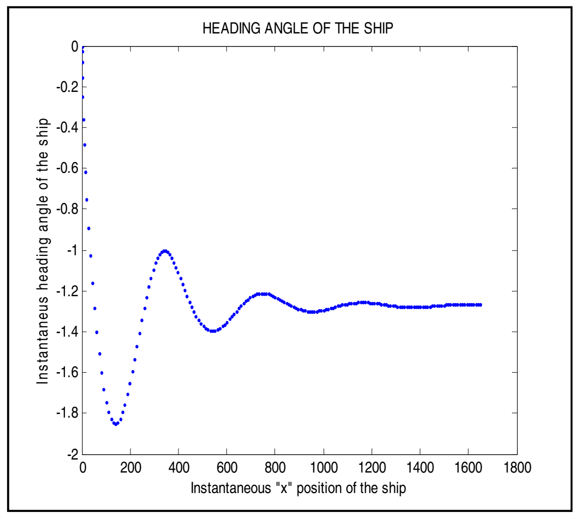

Fig. 7. Instantaneous heading angle of the ship against position 9 km (Case 2).

VI. COMBINED COMMUNICATION BEAM – PID SHIP CONTROLLER

In this section, we demonstrate the high performance of this communication beam based navigation by putting together the three new modules developed and reported in this paper:

(a) Adaptive, digital control of land to ship communication antenna beam. At present, all ship controllers use additional onboard and shoreline sensors to feed ship position and speed data to the PID controller. In this paper we report a new way of ship control, where the PID controller navigates the ship by using the shore to ship communication signals, without any extra sensors needed to trigger the PID controller action to change the rudder angle.

(b) The ship PID controller driven by antenna beam error correction.

(c) The computer simulated dynamics of a ship being guided by the integrated communication-navigation system, towards its dock in a harbor.

The ship's path is specified in a way that it will cross the two predefined boundaries as shown in Fig. 6. The ship will initially travel in an upwards direction until it passes out of the second boundary and the integrated system will automatically adjust the heading of the ship so that it is guided back in to the desired region. The ship will continue in the downwards direction and after it passes the first boundary, again it will be guided back into the lane bounded by the two boundaries. Eventually, it will reach its dock successfully.

Figure 8 shows the ship navigation for the integrated communication and navigation system. It is seen that the ship has been guided back into the lane when it passes the second boundary. The detection of the ship straying out of the safe track set to it is determined by measuring the power density of the signal received on board the ship. If the power density at the onboard communication receiver drops below a preset value, it is an indication that the ship has strayed out of the upper border line of the track. Similarly, if the received power density increases above a preset value, it is an indication that the ship is out of the lower boundary line of the track and is straying closer to the coastline. In either case the communication receiver triggers into action the control of the rudder to bring the ship back into the safe track. Furthermore, it is also seen in Fig. 8 that when the ship goes below the first boundary at about (700 km and 500 km) it has been guided back to the correct ship lane. The ship eventually reached its dock successfully.

Figure 9 shows the instantaneous turning rate of the ship for the communication-navigation integrated system. From the graph (where the angles are in radians), the largest positive turning rate is approximately 20° per second whereas the largest negative turning rate is -17.2° per second. The values of the largest positive turning rate and largest negative turning rate are beyond the limits. Although there are large turnings in the middle stage of the ship navigation, the overall performance has not been affected. The ship succeeded in getting its desired heading angle and reached its dock. In Fig. 7 it is seen that the turning rate remains nearly unchanging after the ship's desired heading angle is found. In this paper we have not taken into consideration the need not only to navigate the ship along the track set by the port authorities, but also to avoid collision with other ships or fast boats that may stray into its path. This aspect of navigation is not considered herein. We are addressing collision avoidance as a separate issue at this time, and at a later stage hope to connect it to seek a new system that integrates communication, navigation and collision avoidance all using a single system operating in a signal carrier and narrow bandwidth.

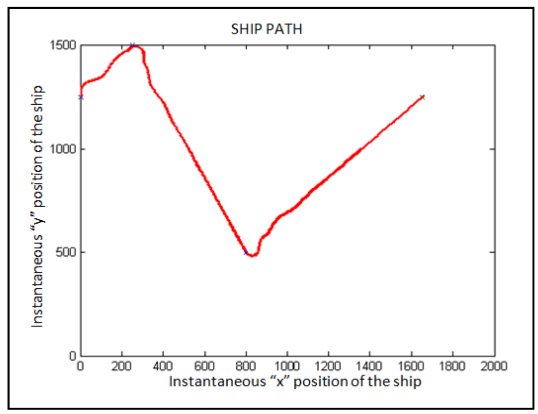

Fig. 8. Instantaneous position of the ship (guided by the integrated system).

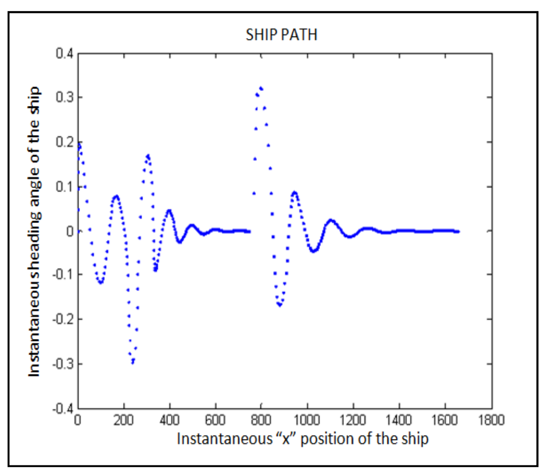

Fig. 9. Instantaneous turning rate of the ship (Integrated System).

VII. CONCLUSION

The main object of the integrated communication-navigation system was to develop a practical land-to-sea communication system using smart antennas, that would also navigate the ship to its dock (harbor destination). This was satisfactorily accomplished and tested for three different cases. For the ship communication system, a multi-element digitally beam steerable antenna is used in order to design a suitable land based communication system. An algorithm for keeping the ship within the half-power-beam-width (HPBW) has been developed, and as a further step, this algorithm has been used to navigate the ship along a prescribed path to its dock. The electromagnetic beam used for a shore to ship communication system was used successfully to perform two important functions of the navigation systems: (a) to step by step steer or show the ship the trajectory it should follow to get to the dock. The ship is kept close to the trajectory by making it move along the radiation beam to keep it at the center of the beam as the beam moves along the trajectory leading the ship. The ship's rudder is controlled by the variations in the transmitted power received on board the ship. (b) If the ship should stray away from the prescribed boundaries on either side of the trajectory, the marginal difference in the electromagnetic power received by the ship's communication receiver is used to control the rudder of the ship to guide it back to the trajectory and within the boundaries on either side of the trajectory.

REFERENCES

[1] J. E. Rhodes, *Field Antenna Handbook*, U. S. Marine Corporations, 1999.
[2] T. Perez, *Ship Motion Control: Course keeping and Roll Stabilisation Using Rudder and Fins*, Springer-Verlag London Limited, 2005.
[3] B. K. Rødseth, Å. Tjora, and F. Drezet, *European Framework for Safe, Efficient and Environmentally-friendly Ship Operations*, in Sustainable Surface Transport, 2000.
[4] A. R. J. Ruiz and F. S. Granja, "A short-range ship navigation system based on ladar imaging and target tracking for improved safety and efficiency," *IEEE Trans. Intelligent Transportation Systems*, vol. 10 , no. 1, pp. 186-1975, 2009.
[5] D. Dooling, "Navigating close to shore," *IEEE Spectrum*, vol. 31, no. 12, pp. 24-31, 1994.
[6] Z. S. Ping and C. Yu, "Modern ship-to-shore data communications technology," *Proc. IEEE Conf. Electric Information and Control Engineering (ICEICE)*, pp. 4280-4283, 2011.
[7] F. Bekkadal and K. Yang, "Novel maritime communications technologies," *Proc. IEEE Microwave Symposium (MMS)*, pp. 338-341, 2010.
[8] F. Bekkadal, "Emerging maritime communications technologies," *IEEE Proc. Conf. Intelligent Transport Systems Telecommunications, (ITST)*, pp. 358-363, 2009.
[9] W. Rudge, K. Milne, A. D. Olver, and P. Knight, *The Handbook of Antenna Design*, vol. 2, London, U. K. : Peter Peregrinus Ltd. 1983.
[10] P. R. P. Hoole, *Smart Antennas and Signal Processing*, WIT Press, UK, 2001.
[11] X. Wang, P. R. Hoole, and E. Gunawan, "An electromagnetic-time delay method for determining the positions and velocities of mobile stations in a GSM network," *Progress In Electromagnetics Research*, vol. 23, pp. 165-186, 1999.
[12] P. R. Hoole, K. Pirapaharan, and S. R. Hoole, "An electromagnetic field based signal processor for mobile communication position-velocity estimation and digital beam-forming: an overview," *The Journal of the Japan Society of Applied Electromagnetics and Mechanics*, vol. 19, pp. S33-S36, Fall 2011.
[13] T. Fossen, *Handbook of Marine Crafts Hydrodynamics and Motion Control*, John Wiley, New York, 2011.
[14] T. Fossen, *Guidance Control of Ocean Vehicles*, John Wiley, New York, 1994.

Paul R. P. Hoole was born in Jaffna, Sri Lanka in 1958. After having his basic schooling in Jaffna, he earned all his degrees, first degree to postgraduate, in the United Kingdom. He holds an M.Sc. degree in Electrical Engineering with a mark of distinction from the University of London and an M.Sc. degree in Plasma Science from University of Oxford. His PhD is from the University of Oxford. In his engineering career he has spent time in Singapore, Papua New Guinea, USA, Sri Lanka, and Malaysia. After a long career as a Professor of Electrical Engineering, because of his interests in lightning engineering, he has just embarked on a job as a Professor of Electrical and Electronic Engineering at the Papua New Guinea University of Technology in Lae, PNG.

Prof. Hoole has authored several papers and books in engineering. His latest book (with K. Pirapaharan and S. R. H. Hoole), *Electromagnetics Engineering Handbook*, was released by WIT Press, UK, in June 2013. Beyond the time he devotes to engineering teaching and research, Prof. Hoole also spends time studying and teaching the Bible applied to contemporary times in seminaries and churches. He is married to a medical doctor, Chrishanthy, and they have three children: Esther, Ezekiel and Elisabeth.

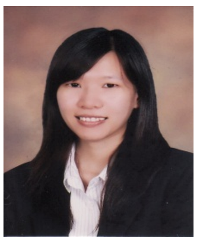

Ong Syin Thon was born in a small town in Kedah, Malaysia in the year 1988. Her family, the Ong family, decided to move to an island which is known as Langkawi when she was six years old. Syin Thon's early education starts there from primary going on to secondary. She thereafter continued her pre-university studies for a year in Penang Matriculation College where her main discipline was Physics. She considers herself lucky to have been enrolled into University of Malaya, one of the top universities in Malaysia. Following four years' study majoring in the engineering field, she graduated in Telecommunications in 2011. This paper reports her research for her Telecommunication Engineering degree.

Ms. Ong's career as a software automation test engineer began at Motorola Solutions in Penang and was a valuable experience to her. She learned how important her role as an engineer is and ways to work and communicate with people in this big company. However, she decided to get herself a new career in Kuala Lumpur in order to stay closer to her friends and family. Thus, she became a software consultant at ISA Innovation, which is a small company but definitely a good place to learn new things related to software and solutions.

Ms. Ong enjoys learning new things. Outside of her profession, she wishes to learn a new language, a new musical instrument and so on. She is now in the middle of learning Japanese, hoping that perhaps someday she can travel to Japan without a tour guide.

S. Ratnajeevan H. Hoole, B.Sc. Eng. Hons Cey., M.Sc. with mark of distinction from London, Ph.D. Carnegie Mellon, is Professor of Electrical and Computer Engineering at Michigan State University in the US. For his accomplishments in electromagnetic product synthesis the University of London awarded him its higher doctorate, the D.Sc. (Eng.) degree, in 1993, and the IEEE elevated him to the grade of Fellow in 1995. Prof. Hoole has been Vice Chancellor of University of Jaffna in Sri Lanka, and as Member of the University Grants Commission there, was responsible with six others for the regulation of the administration of all 15 Sri Lankan universities and their admissions and funding. He has contributed widely to the learned literature on Tamil studies and been a regular columnist in newspapers. Prof. Hoole has been trained in Human Rights Research and Teaching at The René Cassin International Institute of Human Rights, Strasbourg, France, and has pioneered teaching human rights in the engineering curriculum.

2013 INSTITUTIONAL MEMBERS

DTIC-OCP LIBRARY
8725 John J. Kingman Rd, Ste 0944
Fort Belvoir, VA 22060-6218

AUSTRALIAN DEFENCE LIBRARY
Northcott Drive
Canberra, A.C.T. 2600 Australia

BEIJING BOOK CO, INC
701 E Linden Avenue
Linden, NJ 07036-2495

DARTMOUTH COLLEGE
6025 Baker/Berry Library
Hanover, NH 03755-3560

DSTO EDINBURGH
AU/33851-AP, PO Box 830470
Birmingham, AL 35283

SIMEON J. EARL – BAE SYSTEMS
W432A, Warton Aerodome
Preston, Lancs., UK PR4 1AX

ENERGY KEN LIBRARY
PO Box 300613
Jamaica, NY, 11430

ENGINEERING INFORMATION, INC
PO Box 543
Amsterdam, Netherlands 1000 Am

ETSE TELECOMUNICACION
Biblioteca, Campus Lagoas
Vigo, 36200 Spain

GA INSTITUTE OF TECHNOLOGY
EBS-Lib Mail code 0900
74 Cherry Street
Atlanta, GA 30332

TIMOTHY HOLZHEIMER
Raytheon
PO Box 1044
Rockwall, TX 75087

HRL LABS, RESEARCH LIBRARY
3011 Malibu Canyon
Malibu, CA 90265

IEE INSPEC
Michael Faraday House
6 Hills Way
Stevenage, Herts UK SG1 2AY

INSTITUTE FOR SCIENTIFIC INFO.
Publication Processing Dept.
3501 Market St.Philadelphia, PA
19104-3302

LIBRARY – DRDC OTTAWA
3701 Carling Avenue
Ottawa, Ontario, Canada K1A OZ4

LIBRARY of CONGRESS
Reg. Of Copyrights
Washington DC, 20559

LINDA HALL LIBRARY
5109 Cherry Street
Kansas City, MO 64110-2498

MISSOURI S&T
400 W 14th Street
Rolla, MO 56409

MIT LINCOLN LABORATORY
244 Wood Street
Lexington, MA 02420

NATIONAL CHI NAN UNIVERSITY
Lily Journal & Book Co, Ltd
20920 Glenbrook Drive
Walnut, CA 91789-3809

JOHN NORGARD
UCCS
20340 Pine Shadow Drive
Colorado Springs, CO 80908

OSAMA MOHAMMED
Florida International University
10555 W Flagler Street
Miami, FL 33174

NAVAL POSTGRADUATE SCHOOL
Attn:J. Rozdal/411 Dyer Rd./ Rm 111
Monterey, CA 93943-5101

NDL KAGAKU
C/0 KWE-ACCESS
PO Box 300613 (JFK A/P)
Jamaica, NY 11430-0613

OVIEDO LIBRARY
PO BOX 830679
Birmingham, AL 35283

DAVID PAULSEN
E3Compliance
1523 North Joe Wilson Road
Cedr Hill, TX 75104-1437

PENN STATE UNIVERSITY
126 Paterno Library
University Park, PA 16802-1808

DAVID J. PINION
1122 E Pike Street #1217
SEATTLE, WA 98122

KATHERINE SIAKAVARA
Gymnasiou 8
Thessaloniki, Greece 55236

SWETS INFORMATION SERVICES
160 Ninth Avenue, Suite A
Runnemede, NJ 08078

YUTAKA TANGE
Maizuru Natl College of Technology
Maizuru, Kyoto, Japan 625-8511

TIB & UNIV. BIB. HANNOVER
Welfengarten 1B
Hannover, Germany 30167

UEKAE
PO Box 830470
Birmingham, AL 35283

UNIV OF CENTRAL FLORIDA
4000 Central Florida Boulevard
Orlando, FL 32816-8005

UNIVERSITY OF COLORADO
1720 Pleasant Street, 184 UCB
Boulder, CO 80309-0184

UNIVERSITY OF KANSAS –
WATSON
1425 Jayhawk Blvd 210S
Lawrence, KS 66045-7594

UNIVERSITY OF MISSISSIPPI
JD Williams Library
University, MS 38677-1848

UNIVERSITY LIBRARY/HKUST
Clear Water Bay Road
Kowloon, Honk Kong

CHUAN CHENG WANG
8F, No. 31, Lane 546
MingCheng 2nd Road, Zuoying Dist
Kaoshiung City, Taiwan 813

THOMAS WEILAND
TU Darmstadt
Schlossgartenstrasse 8
Darmstadt, Hessen, Germany 64289

STEVEN WEISS
US Army Research Lab
2800 Powder Mill Road
Adelphi, MD 20783

YOSHIHIDE YAMADA
NATIONAL DEFENSE ACADEMY
1-10-20 Hashirimizu
Yokosuka, Kanagawa,
Japan 239-8686